



FACULTAD DE CIENCIA Y TECNOLOGÍA
DEPARTAMENTO DE INGENIERÍA QUÍMICA

**VALORIZATION OF SCRAP TIRES PYROLYSIS OIL
(STPO) THROUGH A 2-STAGE
HYDROTREATING-HYDROCRACKING STRATEGY.
PROCESS VARIABLES AND KINETIC MODELING.**

TESIS DOCTORAL

Idoia Hita del Olmo
Marzo, 2015



FACULTAD DE CIENCIA Y TECNOLOGÍA

DEPARTAMENTO DE INGENIERÍA QUÍMICA

**VALORIZATION OF SCRAP TIRES PYROLYSIS OIL
(STPO) THROUGH A 2-STAGE
HYDROTREATING-HYDROCRACKING STRATEGY.
PROCESS VARIABLES AND KINETIC MODELING.**

MEMORIA

**Que para optar al grado de Doctora en Ingeniería Química
presenta**

Doña Idoia Hita del Olmo

Leioa, Marzo 2015

Cuando emprendas tu viaje a Itaca
pide que el camino sea largo,
lleno de aventuras, lleno de experiencias.
No temas a los lestrigones ni a los cíclopes
ni al colérico Poseidón,
seres tales jamás hallarás en tu camino,
si tu pensar es elevado, si selecta
es la emoción que toca tu espíritu y tu cuerpo.
Ni a los lestrigones ni a los cíclopes
ni al salvaje Poseidón encontrarás,
si no los llevas dentro de tu alma,
si no los yergue tu alma ante ti.

Pide que el camino sea largo.
Que muchas sean las mañanas de verano
en que llegues -¡con qué placer y alegría!-
a puertos nunca vistos antes.
Detente en los emporios de Fenicia
y hazte con hermosas mercancías,
nácar y coral, ámbar y ébano
y toda suerte de perfumes sensuales,
cuantos más abundantes perfumes sensuales puedas.
Ve a muchas ciudades egipcias
a aprender, a aprender de sus sabios.

Ten siempre a Itaca en tu mente.
Llegar allí es tu destino.
Mas no apresures nunca el viaje.
Mejor que dure muchos años
y atracar, viejo ya, en la isla,
enriquecido de cuanto ganaste en el camino
sin aguantar a que Itaca te enriquezca.

Itaca te brindó tan hermoso viaje.
Sin ella no habrías emprendido el camino.
Pero no tiene ya nada que darte.

Aunque la halles pobre, Itaca no te ha engañado.
Así, sabio como te has vuelto, con tanta experiencia,
entenderás ya qué significan las Itacas.

C. P. Cavafis.

AGRADECIMIENTOS

Personificando una de mis muchas "Itacas" vitales en forma de esta tesis y echando la vista atrás, resulta impresionante ver el equipaje que se ha ido acumulando en estos 4 años pre-doc. Han sido tantas las experiencias, la gente involucrada, y tan bueno el ambiente creado en el laboratorio que me resulta imposible separar el aspecto científico de la faceta más personal. Toda la gente que aquí menciono, estando o no relacionada con los aspectos técnicos de esta tesis, ha sido parte de ella. Por este motivo, permitidme que en estos agradecimientos en ocasiones prescinda de la seriedad que he intentado plasmar en el resto del documento.

Dar las gracias en primer lugar a mis directores, por haber guiado la batuta en esta sinfonía. Al Dr. Jose María Arandes, por darme esta oportunidad, confiar en mí desde un principio y haber prestado sus consejos y toda su experiencia al desarrollo de esta tesis. Y al Dr. Pedro Castaño, por su gran implicación en este trabajo, y haberme siempre escuchado, orientado y ayudado, tanto en el laboratorio como en el aspecto personal (¡bendito cuaderno para las buenas ideas!). Por la infinita pasión y curiosidad con las que trabajas, quisiera desde estas líneas transmitirte mi más profunda admiración, respeto y cariño. Serás para mí un claro referente durante toda mi carrera, *Boss*. Y gracias también a *tu* Elena por haberme tratado siempre con tanto cariño.

Al Dr. Javier Bilbao, por aportar su enorme visión y sus conocimientos para la conclusión de esta tesis. Al Dr. Gartzzen López, por prestarme todos sus conocimientos *pirolizadores* para acabar con esos neumáticos. Y como no al Dr. Andrés Aguayo, porque no hay vector ni hipermatriz que pueda contener toda la ayuda prestada (ni la paciencia...) en el desarrollo del modelado cinético y en los aspectos más técnicos del trabajo en el laboratorio (¡al final el Matlab funcionó, Andrés!). Muchas gracias a los tres.

Thanks to Prof. Josephine M. Hill, for giving me the opportunity to work under her supervision at the Department of Petroleum and Chemical Engineering at the University of Calgary (Alberta, Canada), and learn from her Group. Also thanks to everyone (especially Julian, Bruno, Anton and Julia), with whom I shared adventures discovering Alberta and the Canadian Rockies during those four months and became my Canadian gang. It was truly an unforgettable experience I will always treasure.

A todos los compañeros con los que he compartido laboratorio durante todo este tiempo y que tanto me han ayudado; Diana, Koke, Bea (nunca pierdas ese sentido del humor, *Dra. Bitri*), Alazne (¡qué grandes ratos junto al reactor! Tenemos el Nobel a un pasito Alaz...), Aitzi Errekatz, Moni (*La Mofetilla* no habría existido sin ti...), Gorka, Lide, Álvaro (momentazos en el Labo 3), Ainara (por tus manos siempre dispuestas a ayudar), Aingeru, Caro, Iñigo, Paula, Elena

(la reina del Hellriser), Aitor Arandia, Aitziber Erkiaga, Aitor Arregi, Itsaso, Maider, Maite y un largo etc. Y en especial a Borja (*Boooooortxi!!!!!!*) por haber sido el mejor compi de mesa que podía haber tenido desde el comienzo y por haberte convertido en un amigo con el que he compartido tantas risas y confidencias. Gracias por haberme aconsejado siempre tan bien, y por llevarme la contraria siempre que hizo falta. También a Rober (*Robbbbiiiiiee!*) y Mikel (*Maaaaaikoooo!!!*) por ser la reencarnación de Zipi y Zape, por vuestra ayuda, sentido del humor y los buenos ratos de tertulia.

¡Y cómo no a los otros dos miembros del selecto club de hijas únicas del laboratorio! A Eva (*always in love!*), por nuestras charlas en el coche y prestarme tu ayuda y ánimos tanto en lo profesional como en lo personal, siempre con una sonrisa. Eskerrik asko Evita! Y como no, a *mi Pitxu*, la Mery (*Jesuuuuussss!!!*), mi compi de fatigas, comidas mexicanas, *poltergeists* en los hoteles, sesiones de cine, de avistamientos de pavos reales y epistólicas introducciones que tanto quitan el sueño al *Boss*. Gracias por haber sido en todo momento mi gran apoyo en el laboratorio, haberme ayudado tanto (sobre todo en este “no tan sencillo” tramo final), y tantas cosas que hemos compartido juntas. Eres sin duda un enorme tesoro personal que me llevo de esta etapa. ¡Te mereces lo mejor, *Pitxu!* ¡Gracias!

También a Jon y Jose (a.k.a. Juanito y Giuseppe), por formar el *engineering trio* y todos los momentos compartidos ya desde aquella primera semana de carrera (allá por el 2005...). Os deseo lo mejor a los dos.

A Coke, con quien he podido compartir las fatigas pre-doc siempre entre risas, platos de paella y alguna caña. ¡Gracias por los ánimos y mucha fuerza amigo, que ya no queda nada!

A mis *Txabelitas*. Cris y Ainara, por todo lo que habéis sido desde que éramos unas enanas, y lo que en tantos años hemos vivido juntas, por tantas risas y recuerdos, y las energías que me habéis prestado. (¡Y muchísimas gracias Cris por el *swag* de la portada!). Espero que podamos seguir llorando juntas de la risa muchos años más.

A todo Ze Arraio, por la inyección de alegría que sois y por los ánimos que todos y cada uno me habéis dado en un momento u otro. Silvia, por tu sensibilidad y tu capacidad sin límites para escuchar y comprender, gracias por todo; Samuel, porque nunca se me olvida reír cuando estás cerca; Irati, porque nunca dejes de bailar; Eli, por esos “*ánimo txiki!*” tan tuyos. Y en especial a mis dos *Pitxutxis*: A Ane (*ayanamari!*), por las mil confidencias, por tu empatía y tu alegría permanente, no la pierdas nunca. Y a ti, Maialen, nire *Maialook*, por esa conexión que nadie entiende, por ser Thelma para Louise, por los *brangelinas*, los viajes, bailes, tatuajes, planes futuros, tantas risas y alguna lágrima, y por ser para mí un claro ejemplo de lo que significa ser fuerte y valiente. Milesker.

A mis *Akapulkos*. A Diego, por las confianzas y tantos consejos, las aventuras en viajes de verano y esa locura tuya tan infalible para hacer reír. Y a ti, Javi, por tanto que me has enseñado, por haber sido más fuerte que lestrigones y cíclopes en tu aventura a pedales (y haber cuidado de un trocito de madera por el camino). Si alguien personifica para mí el poema precedente a estas líneas, sin duda eres tú. Ambos sois *ehpectacula-a-a-a-res!* Eskerrik asko bioi!

A mi *aitite*, en quien tuve el mejor ejemplo de fuerza y vitalidad.

Y finalmente el agradecimiento más importante para mí, y que por ello me gustaría convertir en dedicatoria:

A mis padres, Félix y Begoña. Todo lo que, del modo que sea, hay de mí en este trabajo, es por y gracias a vosotros. Por vuestro afecto y apoyo incondicional, por haberme escuchado y ayudado siempre, y haber sido para mí el mejor ejemplo de tesón, esfuerzo y trabajo, e inculcarme el valor de la educación. Espero en estos 27 años haber poderos hecho sentir tan orgullosos de mí como yo lo estoy de ser hija vuestra. Os quiero muchísimo.

Guztiori, bihotz-bihotzez, eskerrik asko!

Leioa, 22 de Marzo 2015.

INDEX

	<u>Page</u>
OBJECTIVES	1
1. INTRODUCTION	5
1.1. VALORIZATION OF TIRES IN THE WASTE REFINERY	5
1.2. WASTE TIRE MANAGEMENT	8
1.2.1. Composition of tires	8
1.2.1.1. Macroscopic composition	8
1.2.1.2. Microscopic composition	9
1.2.1.3. Elemental composition.	10
1.2.2. Tire valorization strategies	11
1.2.2.1. Material recovery	13
1.2.2.2. Energy recovery	14
1.2.2.3. Chemical recovery	15
1.3. SCRAP TIRE PYROLYSIS	17
1.3.1. Pyrolysis reactors	18
1.3.1.1. Stirred tanks	19
1.3.1.2. Fixed bed	19
1.3.1.3. Fluidized bed	19
1.3.1.4. Screw/rotary kiln	20
1.3.1.5. Conical Spouted Bed (CSBR)	20
1.3.2. ST Pyrolysis products	21
1.3.2.1. Gas fraction	22
1.3.2.2. Char	24
1.4. SCRAP TIRES PYROLYSIS OIL (STPO)	26
1.4.1. Elemental composition	26

1.4.2. Molecular composition	27
1.4.3. Source for chemicals	28
1.4.4. Alternative fuel	29
1.5. HYDROPROCESSING	32
1.5.1. Hydroprocessing characteristics	32
1.5.1.1. Hydrotreating (HT)	33
1.5.1.2. Hydrocracking (HC)	36
1.5.1.3. Side reactions	38
1.5.2. Catalysts	40
1.5.2.1. Metallic function	41
1.5.2.2. Support	42
1.5.3. Kinetic modeling	43
1.5.4. Reactor design	46
1.6. RESEARCH SCOPE	49
2. EXPERIMENTAL	53
2.1. FEEDS	53
2.1.1. Pyrolysis pilot plant unit	53
2.1.2. Synthetic scrap tire pyrolysis oil (SSTPO)	54
2.1.3. Scrap tire pyrolysis oil (STPO) and hydrotreated STPO (HT-STPO)	55
2.2. PRODUCT IDENTIFICATION AND ANALYSIS	58
2.2.1. Gas product identification and analysis	58
2.2.2. Identification and analysis of the liquid products	60
2.2.2.1. Analysis of sulfur content	60
2.2.2.2. Analysis of HT products	63
2.2.2.3. Analysis of HC products	66
2.2.2.4. Reaction parameters	66
2.3. CATALYST PREPARATION	67

2.3.1. Hydrotreating catalysts	67
2.3.2. Hydrocracking catalysts	68
2.4. CATALYST CHARACTERIZATION	70
2.4.1. Metal content	70
2.4.2. N ₂ adsorption-desorption isotherms	70
2.4.3. H ₂ chemisorption	71
2.4.4. X-ray diffraction (XRD)	71
2.4.5. Temperature programmed reduction (TPR)	72
2.4.6. X-Ray photoelectron spectroscopy (XPS)	73
2.4.7. Adsorption-desorption of terc-butylamine	73
2.5. REACTION EQUIPMENTS AND PROCEDURES	75
2.5.1. Hydroprocessing unit description	75
2.5.1.1. Experimental reaction procedure	77
2.5.1.2. Trickle bed hydrodynamic check-up	78
2.6. COKE ON DEACTIVATED CATALYSTS	81
2.6.1. Coke content	81
2.6.2. Raman spectroscopy	81
2.6.3. FTIR-TPO/MS spectroscopy	82
3. HYDROTREATING OF STPO ON NiMo CATALYSTS USING VARIOUS SUPPORTS	85
3.1. PROPERTIES OF THE FRESH CATALYSTS	87
3.1.1. Physical and textural properties	87
3.1.1.1. N ₂ adsorption-desorption isotherms	87
3.1.2. Chemical and structural properties	90
3.1.2.1. Acidity and H ₂ chemisorption	90
3.1.2.2. X-Ray difraction	91
3.1.2.3. XPS	93
3.1.2.4. TPR	94

3.2. HYDROTREATING OF SSTPO	96
3.3. HYDROTREATING OF STPO	99
3.3.1. Hydrodesulfurization	99
3.3.2. Mild hydrocracking and hydrodearomatization	101
4. EFFECT OF PROCESS VARIABLES AND KINETIC MODELING OF THE HYDROTREATING OF STPO ON A NiMo₀/Al₂O₃ CATALYST	107
4.1. HYDRODESULFURIZATION	109
4.1.1. Effect of pressure and temperature	109
4.1.2. Effect of space time	110
4.1.3. HDS kinetic modeling	112
4.2. MILD HYDROCRACKING	116
4.2.1. Effect of pressure and temperature	116
4.2.2. Effect of space time	117
4.2.3. MHC kinetic modeling	118
4.3. HYDRODEAROMATIZATION	123
4.3.1. Effect of pressure and temperature	123
4.3.2. Effect of space time	125
4.3.3. HDA kinetic modeling	126
4.4. SIMULATION AND OPTIMAL OPERATION CONDITIONS	132
5. UPGRADING OF HT-STPO THROUGH HYDROCRACKING ON A PtPd/SiO₂-Al₂O₃ CATALYST	137
5.1. REACTION CONDITIONS	139
5.1.1. Properties of the hydrotreated STPO (HT-STPO)	139
5.1.2. Properties of the fresh catalyst	141
5.2. HYDRODESULFURIZATION	142
5.3. HYDROCRACKING	144
5.3.1. Time on stream	144

5.3.2. Temperature	146
5.4. HYDRODEAROMATIZATION	148
5.4.1. Time on stream	148
5.4.2. Temperature	148
5.5. CATALYST DEACTIVATION	150
5.5.1. HDS, HC and HDA behavior	151
5.5.2. Deterioration of the catalyst properties	151
5.5.3. Coke deposition	154
5.5.4. Composition and nature of coke	155
5.5.4.1. Raman spectroscopy	155
5.5.4.2. FTIR spectroscopy	156
5.5.4.3. FTIR-TPO	157
6. KINETIC MODELING OF THE HYDROCRACKING OF HT-STPO ON A PtPd/SiO₂-Al₂O₃ CATALYST CONSIDERING DEACTIVATION	163
6.1. METHODOLOGY FOR KINETIC MODELING	165
6.1.1. Deactivation models	165
6.1.2. Computation of the kinetic parameters	165
6.1.3. Significance and discrimination of kinetic models	166
6.2. HYDROCRACKING	168
6.2.1. Deactivation model discrimination	168
6.2.2. HC kinetic model fitting	170
6.3. HYDRODEAROMATIZATION	176
6.3.1. Deactivation model discrimination	176
6.3.2. HDA kinetic model fitting	178
6.4. HYDRODESULFURIZATION	182
6.5. SIMULATION AND OPTIMAL OPERATION CONDITIONS	185
6.6. COMPARISON BETWEEN NiMo AND PtPd CATALYST PERFORMANCES	188

6.6.1. Reaction rate	188
6.6.2. Overview	190
7. SUMMARY	195
8. CONCLUSIONS	201
9. NOMENCLATURE	209
10. BIBLIOGRAPHY	217

OBJECTIVES

The necessity to satisfy the energetic demand associated to developed countries and the growing demand of developing countries, together with the depletion of fossil fuels, is highlighting the requirement for the utilization of alternative energy sources. In this scenario, waste refinery aims for obtaining fuels and chemicals from the valorization of different wastes, among of which tires represent for a major challenge, due to their predicted growing amount, the environmental hazards derived from their inappropriate management, and the increasing demand for recycling hydrocarbons. Furthermore, since they are produced from petroleum derivatives, tire valorization contributes to the intensification of the valorization of this exhaustible fossil source.

Material and energy recovery have been the prevailing tire recycling routes in the last decade (accounting for 38-40 % of the total recycled tires), to the detriment of the much less environmentally respectful dumping in landfills. Alternatively, pyrolysis of tires currently represents a promising emerging management route, particularly for its implementation at a large scale. Together with its many technological and environmental advantages, widely reviewed in literature, pyrolysis is a greatly versatile process that allows for co-processing tires together with other wastes (biomass, plastics, coal, etc.), as well as obtaining products with diverse features, among of which scrap tire pyrolysis oil (STPO) represents for the most abundant yet the most economically and energetically interesting product. Among the available pyrolysis reactors, conical spouted bed reactors (CSBR) show great potential for increasing the STPO yield, up to ca. 60 wt%.

STPO consists of a very complex mixture of hydrocarbons with a high calorific power (ca. 44 MJ·kg⁻¹), encouraging properties for its potential use as an automotive fuel in internal combustion engines. However, the significant content of sulfur (0.4-2 wt%), aromatics (ca. 58 wt%) and heavy molecules (boiling point > 350 °C, ca. 30 wt%) appears as a limiting barrier for its use as fuel. In this regard, hydroprocessing is a suitable refinery operation for solving these upgrading issues at once. Thus, the three desired reaction pathways for enhancing STPO composition are hydrodesulfurization (HDS), hydrocracking (HC) and hydrodearomatization (HDA).

The main contribution of this Thesis is to investigate a 2-stage hydroprocessing strategy of STPO consisting in (i) a hydrotreating stage using NiMo supported catalysts and (ii) a hydrocracking stage using a PtPd supported on SiO₂-Al₂O₃ catalyst. The previous experience of the group in hydroprocessing delves with the conversion of model compounds (methylcyclohexane and toluene), pyrolysis gasoline (PyGas) and light cycle oil (LCO). In this works, a wide understanding of hydroprocessing reactions and

kinetic modeling was gained. Considering the innovative STPO applications and also the inherent experimental complexity of the process, scarce information on the topic is available in bibliography.

The research objectives of the first hydrotreating stage are:

- (i) A catalyst discrimination among five different micro and mesoporous supports for the NiMo catalysts using a synthetic STPO feed; $\text{SiO}_2\text{-Al}_2\text{O}_3$, Al_2O_3 , equilibrated FCC, SBA-15 and MCM-41.
- (ii) A parametric study using STPO and the most active catalyst selected in (i) for determining the effect of temperature, pressure and space time.
- (iii) Kinetic modeling of the hydrotreating products using the data collected in (ii) in terms of HDS, mild hydrocracking (MHC) and HDA.

The research objectives of the second hydrocracking stage are:

- (i) A parametric study for determining the effect of time on stream (TOS), temperature and space time over catalyst activity in terms of HDS, HC and HDA.
- (ii) A study of the deactivation due to coke formation from a quantitative and a qualitative perspective.
- (iii) Deactivation kinetic model discrimination and optimization for its integration in a kinetic model that describes the evolution with TOS of the different sulfur species, lump yields and composition fractions at different space time conditions.

The achievement and complexity of the different goals of this Thesis has required of the application of several experimental and mathematical techniques. On the whole, this work has aimed to obtain deep understanding of the 2-stage STPO upgrading hydroprocessing strategy in terms of catalyst properties, deactivation and kinetics, aiming to produce potential high-quality alternative fuels (naphtha and diesel), while obtaining a wide perspective and knowledge that could be applied in forthcoming research.

Section 1

INTRODUCTION

1. INTRODUCTION

1.1. VALORIZATION OF TIRES IN THE WASTE REFINERY

The necessity to satisfy the energetic demand associated to developed countries and the growing demand from developing countries is a mayor political issue within the present socio-economical world scenario. Considering the depletion of fossil fuels (oil and gas), the utilization of alternative energy sources becomes a major issue. Refinery industry is progressively adapting to lower-price heavier feedstock due to the depletion of the higher-price lighter one, so that these adaptations could be used for feeding more unconventional feeds progressively; like carbon, natural gas, wastes and biomass. Moreover, fuels need to comply with increasingly severe restrictions regarding their composition in terms of sulfur, nitrogen, aromatic and olefin content.

Waste refinery is defined as the group of thermo-chemical operations aiming for the production of fuels and chemicals from the valorization of wastes (tires, plastics, sewage sludge, etc.) or secondary refinery streams. Waste refinery requires adaptations or completely new technologies to the ones already in use in the refinery, and hence, the implementation of processes involves of progressive development of reactors, kinetic models, catalysts, catalyst deactivation models and other processes innovations.

Within the waste refinery concept, waste tire valorization is a major driving force for research and innovation. Based on an average rate of waste tires of ca. $6 \text{ kg} \cdot (\text{habitant} \cdot \text{year})^{-1}$ [1], in 2012, $17 \cdot 10^6 \text{ t}$ of waste tires were generated, which correspond to $2.8 \cdot 10^9$ tires. Other estimations based on the 2 wt% of the total waste, compute a rate of waste tire disposal of $7 \cdot 10^6 \text{ t year}^{-1}$ [2], from which $1.15 \cdot 10^6 \text{ t}$ correspond to the EU, while other estimations even double this amount [3].

An increase of the Gross Domestic Product (GDP) of a country also fosters growing vehicle demand as well as tire substitution for safety issues. This trend occurs in a greater extent than that of the extension of the tire lifetime [4]. The significant tire consumption increment in Asia and Oceania in the last years will make these regions the main waste tire source of the next two decades, being China the main producer with $5.2 \cdot 10^6 \text{ t}$ in 2010 (accounting for 60 wt% of the total) [5].

In the EU, waste suppression and vehicle life-cycle-end directives generate the necessity to valorize no less than 40 wt% of tires, whose endpoint is otherwise to be dumped in landfills. Spain has its own rules concerning out-of-

use waste tires management (Royal Decree 1619/2005), which is also subject to the rules established in the Royal Decree 1383/2002, about management of vehicles at the end of their useful life-cycle. In a broader context, tire management is included within the National Integrated Plan of Wastes for the 2008-2015 period, and regulated by the 22/2011 Law from July 28th, of Wastes and Polluted Soils, which replaced the previous 10/1998 Wastes Law from April 21st, and is adapted to the Spanish 2008/98/CE directive about wastes.

European regulations define end-of-life tires as those which, according to their physical state and considering current security regulations, should be intended for recycling or valorization or could not continue in service without being subjected to techniques that extend its useful life. They are also considered as such chambers and tires disposed by their owner, even though if they do not comply with the previously described requirements. The compounds present in tires are non-biodegradable, and due to their shape and mechanical features they have low apparent density and difficult compaction.

Many factors have driven attention towards tire valorization: (i) the environmental damage that is caused by uncontrolled disposal of this type of polymer waste, (ii) the non-biodegradability of tires, (iii) the increasing demand for recycling hydrocarbons, and (iv) its high calorific value, which could allow for its use as a fuel. In the introduction of this Thesis, waste tire management (Section 1.2) will be reviewed. Pyrolysis of tires (Section 1.3) is a major valorization pathway that will be extensively reviewed not only in terms of the different reactors available, but also from the perspective of the valuable products that can be obtained, focusing on the main fraction (pyrolysis oil) and its potential use as an automotive fuel. Considering the composition of the pyrolysis oil (Section 1.4) and the environmental problems aroused from it, hydroprocessing (Section 1.5) appears as an ideal process for its upgrading, and thus will also be reviewed regarding catalysts, kinetic modeling and reactors.

Figure 1.1 shows the valorization pathways available for tires, and the different petrochemical industry manufacturing stages to which each recovered product can be recycled. Even though nowadays energetic recovery is the most common means for tire recycling, the previously detailed legal regulations encourage for other recycling alternatives. Refinery processes allow for obtaining synthetic monomers that can be further polymerized for obtaining virgin polymers that, after being processed (vulcanized) with the required additives to confer them with the required mechanical properties, give way to the final tire product. Once tires are no longer in use, and providing they maintain their original structure intact, they can be directly reused, as a primary recycling strategy. When their physical condition is too damaged, tires can be grinded through different mechanical processes, in such a way that the

rubber structure remains unchanged and the polymer can be recovered. Complete destruction of the tire rubber structure requires of different chemical processes, allowing for the recovery of the original monomer (that can be subjected to vulcanization again), and a liquid fraction that shows great potential towards being used as a fuel, and can be further co-processed in refineries, aiming for adapting its composition and properties to commercial fuel requirements.

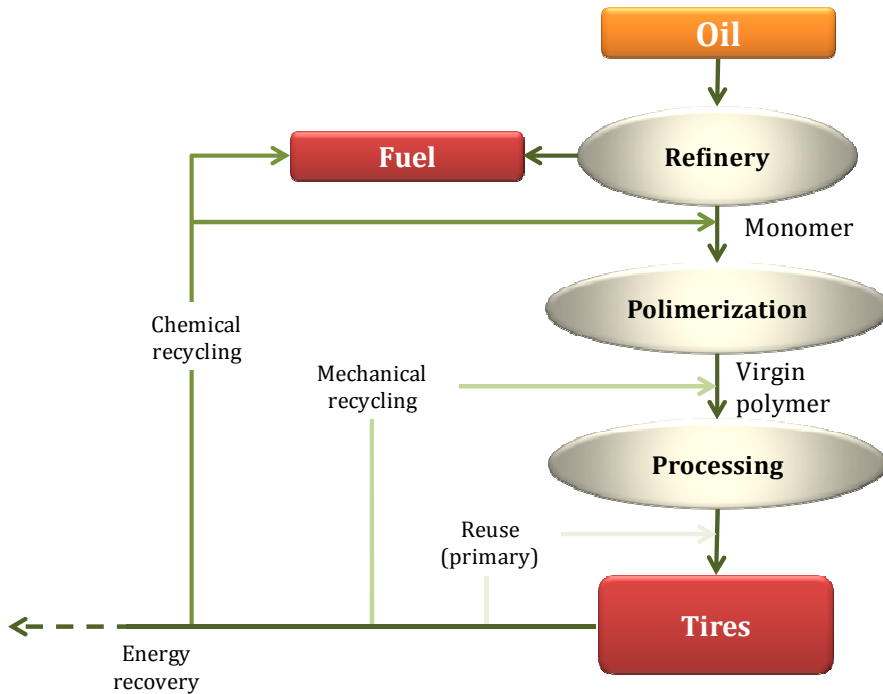


Figure 1.1. Overview of integral valorization of petroleum derived wastes.

1.2. WASTE TIRE MANAGEMENT

1.2.1. Composition of tires

1.2.1.1. Macroscopic composition

Each tire is the result of assembling individual elements with specific properties and composition to achieve the final tire product. These elements of the tire are shown in Figure 1.2:

- (i) *Liner*: Inner coating made of synthetic rubber.
- (ii) *Plies*: layers of different materials piled together. Rubber and textile (nylon) made layers are defined as casing plies and metal reinforced rubber made layers are defined as belt plies.
- (iii) *Bead heel*: Steel wires conforming a ring surrounded by a hard rubber layer.
- (iv) *Sidewall*: Mixture of natural and synthetic rubber, with small amounts of carbon black and additives.
- (v) *Tread*: Natural and synthetic rubber. It is the part of the tire that is in direct contact with the ground, reason why it must be abrasion and traction resistant.

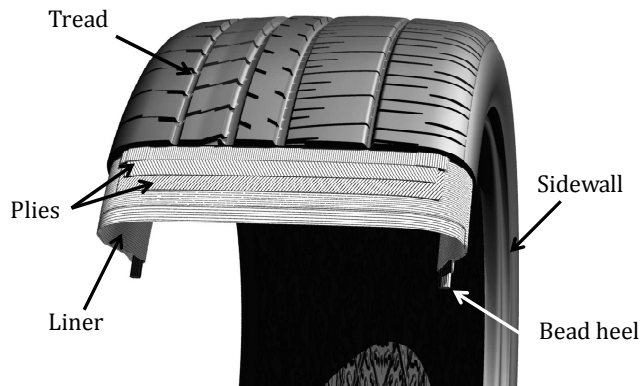


Figure 1.2. Transversal cut of a radial tire.

1.2.1.2. Microscopic composition

Tire compositions differ significantly due to their numerous different applications. The basic materials of tires are carbon black, steel natural rubber (NR) and synthetic rubber (SR), being examples of the SR; Butadiene rubber (BR) and styrene-butadiene rubber (SBR).

Table 1.1 lists the basic material composition of different tires: passenger car tire (PCT) and truck tire (TT). Combining these materials, different properties of tires can be achieved for any specific purpose. Carbon black is used for rubber reinforcement and for increasing the tire resistance towards abrasion and fracture. Vulcanization is the process using sulfur to make cross-linked bonds of rubber fibers, severely increasing the hardness of rubber. For this aim too, and besides using sulfur compounds, manufacturers also use accelerators and catalysts as stearic acid and zinc oxide.

Table 1.1. Typical materials used in tire manufacturing (percentages of the total weight of the finished tire) [6].

Material	PCT		TT	
	USA	EU	USA	EU
Natural rubber (wt%)	14	22	27	30
Synthetic rubber (wt%)	27	23	14	15
Carbon black (wt%)	28	28	28	20
Steel (wt%)	14-15	13	14-15	25
Others ¹ (wt%)	16-17	14	16-17	10

¹ Nylon, fillers, accelerators and sulfur, among others.

Figure 1.3 shows a schematic representation of the molecular structure of polyisoprene as a component of NR (Figure 1.3a) and polybutadiene as an example of SR (Figure 1.3b), together with an example of the structure of polyisoprene chains before and after vulcanization (Figure 1.3c). Vulcanization consists in altering the polymeric structure by adding sulfur or other additives at high temperatures to the structure of rubber in such a way that a new cross-linked structure is formed, with enhanced resistance, durability and mechanical properties. The new cross-linked structure has strong covalent bonds between the long polymer chains, that are no longer able to move independently, with strong forces, and is therefore an insoluble and infusible thermosetting polymer.

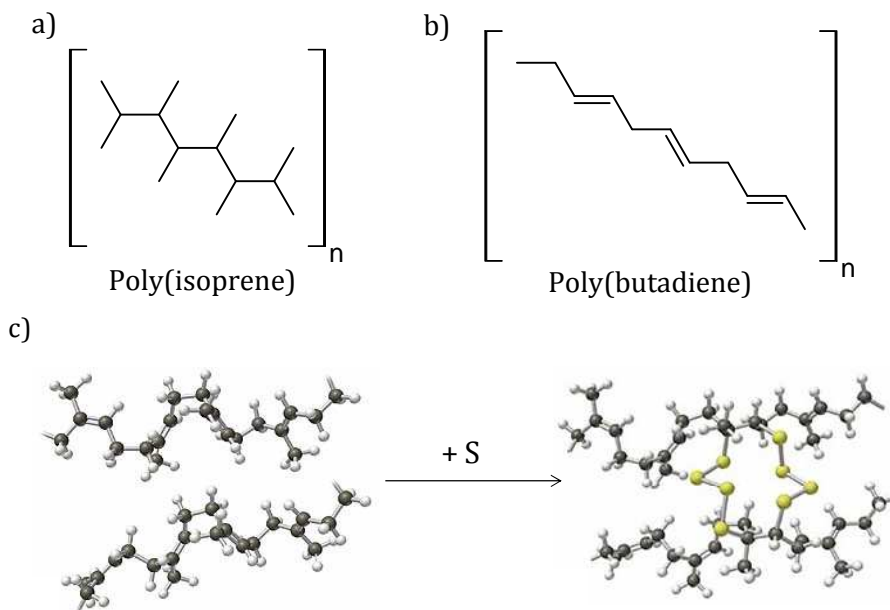


Figure 1.3. Schematic examples of a) NR, b) SR and c) vulcanization of SR.

1.2.1.3. Elemental composition.

Table 1.2 compares the elemental composition of three different PCTs with that of a bicycle tire (BT) and a TT.

Table 1.2. Elemental analysis of different types of three PCTs, BT and TT [7].

Element	PCT ₁	PCT ₂	PCT ₃	BT	TT
C (wt%)	85.9	82.5	86.4	74.5	83.2
H (wt%)	8.0	6.4	8	6.5	7.7
O (wt%)	2.3	5.7	3.4	16.4	6.16
N (wt%)	0.4	0.5	0.5	1.0	1.5
S (wt%)	1.0	1.1	1.7	1.6	1.44
Ash (wt%)	2.4	3.8	2.4	--	--

PCTs have very similar elemental composition between them and compared with TT, whereas BT has significantly more O and N (from additives) and less C and H [2].

1.2.2. Tire valorization strategies

Waste tires are divided into two main categories regarding their condition, according to the European Tire and Rubber Manufacturing Association (ETRMA) criteria: (i) part-worn tires and (ii) scrap tires (ST) (Figure 1.4). Worn tires can be dumped in landfills, which has been the most extended solution to the problem so far. This option is not acceptable because it requires large spaces and is a source of environmental hurdles: development of colonies of insects and rodents, and for starting fires. Increasingly strict environmental policies and environmental concern have aroused the necessity to establish new approaches for waste tire management. Partially worn tires can be also processed for extending their life cycle by reusing or retreading. Retreading of part-worn tires is based on the preliminary preparation of a tire for regeneration, by stripping it of its tread and substituting it for a new one. This is why only tires that keep their steel structure intact can be subjected to this process. Retreading can be carried out through a cold or a hot process [8, 9], vulcanizing at 100 °C or 150-180 °C, respectively. Despite being very economically profitable while generating very little waste, in practice automobile tires are not generally retreaded because of their uncompetitive price against a new tire, poorer quality and safety when used at high speeds [9].

Figure 1.4 shows the three main routes of valorization of ST: material, energy or chemical recovery. The technology of manufacturing rubber products is based on the irreversible vulcanization that takes place between natural and synthetic rubber films, sulfur and other compounds, which form the strong cross-linked structure of rubber (which gives the tire its elasticity, insolubility and infusibility properties). Because of this, recovering chemicals or materials from ST are energetically intense processes based on the mechanical, thermal or chemical destruction of the rubber product [6].

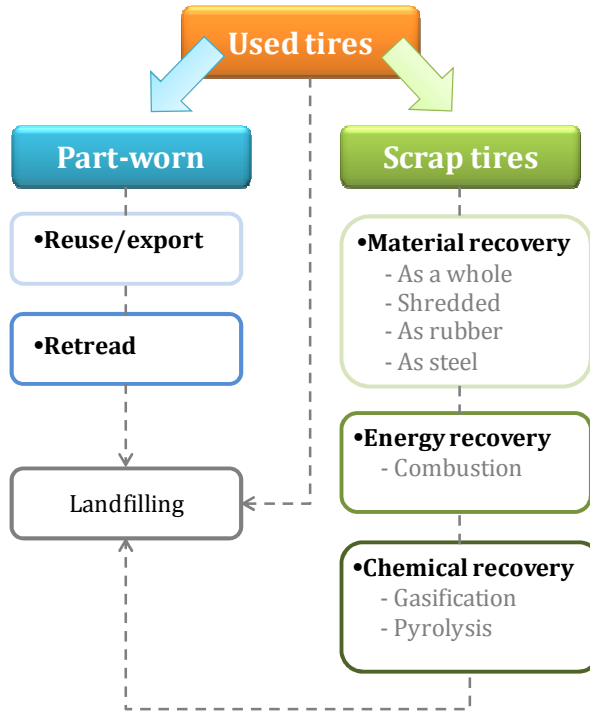


Figure 1.4. Used tire classification and recovery strategies (as established by ETRMA in 2011).

Figure 1.5 shows the trends over the last decade of the different management strategies. In this Figure chemical recovery is not included due to their recent implementation. The amount of partially worn tires recycled has not changed much over time, and still remains minor compared to the amount of wheel intended for material and energy recovery. Due to the reasons previously explained, landfilling has suffered a significant decline over time, in particular from 2000 when the Landfill Directive and the initiative of establishing National Producer Responsibility schemes were implemented. As a result of this and a decade later, only 5 % of the used tires were disposed in landfills or have unknown recovery routes, while energy recovery and material recovery processes account for 38-40 % of the total disposed tires each (ETRMA).

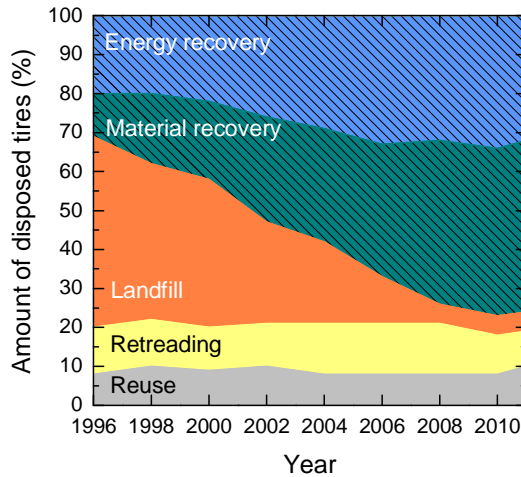


Figure 1.5. ST recovery route trends for the last years, with highlighted emerging routes (stripped areas) (ETRMA in 2011).

Based on the evolution and good perspectives of the three routes of ST valorization, they are more extensively detailed in the forthcoming Sections.

1.2.2.1. Material recovery

This process is the most common means of ST valorization, since ST are used widely as civil engineering material, serving for coastal protection, roads, artificial reefs and seawalls, and insulation for building constructions, among others [10-12]. STs are recovered in a grinded form (rubber materials of different degrees of comminuting), or via a vulcanization process (to obtain rubber regenerates). Grinding of tires can be either (i) primary grinding aiming ST in pieces of a few centimeters, to separate the metals and the rubber, or (ii) secondary grinding to reduce the size of ST even more. Secondary grinding has two variants: mechanical and cryogenic grinding. Mechanical grinding is similar to primary grinding but it is not suitable for obtaining tire pieces smaller than 1 cm. Cryogenic grinding consist on freezing tire pieces below $-100\text{ }^{\circ}\text{C}$, for turning tires into a fragile material [13], and reaching a higher degree of commuting.

1.2.2.2. Energy recovery

One of the possible ways of recovering ST or other disposed rubber products is to use them as an energy raw material. Used tires have a very high calorific value (CV) (32 MJ kg⁻¹). Tire derived fuel appears as a competitive alternative to coal, which has a much lower CV [14]. There are six types of plants for ST energetic valorization:

1. Plants that use exclusively tires: Among these plants there are two possible configurations: (i) combustion, and (ii) thermal degradation (partial combustion, gasification, pyrolysis) and combustion of the produced liquids and/or gases. Option (ii) allows for recovering more carbon black and being more energetically efficient compared with option (i). The plant of Gummi-Mayer (option (ii)) has been operating in Germany since 1973 with a capacity of 40 t day⁻¹ and acceptable emission levels, operating at 1250 °C. Oxford Energy Co. built energy plants in Modesto (California), Sterling (Connecticut), Lackwanna (New York) and Moapa (Nevada), with capacities of 13.7-27·10⁹ tires day⁻¹.
2. Co-combustion plants: Firestone has built this type of co-combustion units in Des Moines (Iowa, US) and Decatur (Illinois, US), treating 0.5·10⁶ tires per year in each plant. The feed to these plants consists in 25 wt% of tires, paper and biomass, among others. The limitation in the proportion of tires is established by emission controls, and the amount of steam generated in the circular boilers is of 9,000 kg_{steam} h⁻¹. The system requires monthly cleaning, so that ashes can be extracted from the bed and deposited in a water pool.
3. Combustion in thermal plants: The Thermoselect swiss-italian plant [15] uses this technology, with a low temperature pyrolysis/degasification unit connected to the process, where 45 % of organic waste is treated, together with urban solid wastes.
4. Combustion in cement plants: The use of ST in cement plants has been implemented in Europe and Japan since the 90s, and it shows the following advantages: (i) reductions in the cost of cement manufacturing (accounting that 25-40 % of the cost of clinker production is attributable to fuel), (ii) low adaptation cost, (iii) no solid wastes are produced, as (iv) ashes are added to clinker. However, this option is controversial due to the high amount of organic volatiles emitted [16, 17]. The percentage of ST valorized in thermal and cement plants in 2004 in the US was estimated to be of 45 wt% and in Germany 50 wt%. It increased 10 % in both countries by 2008. However, the incorporation of 5 wt% of ST in a carbon thermal plant increases Zn

emissions from 15 g h^{-1} to 2.4 kg h^{-1} and also the emissions of other metals increase significantly.

5. Combustion in pulp and paper plants: In the US, at least 12 pulp and paper plants have adapted their kilns, which were designed to use wood wastes as fuel, for co-combustion of TDF. Among them, Waste Recovery Inc. in Dallas (TX) is one of the biggest. In 2008, this industrial sector used around $40 \cdot 10^6$ of ST. However, this application presents a series of drawbacks, like higher costs, emissions and difficulties for a regular supply, compared to traditional fuels (carbon and wood wastes).
6. Incineration: Urban solid waste incinerators generally reject tires given that, due to their relatively high calorific value, they inflame “hot spots”, causing temperature control issues. Furthermore, the residues from the flue gas can contaminate the environment if they are not handled appropriately, and must be disposed in controlled and well-operated landfills to prevent ground and surface water pollution.

1.2.2.3. Chemical recovery

The low volatile and ash content of ST turns them into an ideal material for thermal conversion routes. These technologies are basically: gasification and pyrolysis. Both processes aim to recover valuable chemical products.

1. Gasification: aims to convert ST into a CO and H_2 mixture, also referred as synthesis gas or syngas. Syngas is used as fuel in gas turbines or fuel cells [18], or as a raw material for obtaining a whole range of other fuels and chemicals [19]. Gasification of ST has low yield of dioxins, char, NO_x and SO_2 , and allows for generating electricity with an efficiency of around 34 % (higher than that of incineration) [20].

Most of the studies on ST gasification have been carried out in fluidized beds and using air as oxidizing agent. Xiao et al. [21] proved that during low-temperature gasification the low calorific value (LCV) of syngas could be increased by increasing gasification temperature or decreasing the equivalent ratio (relation between the real air:fuel ratio and the air:fuel ratio required for complete combustion) below $700 \text{ }^\circ\text{C}$, when CO_2 concentration in syngas was lower and CH_4 higher. In the $700\text{-}800 \text{ }^\circ\text{C}$ range, temperature changes had no significant effect over LHV, but less char was yielded. Karatas et al. [22] studied the effect of equivalent ratio (0.15-0.45) on gasification at $700 \text{ }^\circ\text{C}$ confirming the strong effect of this variable on LCV, and CH_4 and H_2 concentrations, all of which decreased upon increasing equivalent ratio. They also

observed that tire particle size did not have significant effect on gaseous concentration or LCV. When comparing air with other oxidizing agent mixes like CO₂ and steam, important improvements in the LCV are observed [23]. Gasification with air and CO₂ or steam mixtures leads to obtaining syngas with higher LCV (30 % higher with air+CO₂ compared to air+steam), and using only steam allows for doubling the LCV value compared to using air and steam.

2. Pyrolysis: Consists on thermo-chemical decomposition of the organic compounds present in ST, and offers an environmentally attractive method for reducing the world's waste tire backlog. It takes place in absence of oxygen, producing three output streams: gas, liquid (oil) and solid (char), all of which present good combustion characteristics [15]. In particular, ST have attracted attention since the 90s as a potential pyrolysis feed [24, 25].

1.3. SCRAP TIRE PYROLYSIS

Pyrolysis of tires is considered one of the most promising alternatives within the possible ST management strategies, particularly for its implementation in a large scale [15, 26]. Pyrolysis is a process that involves devolatilization in an inert gaseous media of the organic compounds contained in the tire, followed by their thermal breakage, obtaining three fractions: gas, liquid and solid.

The main advantages of ST pyrolysis are summarized in Table 1.3. It is a very versatile process that allows for co-feeding tires together with other types of wastes as plastics, coal or biomass, with a high energetic efficiency [24]. Environmentally, it is a more respectful alternative than incineration [15], capable of minimizing the emission of contaminants and pollutants, some of which are harmful for humans, e.g. polyaromatic hydrocarbons (PAHs), CO, CO₂, NO_x, SO_x, etc. Considering that pyrolysis is easily scalable to industrial practice, it can be successfully integrated (both technologically and energetically) in already existing refineries so that gaseous and liquid products can be co-processed. This way, pyrolysis is conceived as a primary treatment which allows for upgrading each product fraction separately, thus improving the profitability of already existing and depreciated refinery units.

Table 1.3. Advantages of the pyrolysis process for ST valorization.

Operational	Environmental	Economical
Treatment together with other wastes	Valorization of potentially hazardous wastes	Integrated into depreciated refineries
Energetic integration	Minimized emissions (PAHs, CO ₂)	Energetic efficiency
Product versatility		

Pyrolysis products are gas, liquid and char [27, 28]. Although we will elaborate more on the interesting products obtained from the pyrolysis of ST in Section 1.3.2, we should point now that the most interesting fraction for its energy and economic value is the liquid so that the most profitable reactor designs are these that obtain higher liquid yields.

1.3.1. Pyrolysis reactors

For kinetic measurements, it is common to use commercial thermogravimetric apparatus, calorimeters, or fast heating microreactors (pyroprobe-type pyrolyzers). However and for studying product distributions in designs more easily scaled up, other reactors are the ones shown in Figure 1.6, all of which can operate at vacuum conditions to facilitate volatilization [26, 29, 30]. Depending on the main aim of the pyrolysis (heat generation, fuel obtention, etc.) a specific type of reactor should be chosen preferably. Due to the unique characteristics of each reactor type, they are discussed in more detail later.

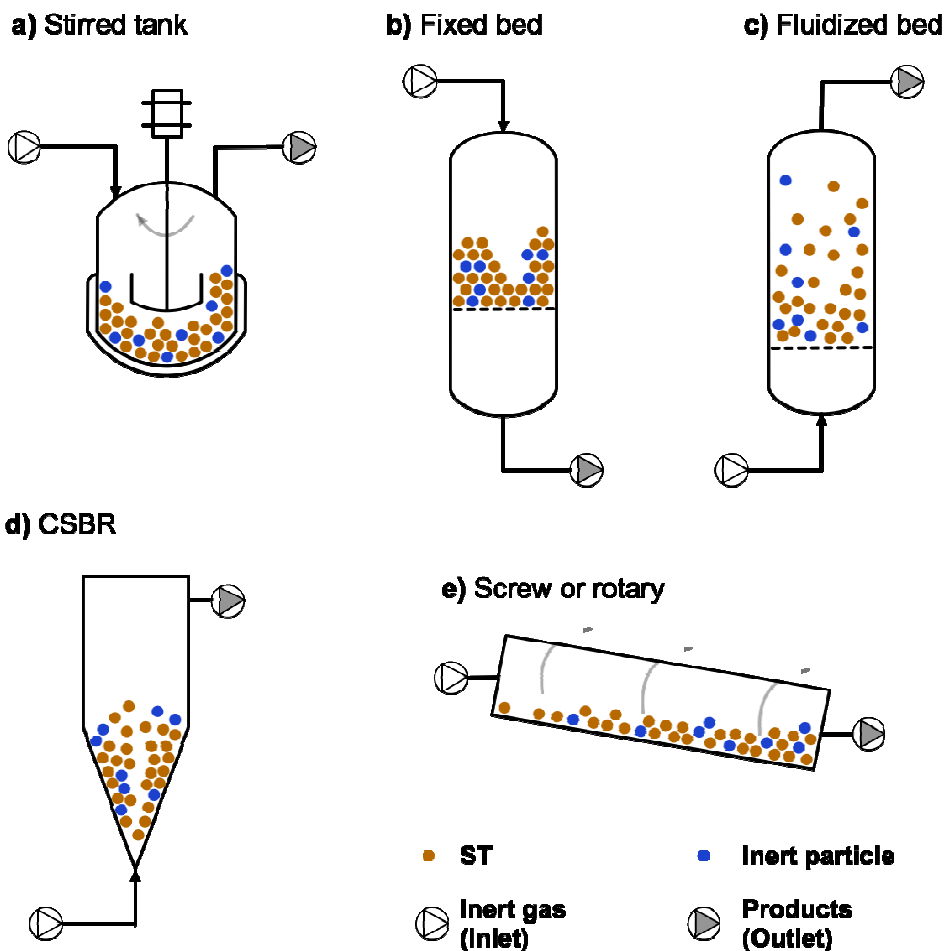


Figure 1.6. Types of pyrolysis reactors.

1.3.1.1. Stirred tanks

These reactors are based in an autoclave-type configuration (Figure 1.6a) where ST are fed discontinuously whereas the inert gas required for the pyrolysis and products flows continuously. De Marco et al. [31] studied the pyrolysis of tires under a N₂ atmosphere in the 300-700 °C range for 30 min. In these conditions, the highest yield was that of char, up to 87.6 wt% at 300 °C. On the other hand, liquid and gas yields increased with temperature up to 38.5 and 17.8 wt% at 700 °C, respectively. In order to save grinding costs, Bianchi et al. [32] are designing autoclaves for processing whole tires.

1.3.1.2. Fixed bed

Pyrolysis in this type of reactors (Figure 1.6b) is generally performed at 450-700 °C. Kouei Industries (Vancouver, Canada) and No-Waste Technology (Reinach, Germany) are two companies that dispose of fixed bed reactors in an industrial scale with a capacity of 16 and 4 t day⁻¹, respectively. Figure 1.7 (grey legend) depicts the product distribution obtained by different authors using fixed bed reactors in the maximum liquid yield conditions of their works. The results [33-39] vary significantly, as they are strongly dependant on the experimental conditions. Depending on the reactor size, variables like temperature, heating rate and feeding rate affect in a different extent, as observed from the wide range of temperatures in which liquid yields have been maximized. As a general trend, an increase in temperature and heating rate implies obtaining higher gas yields.

1.3.1.3. Fluidized bed

Kaminsky and co-workers have extensively studied tire pyrolysis in fluidized bed reactors [40-43] (Figure 1.6c). The Hamburg process is a technology developed by these authors based on fluidized bed pyrolysis of different materials including ST with the main purpose of obtaining basic chemicals and carbon black [40]. Different plants have been built since 1970 at laboratory scale (0.6-3.0 kg h⁻¹), pilot-plant scale (10-40 kg h⁻¹) and industrial scale (120-200 kg h⁻¹) [42]. Figure 1.7 (blue legend) depicts the product yields obtained in maximum oil yield conditions (26-32 wt %) using fluidized bed reactors with different characteristics [44, 45], from a laboratory scale, to a technical scale and finally to a pilot plant scale, obtaining diverse results. Vacuum pyrolysis with fluidized beds requires lower temperatures and allows for increasing the yields of interesting products [29, 30, 46-48].

1.3.1.4. Screw/rotary kiln

These reactors (Figure 1.6e) present important advantages for large-scale operation [49]. Japanese Kobe Steel (Japan), ENEA Research Center (Italy) and University of Kassel (Germany) have pilot plants using this type of reactor [50]. Figure 1.7 (green legend) plots the product yields obtained by Galvagno et al. [51] at the ENEA Research Center when operating at different temperatures. Higher oil yields were obtained operating at 550 °C, together with the lowest gas yields. Char, however, did not appear to be significantly affected by temperature changes.

1.3.1.5. Conical Spouted Bed (CSBR)

Originally studied in batch operation [52], it has now been studied continuously for other wastes [53, 54] and ST [55]. CSBR (Figure 1.6d) allows for obtaining higher yields of interesting products and with greater quality. Figure 1.7 (red legend) shows the product distribution obtained by López et al. [56] working in a continuous regime at 425-600 °C. Comparatively, higher liquid yields were obtained in a CSBR (44.5-55.0 wt%) than with other technologies. Additionally, they observed that working at higher temperatures increased the aromaticity of the oil fraction as well as the quality of the char. These results are due to the interesting features of CSBRs: (i) simple design that does not require a gas distributor [57, 58], (ii) low pressure drop [58, 59], (iii) versatility to be used with particles of different geometries and densities, (iv) vigorous gas-solid contact for avoiding clogging of the reactor due to the stickiness of melted ST [53] and (v) uniform and low residence time of the volatiles in the reactor.

Considering the product distribution data shown in Figure 1.7, the convenience of working with a CSBR reactor when the main pyrolysis goal is to optimize the liquid product yield is evidenced, simultaneously minimizing gas yields.

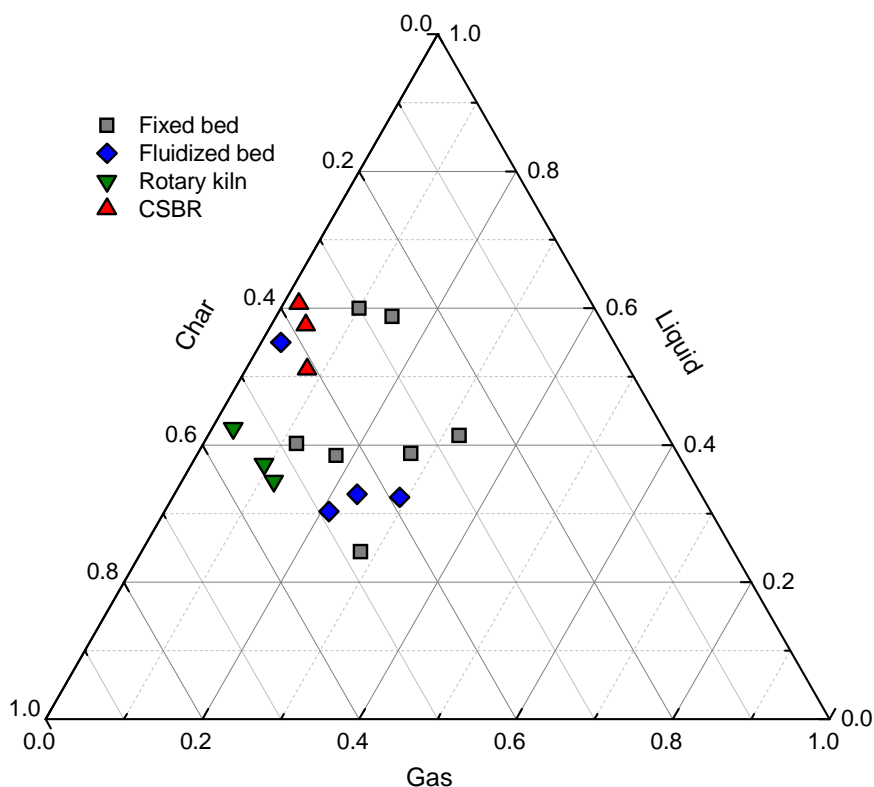


Figure 1.7. Product lump (wt%) in fixed beds, fluidized beds, rotary kilns and CSBRs at different temperatures.

1.3.2. ST Pyrolysis products

Each of the three main fractions obtained for ST pyrolysis (gas, liquid and char) has a broad range of applications, as depicted in Figure 1.8. Gases generally consist on a mixture of paraffinic and olefinic compounds together with smaller amounts of other hydrocarbons, and can be used for supplying the heat required by the process, as it can be energetically self-sufficient [60]. The liquid fraction is normally referred to as scrap tire pyrolysis oil (STPO), and contains valuable chemicals as aromatics, *d*-limonene, and BTX (benzene, toluene, xylenes) fraction, mainly. Furthermore, this STPO presents good characteristics for its use as an automotive fuel, after being upgraded for pollutant and heavy compound removal. Additionally, it also allows for carbon black recovery if burned. Lastly, char obtained from ST pyrolysis can be

activated via different physico-chemical procedures to obtain activated carbon, and also in a Boudouard reactor to obtain Boudouard carbon.

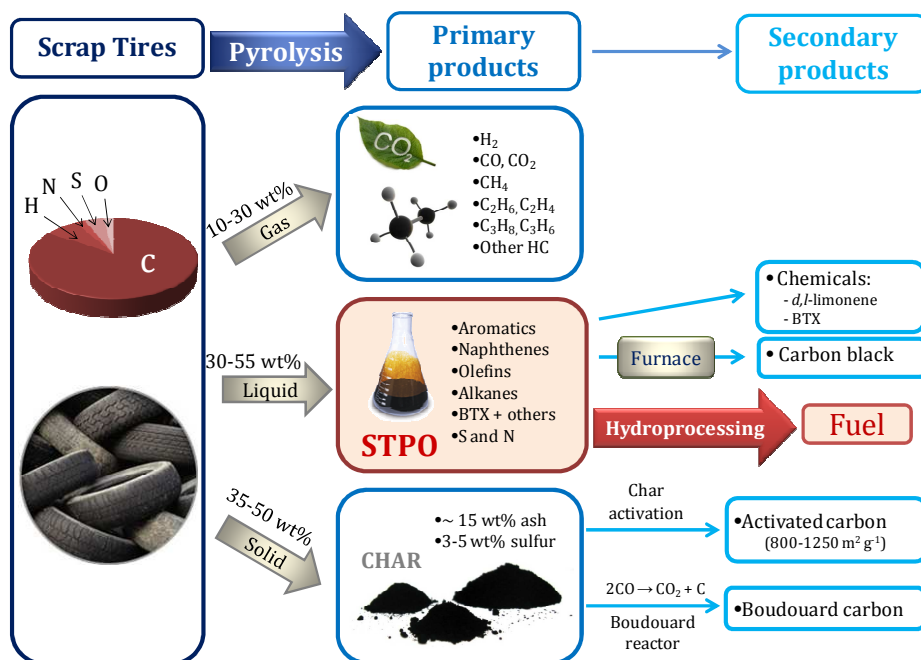


Figure 1.8. Primary and secondary valuable products derived from ST pyrolysis.

As previously explained, product composition is strongly dependant on the technology employed and process conditions, especially temperature, heating rate, pressure and residence time. Therefore, results from different sources may result difficult to compare, due to the heterogeneity on the composition of the raw materials, as well as the composition of the different product lumps.

1.3.2.1. Gas fraction

The gaseous fraction of ST pyrolysis products consist typically of C_1 - C_4 hydrocarbons (paraffins and olefins), H_2 , CO , CO_2 , with traces of SH_2 , SO_2 and NH_3 [48]. SH_2 is produced from the volatilization of sulfur used in the vulcanization, and its concentration in the gas fraction is generally low. Regarding hydrocarbons, methane and particularly butenes (especially butadiene) are predominant [19]. This is due to the fact that the basic

monomers of BR and SBR are precisely butenes, and the ST pyrolysis yield “back” these monomers [19]. Table 1.4 summarizes the composition of the gas fraction obtained by ST pyrolysis using fixed bed reactors, fluidized bed reactors and CSBR, as reported by various authors. The main factor governing the gas composition is the initial composition of ST [42]. Kyari et al. [61] analyzed the variability of gas composition obtained from the pyrolysis of different ST: H₂, 13.8-27.6 vol%; CH₄, 14.1-27.9 vol%; CVs, 29.9-42.1 MJ m⁻³. For the CSBR [56], no CO and very little CO₂ have been detected, with increasing yields of CH₄, C₂, C₃ and C₄ hydrocarbons upon increasing temperature. Dai et al. [45] indicated that, as temperature is increased, the composition of the gas fraction varies in the following way: (i) hydrocarbon content decreases, (ii) CO₂ decreases and CO increases, and (iii) unsaturated hydrocarbon yields (C₂H₄ and C₃H₆) are higher than that of saturated hydrocarbons (C₂H₆ and C₃H₈). This last trend can be explained either by the transformation of saturated hydrocarbons into unsaturated, or thermal decomposition of the tire polymers.

Table 1.4. Composition of gas fraction from various authors as reported in literature.

Ref.	[61] ¹	[31] ¹	[62] ¹	[42] ²	[42] ²	[42] ²	[56] ³
T (°C)	500	500	800	740	750	780	600
Yield (wt%)	2.40	17.2	25.5	20.9	28.5	29.4	8.26
H₂	21.5	--	20.7	0.80	1.30	0.70	--
CO	5.10	4.80	2.6	--	3.80	--	--
CO₂	26.2	9.40	1.5	--	2.00	--	0.002
CH₄	17.3	19.8	44.5	10.2	10.1	10.1	0.55
C₂H₆	8.20	9.10	4.4	--	--	--	0.57
C₂H₄	8.70	9.40	17.3	--	--	--	1.39
C₃	7.30	10.8	3.90	0.7	2.5	3.50	1.53
C₄	5.70	21.3	1.30	0.30	0.20	1.40	3.00
C₅	--	7.6	--	--	--	--	1.22
C₆	--	2.8	--	--	--	--	--
H₂S	--	--	--	1.60	0.20	0.01	--

¹Fixed bed

²Fluidized bed

³CSBR

1.3.2.2. Char

Char derived from ST pyrolysis is a carbon-rich solid material, consisting on the initial carbon black, inorganic compounds (Zn, Ca and Si) and other carbon-based solids generated by repolymerization of the BR and SBR [19, 63, 64]. Typical values of char yield are between 38-40 wt% for temperatures above 500 °C. However and, as before, these values vary greatly upon the technology and conditions employed. The composition and properties of char, like its specific surface (S_{BET}), moisture and H content [65], can be tuned by reactor conditions. As listed in Table 1.5, Li et al. [66] and Galvagno et al. [51] used rotary kiln reactors to determine that an increase in pyrolysis temperature (in the 450-650 °C and 550-680 °C ranges, respectively) also decreases the volatiles content in char. Metal content, however, did not show a defined trend with temperature. A rise in temperature also leads to higher char surface areas [40]. Conesa et al. [67] studied a wider temperature range (450-1,000 °C), observing not only a decrease in volatiles (7.78-1.06 wt%) and H (0.6-0.17 wt%), but also a significant vaporization of Zn at 1,000 °C from char to the gaseous products, decreasing its content from 6.68 to 0.94 wt%.

Char yield and quality are of great importance when evaluating the global economical feasibility of ST pyrolysis. Char itself is an attractive ingredient of tires substituting carbon black [30, 40, 68]. However, as char contains other carbon based solids, its properties differ significantly from the original carbon black [40, 65, 69]. Nevertheless, the economic interest of this route remains due to the increasing demand of carbon black, increasing 4 % year⁻¹. Another immediate pull of char consists in its activation for manufacturing activated carbon [5, 70-72]. Activated carbon from tires can later be used as adsorbent, showing successful performance thanks to its mesoporous structure [73]. The activation methods of ST pyrolysis chars are CO₂ and steam activation, obtaining chars with S_{BET} up to 1,000 m² g⁻¹ [73]. ST pyrolysis char seems to be less reactive towards gasification compared with other carbon sources, due to its low crosslinking degree and little amount of structural imperfections, that act as potential gasification sites [74]. However, with the adequate conditions, specific surfaces comparable to those of commercial activated carbon can be achieved.

Table 1.5. Properties of different pyrolysis chars as reported in literature.

Ref.	[65] ¹	[67] ²	[66] ³	[51] ³	[75] ⁴	[56] ⁴
T, °C	500	450	500	550	500	600
Moisture, wt%	0.4	0.37	2.35	3.57	--	--
Volatiles, wt%	2.8	7.78	16.14	12.78	--	--
Ash, wt%	11.60	8.27	12.32	15.33	--	7.1
C, wt%	90.6	88.19	82.17	85.31	80.3	86.6
H, wt%	0.9	0.6	2.28	1.77	1.30	0.7
N, wt%	0.7	0.1	0.61	0.34	0.30	0.4
S, wt%	2.3	1.9	2.32	2.13	2.70	2.1
Zn, wt%	4.1	6.68	--	4.06	3.80	--
Ca, wt%	1.2	0.13	--	--	--	--
Fe, wt%	0.2	0.04	--	0.54	--	--
Al, wt%	0.15	--	--	1.09	--	--
Si, wt%	0.42	1.69	--	--	--	--
Pb, wt%	--	0.01	--	Tr	--	--
CV, MJ kg⁻¹	30.5	30.8	31.5	30.7	29.3	--
S_{BET}, m² g⁻¹	64	93	--	--	83	116.3

¹Fixed bed²Drop tube³Rotary kiln⁴CSBR

1.4. SCRAP TIRES PYROLYSIS OIL (STPO)

STPO is the most abundant while the most interesting and economically attractive product of the ST pyrolysis. It is a brownish liquid resembling crude oil and consists basically of: (i) the processing liquid as part of the tire formulation, (ii) organic additives, and (iii) tire pyrolysis products [76]. The CV of STPO can be as high as 44 MJ kg⁻¹ [30], comparable to valued fuels, so it requires a separated Section to be analyzed in terms of its composition and potential for being used as alternative fuel.

1.4.1. Elemental composition

Despite the different technologies and operational conditions strongly affecting STPO yield, its composition does not vary as significantly as that of the gaseous fraction (Table 1.6). Sulfur compounds in STPO have their origin in the thermal degradation of the organic additives used as vulcanization agents and accelerators in tire manufacturing [77]. Comparing this data with the elemental analysis of tires listed in Table 1.2, higher amounts of C and H are observed in STPO, together with less oxygen, sulfur and N amounts, that have been either removed in the pyrolysis or retained in the solid fraction. The reaction pathways through which sulfur compounds are produced change with pyrolysis conditions (temperature, pressure and residence time) and yield different amounts of sulfurous compounds in STPO. Some authors have reported values of sulfur in the STPO of 0.3 wt% [33], however the majority of the reported values correspond to ca. 1.4 wt% [34]. Cleavage of the N-S and C-S bonds of N-N'-caprolactam and benzothiazolic additives in tires produce caprolactum and benzothiazole in STPO [78]. Unapumnuk et al. [79] corroborated the crucial role of temperature on S content in STPO, as less S was retained in STPO removed with increasing temperatures, while heating rate plays no significant role. These authors observed that half of the original sulfur remained in the char.

The amount of O and N present in STPO is similar to that of S or even higher, with a high H/C ratio representative of aliphatic and aromatic compounds. O and N compounds have their origin in thermal degradation of stearic acid, sulfur compounds, amines and oxygenated oils used in tire formulation, and should be taken into account when considering STPO for fuel applications, since pre-treatments are required to remove these elements.

Table 1.6. Composition of STPO of various authors as reported in literature.

Ref.	[35] ¹	[66] ²	[19] ¹	[74] ¹	[76] ¹	[80] ¹	[55] ³
T (°C)	600	550	550	550	650	650	550
Yield (wt%)	53.1	44.6	46.1	38.0	48.4	56.0	--
CV (MJ kg⁻¹)	41.2 ^a	41.0	43.3 ^a	40.8 ^a	41.6 ^a	42.4 ^a	--
C (wt%)	87.9	85.6	85.4	84.9	87.6	86.5	87.2
H (wt%)	10.1	9.6	11.4	9.6	10.4	11.7	10.6
N (wt%)	0.5	0.6	0.4	0.4	<1	<1	0.5
S (wt%)	1.3	1.3	0.6	1.6	1.4	0.8	1.2
O (wt%)	0.1	4.0	--	3.5	--	--	0.5
H/C	1.4	1.4	1.6	1.4	1.4	1.6	--

¹Fixed bed reactor²Rotary kiln reactor³CSBR^aHigher

1.4.2. Molecular composition

STPO consists of a very complex mixture of hydrocarbons consisting of [69, 78]: C₆-C₃₇ linear paraffins, particularly C₈-C₁₃; low concentration of alkenes, particularly not condensed butadiene, pentenes, pentadienes and isoprene; high amount of aromatics, naphthenes and terpenes (with a total amount of ca. 65 wt% [81]), particularly limonene, BTX, alkylated single-ring aromatics and up to 5-ring benzopyrenes.

As a general trend, the amount of aromatics in STPO increases with pyrolysis temperature, due to the recombination reactions that take place among aliphatic and aromatic free radicals and also to the cyclization of aliphatic chains [31]. Several authors [34, 82, 83] have reported that the aromatic content in STPO is determined by the original amount of aromatics and olefins in rubber. Olefins and diolefins in particular tend to condense through Diels-Alder, cyclization and dehydrogenation reactions to form aromatics. These reactions are favored at high temperatures so that the amount of aromatics and polycondensed aromatics in STPO increases with temperature [39, 66, 84]. Increasing the residence time of volatiles in the pyrolysis reactor also results in the increase of aromatics and polycondensed aromatics yield in STPO [85].

Sulfur in STPO is in the form of benzothiazole (BTZ) and dibenzothiophene (DBT) and its alkylated forms; methyl, dimethyl and tetramethyldibenzothiophene (M₁DBT, M₂DBT and M₃DBT) [86]. Nitrogen in

STPO is in the form of BTZ too, while oxygen appears as hydroxyl compounds such as phenol, 3-methylphenol and 2-ethyl-1-hexanol [69]. As previously mentioned, these heteroatomic molecules represent for a huge obstacle for using STPO in combustion engines or as fuels.

1.4.3. Source for chemicals

Some of the mentioned molecules composing STPO have economic interest. STPO is an important source of *d*-limonene [77, 87], a high valued chemical used in the formulation of industrial solvents, resins, adhesives, fragrances, among others [34, 77]. Limonene is a cyclic terpene (C₁₀H₁₆) that exists in its *d*- and *l*- form, as *d*-limonene and *l*-limonene. Limonene yields are lower at high temperatures due to secondary reactions taking place, mainly dehydrogenation to form aromatics. Arabiourrutia et al. [88] observed a decrease in *d*-limonene concentration in STPO with temperature from 23.4 wt% at 425 °C to 5.7 wt% at 610 °C. Similarly, Li et al. [66] reported a decrease from 5.4 wt% at 450 °C to 0.07 wt% at 650 °C in *d*-limonene yield in STPO obtained in a rotary kiln reactor. Working in vacuum conditions and decreasing gas residence time can partially avoid sequential reactions of *d*-limonene [77, 89, 90]. López et al. [91] obtained a 60 wt% yield of STPO with a concentration of *d*-limonene of 26.8 wt% working in a CSBR in vacuum conditions, mainly due to the low residence time of volatiles. In the STPO obtained in a CSBR, the concentration of *d,l*-limonene is higher (ca. 27 wt%) than that in the STPO obtained using different reactors [92]. Various reaction pathways have been reported in literature for *d,l*-limonene formation [48, 77, 93], many of them agreeing on poly-isoprene (in the NR) cracking through β -scission and intramolecular cyclization. In parallel, isoprene could dimerize through a Diels-Alder pathway. Finally, and if temperature and/or residence time are high enough, *d,l*-limonene further dehydrogenates to aromatics [48]. Stanciulescu and Ikura [94, 95] used a two-stage distillation to obtain naphtha in the first stage, and *d*-limonene enriched naphtha in the second one. Then, they used *d*-limonene enriched mixture to obtain ethers by alkyloxidation [96].

STPO is also a potential source of light aromatics such as BTX, which are valued commodities [77, 89, 97], whose uses were widely reviewed by Weitkamp et al. [98]. The BTX composition in STPO is inversely proportional to that of *d*-limonene, as BTX is formed through *d*-limonene dehydrogenation [66]. Li et al. [66] have proposed optimal pyrolysis conditions for obtaining high yields of BTX: benzene, 2.09 wt%; toluene, 7.05 wt%; and xylene 2.01 wt%. Furthermore, post pyrolysis selective condensation, distillation, and catalytic pyrolysis can further increase the yields of BTX. Williams and Brindle [99] attempted selective temperature condensation of STPO to concentrate high value aromatics using three separate condensers at different

temperatures (100-250 °C). Another approach for increasing the BTX proportion in STPO is using a catalyst in the pyrolysis [100], which is known as catalytic pyrolysis or catalytic cracking. Williams and Brindle [44, 101] used a HY and HZSM-5 zeolites in a two-stage pyrolysis process (pyrolysis reactor followed by a catalytic reactor for the gaseous products) and found that, generally, increasing the catalyst/feed ratio had a positive effect on BTX yields, with maximums of 5 wt% benzene, 24 wt% toluene, 20 wt% *m*- and *p*-xylenes, and 7 wt% *o*-xylene. HY zeolite catalyst gave way to higher concentrations of BTX compared to HZSM-5 [101]. Olazar et al. [92] observed the following in aromatic yields: 20.2 wt%, without catalyst; 32.5 wt%, HZSM-5 zeolite catalyst; and 40.5 wt%, HY zeolite catalyst; with BTX maximum yields of 4.15 wt% of benzene, 7.39 wt% of toluene, and 6.59 wt% of xylene using HY zeolite.

1.4.4. Alternative fuel

Table 1.7 compares the fuel properties of STPOs reported in literature with those of a gasoil (GO) and a light fuel oil (LFO). Considering its CV, its boiling point (BP) and its storage stability [19], STPO is an interesting alternative to naphtha (BP = 35-216 °C), diesel (BP = 150-360 °C) or fuel oil (BP = 150-390 °C) [31, 34]. STPO has higher CV than that of the ST from which the STPO is obtained. The flash point of STPO is generally lower compared to that of petroleum refined fuels, due to the fact that STPO has a significant amount of volatile hydrocarbons, aromatics and olefins [26]. The carbon residue is higher than that of GO and LFO, so it should be taken into account when using STPO as fuel to avoid coke formation in the engine injectors. Moreover, STPO can present particles of sand, char, or alkali metals that can lead to problems in the engine pieces and performance, and also cause negative environmental and health impact [74].

A way to decrease the gasoil fraction of STPO and increase the proportion of gasoline and diesel, which are the most demanding fuel fractions, is to use catalytic pyrolysis, e.g. using a HZSM zeolite catalyst allows for obtaining a lighter STPO with less amount of aromatics included within the naphtha BP range, while a HY zeolite catalyst gives way to a higher proportion of diesel BP range compounds, with higher proportion of BTX [44, 92, 101]. Due to the compositional effect of catalytic pyrolysis, it should also be considered that the CV of the STPO obtained by a catalytic process is slightly lower than that of the STPO obtained by thermal pyrolysis, but still higher than that of the original rubber.

Table 1.7. Properties as fuels of different STPO and petroleum derived fuels.

Property	[38] ¹	[66] ²	[37] ³	GO	LFO	[55] ⁴
Flash point, °C	20	17	65	75	79	--
Carbon residue, %	2.2	1.78	--	<0.35	--	--
Density, kg L ⁻¹	0.910	0.962	0.833	0.780	0.890	0.894
Viscosity 40 °C, cSt	6.30	--	--	3.3	21.0	--
C, wt%	88.0	84.3	79.6	87.1	85.5	87.2
H, wt%	9.4	10.4	10.0	12.8	12.4	10.6
N, wt%	0.45	0.42	0.94	0.05	0.15	0.45
S, wt%	1.5	1.54	0.11	0.9	1.4	1.22
IBP, °C	100	--	38.5	180	200	128.5
90 % BP, °C	355	--	--	--	--	455
CV, MJ kg ⁻¹	42.0	41.7	42.7	46.0	44.8	--
Ash, wt%	Tr	Tr	--	0.01	0.02	--
Moisture, vol%	4.6	0.88	--	0.05	0.1	--

¹Stirred tank²Rotary kiln reactor³Fixed bed reactor⁴CSBR

Several studies have been conducted in diesel engines using STPO as fuel. Ilkilic and Aydin [102] proved that up to 75 wt% of STPO could be blended with diesel without modifying the engine performance. However, they observed an increase of hydrocarbon, CO and SO_x emissions. These results were also observed by Murugan et al. [10] who could feed up to 70 wt% of STPO. Murugan et al. [10, 103] have gone even further, proving that a mixture of 90 wt% of a STPO and 10 wt% diesel is still operative accounting the removal of moisture, desulfurization and distillation of the STPO. Hariharan et al. [104] studied the effect of adding diethyl ether as an ignition improver to a mixture of STPO and conventional diesel fuel, observing a decrease in NO_x emissions. However, due to the high content of aromatics and low hydrogen-to-carbon ratio, hydrocarbon and CO emissions were 38 % higher compared with those of conventional diesel.

Together with the high concentration of aromatic compounds, the amount of sulfur in the STPO appears as an obstacle for using this liquid as an alternative fuel. This is due to the strict environmental legislation that limits its amount in gasoline and diesel. Williams et al. [38] investigated SO_x and NO_x emissions in the combustion of STPO, observing much higher emissions than that for diesel in the same conditions. This result was directly related to the higher S content in STPO (1.45 wt%) compared to diesel (0.2 wt%). An

approach to reduce sulfur in STPO has been the catalytic pyrolysis using catalysts such as MgCl_2 [105], $\text{Ca}(\text{OH})_2$ [102], CaO and NaOH [33]. Nevertheless, sulfur removal did not surpass 34-35 wt%.

At this stage we can summarize the barriers affecting the implementation of STPO as an alternative fuel as follows: (i) the amount of sulfur and heteroatomic molecules, principally and according to the literature in the form of benzothiazole and alkylated DBTs, (ii) the amount of aromatics, heavy condensed ones in particular and (iii) the boiling range of the STPO obtained by pyrolysis which include heavy molecules in the range of gasoil. All this barriers cause troubles in combustion engines.

In this Thesis, the hydroprocessing of STPO has been studied in order to solve these three issues mentioned before. In the following Section we will go through the hydroprocessing reactions, catalysts, kinetic models and reactors.

1.5. HYDROPROCESSING

Hydroprocessing is a key refinery conversion process using high temperatures and partial pressures of hydrogen for removing pollutants, heteroatoms and increase the value of the feedstock [106]. In principle, it seems an interesting technology for solving the compositional barriers presented by STPO to be used as an alternative gasoline or diesel. Thus, in this Section we review the hydroprocessing reaction features, conditions, reactors and catalysts.

1.5.1. Hydroprocessing characteristics

There are two main types of hydroprocesses, each of which has different reactions taking place as a function of process severity that is measured in terms of temperature, pressure, space time and catalyst:

- Hydrotreating (HT) is generally considered as the process to perform hydrogenation and hydrogenolysis reactions. i.e. the removal of C=C and C-X bonds where X = C, S, N, metals, among others. The different heteroatoms give way to processes specifically designed to remove that type of bond: hydrodesulfurization (HDS), hydrodearomatization (HDA), hydrodemetalization (HDM) and hydrodenitrogenation (HDN).
- Hydrocracking (HC), is considered as the process to perform hydrogenation, hydrogenolysis and cracking reactions. According to the conversion required, two types of sub-processes can be distinguished: mild-hydrocracking (MHC) and severe-hydrocracking (SHC).

Figure 1.9 shows the process conditions required for each hydroprocess described before. HT is performed using temperatures of ca. 350 °C and partial pressures of hydrogen of 120 bar, whereas these values increase up to 450 °C and 250 bar for HC, respectively.

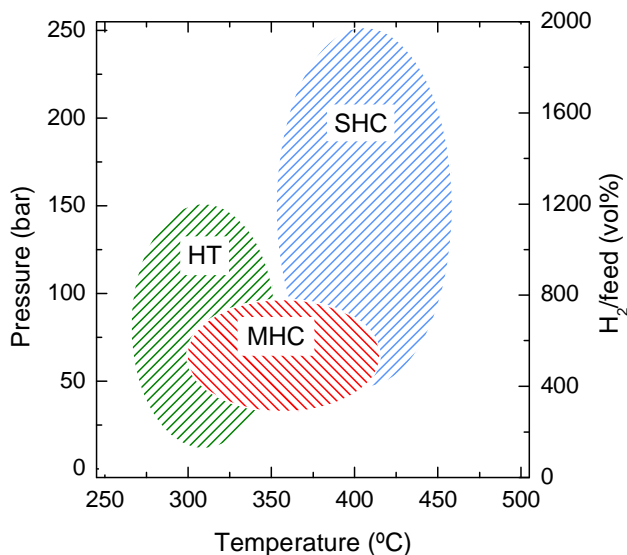


Figure 1.9. Standard conditions of hydroprocessing units.

1.5.1.1. Hydrotreating (HT)

HT involves two types of reaction: hydrogenation and hydrogenolysis. Hydrogenation is defined as a reaction in which hydrocarbons are saturated by the breakage of π -bonds of C present in olefins and aromatics. These reactions are generally reversible and exothermic. Hydrogenation of olefins is relatively fast reaction and can take place even at atmospheric pressure, decreasing its rate upon increasing their molecular weight [107]. Hydrogenation of aromatics, however, requires of much higher pressures of hydrogen to achieve its saturation, due to the resonance stabilization of π -electrons. Hydrogenation rate of aromatics generally increases with the number of aromatic rings present [108].

Hydrogenolysis involves the breakage of σ -bonds of C-X, being X = C, S, N, O or metal, with the help of hydrogen. The main sub-reactions in hydrogenolysis are hydrodesulfurization (HDS), hydrodenitrification (HDN), hydrodearomatization (HDA), hydrodemetallization (HDM) and hydrodeoxygenation (HDO). HDS, HDN, HDA and HDM are especially relevant for petroleum-derived feedstock, whereas HDO is more interesting for biomass-derived feedstock. For STPO and according to the composition describe before (Section 1.4) the most relevant hydrogenolysis reactions are HDS, HDN and HDA.

HDS occurs through two different pathways: hydrogenolysis and hydrogenation or hydrogenation and hydrogenolysis [109-112]. The former pathway is named as “direct” desulfurization (DDS) whereas the latter is the “indirect” route. Figure 1.10 shows the direct and indirect pathways of desulfurization of a representative S-molecule contained in the STPO as is DBT. The catalyst and reaction conditions strongly affect which pathway is dominant.

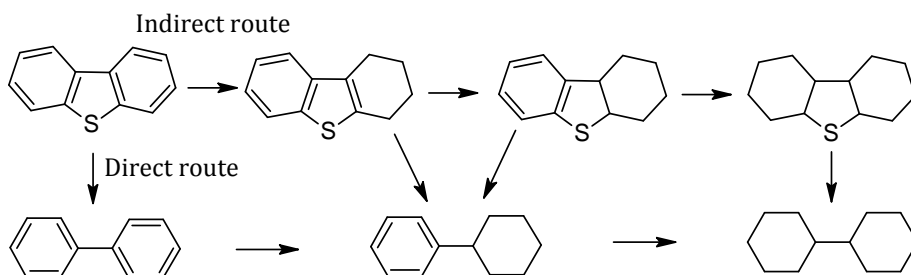
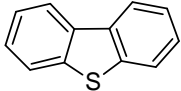
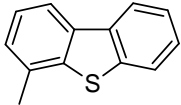
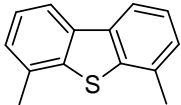
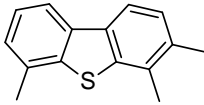


Figure 1.10. HDS of DBT pathways.

The rate of HDS is strongly dependent on the “molecular environment” of C-S bond, so that methyl or benzyl groups near this bond could decrease HDS rate several orders of magnitude [113]. Table 1.8 shows relative HDS rates of different sulfur containing molecules representative of diesel. This reactivity can be ordered as follows: thiophene (T) > alkylated thiophene > benzothiophene (BT) > alkylated BT > dibenzothiophene (DBT) and alkylated DBT without substituents in positions 4 or 6 > alkylated DBT with substituents in positions 4 or 6 > alkylated DBT with substituents in positions 4 and 6 (4,6-DMDBT) [114]. In the STPO, the most refractory S-containing molecules are 4-MDBT and 4,6-DMDBT [115].

Table 1.8. Relative HDS rates of different sulfur containing molecules [116] present in STPO.

Molecule	Name	Relative rate
	Dibenzothiophene	30
	Methylthiophene	5
	Dimethylthiophene	1
	Trimethylthiophene	1

Nitrogen in STPO is found in the form of benzothiazole (BTZ), which also contains sulfur. Since nitrogen is linked to the molecule by three bonds, before nitrogen can be removed from these structures, the aromatic ring must be saturated and opened through hydrogenolysis pathways [116]. In contrast to HDS, which may not require complete hydrogenation of the S-ring, HDN generally occurs through hydrogenation of the N-ring, as shown in Figure 1.11 for a BTZ molecule. Under HDN conditions, aromatic ring saturation is slightly more thermodynamically favored than N ring saturation, but the N ring is always hydrogenated first due to kinetic factors [117]. This way, the removal of S and N from BTZ occurs through an amine intermediate, releasing H_2S and NH_3 as products.

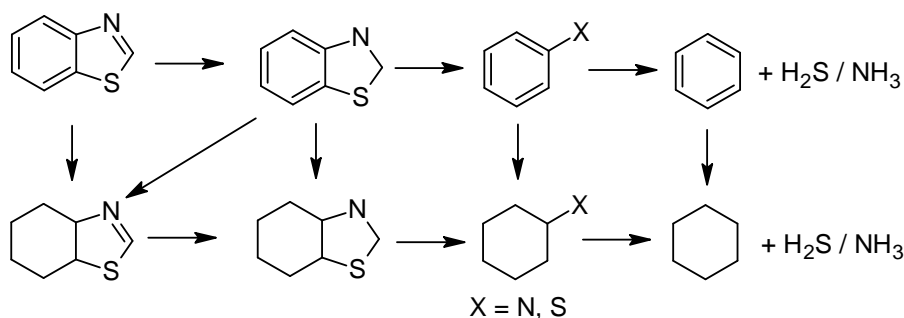


Figure 1.11. Kinetic scheme of BTZ HDN.

HDA consists mainly in the hydrogenation of an aromatic ring to form either naphthenes or lighter products derived from further hydrogenation and/or cracking of these rings, such as n-alkanes [118]. The reactivity of tri- and diaromatic compounds has been reported to be higher than that of monoaromatics [119], and thus, the conversion of monoaromatics appears as the real challenge regarding HDA. Figure 1.12 shows a simple example of aromatic ring hydrogenation and further cracking. The double bonds of toluene are sequentially hydrogenated to give way to the formation of methylcyclohexane, that will most likely undergo aliphatic chain scission to form cyclohexane and CH_4 as products. Partial H_2 pressure is the most important parameter controlling HDA. Depending on the type of feedstock, the necessary H_2 partial pressure can vary as much as 40 vol% to reduce the aromatic content down to 10 vol% [120].

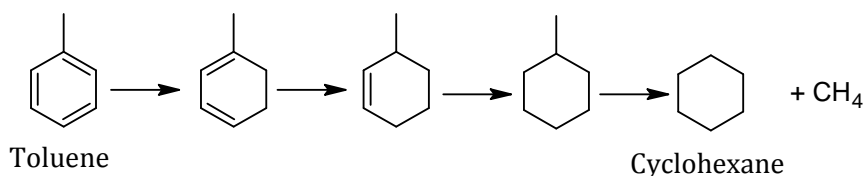


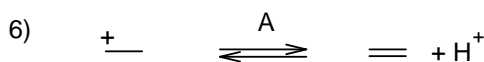
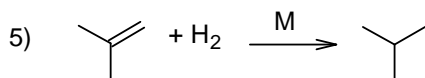
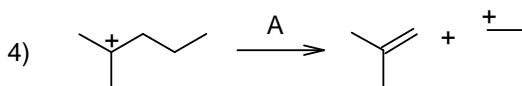
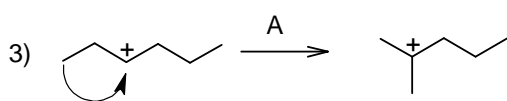
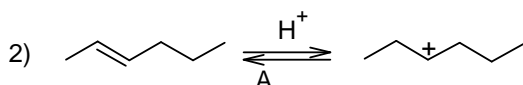
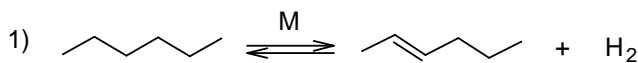
Figure 1.12. HDA of toluene.

1.5.1.2. Hydrocracking (HC)

This process involves the same reactions taking place in HT plus the cracking of hydrocarbons. Thus, HC requires a strong acidic catalyst and a metallic function for the HT so it is a bifunctional catalyst. Cracking involves carbenium-ion intermediates that have their own particular chemistry [121]. Figure 1.13 shows the mechanism of transformation of STPO representative molecules (paraffins and naphthalene) involving aliphatic cracking, ring opening, or dealkylation. The bifunctional catalyst used in HC determines that there are two types of reactions involved [122, 123]: those occurring on the metallic sites and those occurring on the acidic sites. Hence, some authors indicate that the mechanism is dual: metallic and acidic. In paraffin cracking (Figure 1.13a) Step 1 involves adsorption of a paraffin molecule on the metal site, followed by dehydrogenation to form an olefin. In the step 2, olefin protonation takes place on an acidic site and forms a carbenium ion. Step 3 involves the rearrangements of this carbenium ion in order to stabilize the charges, normally by isomerization. Step 4 requires a β -scission of the ion producing an olefin and a smaller carbenium ion. The olefin can either undergo further cracking on an acid site, or react with H_2 in a metal site to form a saturated iso-paraffin (step 5). The carbenium ion from step 4 can also convert

to a paraffin by deprotonation (step 6). In the case of naphthalene [124] (Figure 1.13b), it is hydrogenated to tetralin in the first place, and then the hydrogenated intermediates migrate to acidic sites where further hydrogenation, isomerization, and saturated ring opening and dealkylation take place.

a)



b)

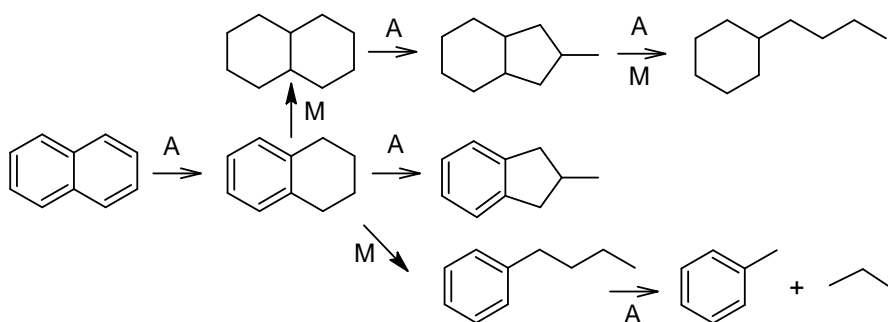


Figure 1.13. Examples of a) aliphatic cracking, b) ring opening and dealkylation reactions.

1.5.1.3. Side reactions

There are several parallel reactions involved in HT and HC, among of which the most relevant ones for the hydroprocessing of STPO are product recombination, catalytic poisoning (with NH_3 or H_2S) and coke formation. Recombination involves that olefins react with H_2S to form mercaptanes. A common strategy to remove these compounds is to dispose a hydrotreatment catalyst layer or an additional adsorbent bed selective towards mercaptanes. Catalyst poisoning occurs when impurities of the feed (generally S and N) block or modify the nature of the metallic and/or acidic phase of the catalyst, and also due to the formation of determinate heavy products like unsaturated hydrocarbons [125, 126].

Coke formation during the HC and HT of residues of similar properties to STPO is due to the direct deposition of the heavier molecules of the STPO, what is known as Conradson coke, or due to the formation of inactive hydrocarbons on the metallic or acidic sites. The term “coke” includes all the carbonaceous materials that remain adsorbed on the catalysts. The general expression of coke is $(\text{CH}_x)_n$, where the “x” value is approximately 2 for undeveloped coke and close to 0 for very developed or condensed coke [127]. Coke deposition is also affected by different properties of the catalyst, as are: (i) porous structure, (ii) total acidity and (iii) acidic strength of the sites [125]. While total acidity is beneficial in terms of HC performance, it is also causing a higher level and more rapid deactivation due to polymerization and aromatic condensation reactions taking place more rapidly. As studied by Castaño et al. [125] on the HC of LCO over zeolitic supports, much more condensed aromatics could be detected in soluble coke compared to that in the original feed, as the high catalytic acidity favored the formation of coke precursors inside the microporous catalytic structure.

A simplified scheme of coke formation is shown in Figure 1.14a, as proposed by Cerqueira et al. [128]. As observed, coke formation involves several consecutive reactions of varying complexity depending on the reactant molecule. Alkanes undergo cracking and then hydrogen transfer reactions to form olefins. Then, these oligomerize into naphthenes that undergo hydrogenation to produce aromatics, which are then converted into soluble coke. This soluble coke is trapped inside the porous structure and is then converted into insoluble coke through combinations of the previously mentioned type of reactions. An example of coke formation from an aromatic molecule is depicted in Figure 1.14b. Two aromatics can react and, after an alkylation step, they undergo dehydrogenative coupling, creating a cyclopentane cycle. This cycle converts into an anthracene molecule (through isomerization and HT reactions), which further develops into bulkier

compounds, often referred to as heavy poly nuclear aromatic hydrocarbons (HPNA) [129]. A similar coke formation mechanism was proposed by Guisnet and Magnoux [130].

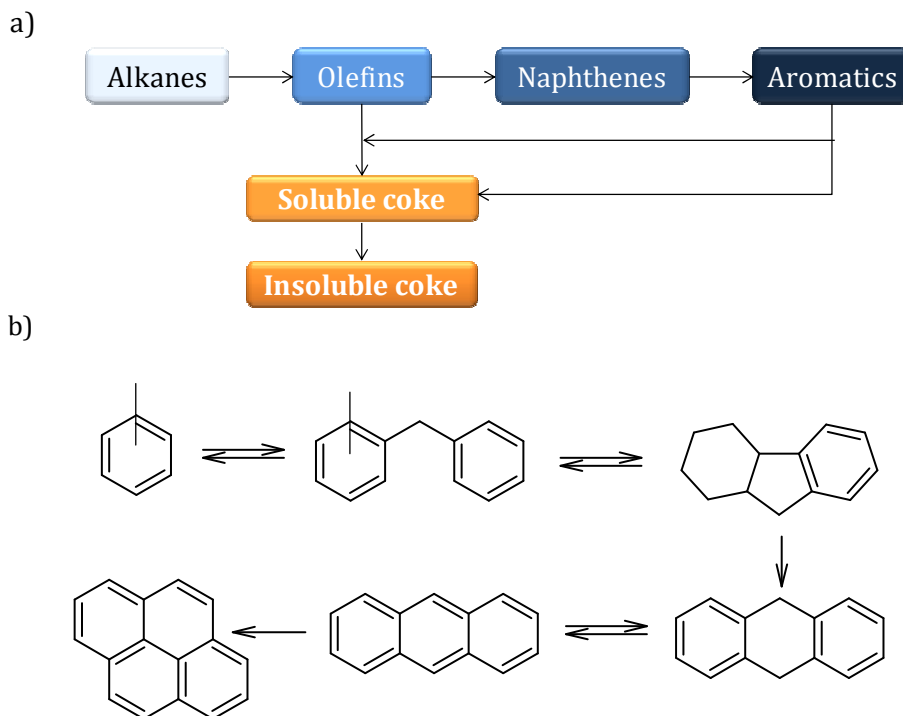


Figure 1.14. Examples of a) mechanism of coke formation from various reactant molecules and b) coke formation reaction from aromatics.

Other source of catalyst deactivation in HT and HC is metal sintering [131], which occurs as a consequence of the high temperatures employed. However, the most frequent cause of deactivation is coke deposition, reason why temperatures are raised during the lifetime of the catalyst, in an attempt to maintain catalyst activity [120]. The problem is that, as the temperature is increased, the rates of coke formation and metallic sintering are higher so that the catalyst lifetime decreases even further.

1.5.2. Catalysts

Demand for cleaner fuels has led a relevant subject of environmental catalysis research. Table 1.9 shows the current US Environmental Protection Agency (EPA) regulations for diesel fuels (including non-road diesel fuels), together with earlier fuel specification data in the US. Reducing highway diesel fuel sulfur content from 500 ppm down to 15 ppm, implies that refineries are facing major challenges to meet these specifications along with the required aromatic contents. More active HT and HC catalysts have solved these challenges, achieving major advances since the last decade of the past century in terms of catalytic activity (Figure 1.15), as environmental concern acquired greater significance, reaching ultra low sulfur diesel (ULSD) levels of 15 ppm worldwide, as shown in Figure 1.16 for the sulfur specification trends of the last 2 decades in the US, Japan and the EU.

Table 1.9. US EPC sulfur regulations (content in ppm) for diesel and jet fuels [114].

Category	Year			
	1989	1993	2006	2010
Highway diesel	5,000	500	15	15
Non-road diesel	20,000	5,000	500	15
Jet fuel	3,000	3,000	3,000	3,000

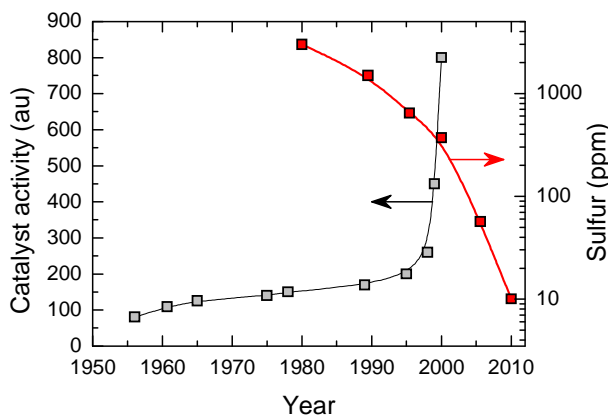


Figure 1.15. Trend of catalyst activity improvement and sulfur restrictions in the recent years.

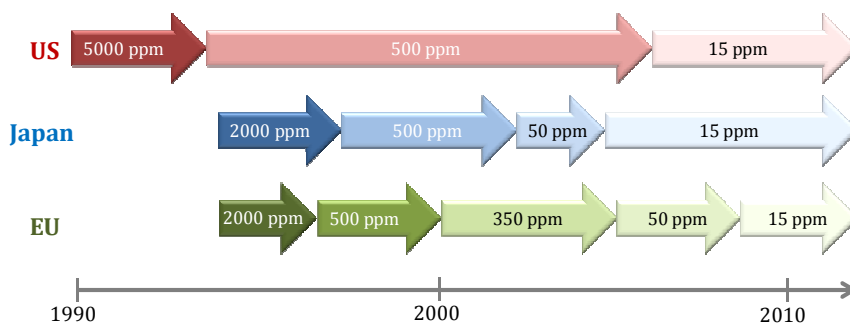


Figure 1.16. Trends in diesel sulfur fuel specification for highway transportation vehicles.

Among commercial HT catalysts, the STARS (Super Type II Reaction Sites) and NEBULA (New Bulk Activity) catalyst series from Albemarle have outstanding performance. On the one hand, CoMo STARS are suitable for HT streams with high sulfur content (100-500 ppm), reaching S levels of 10-20 ppm for 400 days. On the other hand, NiMo STARS are suitable for feedstock of less than 100 ppm S and are able of reaching 2-5 ppm S level. CoMo CENTINEL (Criterion Catalysts and Technologies) catalysts are suitable for treating high sulfur-containing feedstock, while NiMo CENTINEL require feedstock with less than 50 ppm of sulfur [132].

1.5.2.1. Metallic function

The commonly used metallic functions are [133]: (i) non-noble metal sulfides of the groups VI A (Mo, W) and VIII A (Co, Ni), or combination of these, based on the synergic effects that are created between two or more metals; and (ii) noble metals (Pt, Pd, Ir, among others) in its reduced form. The composition of the HT and HC catalyst is tailored for each specific feed or products. As listed in Table 1.10, the most common combinations of active elements in HT catalysts are the CoMo, NiMo, and NiW families. The concentrations of the metals is usually 1-4 wt% for Co and Ni, 8-16 wt% for Mo and 12-25 wt% for W. CoMo catalysts are excellent for HDS, but are less active for HDN and hydrogenation of aromatics. NiMo catalysts, on the other hand, are very good at HDN and MHC of aromatics. NiW catalysts present a very high aromatics hydrogenating activity, but their use has been limited due to their higher cost [117]. Noble metals are more active towards hydrogenation and hydrogenolysis reactions, but are limited to feeds with low sulfur levels to avoid metal poisoning.

Table 1.10. Metallic functions for hydroprocessing bimetallic catalysts.

Metal	Common application	Activation method	Hydrogenating activity
CoMo	HT (HDS)	Sulfidation	Mild
NiMo	HT (HDS and HDN)	Sulfidation	High
NiW	HT and MHC	Sulfidation	Very high
PtPd	HT and SHC	Reduction	High

Based on the fact that STPO contains high amounts of aromatics, sulfur and heavy molecules, the approach of this Thesis is to work in sequenced steps using different metallic functions: (i) HT of STPO using NiMo sulfide catalysts and (ii) HC and deep HDS of hydrotreated STPO using a PtPd catalyst.

1.5.2.2. Support

HT catalysts consist of a metallic function supported on a porous carrier, whereas HC catalysts consist of a metallic function supported on an acidic porous carrier. Thus, the support used for HT should have low acidity to avoid coke formation and maximum porosity to enhance metallic exposure, whereas the HC catalyst would have similar features and additional acidity to promote cracking reactions.

The most commonly used HT supports are γ -Al₂O₃ and amorphous SiO₂-Al₂O₃ (ASA) [134]. Different studies have been carried out aiming for improving catalyst performance using mixed oxides as catalytic supports, such as: Al₂O₃-TiO₂ [135-138], Al₂O₃-ZrO₂ [139] or Al₂O₃-MgO [140]. Metal and support can be either physically mixed or with the metal impregnated on the support for enhancing the interaction between the two functions [141-144]. Equally to what happens with the metallic function, the support is selected based on the composition of the feedstock and the required conversion level, among other factors.

For HC catalysts, the support needs to have a cracking functionality with stronger acidic sites [142, 145]. In this sense, crystalline zeolites like HZSM-5, HY, or H β have been widely investigated [146-151]. However, their micropores show difficulties for the diffusion of heavy molecules like the ones present in STPO. The usage of zeolites as an additive for amorphous acidic supports as γ -Al₂O₃ (in less than a 3 wt%) has an important effect in the catalyst activity and selectivity [152, 153].

Silica-based mesoporous materials represent for an expanding area of catalytic supports particularly interesting for the HT and HC of feeds like STPO [154]. In particular MCM-41 and SBA-15 show a highly ordered hexagonal array of mesopores with a narrow pore size distribution interesting for this application [155-157]. The performance of MCM-41 and SBA-15 has been widely studied as HT supports [158-162]. The addition of P, Ti or Zr to an SBA-15 support could enhance its morphological properties and provide a better metal dispersion [158-165]. Indeed, several authors have reported the benefits of these mesoporous materials in HT [166-169].

Activated carbons are also interesting supports for HT and HC reactions, considering their high surface area and tunable porous and acidic features [170]. Acidity of AC can be increased using H_3PO_4 [171, 172], as after activation, thermally stable phosphorus complexes remain in the AC surface enhancing its acidic properties. Different types of functional groups (carboxyls, lactones and phenols, mostly) can be added to the AC surface by air-oxidation [173], or chemical treatment with different acids like HNO_3 [174, 175] or H_2SO_4 [176]. The carbon atoms located on the surface of the AC crystallites act as active centers and show a tendency to chemisorb elements like O, H, N or S, which form surface complexes responsible for most of the physico-chemical properties of the solid material, being the oxygen complexes the most important ones [177]. Internal and external surface of activated carbon can be modified by adding functional groups, small or large molecules/species and also by using macromolecules [178]. This type of supports have been studied in the hydrotreatment of heavy and complex feedstocks [179-181], also in the form of carbon nanofibers [182, 183], and subjected to modifications with zeolites [184].

1.5.3. Kinetic modeling

According to the composition of STPO, the most interesting reactions involved in hydroprocessing are HDS, HDA and HC, so in this Section different approaches for modeling the kinetics of product lumps and compositional fractions will be analyzed.

HDS kinetics can be explained by the Langmuir-Hinshelwood (LH) expression, as the most common for heterogeneous catalysis [117]. For a given i species, the reaction rate results:

$$r_i = \frac{k_i p_i}{(1 + \sum K_j p_j)^n} f(p_H) \quad (1.1)$$

Where k is the kinetic constant, p_H the hydrogen partial pressure, K_j is the adsorption constant of other j species adsorbed on a given type of site, p_j the partial pressure of those species, and n is a constant. According to this expression, HDS is favored by more severe temperature and H_2 partial pressure conditions, and hindered by the presence of other compounds, especially aromatics, H_2S and NH_3 , which act as reaction inhibitors, limiting the extent of HDS reactions [117], and also acting as poisons for the catalyst. This type of expression has been commonly applied to study the HDS kinetics of DBT-type model compounds [185, 186], but has also proven to be valid for the study of HDS of real heavy feedstock like FCC gasoline [187] and VGO [188].

Regarding HC, different kinetic modeling approaches have been reported in literature, with a varying development degree, as extensively reviewed by Ancheyta [189]. Due to the complex composition of the refinery streams, considering each compound independently implies designing a kinetic model of great complexity that may present several analytical drawbacks, as a great amount of parameters need to be estimated. To minimize this problem, compounds can be grouped in lumps, in a much simpler kinetic model design. For a brief review, kinetic models can be based on: (i) lumping technique, (ii) continuous mixtures and (iii) single-event kinetic models (SEKM).

The lumping technique (which has been used for explaining HDA and MHC reactions in this Thesis) is based in grouping the compounds of a complex mixture into big groups generally according to a boiling point criteria. Its complexity can vary from simple models of 4 lumps, to more complex ones, generally assuming first order reactions. Callejas and Martinez [190] studied the kinetics of the HC of a Maya crude residue by considering light oil (LO) and gases as products, in a very simple 3-lump model. Orochko et al. [191] contributed with introducing the different concentrations as molar fractions. Botchwey et al. [192] (Figure 1.17a) proposed a little more complex kinetic model of 4 lumps (divided by boiling temperature cuts) for the HT of bitumen derived heavy gasoil from Athabasca over a $NiMo/Al_2O_3$ catalyst, in which 5 parameters needed to be calculated. Depending on the temperature regime, some stages were negligible. Considering this effect of temperature, they also proposed another model (Figure 1.17b) in which HT stages and HC stages (dotted lines) acquire different relevance based on the hydroprocessing temperature. A more developed model of 5 lumps was proposed by Sánchez et al. [193] for the HC of heavy oils (Figure 1.17c), considering unconverted residue, VGO, middle distillates, naphtha and gases, in which 10 kinetic parameters had to be estimated from fixed-bed experimental data. This model was developed mainly for HT of heavy petroleum fractions at moderate conditions with low conversion level. Another approach for lumping models is considering groups of pseudocomponents, defining lumps not only by boiling

point criteria, but also considering the nature of their main chemical bonds. This type of model was proposed by Krishna and Saxena [194] (Figure 1.17d) defining 7 lumps by chemical compound type (aromatics, naphthenes and paraffins) and considering “heavy” compounds those above the cut temperature and “light” those ones below.

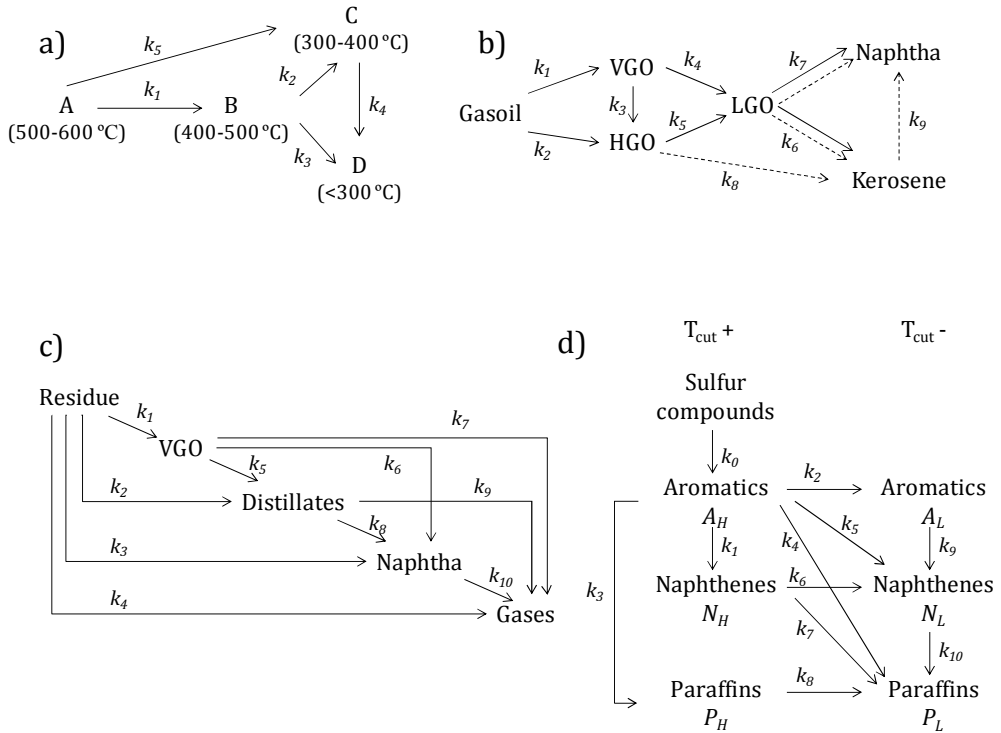


Figure 1.17. Examples of lumping-based kinetic models as reported in literature.

Laxminarasimhan and Verma [195] developed a kinetic modeling considering the continuous change of the characteristics of the lumps inside the reactor, characterizing them by their boiling point (BP) temperature. These models quantifying the evolution of the reaction have been further developed [196], and Elizalde et al. [197] recently reported the application of this continuous lumping modeling to heavy crude oil HC in moderate conditions in an isothermal fixed-bed reactor. However, distillation curves present some difficulties when analyzing heavy oil fractions, since the initial and final boiling point are not accurate during heavy experimentation.

Another important advance in kinetic modeling was the consideration of each individual reaction step within what is commonly referred to as single

event kinetic modeling (SEKM) [198, 199]. In this approach, the different lumps are defined according to the structure of the compounds present in the reaction mixture. Froment [200] has extensively reviewed the SEKM technique, illustrated it by means of methanol-to-olefins and catalytic cracking of oil fractions, and highlighted that other important processes with complex feedstock like catalytic reforming, HC, alkylation and isomerization can be modeled by this SEKM concept. Structure-oriented lumping is more detailed and represents for a more “realistic” modeling as it considers the chemical transformations taking place during the reactions in terms of molecular structure, and describes reaction kinetics as a large number of pseudocomponents. Parameter values are not dependant on the properties of the feed and, even though the number of parameters to be calculated can be reduced, sufficient experimental data are required.

1.5.4. Reactor design

Trickle bed reactors are the most commonly used technology in hydroprocessing. In this type of multiphasic reactors we should distinguish: gas (H_2 , H_2S , NH_3 and inerts), liquid (hydrocarbons and in our case STPO) and a stationary solid phase (catalyst). Trickle beds consist basically in fixed beds of catalyst with cocurrent downflow of gas and liquid phase reactants to produce gas and/or liquid phase products [201]. Other hydrodynamic regimes, like bubbling beds, involve upflow cocurrent contact between the gas and the liquid.

The main concern regarding this type of reactors is to prevent maldistribution of gas and liquid, as well as ensuring a good wetting of the catalyst particles as dry regions result in lower conversions [131]. In the hydroprocessing reactors, the catalyst bed is divided placing less active catalyst first (up in the reactor) and more active catalyst later (down in the reactor). This division has different aims: (1) protecting the most active catalyst (normally more expensive) from deactivation, (2) redispersing the liquid so that the wetting of the catalyst in each bed is more homogeneous, (3) using the voids between the beds as quenching boxes for two purposes: (3a) cooling down the feed for reaching higher conversions in reversible exothermic reactions like hydrogenations and some hydrogenolysis, and (3b) decreasing the concentration of H_2S and NH_3 formed as byproducts that reduce the activity of the catalyst. Figure 1.18 shows an illustrative scheme of the trickle bed reactor used in HT and HC reactions. The typical bed configuration is a guard catalyst (bed 1); HDS, HDN and HDM catalyst (bed 2); and HC catalyst (bed 3). The temperature can increase up to 30 °C in the each bed due to exothermic reactions taking place [134], so quenching is usually carried out with recirculated H_2 streams [202, 203]. The main elements of the industrial

trickle bed reactor are: (i) a tube with holes for feeding H_2 without pre-heating as a refrigerant agent (also improves flux distribution and mix with the liquid), (ii) an inlet liquid distributor tray, and (iii) a redistributor tray where phases are mixed (below the quenching boxes).

When working in trickle-bed regime in a laboratory scale, different reactor scale and mass-transfer considerations should be taken into account, to ensure reactor dimensions and hydrodynamic conditions are adequate for obtaining kinetic data. The corresponding calculations for the hydroprocessing used in this Thesis are detailed in Section 2.5.1.2.

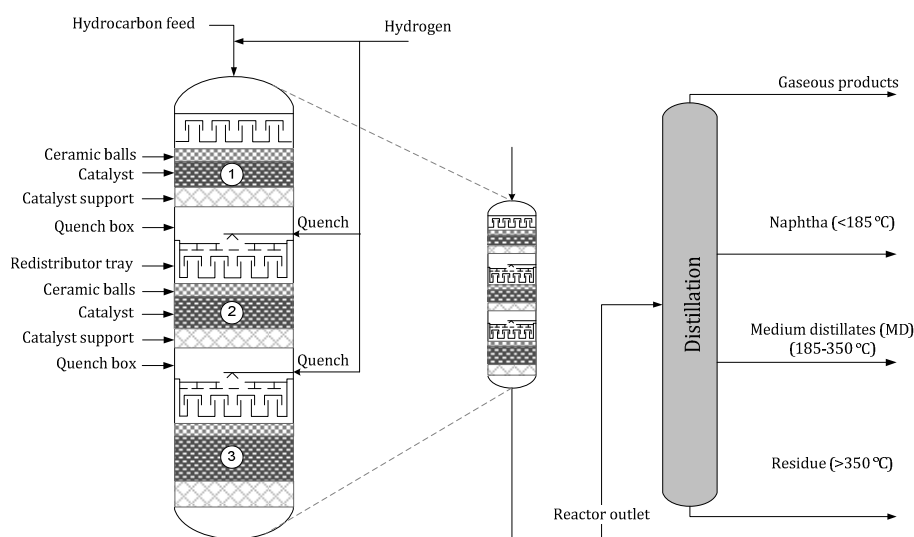


Figure 1.18. Disposition of three catalyst beds in series with intermediate quenching, for the hydroprocessing of a heteroatomic heavy feed with metals (Adapted from Álvarez et al. [204]).

Hydroprocessing reactors for heavy feedstock involve faster deactivation rates and therefore, the catalyst needs to be replaced more often. This is achieved in practice by using moving bed or bubbling fluidized bed reactors. Bubbling fluidized bed reactors are commercialized under the names H-Oil, LC-Fining and T-Star. One of the main advantages of fluidized bed reactors is that they require of smaller catalyst particles, and thus, minimize diffusional limitations and achieve higher conversions. T-Star license allows for operating in MHC regime with conversions between 35-70 wt% and H_2 partial pressures of 50-110 bar. H-Oil and LC-Fining processes generally operate in HC conditions but within different regimes: (i) low conversion

(< 65 wt%), achieving a 1 wt% of sulfur, and (ii) high conversion (approximately 90 wt%), with almost total destruction of the treated gasoil.

1.6. RESEARCH SCOPE

Considering all the previous, this Thesis focuses on the hydroprocessing of STPO with the main goal of upgrading its composition in terms of sulfur removal and reduction of aromatics through HDS and HDA reactions, and also redistributing its lumps (naphtha, diesel and gasoil) in terms of boiling point via mild hydrocracking (MHC). To this aim, a 2-stage hydroprocessing strategy has been applied, as shown on the left side of Figure 1.19.

- (i) **Hydrotreating.** STPO undergoes a HT stage using NiMo catalysts. In this stage, different NiMo catalysts over various micro- and mesoporous supports have been prepared, characterized and tested in terms of HDS, HDA and MHC. A previous catalyst screening with a synthetic STPO (SSTPO) has been carried out for selecting the most active catalyst towards HT. The results corresponding to this study are collected in Section 3. For obtaining further understanding of HT of STPO, and in order to obtain kinetic data for developing kinetic models, a study on the effect of the main process variables (temperature, pressure and space time) has been carried out over a NiMo/Al₂O₃ catalyst. This parametric study and its corresponding kinetic modeling constitute Section 4 of this work.

- (ii) **Hydrocracking.** Hydrotreated STPO (HT-STPO) is hydrocracked over a PtPd/SiO₂-Al₂O₃ catalyst for studying the effect of temperature and space time on HDS, HDA and MHC terms. Additionally, the study of the effect of temperature on catalyst deactivation and coke content and composition has been carried out, using various characterization techniques. All this information has been collected and detailed in Section 5. In order to obtain further understanding of the HT-STPO hydrocracking kinetics, Section 6 delves in the kinetic modeling of the HDS, HC and HDA considering the effect of catalyst deactivation (and its dependence on different possible coke precursors) with time on stream, for different space time conditions.

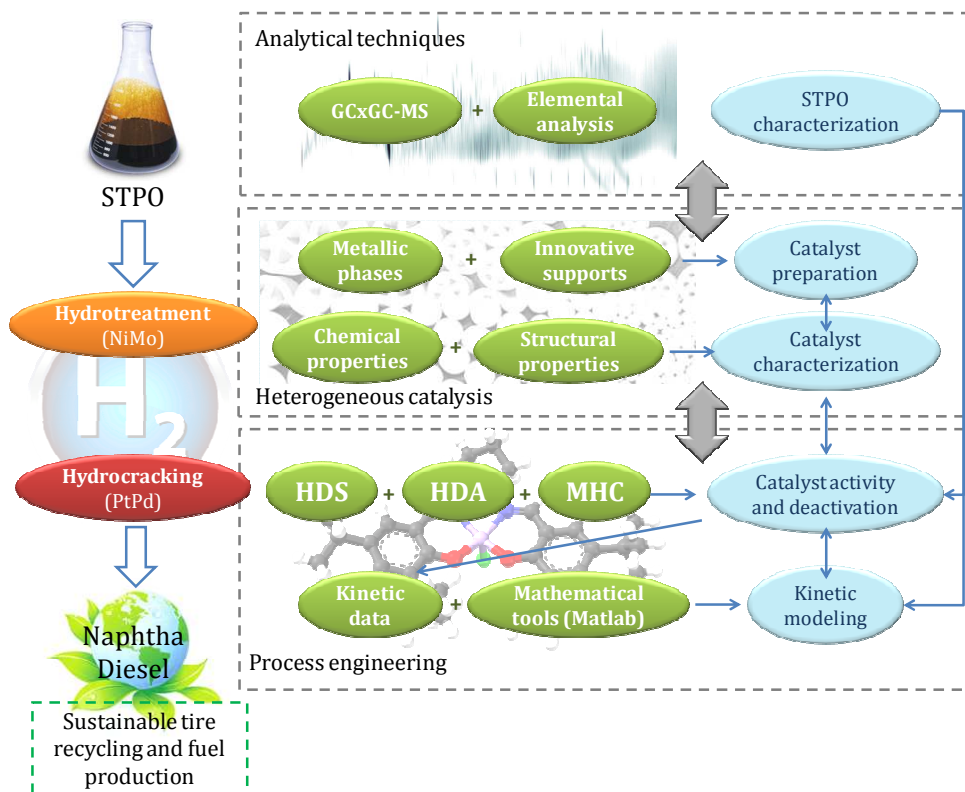


Figure 1.19. 2-stage HT-HC strategy and discipline contextualization for STPO upgrading.

The research scope of this Thesis is based on three main knowledge areas: (i) characterization of hydrocarbons, (ii) heterogeneous catalysis, by preparing, characterizing and correlating catalytic properties with their activity, and (iii) process engineering, focusing in catalyst activity, deactivation and kinetic modeling.

Section 2

EXPERIMENTAL

2. EXPERIMENTAL

2.1. FEEDS

2.1.1. Pyrolysis pilot plant unit

The scrap tires pyrolysis oil (STPO) has been obtained in a continuous pyrolysis pilot plant unit as the one shown in Figure 2.1 and previously described by Elordi et al. [205]. The main components of the pilot plant are: (i) a solid feeding device, (ii) a gas feeding device, (iii) a pyrolysis reactor, (iv) a device for retaining the fine particles from the stream of volatile products (cyclone and filter), (v) a liquid collection section and (vi) a system for gas product analysis.

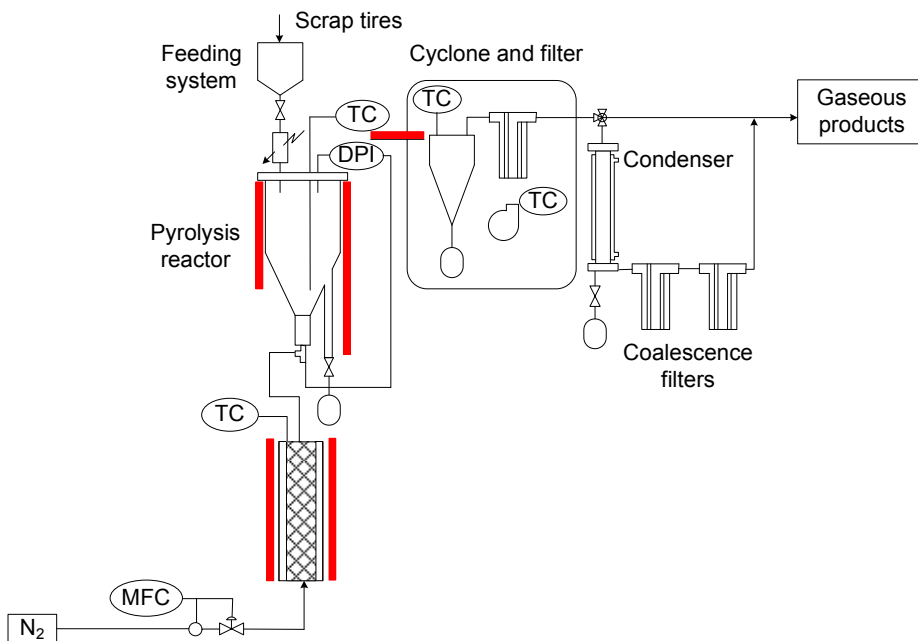


Figure 2.1. Waste tires pyrolysis plant unit scheme.

The solid feeding device (for previously grinded scrap tires) consists of a pneumatically actuated ball valve and a hopper. The feed-rate is controlled by varying the number of load-unload cycles in the valve, which allows for feeding up to 5 g min^{-1} of tire. The N_2 flowrate is controlled by a mass-flow controller that allows for feeding up to 30 L min^{-1} . Prior to entering the reactor,

the gas stream is heated up to the reaction temperature by means of a pre-heater.

The main element of the plant is the spouted bed reactor of conical geometry with a cylindrical upper section. The total height of the reactor is 34 cm, the height of the conical section is 20.5 cm, and the angle of the conical section is 28°. The reactor can operate from the regime of incipient spouted bed to a vigorous regime of jet spouted bed (or diluted spouted bed).

Volatile products leave the reactor together with the inert gas (N₂) and the finest carbon black particles.

2.1.2. Synthetic scrap tire pyrolysis oil (SSTPO)

A synthetic feed (SSTPO) has been prepared with the composition shown in Table 2.1. These compounds have also been selected by their chemical nature: naphthenes (*d*-limonene) and aromatics (1H-indene, toluene), some of which are sulfur-containing compounds (BTZ, DBT and 4,6-DMDBT). The different nature of the sulfur compounds also allows for studying the HDS reactivity of each compound separately.

The reactants used to prepare the SSTPO feed for the HT process are: *d*-limonene (Panreac Química, 95 wt%), toluene (Merck, 99 wt%), benzothiazole (Sigma Aldrich, 96 wt%), 1H-indene (Alfa Aesar, 90+ wt%), dibenzothiophene (Sigma Aldrich, 98 wt%), and 4,6-dimethyldibenzothiophene (Sigma Aldrich, 97 wt%). Before feeding the mixture to the HT unit, the synthetic feed was diluted in *n*-C₁₀ (50 N m³/m³) (Alfa Aesar, 99 wt%).

Table 2.1. SSTPO composition.

Compound	Composition (wt%)
<i>d</i> -limonene	58.5
Toluene	25.4
BTZ	8.74
1H-indene	7.27
DBT	0.045
4,6-DMDBT	0.045

2.1.3. Scrap tire pyrolysis oil (STPO) and hydrotreated STPO (HT-STPO)

The composition of STPO and HT-STPO, determined by bi-dimensional gas chromatography coupled with mass spectrometry (GCxGC-MS), is detailed in Table 2.2. Equally to SSTPO, STPO was diluted in *n*-C₁₀ (50 N m³/m³) to be processed.

Table 2.2. STPO and HT-STPO composition.

Compound group	Composition (wt%)	
	STPO	HT-STPO
Paraffins and isoparaffins, P+iP	2.39	35.36
Olefins, O	7.11	0
Naphthenes, N	34.67	22.01
1-ring Aromatics, A ₁	38.14	31.89
2-ring Aromatics, A ₂	17.69	10.74

The average molecular weight of STPO is 238.12 g mol⁻¹ and the density at 15 °C of 0.8939 g cm³, according to the API Technical Data Handbook 2B2.3 procedure and the ASTM 23B rule, respectively.

Cetane number (CN) of STPO is 23.71, as obtained by the predictive method specified by Yang et al. [206], which correlates 12 hydrocarbon groups in the diesel fraction determined by liquid chromatography and their contribution to CN.

The most characteristic STPO and HT-STPO properties have been summarized in Table 2.3, obtained from the corresponding ASTM standards and elemental analysis. The elemental analysis has been carried out at the SGIKER service at the University of the Basque Country (UPV/EHU). For the determination of C-H-N composition a LECO TruSpec CHN Macro apparatus has been used based on a 3-stage cycle: purge, combustion and analysis. After the purge, complete combustion of the sample is carried out in a furnace at 950 °C in O₂ atmosphere. Combustion gases are collected, and then C is measured as CO₂ via infrared (IR) detectors, H is measured as H₂O in a H₂O detector, and a small gas sample contacts Cu to transform NO_x into N₂ to measure its content with a thermal conductivity detector (TCD). The content of sulfur is measured in a separate module (TruSpec S) using a high sensitivity IR-detector for SO₂ analysis. The amount of oxygen is obtained by difference.

The simulated distillation (SD) results carried out according to the ASTM D 2887 standard, are represented in Figure 2.2 and listed in Table 2.4.

STPO has an initial boiling point (IBP) of 128.5 °C. The medium boiling point is 314.0 °C, while the final boiling point (FBP) is at 539.4 °C. The IBP of the mixture is in the naphtha fraction (35-216 °C). However, the main STPO fraction is within the medium distillates boiling point range (216-350 °C). The final boiling point (FBP) of the mixture is 539.4 °C, which corresponds to a gasoil fraction (> 350 °C). The SD curve for HT-STPO has very similar characteristics (IBP, 109.4 °C; FBP, 537.9 °C), being the main difference a higher amount of lighter compounds in the naphtha fraction.

Table 2.3. Properties of the STPO and HT-STPO.

	STPO	HT-STPO
Density, 15 °C(g cm ⁻³)	0.894	0.860
IBP-FBP (°C)	128.5-539.4	109.4-537.9
T ₅₀ -T ₉₅ (°C)	314.0-489.9	317.4-494.1
Cetane number	23.71	24.60
<hr/>		
Total C (wt%)	87.20	88.95
Total H (wt%)	10.60	11.02
Total S (wt%)	1.22	0.02
Total N (wt%)	0.45	--
Total O (wt%)	0.53	0.01

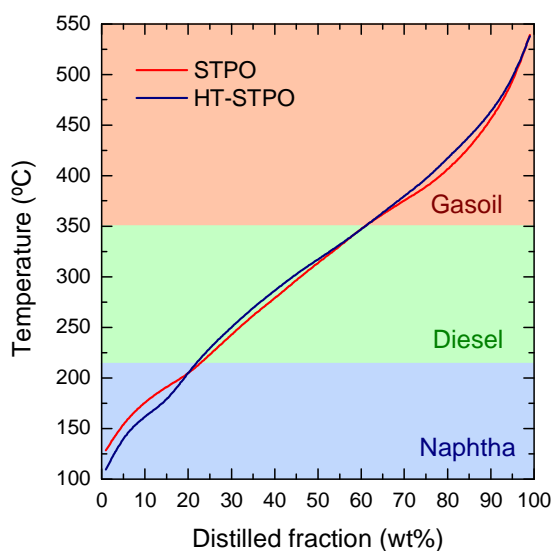


Figure 2.2. Simulated distillation curves of STPO and HT-STPO.

Table 2.4. Simulated distillation results for STPO and HT-STPO.

Dist. fraction (wt%)	Temperature (°C)	
	STPO	HT-STPO
IBP	128.5	109.4
5	156.1	143.1
10	176.6	162.7
20	203.5	205.5
30	242.9	250.4
40	278.8	286.6
50	314.0	317.4
60	347.9	346.8
70	375.6	379.9
80	405.9	417.5
90	455.0	462.4
95	489.9	494.1
FBP	539.4	537.9

Sulfur speciation for SSTPO, STPO and HT-STPO is detailed in Table 2.5, as determined by GC, and following the classification criteria specified in Section 2.2.2.1. The amount of sulfur present in HT-STPO is significantly lower than that of SSTPO and STPO, and quantitatively HT-STPO sulfur concentration follows the same trend than STPO, with M₃DBT species being the most abundant.

Table 2.5. Sulfur speciation for the different hydroprocessing feeds.

Compound	SSTPO (ppm)	STPO (ppm)	HT-STPO (ppm)
Total sulfur	20,788	11,600	1,985
BTZ	20,669	3,794	
DBT	70		
M ₁ DBT		182	38
M ₂ DBT	49	752	144
M ₃ DBT		3,460	1,019
M ₄ DBT		3,412	784

2.2. PRODUCT IDENTIFICATION AND ANALYSIS

After condensing the liquid products, gases have been analyzed online in a gas micro-chromatograph (micro-GC). Liquids are periodically sampled (at 1 h intervals) and analyzed via gas chromatography (GC) to determine both its composition and sulfur content.

2.2.1. Gas product identification and analysis

The equipment used for online gas product identification has been a Varian CP-4900 Micro-Chromatograph. The unit has three modules located inside a case that can be thermally conditioned within 0-150 °C. Each module is composed of a thermal conductivity detector (TCD) and one of the following columns: (i) molecular sieve (MS5A), to separate the permanent gases: H₂, O₂, N₂, CH₄ and CO; (ii) CPSiL column (8 m x 2 μm), to separate the C₅-C₁₀ hydrocarbons; and (iii) Al₂O₃ column, to separate the C₃-C₄ hydrocarbons.

The gas output stream is sucked and accesses the injector through an insulated line, after being filtered to keep the solid particles and condensed products from entering the unit. The injector has a 10 μL loop for sampling, amount that is defined by modifying sucking and injection times.

The injector sends the sample to the column by sucking by means of a vacuum pump connected to the outlet of the column. The unit has a backflush configuration, by means of the actuation of a restrictor that allows the circulation of He in the opposite direction through the pre-column, dragging the heavy products to vent, while the light products are sent to the analysis column, to be separated and analyzed by the TCD detector. This option maintains the columns clean of heavy products.

The sample and carrier gases flow separately through the TCD. The micro-GC operating conditions and data acquisition are registered by using Varian Star Chromatography Workstation software. The analysis conditions are specified in Table 2.6. Every 20 s a gas sample is injected at 110 °C and analyzed for approximately 4 min. The compounds analyzed in every column, their corresponding retention times and calibration factors are listed in Table 2.7. Calibration of the micro-GC and identification of the gas products has been done by using a gas standard (Air Liquide), with the following composition (balanced in He): CH₄ (1.37 vol%), C₂H₆ (0.94 vol%), C₂H₄ (1.98 vol%), C₃H₈ (1.41 vol%), C₃H₆ (2.85 vol%), C₄H_{10-n} (1.39 vol%), C₄H₈ (0.94 vol%), CO (2.05 vol%), CO₂ (2.86 vol%). Calibration factors have been obtained from the analysis of the gas standards, by referring them to CH₄.

Table 2.6. Analysis conditions for the different chromatographic columns.

	MS5A	CPSiL	Al ₂ O ₃
Sampling time (s)	20	20	20
Sample temperature (°C)	110	110	110
Injector temperature (°C)	110	110	110
Column temperature (°C)	120	120	110
Injection time (s)	40	100	20
Backflush time (s)	15	-	18
Analysis time (s)	260	260	260
Sample pressure (bar)	1.38	1.38	1.59

Table 2.7. Retention times and integration factors of the gas compounds.

Molecular sieve		
Compound	t _{ret} (min)	Factor
H ₂	0.530	--
CH ₄	0.697	1.00
CO	0.930	1.65
CPSiL		
Compound	t _{ret} (min)	Factor
Isopentane	0.325	0.52
n-Pentane	0.347	0.52
2-Methylpentane	0.371	0.41
3-Methylpentane	0.399	0.41
Cyclopentane	0.419	0.41
n-Hexane	0.477	0.36
Methylcyclopentane	0.501	0.41
Benzene	0.595	0.42
Cyclohexane	0.624	0.41

Table 2.7. (Continuation).

Al₂O₃		
Compound	t _{ret} (min)	Factor
Etane	0.323	1.19
Ethylene	0.330	1.28
Propane	0.345	1.02
Butane	0.383	1.89
Butene	0.400	1.89

2.2.2. Identification and analysis of the liquid products

2.2.2.1. Analysis of sulfur content

The determination of the sulfur content in the liquid products (for both HT and HC processes) has been carried out in an Agilent Technologies 7890A GC System, provided with a pulsed flame photometric detector (PFPD), and the following characteristics: (i) an Agilent Technologies 6850 ALS GC Autosampler, with 16-sample capacity and provided with a 10 μ L syringe, (ii) an insulated injector, (iii) a capilar column: HP-PONA (length, 50 m; internal diameter, 0.20 mm; thickness, 50 μ m), and (iv) a flame ionization detector (FID). The analysis conditions are listed in Table 2.8.

Previous to sulfur content measurements, calibration lines have been defined by using benzothiazole (BTZ) (the most abundant sulfur-containing compound present in STPO). The analysis conditions used for the calibration line measurements are the same as the ones specified for the product sample analysis.

Three different calibration lines have been used (Figure 2.3), adequate for the different sulfur content ranges expected: (i) One calibration line using a split ratio of 100:1 and a 32 sulfur signal attenuation value to measure sulfur on the products obtained from the hydrotreating of synthetic STPO, (ii) a calibration line using a split ratio of 300:1 and a 256 sulfur signal attenuation value to measure sulfur on the products obtained from the hydrotreating of STPO and (iii) another calibration line using a split ratio of 300:1 and a 64 sulfur signal attenuation value to measure sulfur on the products of the hydrocracking of HT-STPO. The n parameter (calibration coefficient) has been considered as a constant ($n = 0.42$) based on the coefficients for PFPD-FID analysis reported by Del Río et al. [207].

Table 2.8. Chromatographic analysis conditions for the sulfur content measurements.

Section	Variable	Value
Oven	T ₀ (°C)	30
	t ₀ (min)	3
	R ₁ (°C min ⁻¹)	15
	T ₁ (°C)	235
	t ₁ (min)	1
	R ₂ (°C min ⁻¹)	30
	T ₂ (°C)	320
	t ₁ (min)	20
Injector	T (°C)	150
	P (bar)	1.9
	Column flow (mL min ⁻¹)	0.85
	Split ratio	300:1
FID	T (°C)	320
	H ₂ flow (mL min ⁻¹)	30
	Air flow (mL min ⁻¹)	400
	Make up flow (mL min ⁻¹)	25
PFPD	T (°C)	250

The complete sulfur distribution of STPO is shown in Figure 2.4a. An intense peak can be clearly distinguished at 20 min, corresponding to BTZ. A wide distribution of alkylated dibenzothiophenes (DBTs) appears in the 24-32 min retention time range. Focusing on this region, different groups of DBTs can be distinguished, by correlating their retention time with the number of C atoms on their alkyl substituents (Figure 2.4b), as stated by Wang et al. [208]. This way, four lumps have been defined, taking into account the number of C atoms in their substituents, as follows: M₁DBT, M₂DBT, M₃DBT and M₄DBT.

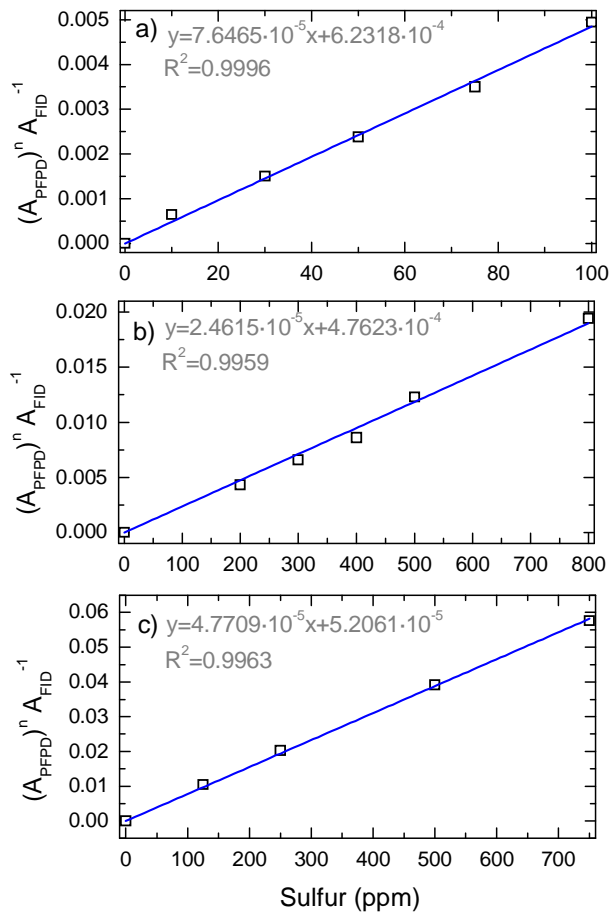


Figure 2.3. Calibration curves obtained from BTZ standards used for the sulfur content calculations on a) SSTPO hydrotreating products, b) STPO hydrotreating products and c) HT-STPO hydrocracking products.

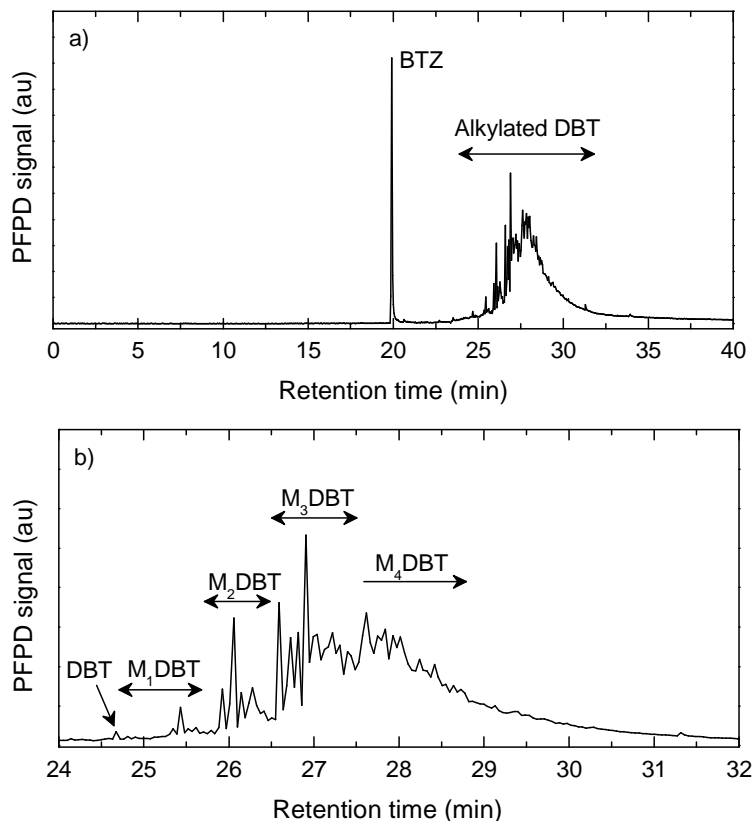


Figure 2.4. a) Total sulfur distribution in STPO and b) speciation of alkylated DBTs in STPO according to their retention times.

2.2.2.2. Analysis of HT products

The identification of the liquid reaction products from both HT and HC runs has been carried out in an Agilent Technologies 5975C inert XL Mass Spectrometer coupled in line with an Agilent Technologies 7890A Gas Chromatograph, provided with the following components: (i) an Agilent Technologies 7683B series Autosampler, with 8-sample capacity and provided with a 10 μL syringe, (ii) an insulated injector, (iii) two capilar columns coupled in-line (Non polar DB-5 ms J&W 122-5532, length, 30 m; internal diameter, 0.25 mm, and Polar TRB-50 HT, length, 6 m; internal diameter, 0.25 mm). The analysis conditions are listed on Table 2.9.

Table 2.9. Chromatographic analysis conditions for liquid products.

Section	Variable	Value
Oven	T_0 (°C)	40
	t_0 (min)	20
	R_1 (°C min ⁻¹)	1
	T_1 (°C)	260
	t_1 (min)	0
Injector	T (°C)	350
	P (bar)	1.97
	Column flow (mL min ⁻¹)	0.75
	Split ratio	40:1
Detector	T (°C)	350
	H ₂ flow (mL min ⁻¹)	20
	Air flow (mL min ⁻¹)	450
	Make up flow (mL min ⁻¹)	25

Figure 2.5c shows a bi-dimensional GCxGC chromatogram obtained from the analysis of the liquid products of the HT of STPO, along with its corresponding projections according to the retention time (Figure 2.5a) and time in the second dimension (2DRT) (Figure 2.5b). From this chromatogram, three different fractions can be defined according to a boiling point criteria (1DRT projection), as follows: naphtha (35-216 °C), diesel (216-350 °C) and gasoil (>350 °C). Furthermore, 5 lumps have been identified according to their reactivity (2DRT projection), as are: (i) paraffins and isoparaffins, P+iP, (ii) olefins, O, (iii) naphthenes, N, (iv) 1-ring aromatics, A₁, and (v) 2-ring aromatics, A₂. The quantification of each lump described in the 2DRT projection has been performed by a Gaussian deconvolution, as shown in Figure 2.5d,e,f.

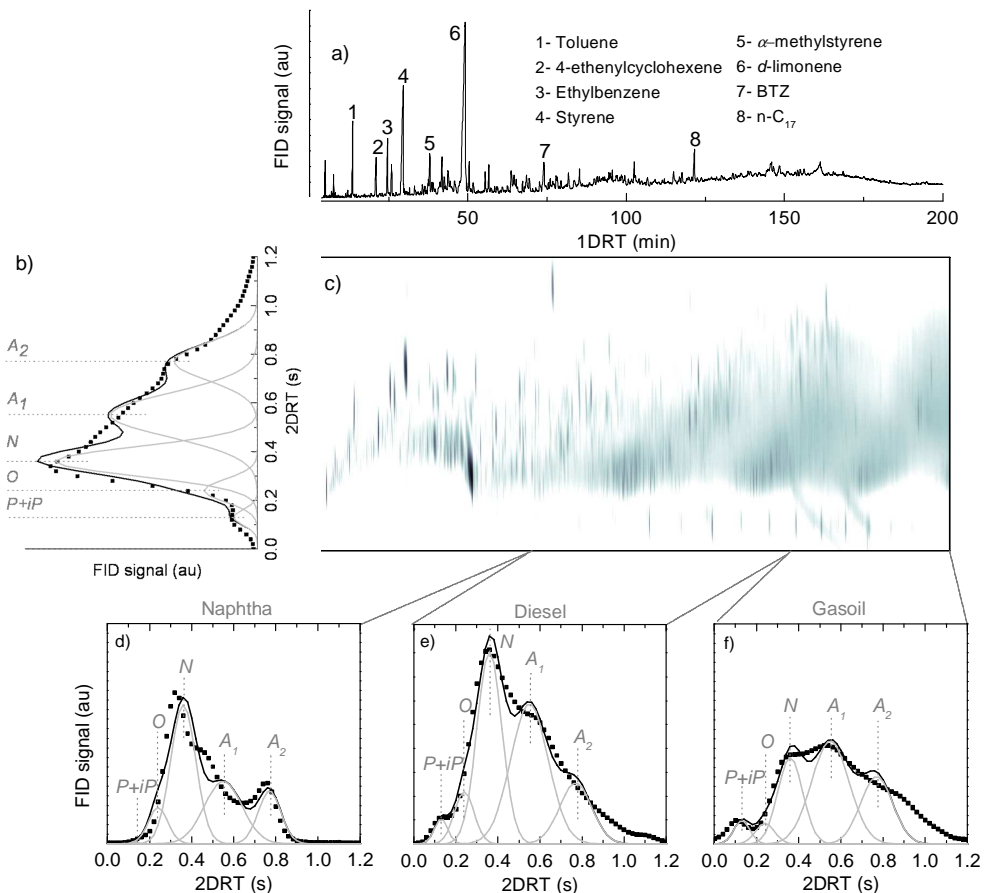


Figure 2.5. a) First dimension retention time (1DRT) projection and b) second dimension retention time (2DRT) projection of a c) bi-dimensional chromatograph of STPO with the corresponding deconvoluted profiles in the second dimension. Deconvoluted profiles of the second projection corresponding to d) naphtha, e) diesel and f) gasoil fractions.

2.2.2.3. Analysis of HC products

HC products have also been identified by bi-dimensional chromatography, following the same procedure specified for the HT products (Figure 2.5). The three fuel fractions have been divided following the same boiling point criteria. However, in HC products a liquefied petroleum gas (LPG) fraction has also been quantified, since much lighter products are formed.

2.2.2.4. Reaction parameters

Different conversions have been defined for the evaluation of the activity, from the concentration of sulfur, mass fraction of gasoil yield, and mass fraction of aromatics, in both STPO and reaction products:

Hydrodesulfurization conversion

$$X_{\text{HDS}} = \frac{S|_{\text{STPO}} - S|_{\text{prod}}}{S|_{\text{STPO}}} \quad (2.1)$$

Mild hydrocracking conversion

$$X_{\text{MHC}} = \frac{X_{\text{Gasoil}}|_{\text{STPO}} - X_{\text{Gasoil}}|_{\text{prod}}}{X_{\text{Gasoil}}|_{\text{STPO}}} \quad (2.2)$$

Hydrodearomatization conversion

$$X_{\text{HDA}} = \frac{X_{\text{Arom}}|_{\text{STPO}} - X_{\text{Arom}}|_{\text{prod}}}{X_{\text{Arom}}|_{\text{STPO}}} \quad (2.3)$$

As a tool for the kinetic modeling, H_2 concentration in the media has also been calculated following the methodology reported by Riazi and Roomi [209] from H_2 solubility data in hydrocarbons and petroleum fractions.

2.3. CATALYST PREPARATION

Two different types of catalysts have been used in this Thesis:

- (i) NiMo and NiMoP catalysts over different commercial and synthetic supports.
- (ii) A PtPd catalyst over a SiO₂-Al₂O₃ support.

Type (i) catalysts have been used for hydrotreating of STPO purposes, and the type (ii) catalyst has been used for the hydrocracking of the HT-STPO.

2.3.1. Hydrotreating catalysts

Different types of supports have been used for the NiMo catalysts:

- (i) Two commercial NiMo (1-5 wt% Ni, 10-20 wt% Mo) catalysts supported over SiO₂-Al₂O₃ (ASA) and Al₂O₃ (ALM) have been used. Their composition is subjected to commercial secret and therefore the suppliers are not mentioned.
- (ii) One commercial spent FCC catalyst regenerated at 550 °C for 12 h.
- (iii) Mesoporous MCM-41 and SBA-15 supports (provided by Ibercat S.L., Madrid) prepared following the procedure determined by Tanev and Pinnavaia [210] and Zhao et al. [211], respectively.

Except for the commercial ASA and ALM, for the rest of the catalysts the metallic phases have been impregnated at Ibercat S.L. by following the scheme shown on Figure 2.6. Previous to impregnation, the necessary amount of precursor salt was diluted in water and then mixed with the support at a 20:1 water to support ratio and stirred for 24 h. After that, the catalyst was dried in air and finally calcined in a N₂ atmosphere to either impregnate the following metal or obtain the final catalyst, which was tableted and sieved to obtain the right particle size (0.15-0.30 mm).

It is important to mention that only the FCC, MCM-41 and SBA-15 supported catalysts have been doped with P.

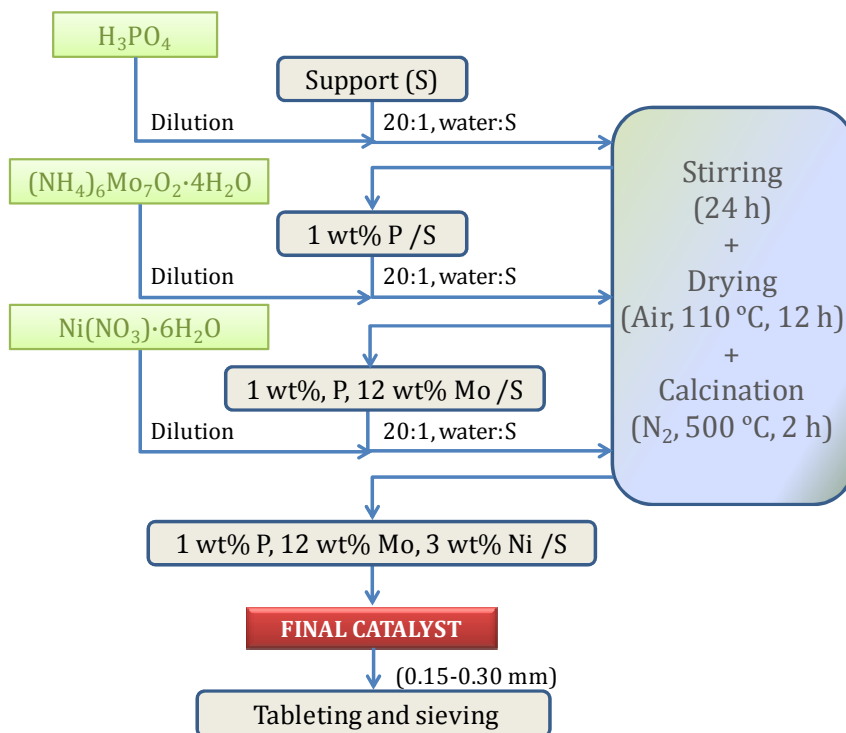


Figure 2.6. Metal incorporation procedure for the supported NiMoP catalysts.

2.3.2. Hydrocracking catalysts

The incorporation of the Pt and Pd metallic phases to the $\text{SiO}_2\text{-Al}_2\text{O}_3$ (ASA) support has been carried out by following previously established procedures [212, 213], as depicted in Figure 2.7.

The catalyst has been prepared by impregnation of the support at $80\text{ }^\circ\text{C}$ and $\text{pH} = 7$ with aqueous solutions of $\text{Pt}(\text{NH}_3)_4(\text{NO}_3)_2$ (Alfa Aesar) and $\text{Pd}(\text{NH}_3)_4(\text{NO}_3)_2$ (Stem Chemicals). $\text{pH} = 7$ was regulated by adding NH_3 or NH_4NO_3 solution drops when necessary. Once adsorption equilibrium has been reached, a Rotavapor removes the excess water. The catalyst is then dried at $110\text{ }^\circ\text{C}$ for 12 h in an oven and calcined for 3 h at $500\text{ }^\circ\text{C}$ in air, following a ramp of $2.5\text{ }^\circ\text{C min}^{-1}$.

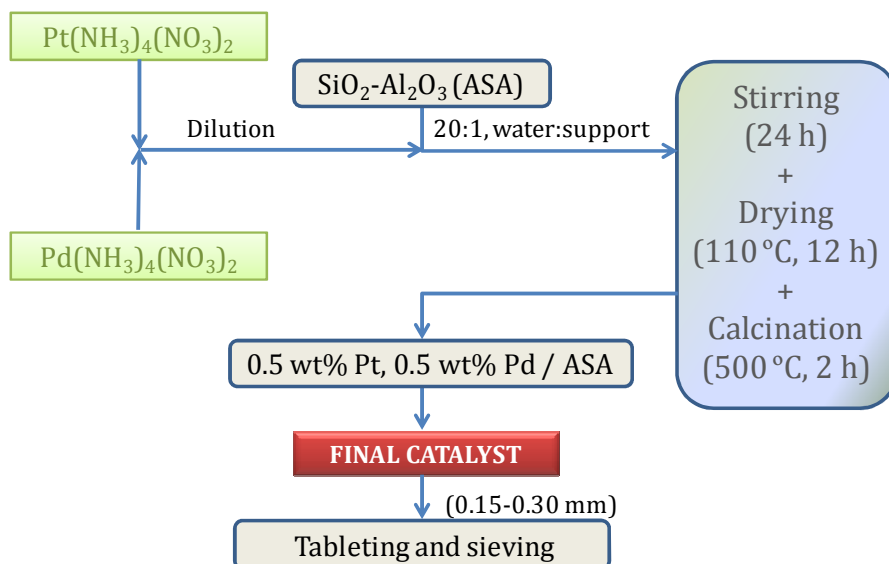


Figure 2.7. Metal incorporation procedure for the PtPd catalyst.

In summary, Table 2.10 lists all the catalysts used in this Thesis, specifying their metallic phases, support, and corresponding name designation.

Table 2.10. Catalyst designation.

Name	Metallic phase	Acidic phase/support
NiMo/ALM	Ni-Mo	Commercial Al ₂ O ₃
NiMo/ASA	Ni-Mo	Commercial SiO ₂ -Al ₂ O ₃
NiMo/FCC	Ni-Mo	FCC
NiMo/MCM	Ni-Mo	MCM-41
NiMo/SBA	Ni-Mo	SBA-15
PtPd/SiO ₂ -Al ₂ O ₃	Pt-Pd	SiO ₂ -Al ₂ O ₃

2.4. CATALYST CHARACTERIZATION

2.4.1. Metal content

The metal content on the catalyst samples has been determined by ICP-AES on the Geology Department of the Faculty of Science and Technology of the University of the Basque Country (UPV/EHU), on a Thermo quadrupolar mass spectrometer (XSeries 2 model) with a plasma source, equipped with a Xt interphase, shielded torch, and concentric nebulizator. The equipment calibration was carried out by using multielemental solutions of 1000 ppm, and the result quality control was made with multielemental solutions that were prepared similarly to the calibration ones.

The dissolution was carried out by acidic attack in closed PFA Savillex® containers, following the procedure that is described:

1. Approximately 50 mg of sample are weighed.
2. 3 mL of a 1:2 mixture of HNO₃:HF were added to the sample, and then the solution was heated up to 90 °C for 24 h.
3. The titration of fluoride excess was performed by adding HClO₄, and then evaporating in a hotplate.
4. Chlorides were measured by adding HCl in a hotplate at 90 °C for 24 h, and evaporating the HCl until a solid waste is obtained.
5. The sample was diluted again in HNO₃ to a dilution factor of 1:2500.

2.4.2. N₂ adsorption-desorption isotherms

The structure of the fresh catalysts has been studied on a Micromeritics ASAP 2010 equipment, obtaining information about the BET specific surface, micro-mesoporous volume, pore size distribution and average pore diameter.

Gas adsorption-desorption techniques for specific surface determination (S_{BET}) particularly with N₂, are based on multilayer adsorption, and the application of the simplified Brunauer-Emmett-Teller (BET) equation on the 0.01-0.2 relative pressure interval. The micropore area has been determined by the t-method, which is based on the Harkins-Jura equation. Total pore volume is obtained from the total quantity of adsorbate at the inflexion point on the high-pressure plateau, according to the Gursvitsch method. Mesopore volume is calculated from the difference of total pore volume and the micropore volume obtained with the t-method. Pore size

distribution and average pore diameter are determined with the BJH (Barrett-Joyner-Halenda) method.

Before carrying out the analysis, it is important to consider that the amount of sample needed must ensure a minimum specific surface of 10 m², but introducing at least 100 mg of solid. The experimental procedure consists in (i) a previous degasification stage at 150 °C and 2·10⁻³ mmHg vacuum to remove impurities from the sample, followed by (ii) a N₂ adsorption-desorption in multiple equilibrium stages until the sample is saturated at -200 °C liquid N₂ [214], within the 0.01-1 relative pressure range.

2.4.3. H₂ chemisorption

H₂ uptake has been obtained by means of H₂ chemisorption following the double isotherm method, from the volume of physis- and chemisorbed H₂ in a Quantachrome Autosorb-iQ-C-XR apparatus. Two stages of adsorption are carried out with a stripping with He in between to remove the physisorbed fraction. Then, the amount of chemisorbed H₂ is obtained from the difference between the results of the first adsorption minus the corresponding to the second one, as established by Gayubo et al. [215]. Stabilization of the sample was carried out at 35 °C under a He flow, and then the gas was changed to H₂ to perform chemisorption. Finally, temperature was raised at a 5 °C min⁻¹ rate up to 400 °C and maintained for 4 h. The metallic surface can be obtained knowing the adsorbate area and considering the stoichiometry of the gas per every exposed metallic atom.

2.4.4. X-ray diffraction (XRD)

XRD analyses were carried out on the SGIKER service at the University of the Basque Country (UPV/EHU).

High angle patterns were collected by using a Philips X'Pert PRO automatic diffractometer operating at 40 kV and 40 mA, in theta-2theta configuration, secondary monochromator with Cu-K α radiation (= 1.5418) and a PIX cell solid state detector. Data were collected from 3.5° to 60° (step size = 0.026° and time per step = 900 s, total time: 2 h) at room temperature. A fixed divergence and antiscattering slit giving a constant volume of sample illumination were used.

XRD low angle data were collected on a Bruker D8 Advance diffractometer equipped with a Cu tube, Ge(111) incident beam monochromator (fixed slit = 1 mm) and a Sol.X energy dispersive detector (fixed slit: 0.06 mm). The sample was mounted on a zero background silicon wafer embedded in a generic sample holder. Data were collected from 0.6° to

5° (Step size = 0.015° and time per step = 100 s, total time: 8 h) at room temperature. A variable divergence and antiscattering slit V_4 was used.

X-ray diffraction is widely used to study the inner structure of crystalline solids given that every crystalline solid has its own characteristic diffractogram. It also allows for qualitative and quantitative identification of the crystalline compounds in a sample, crystal size determination, polymorphism studies, etc. X-rays with a wavelength of approximately 1 Å are used, because that is the interatomic distance in the crystals, which allows for interference phenomena to occur. When a X-ray is incident on a crystal, it is diffracted on a particular direction that is characteristic of the crystal, according to Bragg's law:

$$n\lambda = 2d \sin \theta \quad (2.4)$$

Diffractograms show a series of diffraction maximums which correspond to reflections, that appear at certain angular positions (Bragg's angle, 2θ). The whole set of diffractions describes the nature of the crystal, that can be studied by comparing its diffractogram with the characteristic diffraction of pure phases.

2.4.5. Temperature programmed reduction (TPR)

Essays were carried out in a Micromeritics 2920 Autochem, according to the following procedure: (i) approximately 0.4 g of sample are weighed for each experiment in a quartz tubular reactor, (ii) then the sample is stabilized under a 30 mL min⁻¹ gas flow (10 vol% H₂:Ar mixture) at room temperature, and (iii) when steady state is reached, the temperature is increased linearly following a ramp of 5 °C min⁻¹ up to 1000 °C. H₂ uptake is registered in a TCD detector.

TPR analysis allows for the identification of reducible species on the catalytic surface and the temperature at which the reduction of each species occurs, by subjecting the sample to a temperature ramp in the presence of a reductor gas (typically H₂). The concentration of the gas mixture downstream can be determined by measuring the H₂ consumption, obtaining the total H₂ uptake. This technique also provides information about the metal-support interaction. Generally, the stronger the interaction, the higher the reduction temperature.

2.4.6. X-Ray photoelectron spectroscopy (XPS)

XPS measurements were performed on the SGIKER service at the University of the Basque Country (UPV/EHU). A SPECS system equipped with Phoibos 150 1D-DLD analyzer and Al K α (1486.6 eV) monochromatic radiation source. An initial scan was performed (wide scan: step energy 1 eV, dwell time 0.1 s, pass energy 40 eV) and then a detailed analysis of the present elements was performed (detail scan: step energy 0.1 eV, dwell time 0.1 s, pass energy 20 eV) with an electron outcome angle of 90°. The C 1s peak was established at 284.6 eV to correct the charge effect and the spectrometer was previously calibrated with the Ag 3d 5/2 peak (368.28 eV). The spectra were adjusted by CasaXPS 2.3.16 software, modeling the Gauss-Lorentzian contributions.

2.4.7. Adsorption-desorption of *tert*-butylamine

Total acidity and acidic strength distribution has been determined by *tert*-butylamine adsorption, combining thermogravimetric analysis and differential scanning calorimetry, and followed by a temperature programmed desorption (TPD) of the chemisorbed *tert*-butylamine.

Tert-butylamine provides a number of advantages over other basic compounds commonly used for this kind of analysis such as NH₃ or pyridine. Compared with pyridine, it has a higher vapor pressure, providing higher concentration gradient and, secondly, it has less steric impediments to penetrate in the porous structure due to its shorter molecular chain [216]. Regarding ammonia, *tert*-butylamine has higher molecular mass, which improves the measurement sensibility, especially when the sample has a very low acidity. *Tert*-butylamine can characterize highly acidic centers, with heats of adsorption higher than 200 kJ mol⁻¹, while ammonia (a stronger basis), characterizes weaker acidic centers [217].

The differential adsorption of *tert*-butylamine and subsequent temperature programmed desorption have been carried out in a Setaram a TG-DSC 111 calorimeter (that allows for simultaneous measurement of mass and enthalpy variations), coupled with a Balzers Instrument Thermostar mass spectrometer using a thermally insulated line (to avoid product condensation). *Tert*-butylamine has been dosed with a Harvard syringe pump.

The experimental procedure to carry out the differential calorimetry consists in: (i) pre-treatment of the sample with He (160 mL min⁻¹) at 550 °C for 30 min to remove impurities, (ii) temperature stabilization at 150 °C with a 20 mL min⁻¹ He flow, (iii) sample saturation by continuous injection of *tert*-butylamine (150 μ L min⁻¹) at 100 °C, and (iv) stripping of the sample with

He (20 mL min^{-1}) to eliminate the physisorbed fraction of adsorbate. The TPD was performed by heating the sample up to $550 \text{ }^\circ\text{C}$ with a heating rate of $5 \text{ }^\circ\text{C min}^{-1}$ in He (20 mL min^{-1}). The mass spectrometer registers the signal corresponding to butenes (the products of *tert*-butylamine cracking), and the area under the TPD curve is proportional to the amount of it that has been adsorbed and therefore, to the total acidity. The temperature of desorption is indicative of the strength of the acidic sites (*tert*-butylamine adsorbed in stronger sites cracks at lower temperatures than that adsorbed in less acidic sites).

2.5. REACTION EQUIPMENTS AND PROCEDURES

2.5.1. Hydroprocessing unit description

The reaction unit used for the hydroprocessing runs (HT with NiMo catalysts and then HC with a PtPd catalyst) has been a Microactivity-Pro from PID Tech, designed for the study of catalytic processes at a laboratory scale, and able to simulate the reactions that take place in an industrial hydroprocessing unit up to 100 bar and 700 °C. The control and data acquisition have been carried out by using Processa software, which allows for programming a sequence of previously designed sessions, so that the reaction unit can work autonomously. The unit has a security system of temperature (reactor and oven), pressure, level and flow alarms that are integrated on a microprocessor independent of the computer, as well as commands for sequenced session inhibition in case any of the alarms is active.

The hydroprocessing unit scheme (Figure 2.8) can be divided into five different sections: (i) gas feeding, (ii) liquid feeding, (iii) mixture and pre-heating of reactants, (iv) reaction, and (v) sample collection zones.

(i) Gas feeding zone:

This zone has four gas input lines. Each line (provided with a cutoff valve and a check valve to keep products from flowing backwards in the line), has a Bronkhorst High-Tech B.V. mass flow controller, which allows for operating at pressures within the 0-100 bar range. The gases that are fed are the following:

- Gas 1: Nitrogen. It is used for conditioning and cleaning the reactor. Maximum flow: 200 mL min⁻¹.
- Gas 2: Synthetic air. Used for catalyst regeneration. Maximum flow: 200 mL min⁻¹.
- Gas 3: Hydrogen. Reactive and pre-treatment gas, used to reduce the metallic phase of the catalyst. Maximum flow: 250 mL min⁻¹.
- Gas 4: H₂S diluted in H₂ (10 vol%). Used for the pre-sulfidation of NiMo catalysts. Maximum flow: 250 mL min⁻¹.

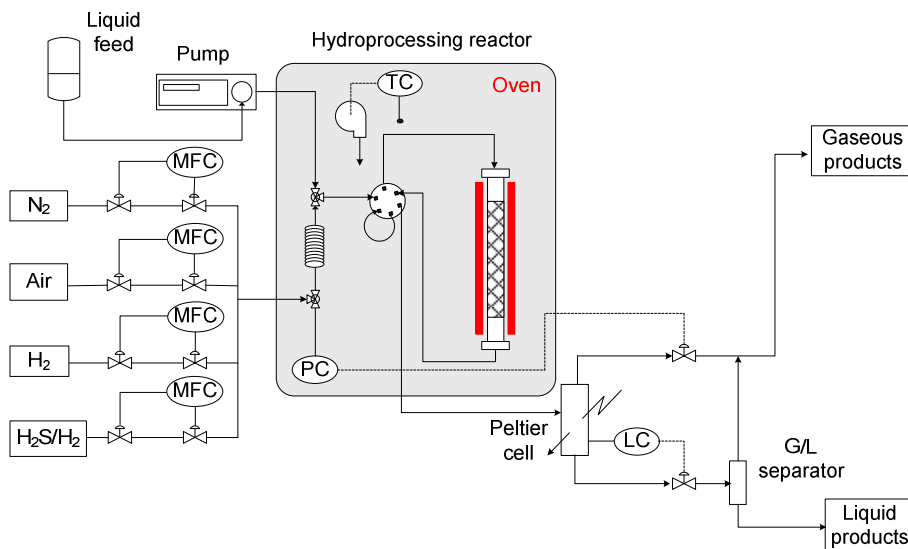


Figure 2.8. Hydrogenation unit scheme.

The four gas lines are connected in a distributor with a unique gas-feed outline.

(ii) Liquid feeding zone:

Liquids are fed by using an alternative positive displacement HPLC Gilson 307 pump, with a 5SC head, that allows for feeding liquids within the $0.01\text{-}5\text{ mL min}^{-1}$ flow range, up to 600 bar and $40\text{ }^{\circ}\text{C}$. The pump is also equipped with a pressure restrictor that generates an overpressure of 30 bar, to improve its performance.

(iii) Reactive mixing and pre-heating zone

Gas and liquid streams circulate inside an oven, which is heated at $100\text{ }^{\circ}\text{C}$ by means of a forced-convection electric heater. This way, condensation in tubings and other elements is avoided.

The pumped liquid feed reaches a T-shaped mixer (with low dead volume) where it contacts the hot gas H_2 stream. The gas stream drags the liquid feed towards the reactor. Before entering the reactor, the reactive stream goes through a pneumatically actuated 6-port Valco valve which allows for directing the reactive stream towards either the reactor, or the gas exit (derivation towards the Peltier cell, without going through the reactor).

(iv) Reaction zone

The fixed-bed downflow reactor is a stainless steel cylindrical tube, with a diameter of 0.8 cm, 30.3 cm length and an internal volume of 15 cm³. A porous plate of 2 mm thickness is located at 12.8 cm from the reactor base, to hold the catalyst bed.

The reactor operates isothermally, and is located within a furnace consisting of a stainless steel case inside of which the resistance is placed, covered in a refractory material. In the middle of the reactor, a K-type thermocouple measures the temperature, connected to a TOHO TTM-005 controller (which allows for controlling and monitoring).

Given the characteristics of the feed, trickle bed regime is reached in the reactor.

(v) Product output and sampling zone

After exiting the reactor, the product stream goes through a 6-port Valco valve, from where is redirected to a liquid/gas separator. This separator, at reaction pressure, condenses liquids at 0 °C cooled by means of a Peltier cell, and is provided with a high resolution capacity sensor, calibrated for the reaction products.

The gas stream is depressurized with a micrometric valve actuated by PID control. This valve allows for a constant gas-flow output and keeps pressure from oscillating.

The liquid stream separated in the condenser is redirected to a second depressurized deposit that also acts as a G/L separator. The gas stream is sent to a T-shaped mixer where it joins the gas stream that comes from the Peltier condenser, and reaches the gas sample analysis chromatograph (Varian CP-4900 Micro Gas Chromatograph). The liquid products stored in the second deposit are periodically sampled (1 h) by opening an electronically actuated ON/OFF valve.

2.5.1.1. Experimental reaction procedure

The reactor loading is carried out as follows: first of all, an adequate amount of catalyst is weighed and mixed with carborundum (CSi, $d_p = 0.5$ mm). Carborundum is a slightly compressive material that avoids the formation of gas-flow preferential routes in the reactor. Afterwards, above and below the catalyst bed, a 20 mm CSi layer is placed to keep the catalyst from being dragged by the gas.

As previously mentioned, the different experimental stages can be designed and configured sequentially by using Processa software, as it follows:

Session 1: The position of the valves is checked, so that the run can be launched correctly. This session lasts for 1 min.

Session 2: Pretreatment of the catalyst. This stage is required for metallic and bifunctional catalysts. A flow of activating gas goes through the reactor (50 mL min⁻¹ of H₂S/H₂ for NiMo catalyst sulfidation; 30 mL min⁻¹ H₂ and 50 mL min⁻¹ N₂ for PtPd catalyst reduction), and the temperature is raised up to 400 °C by following a 5 °C min⁻¹ ramp. Once activation temperature is reached, it is maintained for 4 h.

Session 3: Cooling. The required reaction temperature is established as setpoint, and the flowrate is maintained either at 50 mL min⁻¹ H₂S/H₂ for reactions with NiMo catalysts, or at 100 mL min⁻¹ H₂ in the case of the PtPd catalyst, for 1 h.

Session 4: Pressurization. The reactor is pressurized introducing 150 mL min⁻¹ H₂, for 1 h.

Session 5: Reaction. For the first hour, the liquid flow is set on the pump and it is stabilized, until the adequate pressure is reached in the pump head. At the beginning of this session the Peltier cell is also turned on so that it starts cooling. Both H₂ and liquid feed (hydrocarbons) are flowing through the catalytic bed, with the gas product being sampled every 10 min to the gas chromatograph.

Session 6: Cooling and depressurizing. Both hydrocarbons and H₂ flows are cut, and a 50 mL min⁻¹ N₂ stream goes through the reactor so that the catalyst is kept in an inert atmosphere while temperature and pressure drop. This session lasts for 1 h.

Session 7: Valve closing. Similar to session 1, all valves are closed and data acquisition stops. This session lasts for 1 min.

2.5.1.2. Trickle bed hydrodynamic check-up

In this work, HT and HC runs are carried out in trickled bed regime (gas/liquid/solid contact). One of the most important considerations when working in this regime is that the convection time (t_c) or space time (τ) should be in the same order of magnitude as the reaction time (t_r). This ratio is known as the Damköhler number (Da).

$$Da = \frac{\tau}{t_r} = \frac{t_c}{t_r} \approx 1 \quad (2.5)$$

Where:

$$t_c \approx \frac{L}{u_L} = \frac{V}{F_L} \tau \quad (2.6)$$

Where u_L is the superficial liquid velocity, L the reactor length, F_L is the liquid flow-rate, and V the reactor volume. Considering these equations, the dimensions of the reactor specified in Section 2.5.1, a reaction time of 6 h, and a space time of $0.241 \text{ g}_{\text{cat}} \text{ h g}^{-1}_{\text{feed}}$, the calculated value of D_a was of 0.83.

Reactor dimensions are another important factor to consider. In this regard, its diameter (d_r) and the particle size should comply with the relation in Eq. 2.7, in order to avoid the so-called “wall effect”, consisting in flow non-uniformities caused by voids close to the wall. The value of this number has been of 26.7.

$$\frac{d_r}{d_p} > 20 \quad (2.7)$$

A criteria for calculating the minimum bed length as a function of the particle diameter is defined in Eq. 2.8, where n is the reaction order. That correlation requires the calculation of a relation between the dispersion time and convection time, ratio commonly referred to as Peclet number, defined in Eq. 2.9, and which includes a diffusion coefficient (D_m). This coefficient can be defined from a correlation consisting on the sum of the effective diffusion coefficient (D_{eff}) and the convection term (Eq. 2.10), where Θ is a factor depending on the particle size.

$$L > 20n \ln\left(\frac{1}{1-X}\right) \frac{d_p}{\text{Pe}_p} \quad (2.8)$$

$$\text{Pe}_p = \frac{d_p u_L}{D_m} \quad (2.9)$$

$$D_m = D_{\text{eff}} + \Theta d_p u_L \quad (2.10)$$

For low Reynolds (Re) number values, $d_p u_L \ll D_{\text{eff}}$, and therefore $D_m \approx D_{\text{eff}}$. Re is defined as shown in Eq. 2.11, where ρ_L is the density of the liquid feed and μ the viscosity.

$$\text{Re} = \frac{d_p u_L \rho_L}{\mu} \quad (2.11)$$

For a density value of 0.894 kg m^{-3} for STPO and a viscosity of $8.59 \cdot 10^{-4} \text{ N s m}^{-2}$ for $n\text{-C}_{10}$ (assumed equal to that of the $50\text{-}50 \text{ N m}^3/\text{m}^3$ mixture of $n\text{-C}_{10}$ and STPO), the value of Re is $5.26 \cdot 10^{-6}$. Therefore, considering

all the previous and from calculation of Eqs. 2.8-2.10, the value of the Pe_P number has been of 1.01 and the calculated minimum bed length of 2.32 cm.

In order to determine intrinsic kinetics, gradients through the bed (both mass and heat transfers) need to be negligible. One criterion for excluding mass-transfer limitation is to assume that the ratio of the mass-transfer time over the reaction time is very small. This ratio is known as the Carberry number (Ca), and in first order kinetics a deviation of less than 5 % is generally applied. Mass-transfer time scales with the square of the characteristic diffusion length (l) over the dispersion coefficient (D_m).

$$Ca = \frac{t_m}{t_r} < 0.05 \quad (2.12)$$

$$t_m \approx \frac{l^2}{D_m} \quad (2.13)$$

Assuming that diffusion length is equal to particle diameter, D_{eff} is $5 \cdot 10^{-9} \text{ m}^2 \text{ s}^{-1}$ [218], and t_r is 6 h, the value of Ca is of $8.3 \cdot 10^{-4}$, much lower than the established limit of 0.05.

2.6. COKE ON DEACTIVATED CATALYSTS

2.6.1. Coke content

The amount of coke deposited on spent catalysts has been determined by means of air combustion in a TA Instruments TGA Q5000 IR thermogravimetric (TG) apparatus, coupled in line with a Balzers Instruments Thermostar mass spectrometer (MS), using a temperature programmed oxidation (TPO) profile.

The standard procedure to determine coke content has been similar to that reported by Ibáñez et al. [126], and has consisted in an initial stripping with N₂ (50 mL min⁻¹), before the sample was stabilized at 100 °C before temperature was raised up to 550 °C with a 5 °C min⁻¹ ramp. Temperature was maintained for 30 min and then the sample was cooled down again to 100 °C. Gas was switch to air (50 mL min⁻¹) and stabilized for 5 min. Then, the sample was heated by following a 5 °C min⁻¹ ramp up to 500 °C, maintaining that temperature for 2 h for obtaining complete coke combustion. Finally, the sample was cooled down to room temperature. During the whole analysis, signals of temperature, mass, and mass derivative were registered by the TGA, as well as CO, CO₂ and H₂O signals in the mass spectrometer.

Coke content (C_c , wt%) is defined from the mass of deactivated catalyst (m_0) and the mass of remaining catalyst after coke is burnt (m_{cat}).

$$C_c = \frac{m_0 - m_{cat}}{m_{cat}} \quad (2.14)$$

2.6.2. Raman spectroscopy

Raman spectroscopy was carried out for studying the nature of the deposited coke on spent catalysts. Analyses were carried out in a confocal Renishaw microscope at the Singular Laboratory of Coupled Microscopies (LASPEA) at the University of the Basque Country (SGIKER, UPV/EHU). An excitation wavelength of 514 nm has been used, and the fluorescence caused by coke has been subtracted from the spectra.

The catalyst sample (3-5 mg) was placed in a small container and located in the trajectory of the laser beam. By means of an optical microscope, the laser beam is redirected to different representative spots of the sample, avoiding possible signal aberrations caused by more coke-concentrated

sample spots. Analyses are carried out in an inert N₂ atmosphere to avoid sample degradation and coke combustion.

2.6.3. FTIR-TPO/MS spectroscopy

This technique has allowed for studying the aromatic and aliphatic nature of coke. Coke combustion has been carried out in a Specac catalytic chamber connected to a FTIR Nicolet 6700 spectrometer. The chamber is provided with a sample holder (for tablets) in a closed system, in which gases can be introduced, and also reach vacuum conditions (by means of a Vacuubrand rotatory pump). A temperature control system allows for reaching temperatures of up to 700 °C.

The experimental procedure was previously reported by Ibáñez et al. [219] and consists of tableting a deactivated catalyst sample (approximately 10 mg) with about 160 mg of KBr (Aldrich, > 99 % purity) in a press. The tablet is introduced in the chamber and is subjected to vacuum conditions at 100 °C for 1 h to remove impurities. Then, vacuum is removed and air (60 mL min⁻¹) is introduced in the chamber. Once the sample background is registered, a 5 °C min⁻¹ ramp is launched up to 550 °C, maintaining this temperature for 2 h to obtain complete coke combustion. During the ramp, infrared spectra are registered with a 0.2 min⁻¹ frequency. Simultaneously to combustion, CO₂ signal is registered in an OmniStar ThermoStar mass spectrometer.

Section 3

HYDROTREATING OF STPO ON NiMo CATALYSTS USING VARIOUS SUPPORTS

Note: Part of the results of this Section have been published in the following paper(s):

I. Hita, A. Gutiérrez, M. Olazar, J. Bilbao, J.M. Arandes, P. Castaño, Fuel 145 (2015) 158-169.

3. HYDROTREATING OF STPO ON NiMo CATALYSTS USING VARIOUS SUPPORTS

Hydrotreatment refinery units have shown good performance for treating heavy feedstock, reducing their heteroatom content and adjusting their properties to meet product specifications [220-222]. However, existing processes need to be further optimized and intensified in terms of operational conditions and catalyst in order to adapt hydrotreatment units for new feeds. NiMo catalysts supported on Al_2O_3 have been widely used for heavy petroleum feedstock hydroprocessing with good performances [223-225]. However, improvements can be achieved using different supports with tailored porosity, like zeolites [146], mesoporous HMS [226], SBA-15 [109] or MCM-41 [158, 227, 228].

As the first step of the 2-stage HT strategy defined in Figure 1.19 of Section 1.6, in this Section, the main aim is to compare the performance and the effect of the different physico-chemical properties of five different NiMo catalysts on the hydrotreating of a model SSTPO and real STPO, regarding the three main goals for its upgrading, as are: (i) hydrodesulfurization (HDS), (ii) mild hydrocracking (MHC) and (iii) removal of aromatic compounds (HDA).

The catalyst study has been carried out at the following experimental conditions:

- Time on stream (TOS): 0-8 h
- Space time (τ): $0.241 \text{ g}_{\text{cat}} \text{ h g}^{-1}_{\text{feed}}$
- Temperature: 275-350 °C (SSTPO), 300-375 °C (STPO)
- Pressure: 65 bar
- H_2/feed volumetric ratio: $1,000 \text{ N cm}^3/\text{cm}^3$

The components of the product stream have been grouped by following two different criteria:

- (i) Boiling point: naphtha (35-216 °C), diesel (216-350 °C) and gasoil (> 350 °C).
- (ii) Nature of the chemical bonds: (i) paraffins and isoparaffins, P+iP, (ii) olefins, O, (iii) naphthenes, N, (iv) 1-ring aromatics, A_1 , and (v) 2-ring aromatics, A_2 .

Hydrodesulfurization (HDS), hydrodearomatization (HDA) and mild hydrocracking (MHC) conversions have been defined in Section 2.2.2.4.

3.1. PROPERTIES OF THE FRESH CATALYSTS

As specified in Section 2.3.1, five different NiMo catalysts have been used for the catalyst screening with synthetic STPO. The corresponding designation for the catalysts was also shown in Table 2.10.

3.1.1. Physical and textural properties

3.1.1.1. N₂ adsorption-desorption isotherms

The compositional and textural properties of the fresh NiMo catalysts are shown in Table 3.1, as determined by ICP-AES and N₂ adsorption-desorption isotherms. For all the catalysts, the metal loading is very similar. NiMo/MCM, NiMo/SBA and NiMo/FCC catalysts have been loaded with a small amount of P since it has proven to improve their stability and enhance their catalytic performance [226]. Both commercial NiMo/ASA and NiMo/ALM catalysts show very similar physical properties regarding specific surface (286-278 m² g_{cat}⁻¹), pore size (73-82 Å), and distribution, whereas the differences between the NiMo/FCC, NiMo/MCM and NiMo/SBA catalysts are significant. The highest value of the pore volume is for the SBA-15-supported catalyst, with 0.55 cm³ g⁻¹, while this value drops to 0.083 cm³ g⁻¹ for the NiMo/FCC catalyst. The FCC catalyst is also the one with the lowest specific surface, with the widest average pore size (266 Å). MCM catalyst has the lowest average pore diameter. At a relative pressure of 0.5, NiMo/ASA, NiMo/ALM and NiMo/SBA catalysts show very little difference between the values of the adsorbed-desorbed N₂ volume (4-6 cm³ g⁻¹). The highest difference is for the MCM catalyst (14 cm³ g⁻¹), while the microporous FCC catalyst shows no significant difference in this value due to its almost overlapped N₂ adsorption-desorption branches.

Table 3.1. Compositional and textural properties of the fresh NiMo catalysts.

	NiMo/				
	ASA	ALM	MCM	SBA	FCC
Ni (wt%)	2.98	2.26	2.21	2.40	3.04
Mo (wt%)	7.31	7.97	8.09	8.50	7.34
P (wt%)	--	--	0.63	0.74	0.89
S_{BET} ($\text{m}^2 \text{g}_{\text{cat}}^{-1}$)	286	278	477	309	89
$V_{\text{P}/\text{P}0=0.2}^{\text{Ads}}$ ($\text{cm}^3 \text{g}_{\text{cat}}^{-1}$)	82	80	137	88	24
$V_{\text{P}/\text{P}0=0.5}^{\text{Ads}}$ ($\text{cm}^3 \text{g}_{\text{cat}}^{-1}$)	118	117	183	117	27
$V_{\text{P}/\text{P}0=0.5}^{\text{Des}}$ ($\text{cm}^3 \text{g}_{\text{cat}}^{-1}$)	121	123	196	121	28
Pore volume ($\text{cm}^3 \text{g}_{\text{cat}}^{-1}$)	0.54	0.55	0.40	0.55	0.083
Average pore diam. (\AA)	73	82	58	113	266

As seen in Figure 3.1a, all catalysts show N_2 isotherms corresponding to IV-type adsorption branch and with H1-type hysteresis, very similar to those reported in literature for the SBA-15 [163, 229] and MCM-41 [228, 230] mesoporous materials. The H1-type hysteresis loop of the isotherms is characteristic of a percolation effect caused by small metal oxide particles located within the mesopores, that lead to the formation of ink-bottle type pores [231]. As can be deduced from the values shown in Table 3.1 for a relative pressure value of 0.2, the amount of micropores and total pore volume of NiMo/ASA, NiMo/ALM and NiMo/SBA catalysts is very similar ($0.54\text{-}0.55 \text{ cm}^3 \text{g}_{\text{cat}}^{-1}$), while the MCM-41-supported catalyst shows the highest amount of micropores with a lower total pore volume.

The pore volume distributions of the fresh catalysts are shown in Figure 3.1b. NiMo/ALM catalyst shows a wide pore diameter distribution, while both NiMo/MCM and NiMo/FCC catalysts show a much narrower distribution, with a particularly significant low porosity of the FCC-supported catalyst, in agreement with the desorption branch in the N_2 isotherms (Figure 3.1a). The SBA catalyst shows a two-peak distribution (two maxima are present), which corresponds to the double-loop shaped adsorption-desorption isotherm.

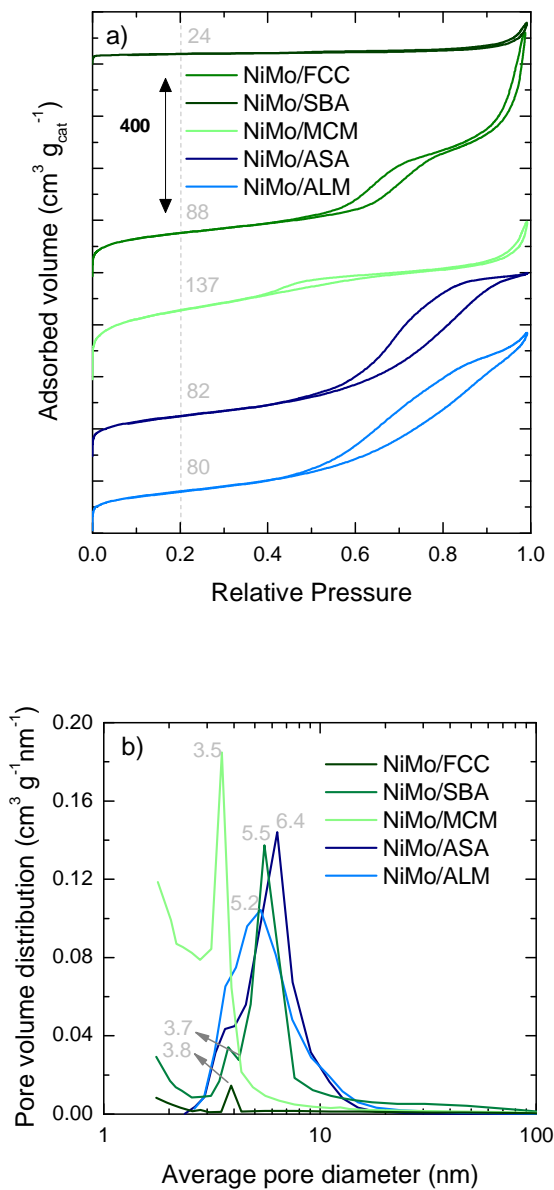


Figure 3.1. a) N₂ adsorption-desorption isotherms and b) pore volume distributions of the fresh NiMo catalysts.

3.1.2. Chemical and structural properties

3.1.2.1. Acidity and H₂ chemisorption

The *tert*-butylamine (t-BA) TPD profiles of the catalysts in the range of 250-350 °C are shown in Figure 3.2 and the total acidity is displayed in Table 3.2. The t-BA adsorbed on sites with stronger acidity cracks at lower temperatures releasing butene as the main cracking product, registering this signal ($m/z = 56$) in the MS. Depending on the cracking temperature, different types of acidity can be distinguished. None of the catalysts showed a significant peak at low temperature (~180-200 °C), confirming that all the acidic sites of the catalysts have a weak acidic nature [232], with their TPD maximum at 250-300 °C for the NiMo/MCM, NiMo/SBA and NiMo/FCC catalysts, and 300-325 °C for the NiMo/ASA and NiMo/ALM catalysts. The lack of strong acidic sites might be due to coverage of the stronger acidic sites with metal particles. NiMo/MCM has the highest total acidity, while the acidity of NiMo/ASA, NiMo/ALM and NiMo/SBA is very similar and the NiMo/FCC is the least acidic of all. Regarding the strength of the acidic sites, they show the following support trend: FCC > SBA-15 \approx MCM-41 > ASA > ALM .

Regarding the H₂ uptake (measured by H₂-chemisorption) displayed in Table 3.2, NiMo/FCC catalyst shows the highest value ($17.1 \cdot 10^{-3} \text{ cm}^3 \text{ g}_{\text{cat}}^{-1}$), meaning it has the best metal dispersion, followed by NiMo/MCM ($13.0 \cdot 10^{-3} \text{ cm}^3 \text{ g}_{\text{cat}}^{-1}$), while this value drops for the NiMo/SBA and NiMo/ALM catalysts ($3.1 \cdot 10^{-3} \text{ cm}^3 \text{ g}_{\text{cat}}^{-1}$ and $2.6 \cdot 10^{-3} \text{ cm}^3 \text{ g}_{\text{cat}}^{-1}$, respectively).

Table 3.2. Chemical properties of the fresh NiMo catalysts.

	NiMo/				
	ASA	ALM	MCM	SBA	FCC
H ₂ uptake ($10^{-3} \text{ cm}^3 \text{ g}_{\text{cat}}^{-1}$)	6.9	2.6	13.0	3.1	17.1
Total acidity ($\text{mmol}_{\text{t-BA}} \text{ g}^{-1}$)	0.512	0.525	0.860	0.471	0.132

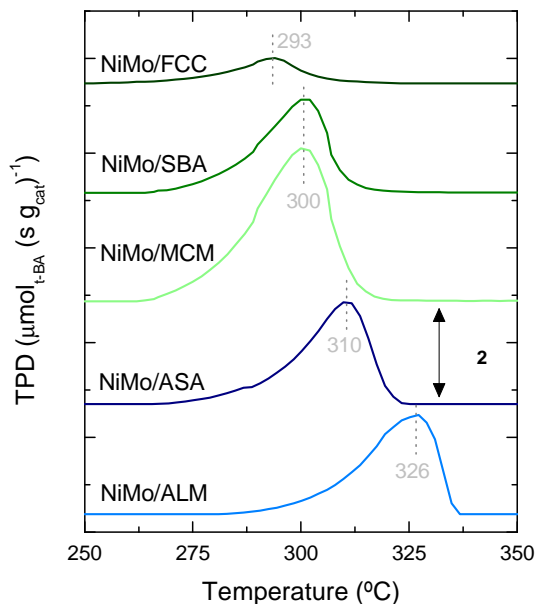


Figure 3.2. Terc-butylamine Temperature Programmed Desorption (TPD) of the fresh catalysts.

3.1.2.2. X-Ray diffraction

Wide-angle XRD was used to study the crystallinity of mesoporous materials (Figure 3.3a). Silica containing catalysts (except for the NiMo/ALM catalyst) show a broad signal between 15° and 35° , which is attributed to amorphous silica [233, 234]. The NiMo/FCC signal shows the typical diffraction peaks that correspond to the structure of faujasite (FAU) zeolite. The XRD pattern corresponding to the NiMo/SBA catalyst reveals the presence of big Mo crystallites on the surface and the formation of crystalline orthorhombic MoO_3 phase, indicating a poor distribution of the metallic function. The patterns corresponding to NiMo/ASA and NiMo/ALM catalysts reveal the poor crystallinity of their supports, given the amorphous nature of their structure. The broad signal in both catalysts between 45° and 50° is due to the presence of Al_2O_3 in the catalytic support, while the broader signal (only noticeable for the $\text{SiO}_2\text{-Al}_2\text{O}_3$) reveals the presence of silica. The small peak at $2\theta = 27.4^\circ$ is due to the formation of MoO_3 crystallites from the Mo impregnated on the catalyst.

Figure 3.3b shows the low-angle XRD patterns for the catalysts supported on mesoporous materials. The SBA-15 catalyst pattern shows a peak at about 1° corresponding to (100) reflection, associated with $p6mm$ hexagonal symmetry [235], as well as the peak present in the MCM-41 pattern. The NiMo/FCC low angle pattern does not provide significant information.

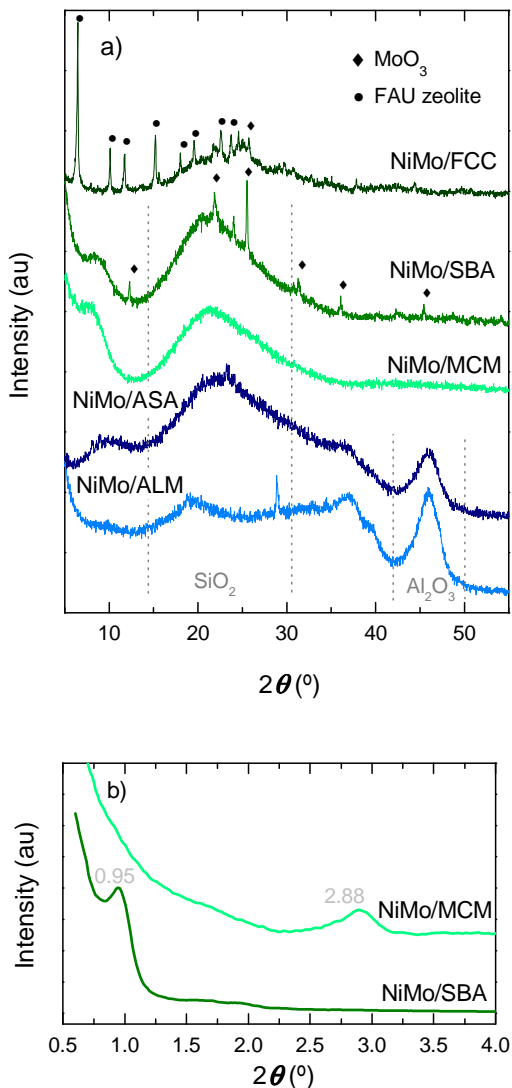


Figure 3.3. a) Wide angle XRD patterns of the fresh catalysts and b) low angle XRD patterns of the mesoporous NiMo/SBA and NiMo/MCM catalysts.

3.1.2.3. XPS

XPS measurements have been made to evaluate the chemical species exposed on the catalyst surface and their proportion. The binding energies of the most intense peaks of O 1s, Ni 2p_{3/2} and Mo 3d_{5/2} are summarized in Table 3.3. The O 1s, C 1s core levels were detected in all catalysts. The Si 2p core level was also detected in all catalysts, except for the NiMo/ALM catalyst. Table 3.3 also compiles the Ni/Mo, Ni/(Si+Al) and Mo/(Si+Al) atomic ratios of the fresh catalysts. In the case of the NiMo/ASA, NiMo/ALM and NiMo/FCC catalysts, the Ni/Mo atomic ratio changes insignificantly upon varying the properties of the catalytic support. Concerning the NiMo/MCM and NiMo/SBA catalysts, more significant differences are observed, which suggests that the support has an effect on the metals exposed on the surface. The exposure level of both Ni and Mo on the catalytic surface follows the support trend: FCC >> ASA > ALM > MCM-41 > SBA-15. The low surface concentration of Ni and Mo species in the NiMo/SBA catalyst is indicative of poor metal dispersion (consistent with XRD results, Figure 3.3a), while a remarkable high metal dispersion is achieved in the case of the NiMo/FCC catalyst, which corresponds to the highest H₂ uptake as deduced from Table 3.2. The deconvolution of the Mo 3d spectra is shown in Figure 3.4. All the catalysts show the same binding energy. The spectra were decomposed into two peaks: one main peak (Mo 3d_{5/2}) and an associated peak (Mo 3d_{3/2}). The signal of metallic Mo (227.7 eV) is not present, proving that Mo surface is oxidated on the catalysts. The presence of Mo-derived oxides (MoO₃) is confirmed in all catalysts by two peaks with binding energies of 232.2 eV (Mo^{VI} 3d_{5/2}) and 235.3 eV (Mo^{VI} 3d_{3/2}).

Table 3.3. Binding energies and atomic ratios of the fresh NiMo catalysts as determined by XPS.

	NiMo/				
	ASA	ALM	MCM	SBA	FCC
O 1s	531.81	531.54	532.6	532.48	531.16
C 1s	284.69	286.24	284.64	284.62	284.61
Si 2p	102.87	--	102.88	102.44	101.9
Ni 2p _{3/2}	856.67	856.37	855.76	856.45	856.32
Mo 3d _{5/2}	232.81	232.41	232.25	232.25	232.07
Ni/Mo	1.143	0.922	0.211	0.452	1.063
Ni/(Si+Al)	0.035	0.042 ¹	--	--	0.163
Mo/(Si+Al)	0.028	0.045 ²	0.077	0.024	0.153

¹Ni/Al

²Mo/Al

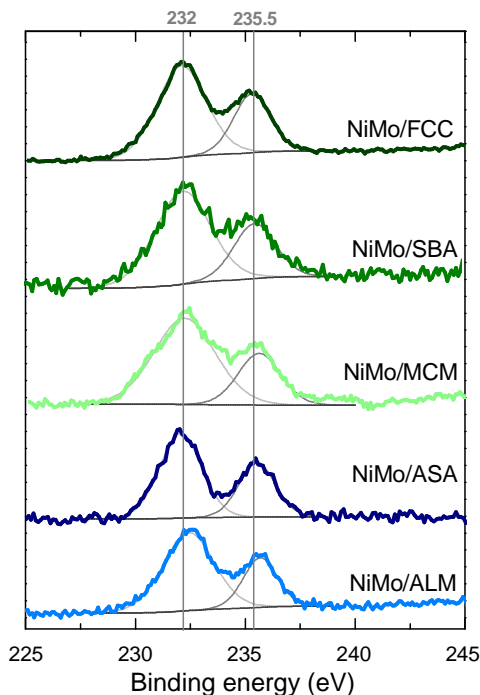


Figure 3.4. Mo 3d XPS spectra deconvolutions of the fresh NiMo catalysts.

3.1.2.4. TPR

The TPR profiles shown in Figure 3.5 have been used to study the reducibility of Ni and Mo particles deposited on the catalytic surface. For the five catalysts, one main reduction peak can be noticed. This peak appears at 370 °C in the NiMo/ASA catalyst and is shifted towards higher temperatures following the trend: ASA < MCM < SBA \approx FCC < ALM. The peak at 370-403 °C is commonly associated with the partial reduction of well-dispersed polymolybdate-like species (i.e. $\text{Mo}^{6+} \rightarrow \text{Mo}^{4+}$). This peak shifted towards higher temperatures for the NiMo/ALM suggests that metals are interacting strongly with the ALM support, even though less metal is being reduced, as deduced from the lower intensity of the peak. The second maximum at 410-440 °C (observed as a separate peak in the NiMo/FCC catalyst but present as a shoulder in the rest of the catalysts) is assigned to the reduction of bulk NiO and MoO_3 from Mo^{6+} to Mo^{4+} . In the case of the NiMo/FCC catalyst, the wider low temperature peak indicates the higher reducibility of the FCC catalyst, compared to the rest of the catalysts, due to the effect of different pore structure and surface acidity [236].

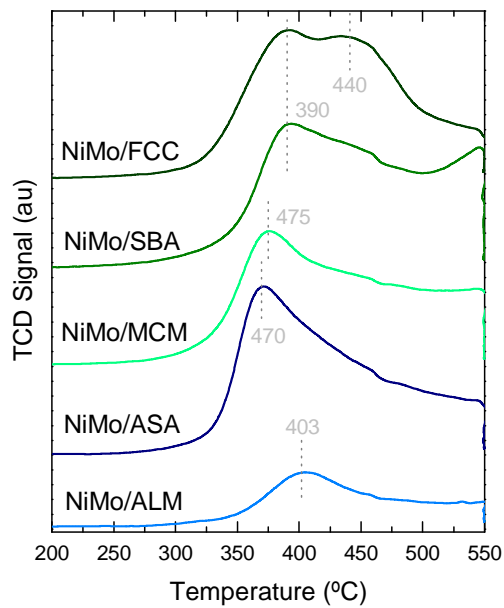


Figure 3.5. H₂-TPR patterns of the fresh catalysts.

3.2. HYDROTREATING OF SSTPO

A preliminary catalyst screening has been performed in the catalytic hydrotreating of a synthetic feed composed of representative compounds of STPO, as listed in Tables 2.1 and 2.5 of Section 2.1.

The three sulfur compounds present in the original feed were: benzothiazole, dibenzothiophene, and 4,6-dimethyldibenzothiophene (BTZ, DBT and M₂DBT, respectively), accounting for a total amount of sulfur of 20,788 ppm. The effect of temperature on the sulfur removal in the synthetic STPO hydrotreating is shown on Figure 3.6. As seen in this figure, temperature has a remarkable effect on the HDS of the synthetic feed, significantly decreasing the concentration of sulfur as the operation temperature is raised. In all cases, the amount of remaining sulfur detected has been lower than 180 ppm, which implies that the HDS conversion has been higher than 99 %. NiMo/ASA, NiMo/ALM and NiMo/MCM were the most active catalysts; reaching sulfur levels lower than 10-15 ppm, particularly at 325-350 °C. These sulfur levels are known (for the diesel fraction) as Ultra Low Sulfur Diesel (ULSD) [237], as plotted in Figure 3.6. The most promising catalysts are NiMo/ASA, NiMo/ALM and NiMo/MCM that reach 10, 3 and 5 ppm of sulfur at 350 °C, respectively. The effect of the temperature is less pronounced for the NiMo/FCC and NiMo/SBA catalysts. For both cases, the products contain around 60 ppm of sulfur at 350 °C, and this value increased at lower temperatures to 100 and 160 ppm at 275 °C for NiMo/SBA and NiMo/FCC catalysts, respectively.

At temperatures higher than 325 °C, BTZ is removed almost completely, especially in the case of NiMo/ASA, NiMo/ALM and NiMo/MCM catalysts. When temperature is lowered, this low BTZ concentration is kept in the case of NiMo/ASA and NiMo/ALM catalysts. However, NiMo/MCM, NiMo/SBA and NiMo/FCC catalysts do not remove so much BTZ at 275 °C. Regarding DBT and M₂DBT (considering the initial concentration shown in Table 2.10), both show lower hydrotreating reactivity than BTZ. In the case of NiMo/ASA and NiMo/ALM catalysts, almost all the remaining sulfur is in the form of M₂DBT, accounting for more than 60 wt% of the total sulfur. For all the catalysts, the amount of BTZ and M₂DBT decreased when raising the temperature, while DBT amount reached a maximum at 300-325 °C, except for NiMo/ALM and NiMo/ASA catalysts, when DBT was only detected at 275 °C. It is well known that the reactivity of sulfur molecules depends greatly on their shape and, therefore, the reactivity of BTZ is much higher than the one of DBT-type compounds and allows almost its total removal [114]. The main reason why the reactivity of these compounds is lower is the shielded environment around the S atom in the molecule [238]. Regarding DBT compounds, two possible

reaction pathways should be considered: direct desulfurization (DDS route) and hydrodesulfurization (HDS route), as schematized in Figure 1.9 of Section 1.6.1.1. Klimova et al. [239] reported that in the case of DBT, the DDS route prevails, while HDS is the principal route for the dibenzothiophenes with alkyl substitutes. Additionally, the presence of methyl groups near the S atom in the M₂DBT molecule hinders its hydrogenolysis reactivity, which can be even 10 times lower than that of DBT [240].

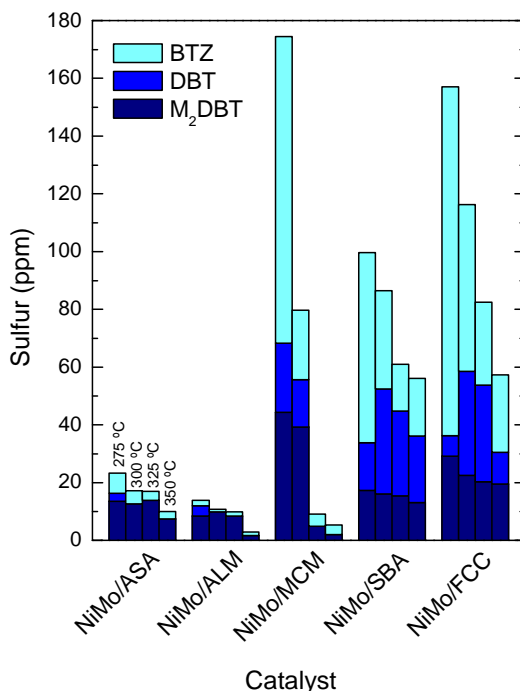


Figure 3.6. Effect of temperature on sulfur removal on the hydrotreating of SSTPO (65 bar; space time, 0.241 g_{cat} h g⁻¹_{feed}; TOS, 8 h).

As previously mentioned, nitrogen is present in STPO in the form of BTZ. Considering the initial nitrogen content (393 ppm) and the remaining nitrogen in the products (also in the form of BTZ), the hydrodenitrogenation (HDN) conversion has been higher than 99 % in all cases, except for the 98.5 % of nitrogen removal achieved at 275 °C with NiMo/MCM and NiMo/ALM catalysts. HDN reactions give way to the presence of NH₃ in the reaction media, and therefore being a possible activity inhibition cause. However, no significant effect or correlation can be established.

The properties of the catalysts (described in Section 3.1) can be correlated with the activity and selectivity based on the results shown. Despite the fact that NiMo/FCC catalyst shows the highest accessibility to Ni and Mo sites and hydrogen uptake, this catalyst has the lowest performance towards HDS, and similar to that of NiMo/SBA, which has much poorer metallic dispersion. Thus, within the conditions employed here, the support plays a critical role governing activity and selectivity of hydrotreating catalysts. Surface area and pore volume do not closely correlate with the catalyst performance but seem to help the diffusion of reactants and products, particularly for the NiMo/MCM catalyst, which displays the highest accessible surface and a very high performance. Furthermore, the acidic properties correlate well with the intrinsic activity in a way that the elimination of sulfur from STPO is determined by a balance between mild total acidities and a high amount of weak acid sites (desorbing t-BA at higher temperatures). This is the reason behind the better performance of NiMo/ALM catalyst.

3.3. HYDROTREATING OF STPO

3.3.1. Hydrodesulfurization

The hydrotreating of STPO has been carried out on NiMo/ASA, NiMo/ALM and NiMo/MCM catalysts at 65 bar; space time, $0.241 \text{ g}_{\text{cat}} \text{ h g}^{-1}_{\text{feed}}$; time on stream, 0-8 h; and in temperature sequences of 300-340-375-300 °C. Figure 3.7 shows the sulfur content of the products at steady state conditions (8 h after the temperature change). Note that the initial sulfur concentration is 11,600 ppm (Table 2.5), approximately half the amount of the synthetic feed. The effect of temperature on the hydrodesulfurization of STPO follows similar trends as those observed for the synthetic feed, decreasing the level of detected sulfur concentration at higher temperatures. All catalysts show relatively similar hydrotreating performance at temperatures higher than 340 °C, obtaining practically identical sulfur concentration in the products (1,000-1,500 and 1,500-2,200 ppm at 375 and 340 °C, respectively), which account for HDS conversions of higher than 80 % as observed in Figure 3.7. BTZ has been completely removed from the feed (3,794 ppm on the STPO), and all the remaining sulfur compounds are substituted DBTs, which are more resistant towards HDS [114]. Most of the sulfur compounds in the products are in the form of M₃DBT and M₄DBT, accounting for the 66-76 wt% and 11-17 wt% of the total, respectively. Small amounts of M₁DBT have been detected only at 300 °C (0.6-2.4 wt %).

All the sulfur compounds are distributed between the diesel and gasoil lumps, whereas naphtha shows virtually zero sulfur levels. Moreover, the sulfur molecules in this naphtha lump react one order of magnitude faster than those of diesel or gasoil [114].

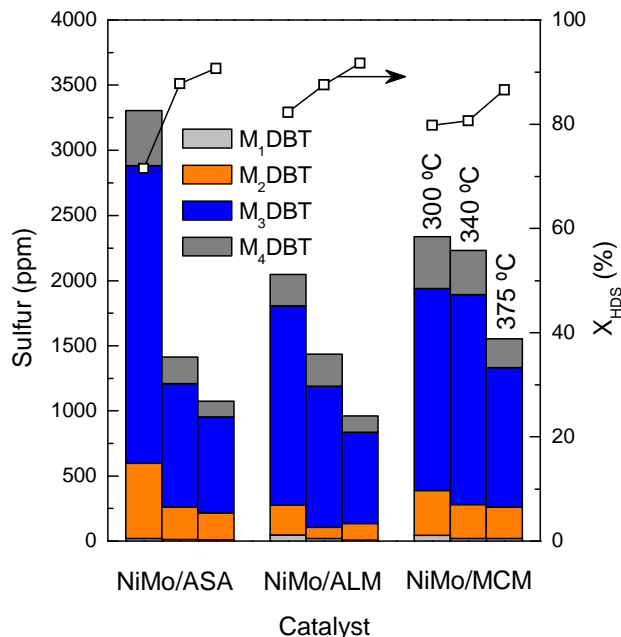


Figure 3.7. Effect of temperature and catalytic support on the HDS conversion and sulfur distribution on the hydrotreating of STPO (65 bar, $0.241 \text{ g}_{\text{cat}} \text{ h g}^{-1}_{\text{feed}}$; TOS, 8 h).

Generally, the levels of detected sulfur have been approximately 10-15 times higher than those corresponding to the products from SSTPO hydrotreating, although the initial concentration of the real feed (diluted) was lower. This effect has previously been reported by Pawelec et al. [241] and Reinhoudt et al. [242] comparing a model feed with refinery feeds: gasoil or diesel. Satterfield and Yang [243] reported some of the more significant effects that should be considered when working with mixed feeds, among of which the following should be highlighted: (i) the presence of inorganic compounds, (ii) molecular weight and structure of reactants and (iii) competitive adsorption effects. The different chemical nature of model and real feedstock heavily controls the hydrotreating performance, and it is also important to consider that catalyst activity suffers a strong inhibition due to the presence of other reactants and products, which is typically considered in the kinetic equation as the adsorption term in the denominator of Lagmuir-Hinshelwood kinetic expression. Real STPO feed is rich in heavy naphthenic and aromatic compounds, some of which are O- and N-containing, remaining in the products after hydrotreating and might have a partial poisoning effect on the catalyst

[244, 245]. This poisoning effect was corroborated by Nagai and Kabe by adding different additive amounts in DBT hydrodesulfurization studies [246]. The presence of aromatics has little effect on hydrotreating, while oxygen compounds inhibit hydrotreating significantly [247]. Interestingly, the inhibiting effect of H₂S is not responsible for this observation, as the concentration of this molecule would be much higher for the synthetic compared to the “real” STPO (double amount of initial sulfur and much higher HDS conversion obtained). Additionally, STPO is rich in olefins and aromatics, some of which tend to polymerize at high temperatures (particularly dienes) causing either catalytic deactivation and/or pore blockage, hindering hydrotreating reactions. In any case, and despite the fact that the synthetic feed has double the amount of sulfur, the higher proportion of substituted DBTs (particularly M₃DBT and M₄DBT, Table 2.5) is responsible for the lower HDS activity for the STPO.

NiMo/ALM and NiMo/MCM catalysts have shown a very similar HDS performance with real STPO, although having different metallic dispersion, especially regarding low Ni site accessibility. Acidity has again proven to be the determinant property regarding HDS. Higher total acidity did not favor the removal of higher amounts of sulfur, as deduced from the NiMo/MCM results, while lower total acidities with mildly strong acidic sites (as those of the NiMo/ALM catalyst) showed the highest HDS performance when hydrotreating real feedstock. Slightly stronger acidic sites were more dependent on temperature effects below 340 °C.

3.3.2. Mild hydrocracking and hydrodearomatization

Mild hydrocracking (MHC), hydrodearomatization (HDA) and hydrodesulfurization (HDS) conversions for the three most active catalysts have been compared in Figure 3.8, at 375 °C. As it can be observed, each one of the three catalysts should be selected depending on the main hydrotreating goal. In this case, the NiMo/ASA catalyst is the most appropriate if the main aim is to eliminate heavy gasoil from the original feed, as it has shown the highest MHC conversion (32.5 %). For achieving higher aromatic compound removal, working with the NiMo/MCM catalysts is the most adequate (X_{HDA} 26.0 %), and if the main goal is to remove sulfur from the feed, the NiMo/ALM catalyst is the most promising with a HDS conversion of 91.7 %.

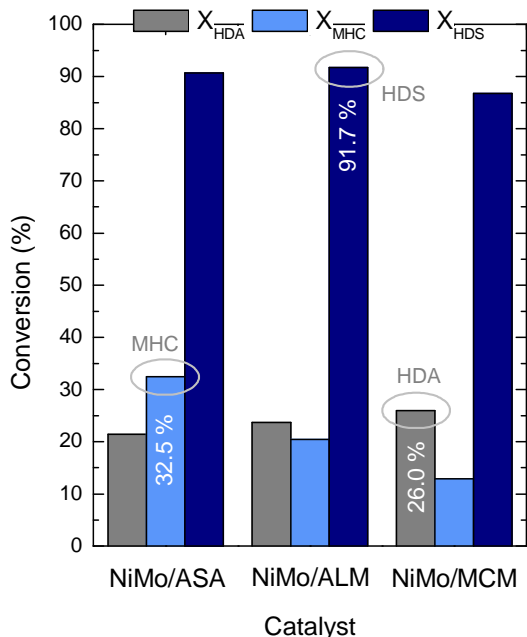


Figure 3.8. Comparison of the different HDA, HDS and MHC conversions for the three catalysts on the hydrotreating of STPO at 375 °C (65 bar; 0.241 g_{cat} h g⁻¹_{total}; TOS, 8 h).

For similar mild hydrocracking levels, higher HDS conversions than that obtained by Cambor et al. [248] on the mild hydrocracking of a vacuum gasoil have been achieved, despite using more acidic supports (zeolites). Ishihara et al. [249] reported the moderate HDA ability of NiMo catalysts, obtaining moderate conversions for the ring hydrogenation of 1-methylnaphthalene and decahydronaphthalene mixture.

Figure 3.9 shows the effect of the catalytic support on the composition of the three main fractions of the liquid product at 375 °C. Diesel yield shows the following support trend: ASA > ALM > MCM. The highest naphtha yield and lowest gasoil yield have been obtained with NiMo/ASA (22.4 wt% naphtha and 20.1 wt% gasoil), while NiMo/MCM yielded the highest amount of gasoil (26 wt%). The distribution of paraffins and isoparaffins, naphthenes and aromatics for each fraction is also shown in Figure 3.9. Paraffins and isoparaffins are mainly found in the diesel lump (between 29.6-33.5 wt% of the fraction), while naphthenes and aromatics are more homogeneously distributed among the different lumps. Naphthenes account for 44-48 wt% of the naphtha lump, paraffins are 25.6-27.2 wt% of the lump, and aromatics

26.3-29 wt%. The proportion of naphthenes and total aromatics varies between 23.4-28.4 wt% and 42-45.5 wt%, respectively. Gasoil lump has 18-20 wt% of paraffins, 22.7-25.4 wt% of naphthenes, and 56.4-59.8 wt% aromatics. The proportion of 1-ring aromatics is 65-75 % of the total aromatics in all lumps except for naphtha, in which this proportion is as high as 80 wt%.

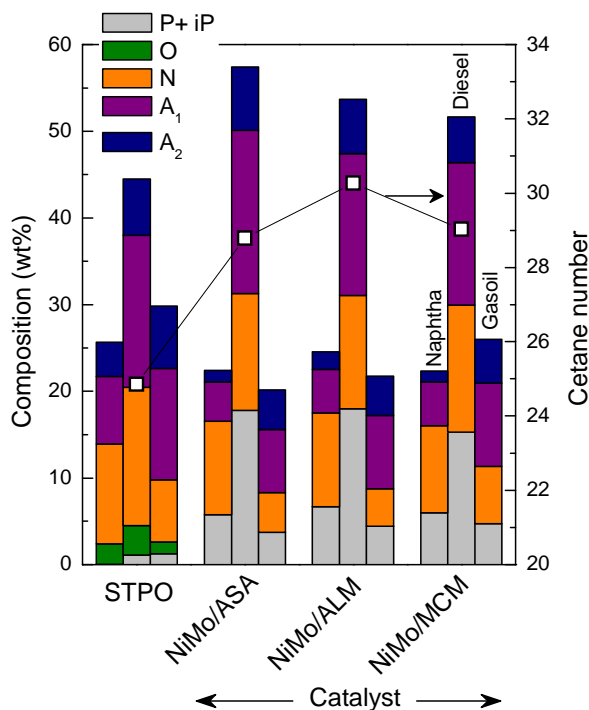


Figure 3.9. Effect of the catalytic support on the liquid product distribution and the cetane number on the hydrotreating of STPO at 375 °C (65 bar; 0.241 g_{cat} h g⁻¹_{feed}; TOS, 8 h).

Regarding diesel cetane number (CN), it has been increased from 25 (STPO) to values between 27-28, mainly due to the significant increase in the amount of paraffins and removal of sulfur, especially BTZ. However, the main contribution to cetane number in diesel comes from the aromatic fraction, which follows the same wt% trend as CN: MCM < ASA < ALM.

Considering these results, both naphtha and diesel lumps have promising chemical properties for being used as fuel blends. However, less content of heavy compounds within the gasoil boiling point range is desired, for purposes of using STPO as a fuel, and therefore, further treatment for fraction redistribution is required. With this aim, and as the second stage of the

hydroprocessing strategy (Figure 1.19), hydrocracking of STPO over more active catalysts towards cracking is required, as will be studied in forthcoming Section 5.

Furthermore, and in order to obtain the required data for developing simple kinetic models for further understanding of HDS, HDA and MHC of STPO over the NiMo/ALM catalyst (selected as the most active), it is necessary to study the effect of different operation variables on the hydrotreating of STPO, as are: (i) temperature, (ii) pressure and (iii) space time. With this aim, a complete variable effect study and kinetic model development is detailed in the following Section.

Section 4

EFFECT OF PROCESS VARIABLES AND KINETIC MODELING OF THE HYDROTREATING OF STPO ON A NiMo/Al₂O₃ CATALYST

4. EFFECT OF PROCESS VARIABLES AND KINETIC MODELING OF THE HYDROTREATING OF STPO ON A NiMo/Al₂O₃ CATALYST

In the previous Section 3.3.1, the NiMo/Al₂O₃ catalyst has proven to be the most active towards HDS (Figure 3.7), with MHC and HDA performances intermediate between those of the NiMo/SiO₂-Al₂O₃ and NiMo/MCM-41 catalysts. Therefore, it has been selected to carry out a parametric study of the hydrotreating of STPO in order to obtain the necessary data for further development of a kinetic model that describes the behavior of the reaction from three different pathway perspectives: (i) HDS, (ii) MHC and (iii) HDA. With this aim, different operating conditions have been studied, as are:

- Time on stream (TOS): 0-8 h
- Space time (τ): 0-0.5 g_{cat} h g⁻¹_{feed}
- Temperature: 300-375 °C
- Pressure: 25, 45 and 65 bar
- H₂/feed volumetric ratio: 1000 N m³/m³

It should be mentioned that results have been studied for a TOS = 8 h, after checking that for TOS > 6 h results reach a constant value, as a consequence of stable trickle bed regime conditions and insignificant deactivation.

Sulfur species, product lumps and composition (for HDS, MHC and HDA, respectively) have been studied by using the same two criteria defined in the previous Sections 2.2.2.1 and 2.2.2.2, and reaction parameters are those specified in Section 2.2.2.4. The main properties of the fresh NiMo/Al₂O₃ catalyst have been detailed in Sections 3.1.1 and 3.1.2.

Kinetic modeling of the different processes concerning heavy hydrocarbons feeds generally needs to take into account a great amount of individual reactions that are affected by temperature, space time, pressure, and time on stream (catalyst deactivation) in different extents. The most common approach for modeling these types of mixtures is considering lumps in which the compounds are grouped according to their specific reactivity. Based on this, and considering the evolution of the different sulfur species and lumps in terms of amount and composition, simple kinetic models have been proposed in this Section for fitting the obtained experimental data on the hydrotreating of STPO.

As previously stated, the objectives of HT-STPO are decreasing the amount of sulfur, gasoil and aromatics. Hence, this Section deals with the kinetic modeling of these steps, which are HDS, MHC and HDA, respectively.

The parameters to be computed in the kinetic model have been the rate constants at the reference temperature (T_{ref}) of 390 °C and the activation energies. The system of equations has been solved by developing a program using Matlab, following the scheme shown in Figure 4.1. The main program reads the experimental data and also contains initial values assigned to the parameters (kinetic constants and activation energies). The objective function is to minimize (with the Matlab *fminsearch* function) the error between the experimental data and the data predicted by the proposed kinetic model, which is obtained from a series of functions that compute the error by integrating the differential equations of the model using the Matlab *ode45* function. Finally, model simulations are plotted and results are displayed in an Excel file.

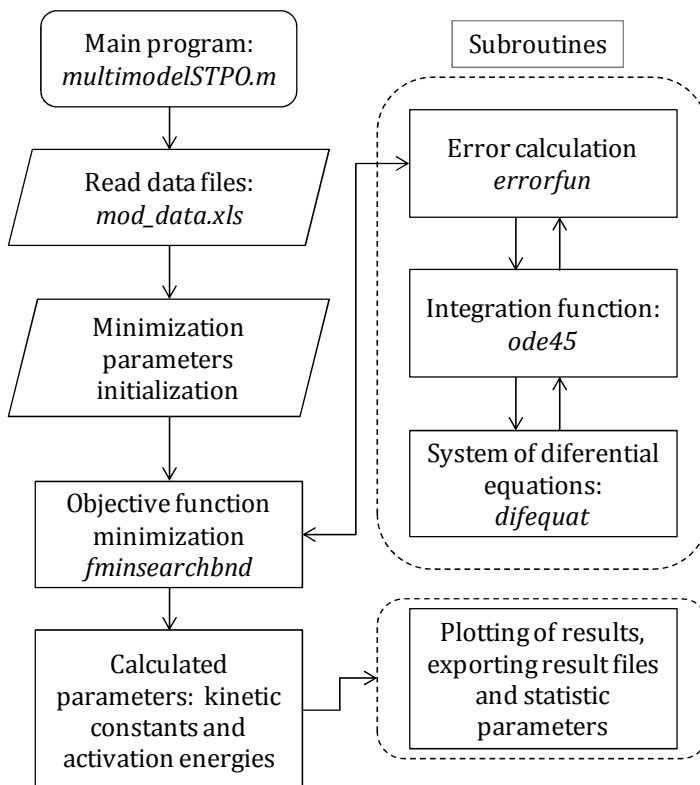


Figure 4.1. Block diagram for the computation of the kinetic parameters.

4.1. HYDRODESULFURIZATION

4.1.1. Effect of pressure and temperature

Figure 4.2 depicts the effect of pressure (25-65 bar) and temperature (300-375 °C) on total sulfur removal and speciation using the NiMo/Al₂O₃ catalyst. An increase in hydrotreating pressure implies a higher total sulfur removal, with total sulfur amounts of 1,669-2,710 ppm, 831-1,852 ppm and 480-1,743 ppm for 25, 45 and 65 bar, respectively. As observed in Section 3.3.1, temperature also has a positive effect on total sulfur removal, increasing HDS conversion almost linearly, and obtaining the highest total HDS conversions at 375 °C in all cases: 85.6 %, 92.8 % and 95.9 % for 25, 45 and 65 bar. The proportions of each sulfur species were: 0.99-2.0 wt% M₁DBT, 8.2-13.1 wt% M₂DBT, 66.0-73.7 wt% M₃DBT and 13.2-21.5 wt% M₄DBT. M₃DBT and M₄DBT remain in higher proportions, as there are more resistant towards HDS [109].

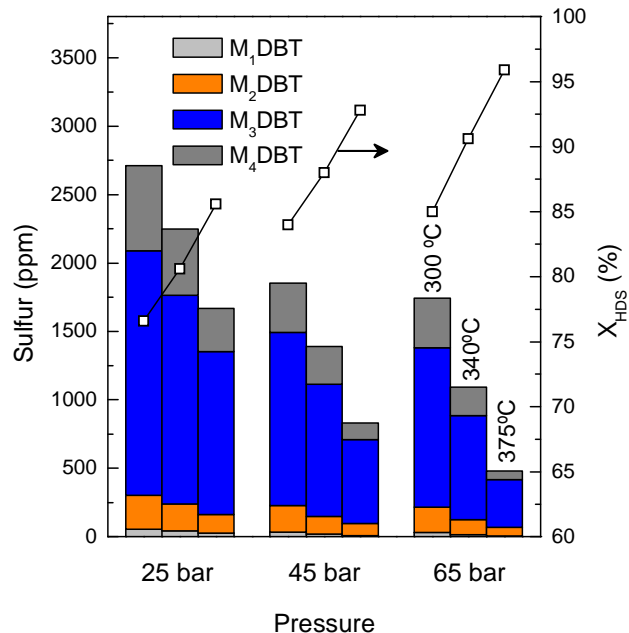


Figure 4.2. Effect of temperature and pressure on the total sulfur removal, conversion and speciation on the hydrotreating of STPO over a NiMo/Al₂O₃ catalyst (space time, 0.241 g_{cat} h g⁻¹_{feed}; TOS, 8 h).

It is well reported in literature that high pressures favor hydroprocessing reactions [250], obtaining lighter fractions with lower sulfur amounts as pressure is increased. Kan et al. [251] observed this effect of the pressure on the sulfur and nitrogen removal on the hydroprocessing of a coal tar for clean fuel production, determining a much significant effect of P over HDN than over HDS. Nakano et al. [252] obtained the same conclusions on the HDS of gas oil using mixtures of Al_2O_3 into SiO_2 hydrogels. A higher level of sulfur removal also implies that more H_2S is present in the reaction media causing an inhibition effect, as studied by Rabarihoela-Rakotovo et al. [253] on the HDS of DBT and 4,6-DMDBT over a $\text{NiMoP}/\text{Al}_2\text{O}_3$ catalyst. Even though such effect has not been clearly observed in product analysis, it should be taken into account for the development of a kinetic model (Section 4.1.3).

Equally to what was observed in Figure 3.7 on the comparison of the HDS performance of NiMo catalysts with different supports, higher temperatures favor total sulfur removal. This effect will be further studied in Section 4.1.3 on HDS kinetic modeling.

4.1.2. Effect of space time

Figure 4.3 shows the evolution of the different sulfur species at different temperatures and space times. As observed, an increase on space time (and therefore in the amount of catalyst loaded in the reactor), significantly affects sulfur removal, obtaining the highest removal rates at higher space times. Yan et al. [251] and Kallinikos et al. [254] reported very similar effect of space time on the HDS of gasoline-diesel type fractions, and gasoil, respectively. At lower space time, and therefore less catalyst loaded on the reactor, contact time decreases and less reaction time is provided.

Considering the original compositions shown in Table 2.5, and the most favorable HDS conditions, at $0.5 \text{ g}_{\text{cat}} \text{ h g}^{-1}_{\text{feed}}$ the M_4DBT -type species are the ones that have been removed in a greater extent, with individual removal conversions of 95-99 %, followed by M_1DBT and M_2DBT (92-98 wt%) and with M_3DBT being the most difficult species to eliminate (85-97 %).

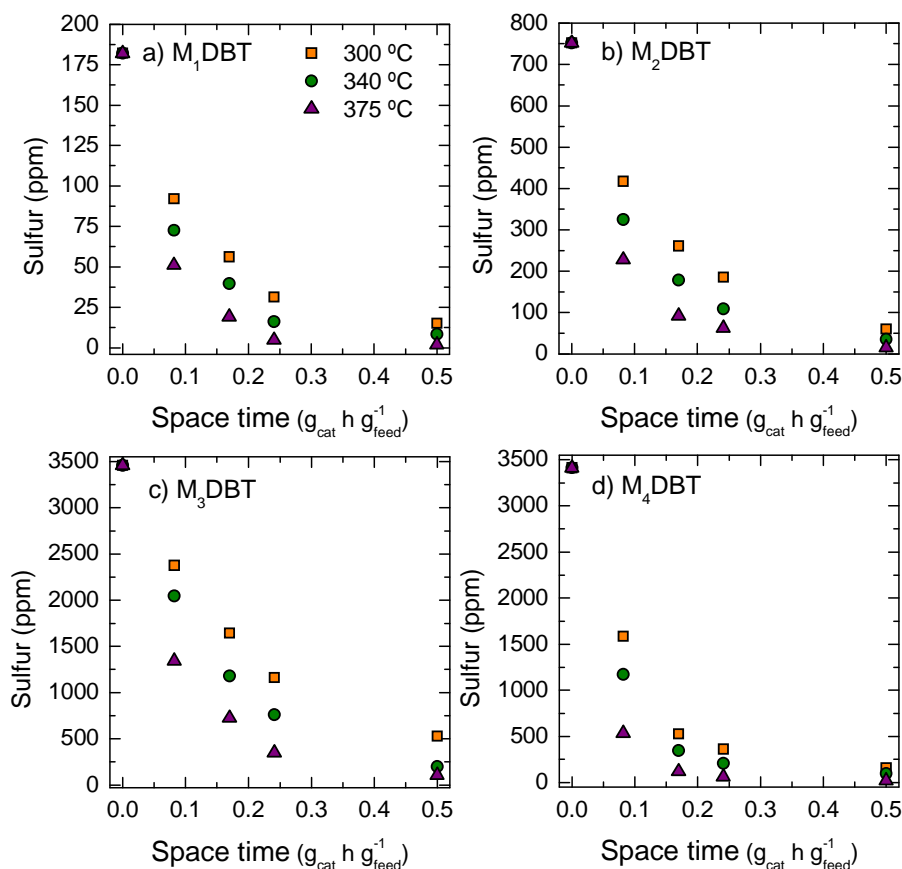


Figure 4.3. Effect of temperature and space time on the removal of the a) M₁DBT, b) M₂DBT, c) M₃DBT and d) M₄DBT species on the hydrotreating of STPO (65 bar; TOS, 8 h).

As pointed in Section 1.6.1.1, sulfur molecules with a higher number of C atoms in their substituents are more resistant towards HDS than less heavily substituted DBTs (Table 1.8). However, comparing Figure 4.3c and Figure 4.3d (with almost identical initial concentrations), for a specific temperature and space time conditions, removal of M₄DBT species occurs faster than that of M₃DBT ones. From this, once again the determining role of the substituent position on HDS is evidenced. Substituent groups located close to the C-S bond can strongly hinder HDS [113, 255]. Considering this, it can be deduced that the methyl- and ethyl- groups in the remaining M₃DBT species are mainly located in 2,4- positions (the closest to the S atom), while M₄DBT species have a much lower proportion of molecules with substituents in these positions and can be removed easily. Kim et al. [256] reported the important differences

between “reactive” S compounds (BTs and substituted BTs) and “refractive” S compounds (4- and/or 6- position substituted DBTs) on the deep HDS of a Saudi Arabian gasoil, confirming that HDS of refractive molecules appears as the great challenge.

4.1.3. HDS kinetic modeling

Langmuir-Hinshelwood (LH) type of mechanism is the most common form of expression for HDS kinetics [189]. In this case, and providing the very high HDS conversions that have been obtained, the inhibition effect of H₂S needs to be considered in the equation, as HDS models are very sensitive towards the concentration of H₂S in the media [257], including an adsorption-desorption equilibrium constant (K_{H_2S}). The reaction rate for each sulfur species has been defined as:

$$\frac{dx_i}{d\tau} = \frac{k'_i x_i x_{H_2}}{(1 + K_{H_2S} x_{H_2S})^2} = \frac{k_i x_i}{(1 + K_{H_2S} x_{H_2S})^2} \quad (4.1)$$

Where k_i is the kinetic constant for the i species, x_i is the mass fraction of the i species, and x_{H_2} and x_{H_2S} the mass fractions of H₂ and H₂S in the reaction media. The reaction order for sulfur has been assumed to be 1. The exponent 2 of the denominator in Eq. 4.1 is representative of the number of active sites in adsorption for H₂S. Additionally, as hydrogen concentration is constant, it has been included in the kinetic constant (k_i), which has been defined by the reparametrized Arrhenius equation.

$$k_i = k_{i,T_{ref}} \cdot \exp\left[\frac{E}{R} \left(\frac{1}{T_{ref}} - \frac{1}{T}\right)\right] \quad (4.2)$$

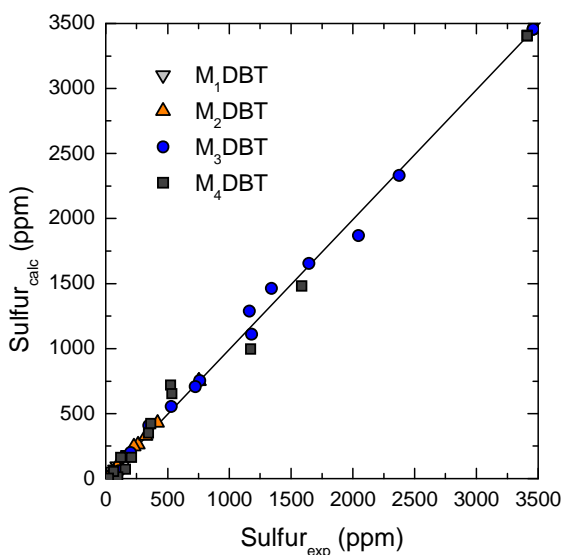
Where $k_{T_{ref}}$ is the kinetic constant at the reference temperature (T_{ref}) of 390 °C, E is the activation energy, R the ideal gas constant and T is hydrotreating temperature.

The obtained parameter values are listed in Table 4.1. The model predicts that HDS of M₄DBT occurs the fastest, followed by M₁DBT and M₂DBT (both species reacting at a very similar rate) and being M₃DBT species those that react the slowest, and the ones that have the highest activation energy. Even though, according to their substituent number, a higher reaction rate could be predicted for M₃DBT species, in practice HDS of M₄DBT species has occurred twice as rapid as that of M₃DBT due to the position of their substituents.

Table 4.1. Kinetic parameters for the HDS model.

Sulfur lumps	$k_{i,390\text{ }^\circ\text{C}}$ ($\text{g}_{\text{feed}} \text{g}_{\text{cat}}^{-1} \text{h}^{-1}$)	E (kJ mol^{-1})
M ₁ DBT	$(2.17 \pm 0.70) \cdot 10^{-5}$	34.30 ± 6.22
M ₂ DBT	$(1.89 \pm 0.59) \cdot 10^{-5}$	33.49 ± 1.41
M ₃ DBT	$(1.44 \pm 0.19) \cdot 10^{-5}$	36.10 ± 3.07
M ₄ DBT	$(2.79 \pm 0.39) \cdot 10^{-5}$	32.38 ± 4.16

The quality and accuracy of the fitting can be evaluated from the parity diagram (Figure 4.4) representing experimental and calculated data, as well as from the comparison between the results predicted by the model equations (lines) and the experimental data (dots) in Figure 4.5.

**Figure 4.4.** Parity diagram for the proposed HDS model.

HDS kinetics has been widely studied with model compounds [258-261]. Egorova and Prins [223] proved that, for Mo catalysts, the direct desulfurization route of 4,6-DMDBT (Figure 1.10) could be significantly enhanced by promotion with Ni and Co. According to the results obtained by Li et al. [261] on the HDS of the same compound, the limiting reaction rate turned out to be hydrogenation and hydrogenolysis of 4,6-DMDBT itself, with higher reaction rates on the rest of the mechanism steps.

Regarding real heavy feedstock, Ferreira et al. [262] recently developed a model that predicted very similar effect of the space time on the evolution of S content in a heavy vacuum residue, also considering the content in metals of the feed. The same positive effect of higher temperatures, pressures and space times previously commented in this Section was reported by Jarullah et al. [263] on the simulation on a trickle bed reactor of the HDS of a crude oil. The LH-based model proposed by Laredo and Cortés [185] studied the kinetics of differently substituted DBTs on the HDS of a gasoil narrow-cut fraction and once again corroborated that a substituent in position 4- greatly hinders HDS. Froment et al. [264] proved that considering structural contribution parameters of substituted DBTs allowed for obtaining a more complete and accurate modeling approach on the HDS of real feeds.

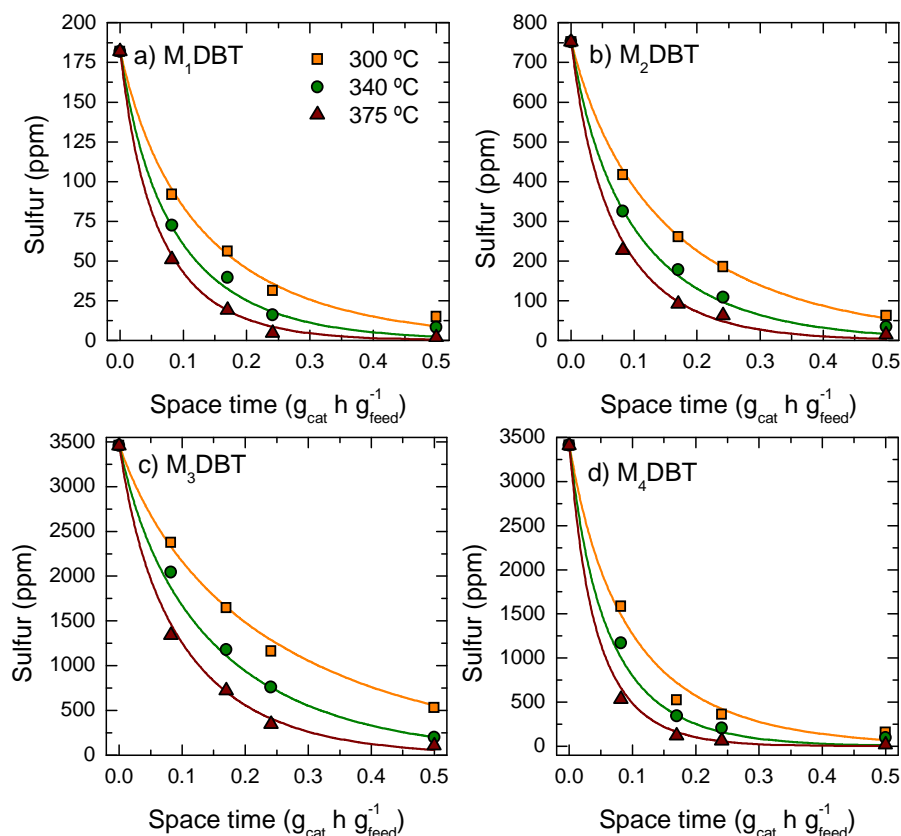


Figure 4.5. Comparison between the experimental data (dots) and predicted data (lines) for the evolution of a) M₁DBT, b) M₂DBT, c) M₃DBT and d) M₄DBT species with space time on the hydrotreating of STPO (65 bar; TOS, 8 h).

From the results shown in Figure 4.5, the evolution with space time of total HDS conversions (X_{HDS}) can be obtained, as displayed in Figure 4.6, from both experimental (dots) and kinetic model prediction (lines). Very accurate results have been obtained, also observing a remarked effect of temperature, especially within the 0-0.24 $\text{g}_{\text{cat}} \text{h g}_{\text{feed}}^{-1}$ range, when variations in space time significantly affect total HDS conversions. At higher space time values, a clear tendency towards a steady state is observed, obtaining almost complete sulfur removals at 340-375 °C.

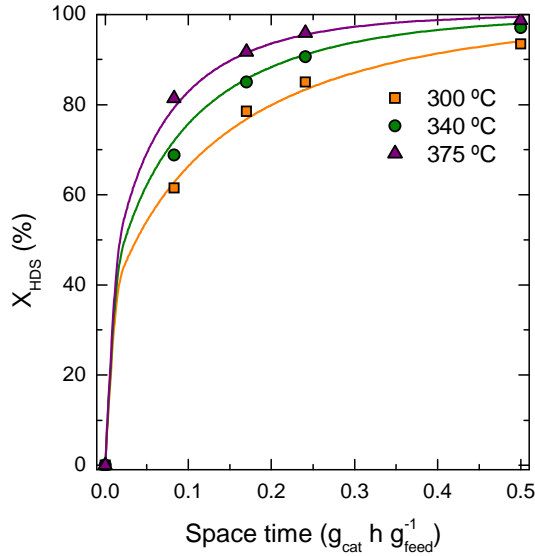


Figure 4.6. Evolution of HDS conversion with space time as obtained from experimental data (dots) and kinetic model prediction (lines).

4.2. MILD HYDROCRACKING

4.2.1. Effect of pressure and temperature

Pressure effect in product lumps is shown in Figure 4.7. As a general trend, an increase in pressure has the same qualitative effect as increasing temperature, as lighter products are obtained (naphtha, 35-216 °C), mainly at the expense of lower amounts of middle distillates (diesel, 216-350 °C), while gasoil yield (> 350 °C) does not suffer significant changes. However, at lower temperatures (300 °C), higher pressures favor the obtention of heavier fractions like diesel and gasoil, as naphtha yield drops. Gutierrez et al. [265] observed the same effect on the hydrocracking of LCO as, at 300 °C, the concentration of middle distillates increased with pressure. This might be attributed to the higher relevance of hydrogenation reactions compared to those of hydrocracking at lower temperatures. As a consequence, hydrogenation of gasoil is favored to form diesel. At 340 °C and up, however, cracking is enhanced towards lighter product formation.

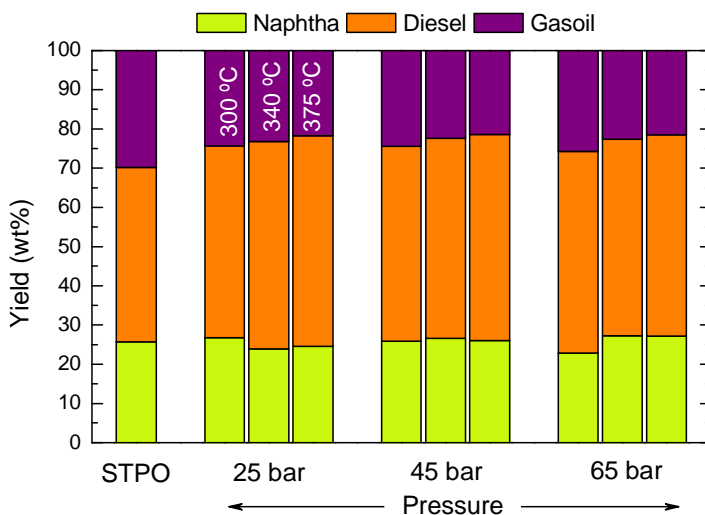


Figure 4.7. Effect of pressure on product yields on the hydrotreating of STPO at three different temperatures (300-340-375 °C; space time, 0.24 g_{cat} h g⁻¹_{feed}; TOS, 8 h).

4.2.2. Effect of space time

The evolution with space time of the different product lump yields (naphtha, diesel and gasoil) at three different temperatures is shown in Figure 4.8. Diesel is the most abundant lump at all temperatures. For values of space time below $0.3 \text{ g}_{\text{cat}} \text{ h g}^{-1}_{\text{feed}}$, significant variations can be seen, especially regarding diesel and gasoil yields. The former increases in approximately 6-9 wt%, while the latter decreases in 7.5-12 wt% upon increasing space time and temperature. The highest diesel yield and lowest gasoil yields are obtained at $375 \text{ }^{\circ}\text{C}$ and $0.5 \text{ g}_{\text{cat}} \text{ h g}^{-1}_{\text{feed}}$, with 54.2 wt% and 20.8 wt%, respectively. Variations with space time in naphtha occur in a much lesser extent, and become more important upon increasing temperature. While at $300 \text{ }^{\circ}\text{C}$ the amount of naphtha remains constant compared to the original feed amount, at $340 \text{ }^{\circ}\text{C}$ it increases up to 24.3 wt% and at $375 \text{ }^{\circ}\text{C}$ up to 25.0 wt% for $0.5 \text{ g}_{\text{cat}} \text{ h g}^{-1}_{\text{feed}}$ conditions.

According to these results, at the entrance of the reactor products consist mainly of gasoil and diesel but, in further positions of the reactor, naphtha becomes more important, especially at temperatures above $340 \text{ }^{\circ}\text{C}$. In any case, and as observed by Rayo et al. [266] in the hydroprocessing of a Maya crude oil, preferentially middle distillates like diesel (more than 50 wt%) are obtained with this kind of supports, with low Brönsted site concentration.

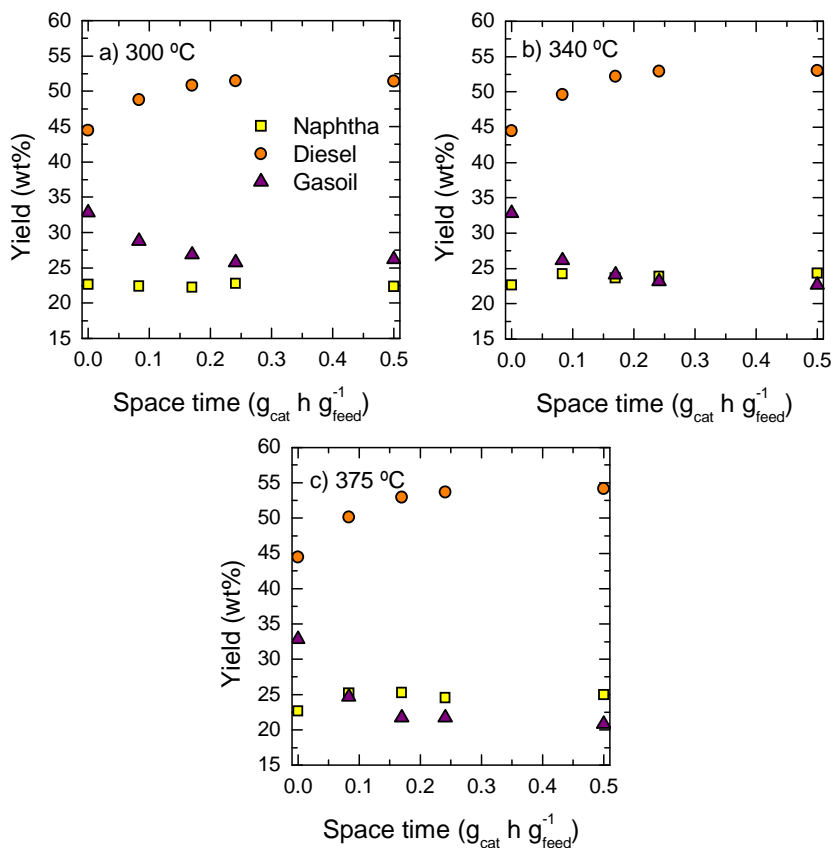


Figure 4.8. Evolution with space time of product lumps on the hydrotreating of STPO at three different temperatures (65 bar; TOS, 8 h).

4.2.3. MHC kinetic modeling

Based on the data shown in Figure 4.8, and on the kinetic models proposed by Ancheyta [189], the kinetic model of Figure 4.9 has been proposed. In it, gasoil \leftrightarrow diesel and diesel \leftrightarrow naphtha transformations have been considered, as well as partial formation of naphtha from heavy compounds in the gasoil range. It should be mentioned that, in this work, no activity decay has been observed with the NiMo/Al₂O₃ catalyst as, performing temperature ramps (375-340-300-375 °C), the catalyst recovered its initial activity at 375 °C. Therefore, coke lump has not been included in the model. In the same way, as only mild hydrocracking has been achieved, no significant gas formation has been measured, and gas lump has also not been included. A

previous model was tested without considering the k_3 constant, but significant improvements were obtained after including the gasoil→naphtha stage.

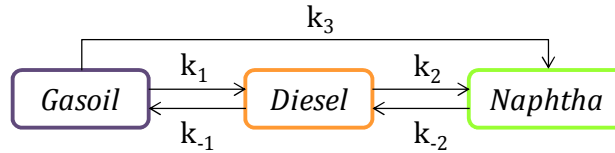


Figure 4.9. Proposed kinetic model for the MHC of STPO.

The equations of the model are:

$$\frac{dx_G}{d\tau} = -k_1 x_G x_H - k_3 x_G x_H + k_{-1} x_D x_H \quad (4.3)$$

$$\frac{dx_D}{d\tau} = k_1 x_G x_H - k_{-1} x_D x_H + k_2 x_N x_H - k_{-2} x_D x_H \quad (4.4)$$

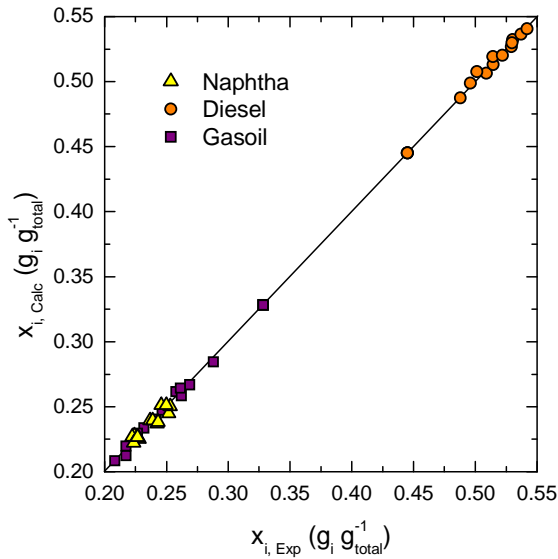
The kinetic constants have been defined following the Arrhenius equation (Eq. 4.2). The system of equations has been solved by following the procedure in Figure 4.1. Hydrogen concentration, as a constant present in every factor of the equations, has been included in the kinetic constant.

The kinetic parameters obtained for the model are summarized in Table 4.2. As observed, the gasoil to diesel conversion rate is higher than the rest, being twice as rapid as the reverse reaction ($k_1 > k_{-1}$). At 390 °C, conversion of diesel to naphtha, however, is less favored and considerably slower than its reverse reaction ($k_2 < k_{-2}$), as very little amount of light compounds within the naphtha boiling point range are being formed, especially below 340 °C. According to the value of k_3 (higher than k_2), it can be deduced that the slight increase in the amount of naphtha is mainly due to the hydrogenation and cracking of compounds originally present in gasoil.

Table 4.2. Kinetic parameters for the MHC model.

Reaction	k_i	$k_{i,390\text{ }^\circ\text{C}}$ ($\text{g}_{\text{feed}} \text{g}_{\text{cat}}^{-1} \text{h}^{-1}$)	E (kJ mol^{-1})
Gasoil→Diesel	k_1	10.23 ± 0.52	11.83 ± 0.76
Diesel→Gasoil	k_{-1}	4.08 ± 0.43	1.87 ± 0.67
Diesel→Naphtha	k_2	4.95 ± 0.69	2.90 ± 1.73
Naphtha→Diesel	k_{-2}	9.83 ± 0.85	0.57 ± 0.17
Gasoil→Naphtha	k_3	7.79 ± 0.49	12.6 ± 3.36

The good fitting of the model can be proved from the parity diagram shown in Figure 4.10, as well as from the comparison between experimental data (dots) and model prediction (lines) in Figure 4.11.

**Figure 4.10.** Parity diagram for the proposed MHC kinetic model.

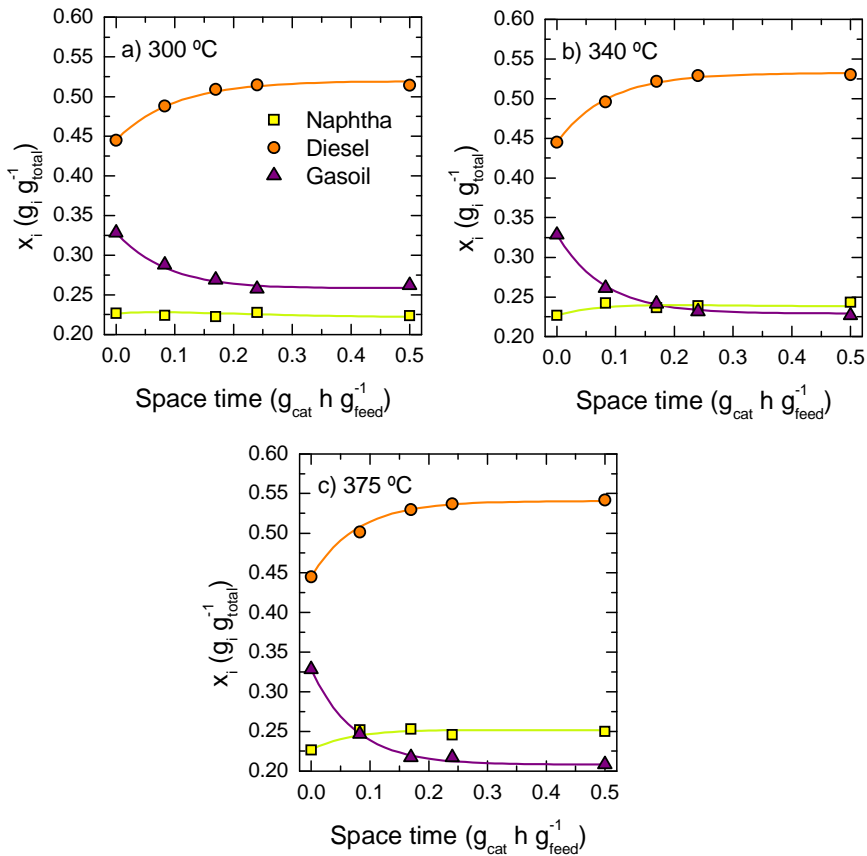


Figure 4.11. Comparison between the experimental data (dots) and predicted data (lines) for the evolution with space time of product lumps (x_i) at three different temperatures (65 bar; TOS, 8 h).

Less information for MHC modeling is available in the literature compared to that reported for HDS. Ramírez et al. [267] proposed a 5-lump model for thermal HC of heavy oils, equal to that previously developed by Sánchez et al. [193] for moderate HC. They determined that vacuum residue (VR) conversion had a higher selectivity towards heavy fractions like VGO, compared to diesel or naphtha. Similar conclusion was reported by Martínez and Ancheyta [268] applying the same 5-lump model on the HC of a heavy residue in a CSTR considering catalyst deactivation. Purón et al. [269] proposed a 4-lump model that considered coke formation on the HC of a vacuum residue (VR) from Maya crude oil over a NiMo/Al₂O₃ catalyst in a batch reactor. As occurs in the results shown in Figure 4.8, they observed that higher reaction temperatures led to the formation of products with a lower

boiling point (10 wt% more of < 450 °C fraction when increasing temperature from 400 to 450 °C), and that the stages of gas formation from coke and equilibrium between coke and lower boiling point products should be considered.

From the results shown in Figure 4.11, the evolution with space time of total MHC conversion (X_{MHC}) has been obtained, as shown in Figure 4.12, comparing the results obtained from experimental data (dots) and model prediction (lines). As corresponds to a catalyst with a moderate total acidity and mild acidic sites, moderate MHC conversions have been achieved, with highest values of 36.6 % at 375 °C and $0.5 \text{ g}_{\text{cat}} \text{ h g}_{\text{feed}}^{-1}$. Temperature has a proportional effect at all the space times studied, enhancing cracking reactions (and therefore X_{MHC}) upon increasing. Space time, on the other hand, has a more remarkable effect in the $0\text{-}0.25 \text{ g}_{\text{cat}} \text{ h g}_{\text{feed}}^{-1}$ range when increasing space time also implies obtaining higher conversions. For higher space times MHC conversion reaches a constant steady value (ca. 21, 30 and 37 wt% for 300, 340 and 375 °C, respectively).

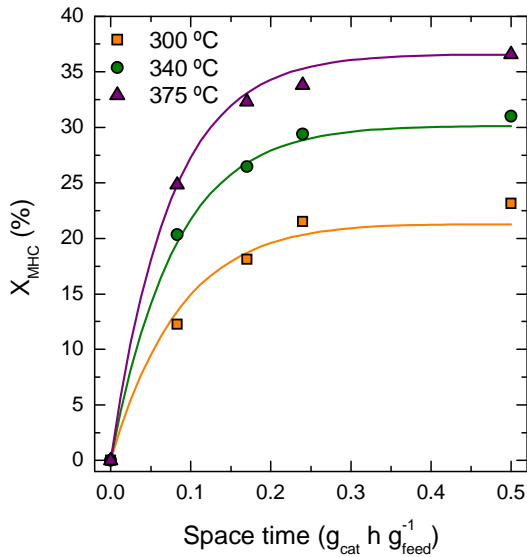


Figure 4.12. Evolution of MHC conversion as obtained from experimental data (dots) and model prediction (lines).

4.3. HYDRODEAROMATIZATION

4.3.1. Effect of pressure and temperature

The effect of temperature on product lumps and composition fractions is shown in Figure 4.13, as grouped as specified in Section 2.2.2.2. Diesel is the main lump at the three temperatures studied, increasing upon the rise of temperature from 50.4 wt% at 300 °C to 53.7 wt% at 375 °C, and obtaining a 6-9 wt% more of this lump compared to STPO. Naphtha and gasoil yields appear in similar proportions, increasing naphtha from 22.8 wt% to 24.6 wt%, and decreasing gasoil from 24.8 wt% to 21.7 wt% when temperature is raised. Naphtha has been increased marginally (1-3 wt%) compared to STPO, but gasoil lump suffers an important decrease of a 9-12 wt%. The main cause for obtaining higher naphtha and diesel yields in the products is the mild hydrocracking and hydrogenation of gasoil. Particularly, the scission of aliphatic chains linked to aromatics in gasoil, and mild ring-opening of naphthenes [270].

Low and mild acidities (with little/no Brönsted sites) have a positive effect towards obtaining more middle distillates fraction, as proven by Rayo et al. [271] on the hydrotreating of a maya crude oil on NiMo/Al₂O₃ catalysts. Additionally, by using a catalyst with low acidity, coke deactivation and hydrocracking of diesel into naphtha are avoided.

In comparison to the original STPO, products show much higher content of paraffins and isoparaffins in detriment of the content of aromatics and naphthenes. The highest amount of paraffins and isoparaffins is obtained working at 340 °C, when more favorable hydrocracking conditions are achieved, increasing by 4.9 wt%, 19.5 wt% and 4.3 wt% compared to STPO in naphtha, diesel and gasoil lumps, respectively. For the three temperatures, paraffins and isoparaffins appear mainly on diesel lump (18-20.6 wt%), and in lower amounts in the naphtha (5-6.6 wt%) and gasoil (4.4-6.1 wt%). The proportion of naphthenes has been decreased by a similar amount (2-3 wt%) in all lumps and in the whole 300-375 °C range. Total aromatics also decrease significantly, with the following trend: gasoil (10-11 wt%), diesel (2-6 wt%) and naphtha (1-2 wt%). The lowest fractions of aromatics are obtained at 340 °C.

With this type of catalyst, high HDS performances are achieved, but only mild aromatic hydrogenation and hydrocracking performances are obtained, as previously observed by Leyva et al. [272] on the hydrotreating of heavy oils with NiMo/SiO₂-Al₂O₃ catalysts. The existence of thermodynamic limitations is also known in the aromatic hydrogenation rate at elevated

temperatures [273] due to the fact that this is an exothermic reversible reaction. Thus, the maximum removal of aromatics has been obtained at intermediates temperatures (340 °C).

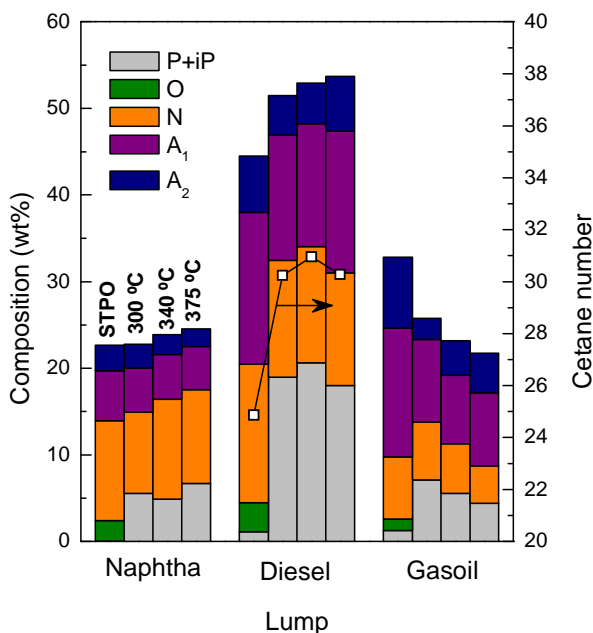


Figure 4.13. Effect of temperature on product lumps, composition and the cetane number on the hydrotreating of STPO over the NiMo/Al₂O₃ catalyst (65 bar; space time, 0.241 g_{cat} h g⁻¹_{feed}; TOS, 8 h).

Figure 4.14 shows the effect of pressure on total product composition. The effect of pressure depends on the hydroprocessing temperature, equally to what was observed in Figure 4.7 for lump yields in hydrotreating. As a general trend, when the catalyst has reached the steady state, paraffinic compounds are majoritary at 300 and 340 °C (ca. 30-35 wt% of the total products), while at higher temperatures pressure has a more remarkable effect and naphthenics and 1-ring aromatics become more important. Contrary to what has been observed in Section 4.2.1 for HDS, pressure does not have a significant effect on total product composition at steady state, as the concentration of the rest of the groups does not suffer significant variations, as follows: naphthenics, 28.1-31.5 wt%; 1-ring aromatics, 27.2-31.8 wt%; 2-ring aromatics, 9.24-12.9 wt%. Olefins have not been detected in the product stream, as their hydrogenation rate is very fast over the metallic sites, even at low pressure and temperature conditions.

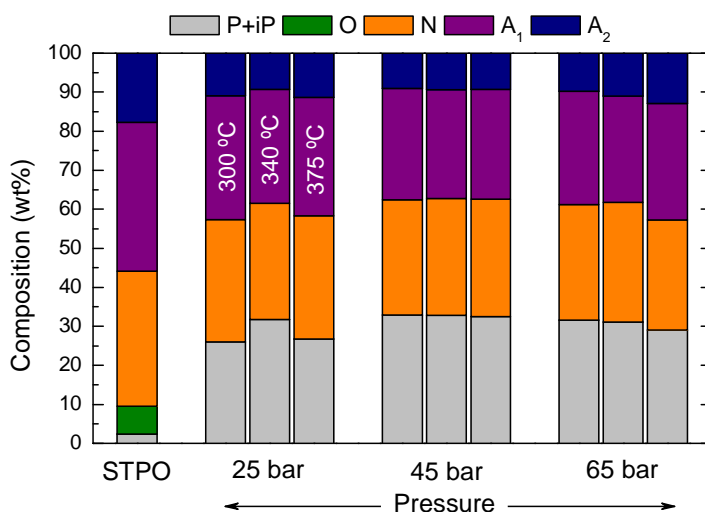


Figure 4.14. Effect of pressure on total product composition on the hydrotreating of STPO at different temperatures (space time, $0.24 \text{ g}_{\text{cat}} \text{ h g}^{-1}_{\text{feed}}$; TOS, 8 h).

4.3.2. Effect of space time

The composition of the products and its evolution with space time is shown in Figure 4.15 for the different temperatures. Paraffinic compounds, naphthenics and 1-ring aromatic structures are the main compositional fractions, followed by 2-ring aromatics.

As observed with the product lumps, significant differences are observed for space times below $0.3 \text{ g}_{\text{cat}} \text{ h g}^{-1}_{\text{feed}}$. These changes occur more rapidly at 340 and 375 °C, when the steady state is reached earlier. The main variations occur in the case of paraffinic compounds, observing an increase from 2.4 wt% in STPO to 31.7 wt%, 32.7 wt% and 32.9 wt% at 300, 340 and 375 °C, respectively, as temperature has a positive effect on cracking reactions. The rapid olefin hydrogenation has a great contribution to the increase in paraffins. Furthermore, naphthenic and aromatics hydrogenation and further ring-opening also play an important role. Taking the data at 340 °C as an example, within the $0\text{-}0.3 \text{ g}_{\text{cat}} \text{ h g}^{-1}_{\text{feed}}$ range, 1-ring aromatics decrease 11 wt%, 2- aromatics 7.4 wt%, while a smaller decrease of 4.8 wt% is observed in the case of naphthenics. According to this, together with olefins, a significant amount of aromatics are being hydrogenated and converted into saturated cycles, to follow subsequent ring opening reactions and finally crack to form paraffins.

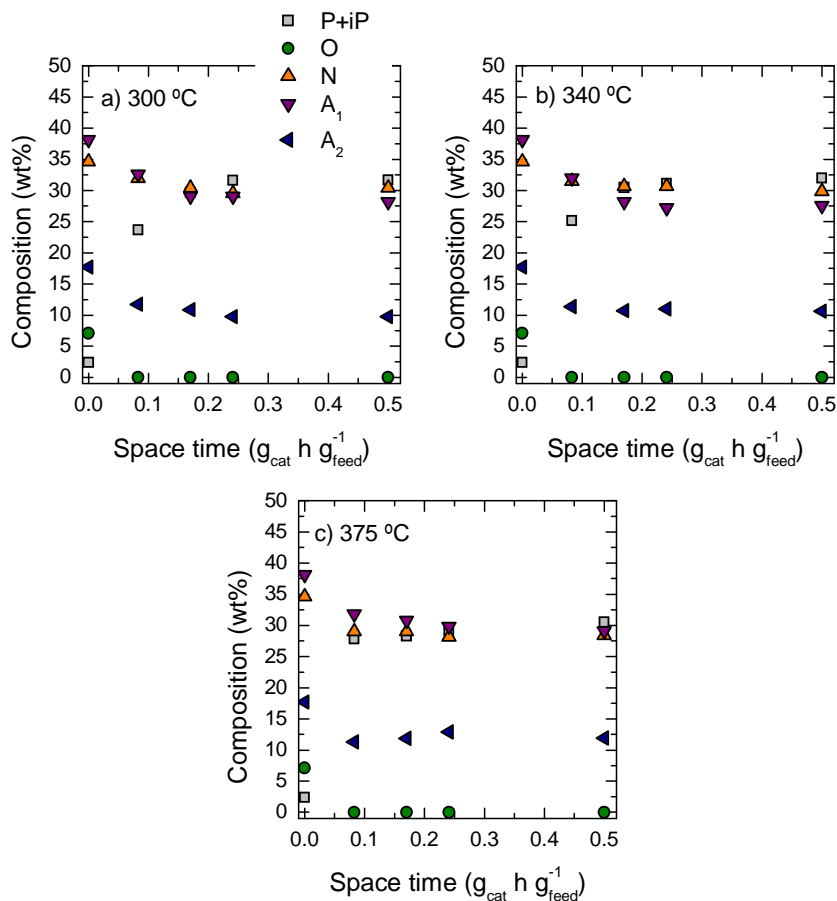


Figure 4.15. Evolution with space time of product composition on the hydrotreating of STPO at three different temperatures (65 bar; TOS, 8 h).

4.3.3. HDA kinetic modeling

Considering the evolution of the different compositional fractions with space time (Figure 4.15), the kinetic scheme in Figure 4.16 has been proposed for the HDA of STPO, based on the models previously developed by Castaño et al. for methylcyclohexane ring opening [141] and toluene hydrogenation [274], and Gutierrez et al. [275] for the hydrocracking of pyrolysis gasoline (PyGas). Paraffins and iso-paraffins are final hydrotreatment products while naphthenics and 1-ring aromatics act as reaction intermediates. Equal calculation procedure to the one previously explained in Figure 4.1 has been applied.

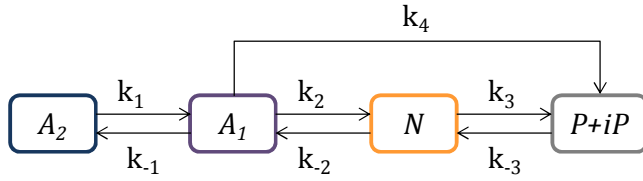


Figure 4.16. Proposed kinetic scheme for the HDA of STPO over a NiMo/ALM catalyst.

The equilibrium constants and kinetic equations of this model are the following:

$$K_1 = \frac{k_1}{k_{-1}} \quad (4.5)$$

$$K_2 = \frac{k_2}{k_{-2}} \quad (4.6)$$

$$K_3 = \frac{k_3}{k_{-3}} \quad (4.7)$$

$$\frac{dx_{A_2}}{d\tau} = -k_1 x_{A_2} x_H + k_{-1} x_{A_1} x_H \quad (4.8)$$

$$\frac{dx_{A_1}}{d\tau} = k_1 x_{A_2} x_H - k_{-1} x_{A_1} x_H - k_2 x_{A_1} x_H + k_{-2} x_N x_H - k_4 x_{A_1} x_H \quad (4.9)$$

$$\frac{dx_N}{d\tau} = k_2 x_{A_1} x_H - k_{-2} x_N x_H - k_3 x_N x_H + k_{-3} x_P x_H \quad (4.10)$$

Equilibrium constants have been defined according to the Van't Hoff equation:

$$K_i = K_{i,T_{ref}} \exp \left[\frac{\Delta H}{R} \left(\frac{1}{T_{ref}} - \frac{1}{T} \right) \right] \quad (4.11)$$

In this approach, the parameters to compute have been the kinetic constants (k_1 , k_2 , k_3 and k_4) of the A_2 and A_1 hydrogenations, ring opening and chain scission reactions, and the equilibrium constants, from where the reverse kinetic constants (k_{-1} , k_{-2} , k_{-3}) have been calculated.

Despite showing the evolution of olefins in Figure 4.15, they have not been included in the model due to their complete hydrogenation, differently to what Gutierrez et al. [275] considered. Another difference between the two

models is that, for STPO, aromatics have been differenced as 1-ring and 2-ring structures, including one more aromatic hydrogenation stage.

Table 4.3 lists the obtained kinetic parameters for the HDA model. According to the values of k_1 , k_{-1} , and k_2 , it can be deduced that hydrogenation of 2-ring aromatics represents for the most relevant reaction. In this case, hydrogenation of A_2 aromatics occurs more rapidly than its reverse reaction ($k_1 > k_{-1}$). However, in the same conditions, the reversibility of A_1 aromatics is more favored towards dehydrogenation ($k_2 < k_{-2}$). Due to the low cracking ability of the catalyst, ring opening and aliphatic chain scission reactions occur in a much lesser extent, as deduced from their corresponding low kinetic constants.

Table 4.3. Kinetic parameters for the HDA model.

Reaction	k_i	$k_{i,390\text{ }^\circ\text{C}}$ ($\text{g}_{\text{feed}} \text{g}_{\text{cat}}^{-1} \text{h}^{-1}$)	E (kJ mol^{-1})
Hydrogenation	k_1	$(3.71 \pm 0.15) \cdot 10^2$	0.61 ± 0.29
Dehydrogenation	k_{-1}	$(1.49 \pm 0.15) \cdot 10^2$	
Hydrogenation	k_2	$(1.57 \pm 0.36) \cdot 10^2$	92.01 ± 11.43
Dehydrogenation	k_{-2}	$(1.66 \pm 0.36) \cdot 10^2$	
Ring opening	k_3	$(1.71 \pm 0.11) \cdot 10^2$	22.78 ± 2.15
Cyclization	k_{-3}	16.3 ± 0.11	
Chain scission	k_4	1.71 ± 0.11	69.73 ± 2.56

The accuracy of the model prediction can be seen in Figure 4.17 and Figure 4.18, corresponding to the parity diagram and fitting of the model prediction, respectively.

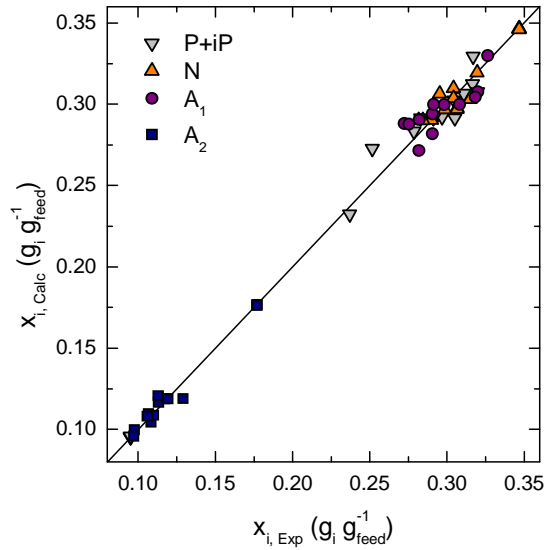


Figure 4.17. Parity diagram for the proposed HDA kinetic model.

In Figure 4.18, a clear effect of the temperature is observed, as steady state is reached more rapidly when working at higher temperatures. Additionally, temperature has an effect on final compositions. At higher temperatures, lower amount of total paraffinic compounds is obtained, together with higher total aromatics amount. The composition of naphthenics is not significantly affected. For a given space time conditions, similar trend for aromatics was reported by Tang et al. [276] on the low temperature mild hydrotreatment of a coal distillate. Several authors [277-279] have reported the effect of space time on aromatic hydrogenation kinetics, predicting higher hydrogenation rates at higher space time values, same trend to what has been observed in Figure 4.18.

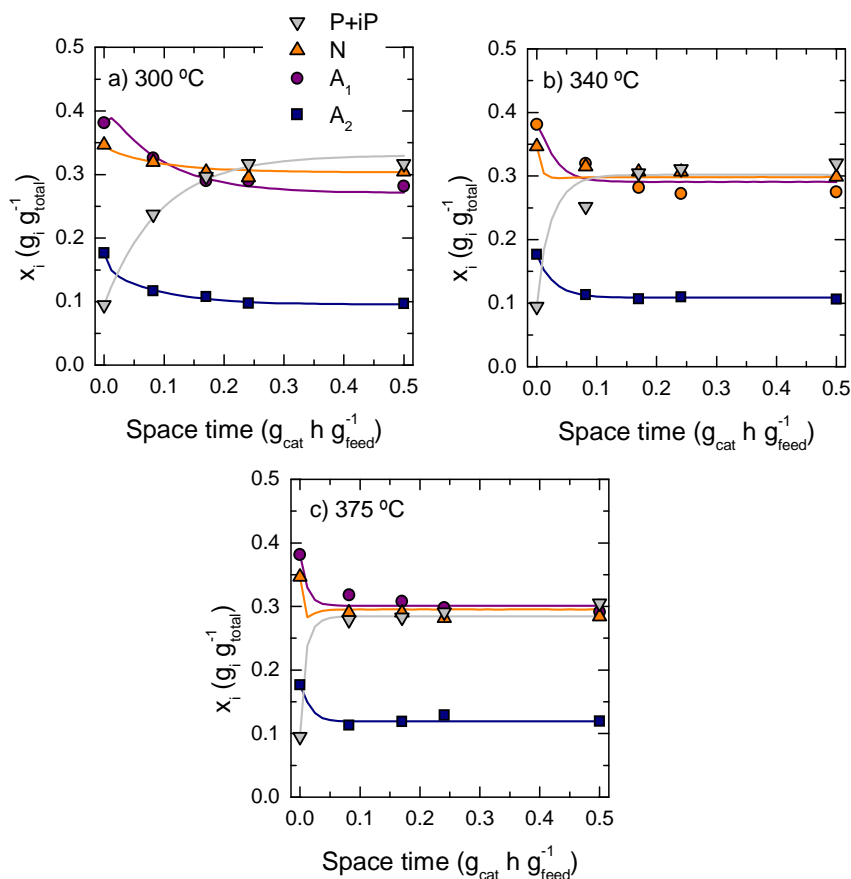


Figure 4.18. Comparison between the experimental data (dots) and predicted data (lines) for the evolution with space time of product composition on the hydrotreating of STPO (x_i) at three different temperature conditions (65 bar; TOS, 8 h).

Figure 4.19 shows the evolution of HDA (X_{HDA}) conversion with space time for experimental data (dots) and the kinetic model prediction (lines). For values higher than $0.25 \text{ g}_{\text{cat}} \text{ h g}_{\text{feed}}^{-1}$, constant conversion values are obtained at all the temperatures. Temperature has a significant effect on the space time at which steady state is reached, being faster upon increasing temperature. At $375 \text{ }^\circ\text{C}$, HDA conversion is stationary at $0.09 \text{ g}_{\text{cat}} \text{ h g}_{\text{feed}}^{-1}$ (ca. 24 %) while at $300 \text{ }^\circ\text{C}$ it is not constant until $0.5 \text{ g}_{\text{cat}} \text{ h g}_{\text{feed}}^{-1}$ (ca. 32.5 %). Additionally, considering hydrogenation of aromatics is an exothermic reaction, and therefore is favored by low temperatures [120], higher hydrogenation rates have been obtained at $300 \text{ }^\circ\text{C}$ compared to that of $375 \text{ }^\circ\text{C}$. In this regard,

thermodynamic control is governing HDA reactions over kinetic control, as low temperatures decrease the value of the kinetic constant as defined by Eq. (4.2.).

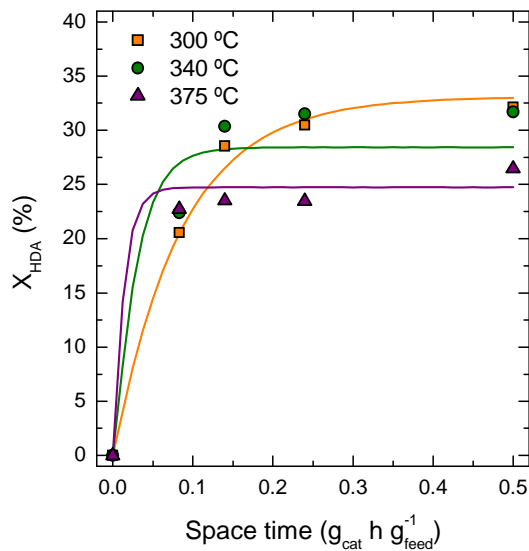


Figure 4.19. Evolution of HDA conversion on the hydrotreating of STPO as obtained from experimental data (dots) and model prediction (lines).

4.4. SIMULATION AND OPTIMAL OPERATION CONDITIONS

Using the three models proposed in this Section for (i) HDS (Section 4.1.3.), (ii) MHC (Section 4.2.3.) and (iii) HDA (Section 4.3.3.), and the corresponding parameters that have been calculated for each one, a simulation of the evolution of each conversion with temperature (300-400 °C) and space time (0-0.5 $\text{g}_{\text{cat}} \text{h g}^{-1}_{\text{feed}}$) has been carried out, as shown in Figure 4.20a-c. The different conversion levels are explained as a color gradient, from the lowest value expected (blue) to the highest one (red).

The graphics evidence the enhancing effect of space time for the three hydroprocessing goals, as it favors both sulfur and aromatics removal (Figure 4.6 and Figure 4.19), as well as the destruction of gasoil as the heaviest lump (Figure 4.12). Temperature, however, affects each reaction pathway differently. HDS is favored upon increasing temperature (Figure 4.20a), and almost total conversions can be achieved within the whole temperature range with space times higher than 0.2 $\text{g}_{\text{cat}} \text{h g}^{-1}_{\text{feed}}$. As for MHC (Figure 4.20b), kinetic control governs the reaction, with temperature having a positive effect enhancing cracking reactions, and therefore the formation of lighter product lumps with smaller molecules. From the simulation for HDA (Figure 4.20c), however, thermodynamic control is deduced, with a reverse effect of higher temperatures, as they displace the equilibrium hindering the hydrogenation of aromatic rings.

According to these results, it can be concluded that for determining the optimal conditions for HT of STPO, a compromise between HDS, MHC and HDA conversions should be established, and especially the last two, since temperature affects them in an opposite way. Within the range of conditions studied in this Thesis, temperatures between 350-360 °C and space times of 0.2-0.3 $\text{g}_{\text{cat}} \text{h g}^{-1}_{\text{feed}}$ allow for obtaining almost complete HDS conversions with good MHC (ca. 35 %) and an acceptable aromatic removal rate (ca. 30 %).

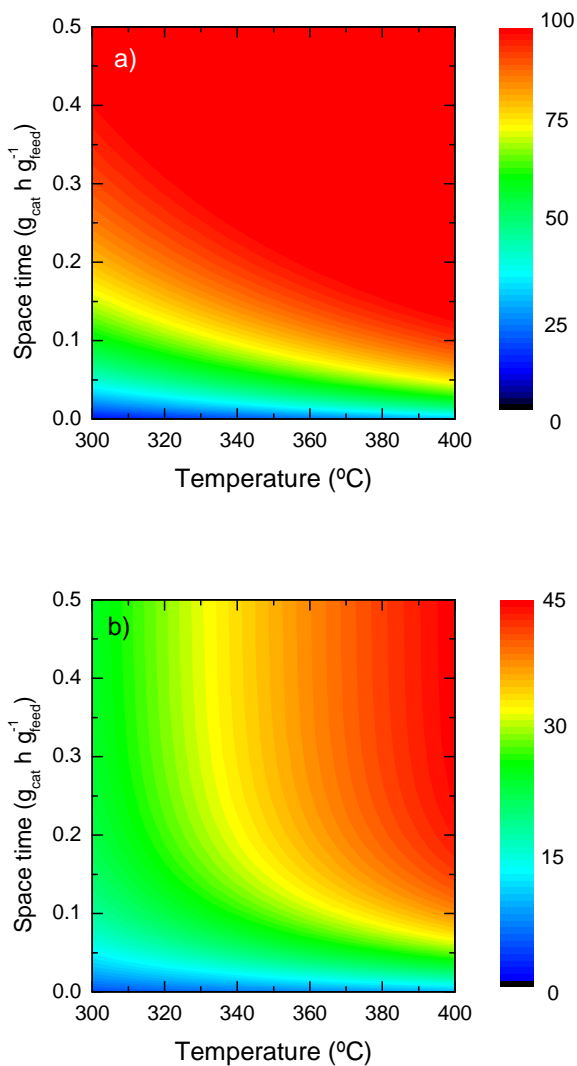


Figure 4.20. Simulation for a) HDS, b) MHC and c) HDA conversion on the hydrotreating of STPO as a function of temperature and space time.

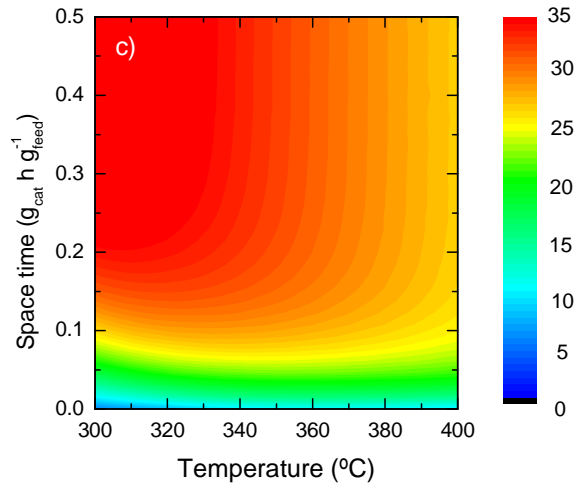


Figure 4.20. Continuation.

Section 5

UPGRADING OF HT-STPO THROUGH HYDROCRACKING ON A PtPd/SiO₂-Al₂O₃ CATALYST

5. UPGRADING OF HT-STPO THROUGH HYDROCRACKING ON A PtPd/SiO₂-Al₂O₃ CATALYST

Considering the results of the previous Sections 3 and 4, the composition of hydrotreated scrap tires pyrolysis oil (HT-STPO) using NiMo supported catalyst is not satisfactory in terms of overcoming the obstacles mentioned in the Introduction of this Thesis: the amount of sulfur (1,985 ppm), high content of aromatics (42.6 wt%), and high amount of molecules within the gasoil boiling point range (21.6 wt%). Our approach in this Thesis for solving these issues has been applying a secondary hydroprocessing stage for reducing even further sulfur, gasoil and aromatics in HT-STPO. The overall objective is not a severe HC since gases and LPGs are less economically attractive products compared to gasoline or diesel. Furthermore, in MHC conditions, catalyst deactivation is less severe [280].

Bifunctional catalysts have been widely used on the hydrocracking of heavy feedstock, with a metallic function for hydrogenation and hydrotreating reactions, and an acidic function for cracking reactions [121]. As stated in Section 1.5.2, common metallic functions are Co, Mo, Ni, W, Va, Ti and W, either combined or in their monometallic form. However, when higher activities are required, noble metals like Pt, Pd, or Pt-Pt have shown better metallic function performance. Despite being more active, noble metal supported catalysts are also prone to sulfur poisoning and therefore the feedstock requires a previous hydrotreatment stage for potential poison (S, N, metal) removal [281], stage that has been extensively detailed in Sections 3 and 4 of this Thesis. However, it has also been reported that the addition of an acidic function can help stabilize the metallic function to partially avoid poisoning and allow for working in high sulfur content conditions [282, 283].

The acidic support enhances cracking reactions in such a way that, the higher the total acidity of the support, the lighter the products obtained. Zeolites provide high total acidity as well as strong acidic sites, but their microporous structure hinders the diffusion of heavy hydrocarbon molecules inside the pores. For avoiding diffusional issues, meso- and macroporous supports appear as an alternative, as are novel mesoporous materials like MCM-41 [284, 285], MCM-48 [286] or SBA-15 [287, 288], the more common Al₂O₃ [289, 290] and SiO₂-Al₂O₃ [291], or either combinations of micro- and mesoporous functions [249, 292]. The importance of the catalyst acidity (especially Brønsted acidic sites) in hydrocracking reactions has been previously reported [123, 293], and therefore, in order to achieve higher HC conversions, it is preferable to use supports with this type of acidic sites (like SiO₂-Al₂O₃), or opt for other acidity-enhancing methods for mesoporous materials [294, 295].

Taking all the previous into account, in this Section a PtPd/SiO₂-Al₂O₃ has been used to study the effect of different process variables on the HC, aiming to obtain a fuel with suitable features for being used as automotive fuel for internal combustion engines [10, 296]. Additionally, catalyst deactivation has been studied both quantitatively and qualitatively based on the previous experience of the Group [125, 126, 219], since it greatly conditions the viability of hydroprocessing [297, 298].

PtPd/SiO₂-Al₂O₃ catalysts have been previously considered as a promising option for a second-stage hydrotreating process, as studied by Reinhoudt and co-workers [242, 299], with either model feeds or real refinery feeds, as diesel, even though much less information on real feeds is available. When working with model compounds as 4,6-DMDBT, Castillo-Araiza et al. [300] observed that each metal was capable of enhancing a specific desulfurization route, either direct or indirect (with a previous hydrogenation step), and that Pt-Pd catalyst were more active towards HDS than the monometallic counterparts. Vít et al. [301] reported the high sensitivity of the characteristics and activity of this type of PtPd/SiO₂-Al₂O₃ catalysts depending on the catalyst precursor. Pt can also act as a HDS promoter of other noble metal catalysts, by acting as hydrogen supplier [302]. Even though it is not their most common application, noble metal catalysts can also provide good HDS performances in their phosphide forms [303].

5.1. REACTION CONDITIONS

The three main reaction pathways involved in the catalytic transformation of HT-STPO have been studied separately: HDS, HC and HDA, in Sections 5.2, 5.3 and 5.4, respectively. The experimental conditions of the HC runs over the PtPd/SiO₂-Al₂O₃ catalyst have been:

- Time on stream (TOS) = 0-6 h
- Space time (τ): 0-0.28 g_{cat} h g⁻¹_{feed}
- Temperature: 440-500 °C
- Pressure: 65 bar
- H₂/feed volumetric ratio: 1000 N cm³/cm³

Product lumps and composition fractions have been defined as specified in Section 2.2.2.2, while reaction parameters have been those of Section 2.2.2.4.

5.1.1. Properties of the hydrotreated STPO (HT-STPO)

All the liquid products obtained from the HT of STPO using different NiMo supported catalysts and reaction conditions (Sections 3 and 4) have been mixed to conform the new feed for the HC reactions (Sections 5 and 6), and will be referred to as HT-STPO. It is important to mention that, in the first stage, STPO was diluted in *n*-C₁₀ (50 N m³/m³) before entering the reactor and the products had almost identical dilution due to the little cracking activity of the NiMo catalysts. In this Section, cracking has been more significant and *n*-C₁₀ has been partially converted to lighter products (mainly paraffins) that appear in the naphtha lump. However, considering that the contribution of the dissolvent to the naphtha lump and paraffinic fraction is small compared to the converted hydrocarbons originally in STPO, all products have been treated together.

The properties of STPO and HT-STPO have been listed in Section 2.1.3 regarding their elemental composition, compositional fractions, simulated distillation curves, and sulfur speciation. Figure 5.1 focuses on the comparison of the two feeds from the perspectives of the main STPO upgrading goals, as are: HDS (remarkable sulfur removal), MHC (higher yields of lighter product lumps), and HDA (improved compositional properties due to the removal of aromatics).

The HC activity of the NiMo catalyst has also allowed for redistributing the product lumps in STPO obtaining a higher amount of naphtha (25.7 wt% in STPO to 27.9 wt% in HT-STPO) and diesel lumps (44.5 wt% to 50.3 wt%) (Figure 5.1a). As for product composition (Figure 5.1b), significant changes are observed, as the concentration of paraffins and iso-paraffins (P+iP) has increased dramatically (2.4 wt% to 35.4 wt%) due to complete olefin hydrogenation, and aromatic ring hydrogenation and further opening, as discussed in Section 3.3. Due to these reasons, total aromatic concentration has been reduced from 55.8 wt% in STPO to 42.6 wt% in HT-STPO. Concerning sulfur concentration (Figure 5.1c), HT-STPO shows significantly lower amounts of all species, with total BTZ removal. Total sulfur has decreased from 11,600 ppm in STPO to 1,985 ppm in HT-STPO, maintaining similar proportions of the DBT species, with the trend: $M_3\text{DBT} > M_4\text{DBT} > M_2\text{DBT} > M_1\text{DBT}$. The reactivity of these species and the relevance of their number of C atoms in their substituents number and position have already been discussed in Sections 3 and 4. However, due to the interest as fuels of STPO and HT-STPO, further hydrogenation and hydrocracking is desired for enhancing their yield.

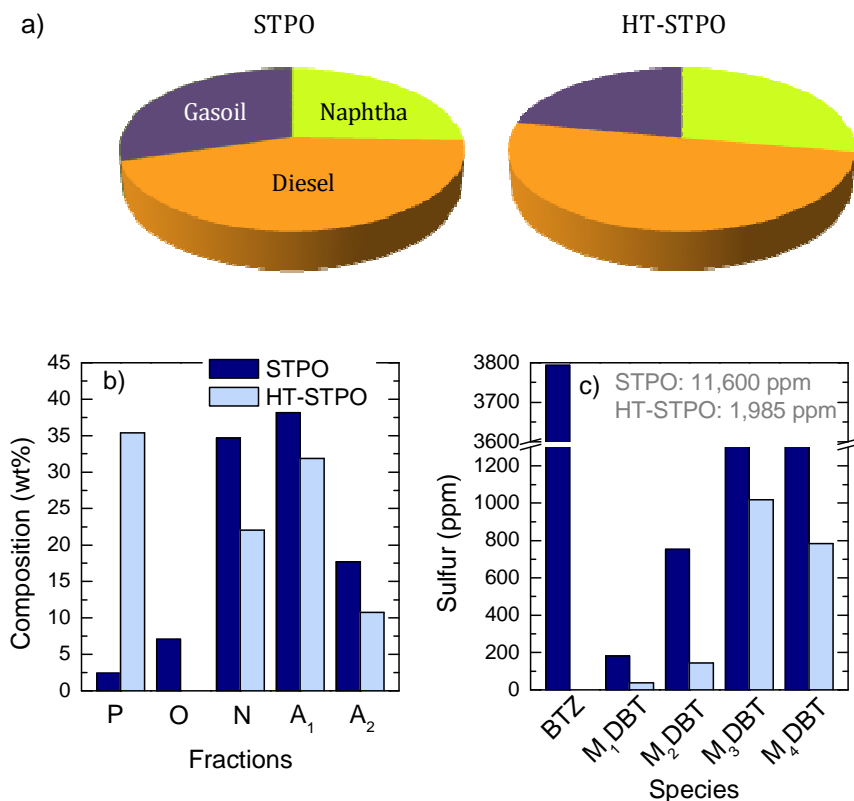


Figure 5.1. Comparison between a) lump yields, b) compositional fractions and c) sulfur species distribution of STPO and HT-STPO.

5.1.2. Properties of the fresh catalyst

The PtPd/SiO₂-Al₂O₃ catalyst has been prepared as specified in Section 2.3.2. The main properties of the fresh catalyst are listed in Table 5.1. Metal content has been determined by ICP-AES, the properties of the porous structure by N₂ adsorption-desorption isotherms, and total acidity has been measured by TPD of t-BA adsorbed at 100 °C, all of which are techniques detailed in Section 2.4. The value of specific surface of this catalyst is comparable to that of the NiMo/MCM catalyst (the one with the best HDA performance) used in Section 3, also with a very similar value of average pore diameter (55.6 Å). Additionally, it shows a higher total pore volume. Total acidity is comparatively lower to that of NiMo catalysts. However, the maximum of the t-BA TPD for the PtPd/SiO₂-Al₂O₃ catalyst (not shown) appears at 250 °C, a much lower value than that of the NiMo catalysts (293-326 °C) which means that, despite having lower total acidity, the acidic sites show a stronger nature and therefore a higher cracking performance is expected [304].

Table 5.1. Properties of the fresh catalyst.

Property	Value
Pt (wt%)	0.76
Pd (wt%)	0.48
<hr style="border-top: 1px dashed black;"/>	
S _{BET} (m ² g _{cat} ⁻¹)	468
Pore volume (cm ³ g ⁻¹)	0.683
V _{P/P0=0.2} ^{Ads} (cm ³ g ⁻¹)	135.7
V _{P/P0=0.5} ^{Ads} (cm ³ g ⁻¹)	216.8
V _{P/P0=0.5} ^{Des} (cm ³ g ⁻¹)	232.0
Average pore diameter (Å)	55.6
<hr style="border-top: 1px dashed black;"/>	
Total acidity (mmol _{t-BA} g ⁻¹)	0.288

5.2. HYDRODESULFURIZATION

The evolution of the total sulfur content with time on stream (TOS) is displayed in Figure 5.2 for different temperatures (440-480-500 °C), together with the corresponding HDS conversions. As observed, both TOS and temperature significantly affect sulfur removal. For TOS = 0-1 h, ULSD levels (< 15 ppm) are achieved, especially at high temperatures (480-500 °C), with HDS conversions higher than 99 %. For higher TOS values, deactivation of the metallic phase becomes relevant and HDS performance drops. The sulfur concentration in the products can be lowered below 100 ppm working at 480-500 °C with conversions above 95 %. However, at 440 °C, sulfur removal is less favored (3 times more sulfur is measured).

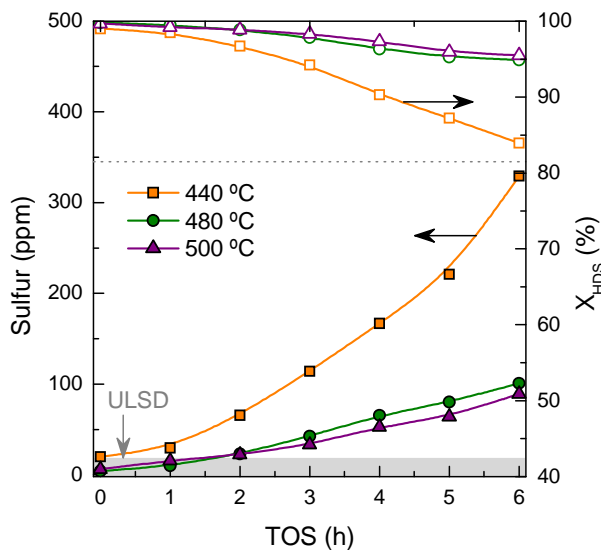


Figure 5.2. Evolution with TOS of the sulfur amount and HDS conversion at different temperatures.

Temperature effect on sulfur speciation at 0 h and 6 h is shown in Figure 5.3. At TOS = 0 h, the sulfur removal is almost complete, with residual amounts of sulfur, especially at 480 and 500 °C. In these conditions (fresh catalyst), M₂DBT species is the most abundant, despite not being the least reactive. However, at steady state conditions, M₃DBT species appears again as the most difficult one to eliminate.

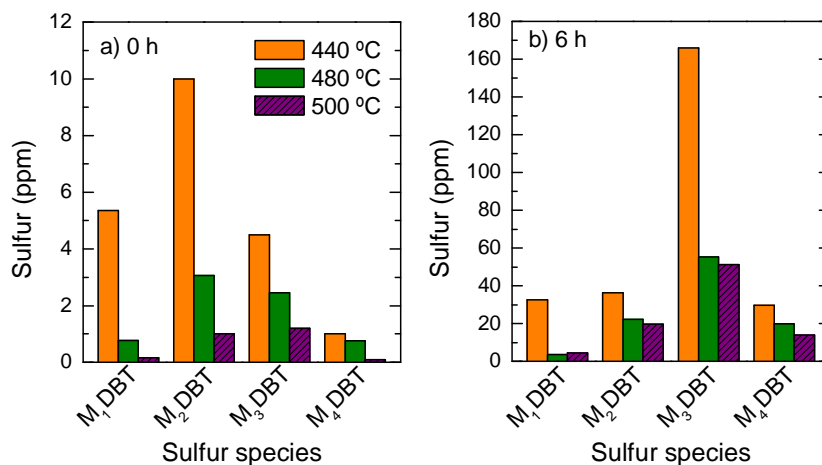


Figure 5.3. Effect of temperature on sulfur speciation in HT-STPO hydrocracking products at TOS a) 0 h and b) 6 h.

5.3. HYDROCRACKING

PtPd catalysts have been widely used for the hydrocracking of refinery streams like LCO [283], gas oils [305, 306], FCC gasoline [307] or heavy oils [308]. $\text{SiO}_2\text{-Al}_2\text{O}_3$ supports have proven to be suitable in moderate HC conditions (when hydrogenation is the main goal), as reported by Kishore-Kumar et al. [279] but, generally, the heavy nature of refinery feedstock (and when severe HC is aimed) requires for using more acidic supports like zeolites. Gutiérrez et al. [283] studied the hydrocracking of LCO using PtPd supported zeolite catalysts demonstrating that the pore topology of the zeolite ($\text{H}\beta$ or HY) could direct the process towards obtaining either naphtha or diesel selectively. Additionally, they concluded that a preliminary hydrotreating stage was necessary in order to avoid a significant initial catalyst deactivation due to sulfur poisoning. Lee et al. [309] reported that including Mg as additive in the catalyst could improve the resistance of this type of catalysts towards sulfur and nitrogen in the dewaxing of a light gas oil.

5.3.1. Time on stream

The evolution of product lumps with TOS is shown in Figure 5.4, at 440 °C and a space time of $0.16 \text{ g}_{\text{cat}} \text{ h g}^{-1}_{\text{feed}}$. These results are plotted together with dashed lines representing the initial amounts of every lump in HT-STPO (those of Figure 5.1a). The LPG lump has now been considered as, for the conditions and catalyst used, the formation of gases as products is significant. During the initial TOS = 0-4 h, the yield of naphtha is the highest (15-40 wt%), followed by diesel (ca. 20 wt%) and gasoil (ca. 3 wt%). The HC performance of the catalyst suffers significant decay and due to that the yield of final products decreases (LPG and naphtha), with a parallel increase of the yield of reactants and intermediates (diesel and gasoil). The steady state is reached after 5 h, similar time to that reported by Gutierrez et al. [277] on the hydroprocessing of light cycle oil (LCO) on a Pd-promoted Pt catalyst supported on a HY zeolite.

Despite the mentioned deactivation, the steady values of the fractions involve higher amount of naphtha and lesser amount of gasoil, compared to the original lumps in HT-STPO (dashed lines). In these conditions, approximately 50 wt% of the $n\text{-C}_{10}$ on the HT-STPO cracks to yield mainly paraffins that are contained in the naphtha lump. As mentioned at the beginning of this Section, the contribution of solvent cracking to the increase in naphtha yield is very small compared to that of heavier hydrocarbons contained in diesel and gasoil (less than 8 wt% of the total increase), and its evolution has not been displayed in the graphs.

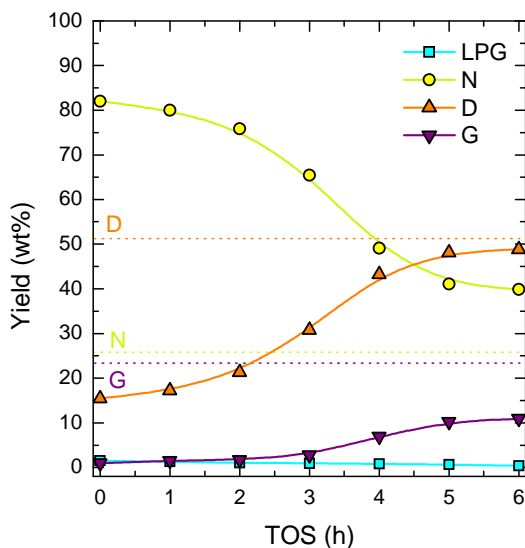


Figure 5.4. Evolution with time on stream of product lump yields in HT-STPO hydrocracking products (space time, $0.16 \text{ g}_{\text{cat}} \text{ h g}_{\text{feed}}^{-1}$; 65 bar; $440 \text{ }^{\circ}\text{C}$).

The result of HDS performance of the PtPd/SiO₂-Al₂O₃ catalyst pointed the deactivation of the metallic function participating in the hydrogenolysis reactions (Figure 5.2). The results of HC performance of the same catalyst show analogous deactivation, indicating that the acidic function is possibly suffering the deactivation (Figure 5.4). Similarly to HDS performance and after 5 h on stream, the catalyst reaches a HC steady state. It is also worth mentioning that with increasing TOS, the color of the products varies, from light yellow during the first hours of reaction to darker brownish tonalities as steady state is reached.

Considering that HT-STPO has been previously hydrotreated, and remaining sulfur is low to affect activity in such great extent, it can be considered that catalytic deactivation occurs mainly due to coke formation, fact that will be studied in upcoming Sections. In order to study deactivation phenomena, both data at 0 h and steady state are valuable. The former gives information of the maximum yields expected if deactivation not occurred, while the latter provides information about the deactivation magnitude. The study of the data collected in the deactivation period is also relevant in order to analyze the different deactivation pathways, and therefore determinate the correct approach to minimize activity loss.

5.3.2. Temperature

HC is not limited by reversible exothermic reactions as it happened for HT (Figure 4.20c), so conversion [121] and selectivity of lighter products [310] increase with temperature. Furthermore, higher temperature also favors faster deactivation rate [311]. The effect of temperature (440-500 °C) on product lumps at TOS = 0 h and 6 h is shown in Figure 5.5. At TOS = 0 h (Figure 5.5a) naphtha yield is higher than 82 wt%. This result is due to cracking of diesel (its yield decreases from 50.3 wt% in the feed to ca. 10 wt% in the products) and gasoil (21.9 wt% in the feed to almost total removal of 1-2 wt%). LPG appears in ca. 3 wt%, and almost all the gasoil fraction is converted. At TOS = 6 h (Figure 5.5b), the yields keep their trends; increasing those of LPG and naphtha and decreasing the yields of diesel and gasoil at higher temperatures. In this case, diesel is the most abundant fraction at 440 °C (48.9 wt%), followed by naphtha (39.9 wt%) and gasoil (10.9 wt%), while at higher temperatures naphtha yield becomes more abundant (59.2 and 69.3 wt% at 480 and 500 °C, respectively). When steady state is reached, a noticeable amount of gasoil is not converted (10.9 wt% of remaining gasoil at 440 °C).

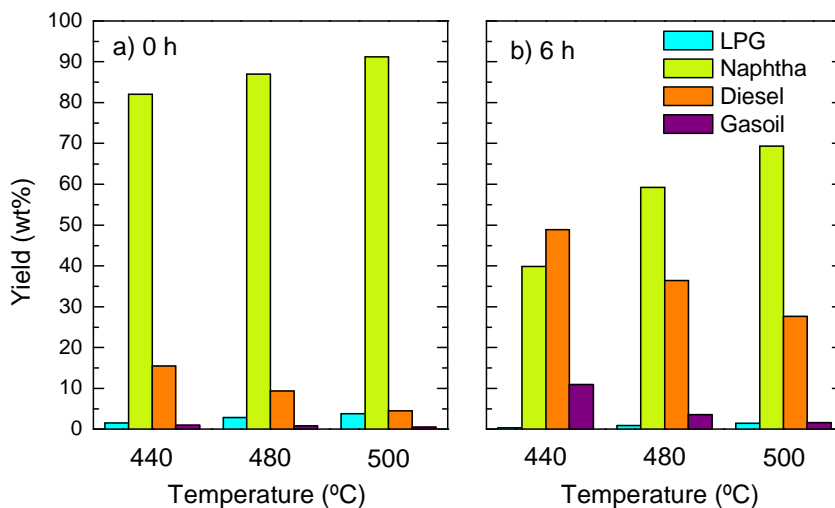


Figure 5.5. Effect of temperature on lump yields in HT-STPO hydrocracking products at TOS a) 0 h and b) 6 h. (65 bar; space time, $0.16 \text{ g}_{\text{cat}} \text{ h g}_{\text{feed}}^{-1}$).

Several authors [269, 312] have proposed that the HC kinetic scheme is a parallel-consecutive set of reactions in which the heaviest fractions (gasoil in our case) converts into lighter fractions (diesel) which, in a consecutive stage, are transformed into even lighter products and/or gases. Reaction temperature can drive the reaction towards the preferential formation of one product lump or another, as seen in Figure 5.5b. This same effect has already been reported in literature [313]. Additionally, the naphtha:diesel ratio can be tuned with both strength and concentration of the acidic sites of the PtPd/SiO₂-Al₂O₃ catalyst [147, 314].

The simulated distillation curves of the feed (HT-STPO) and the HC liquid products obtained at different temperatures and TOS = 6 h are shown in Figure 5.6. These results confirm the previous ones regarding the distribution of the three main product lumps (Figure 5.5b); naphtha, diesel and gasoil. Note that LPG has not been included in this analysis, so the results correspond to the liquid fraction as a whole. It can be seen that, upon increasing temperature, higher proportions of lighter compounds with their boiling point in the naphtha and diesel ranges are obtained, achieving almost complete elimination of the gasoil lump.

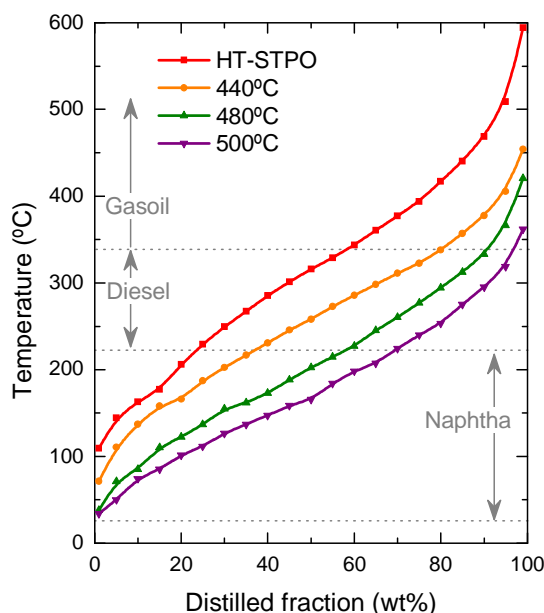


Figure 5.6. Simulated distillation of the HT-STPO hydrocracking products at different temperature conditions (65 bar; TOS, 6 h; space time, 0.16 g_{cat} h g⁻¹_{feed}).

5.4. HYDRODEAROMATIZATION

5.4.1. Time on stream

Time on stream has a significant effect on total product composition, as shown in Figure 5.7. Paraffins and isoparaffins (P+iP) account for the most abundant fraction during the first 4 h. However, their concentration decreases from 68.1 to 46.1 wt%, reaching a steady state at TOS = 5 h. This decrease in paraffinic compounds occurs due to the deactivation of both the hydrogenating and cracking functions, implying also an increase in naphthenics (N) (ca. 4 wt%) but mainly in unsaturated compounds, with 18 wt% more of total aromatics (A_1 and A_2), and accounting for ca. 35 wt% of the total.

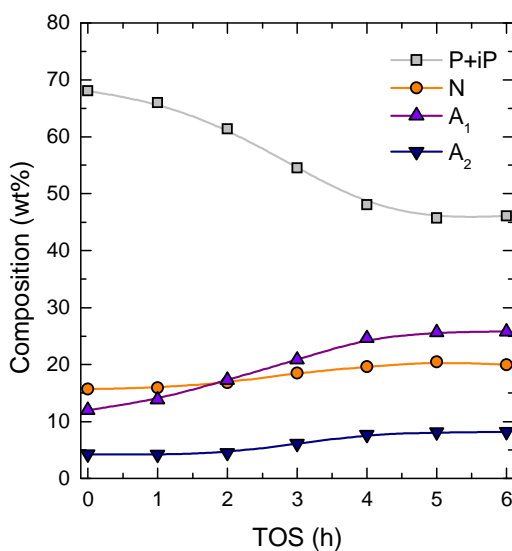


Figure 5.7. Evolution with time on stream of HT-STPO hydrocracking product composition (space time, $0.16 \text{ g}_{\text{cat}} \text{ h g}_{\text{feed}}^{-1}$; 65 bar; $440 \text{ }^\circ\text{C}$).

5.4.2. Temperature

Figure 5.8 shows the total composition of the products at the three temperatures in fresh catalyst (TOS = 0 h) and steady state (TOS = 6 h) conditions. At TOS = 0 h (Figure 5.8a) when cracking reactions occur in a great extent, a remarkable amount of paraffinic compounds are measured increasing

with reaction temperature (66.7-75.7 wt%), and maintaining the same trend after deactivation has taken place. 1-ring aromatics and naphthenics decrease in amount as temperature rises (12.5-9.1 wt% and 16.6-11.6 wt%, respectively), while 2-ring aromatics do not vary much (ca. 4 wt%). The same shape trends are maintained when steady state is reached at TOS = 6 h (Figure 5.8b) for all composition fractions. However, the hydrogenating and cracking functions of the catalyst have been greatly deactivated and paraffins appear in a lower amount (38.7-52.3 wt%), as naphthenics (23.5-16.6 wt%) and total aromatics (37.7-31.0 wt%) are more abundant.

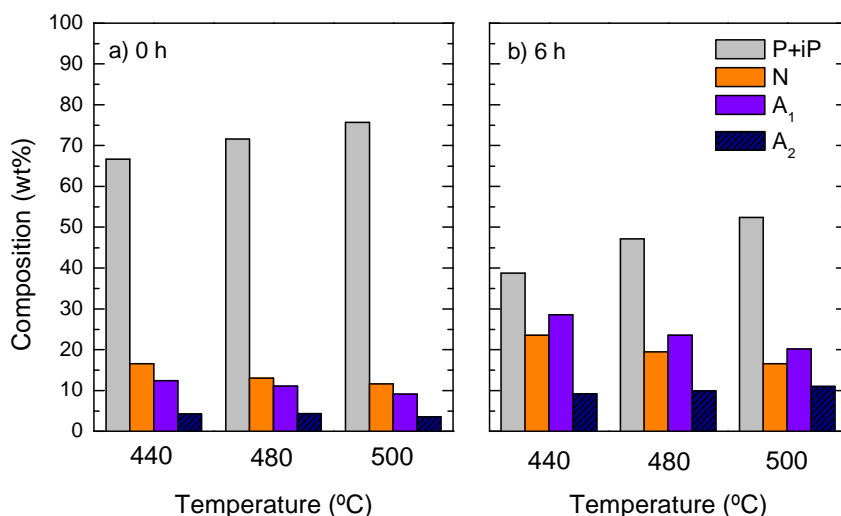


Figure 5.8. Effect of temperature on HT-STPO hydrocracking product composition at TOS a) 0 h and b) 6 h (65 bar; space time, $0.16 \text{ g}_{\text{cat}} \text{ h g}^{-1}_{\text{feed}}$).

Gutiérrez et al. [146, 283] reported a very similar effect of temperature on product composition on the HC of LCO, as higher temperatures enhanced the decrease in the concentration of aromatics, in favor of saturated compounds as naphthenes and paraffins. Calemma et al. [315] also observed lighter compound formation at higher conversion levels on the HC of Fischer-Tropsch (FT) aiming for the production of middle distillates.

5.5. CATALYST DEACTIVATION

In this Section dealing with the HC of HT-STPO, we have observed higher deactivation rates compared to those of HT. As stated in Section 4.2.3, after performing temperature ramps (375-340-300-375 °C), NiMo catalysts recovered their initial activity, so no deactivation was considered. However, the higher cracking activity of PtPd/SiO₂-Al₂O₃ has led to higher deactivation. Several causes can be drawn as the origin of the deactivation [316]: sintering, poisoning and coke fouling.

As reported in literature, PtPd catalysts have proven to be comparatively more active in HT than sulfided NiMo catalysts, but also more prone to H₂S poisoning [317]. At the same time, PtPd catalysts are more suitable for enhancing resistance towards H₂S poisoning than the monometallic counterparts [125]. Yoshimura et al. [281] proved that the affinity of Pt towards H₂S is higher than that of Pd, and the PtPd alloy has an adsorption constant (K_p) lower than that of Pt, which decreases when decreasing Pt/Pd ratio.

We can eliminate sintering as a deactivation cause due to the stability of Pt and Pd sites [125]. Poisoning can occur due to the presence of impurities on the feed or the reaction products. Dealing with STPO and elevated HDS rates, H₂S and NH₃ appear as the main hazards as catalyst poisons, as the former can damage metallic sites and the latter the acidic ones. The main N source in STPO was BTZ, which has been completely removed in the first HT stage, and sulfur can also be considered a minor deactivation cause in our case, since the greatest amount of sulfur has been removed in the first hydrotreating stage. Coke fouling, as a great issue in HC processes [318, 319] that strongly conditions process viability has therefore been considered as the main deactivation cause and is the focus of the deactivation study.

In a previous work [265], we observed the critical effect of temperature on coke formation due to the fact that in some conditions the deactivation by coke is reversible, and in some hydrocracking conditions, coke precursors can also interact with the metallic and acidic phases of the catalyst and crack themselves. This way, deactivation can be partially avoided, reaching a steady coke content that depends mainly on hydrocracking temperature [125].

Furthermore, coke deposition is affected by different properties of the support, as its porous structure and acidic nature (total acidity and strength of the acid sites), as well as metal content and dispersion. Adding Pd in Pt catalyst has proven to improve catalyst stability [281, 320] and, additionally, this modification has also been reported as beneficial regarding coke deposition, as it is lower [282, 317]. This can be explained by the synergic hydrogenation-

hydrocracking effects that occur when using both metals, and help attenuate coke formation.

5.5.1. HDS, HC and HDA behavior

The loss of activity of both the hydrogenating and cracking functions has been evidenced in the results shown in Figures 5.2, 5.4 and 5.7, for HDS, HC and HDA conversions, respectively. Figure 5.9 shows the evolution with TOS of the three conversions as a function of temperature. As observed, temperature favors for obtaining higher conversion values for the three transformations, as they are all governed by kinetic control (higher temperatures imply higher values of the kinetic constant). Please notice that, in Section 4, HDA of STPO over a NiMo/Al₂O₃ catalyst was controlled by thermodynamics.

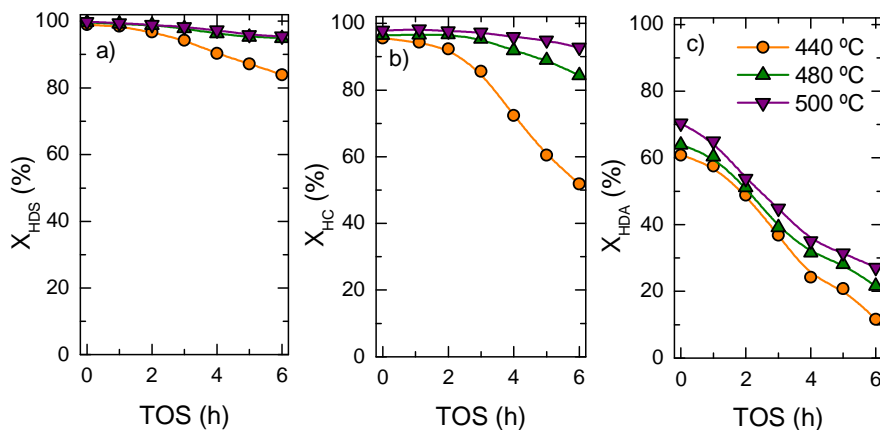


Figure 5.9. Evolution with TOS of the a) HDS, b) HC and c) HDA conversions at different temperature conditions.

5.5.2. Deterioration of the catalyst properties

The properties of the fresh PtPd/SiO₂-Al₂O₃ catalyst were listed in Table 5.1 of Section 5.1.2. The N₂ adsorption-desorption isotherms for the catalysts deactivated at different temperatures, together with their t-BA TPD curves are shown in Figure 5.10. It is worth mentioning that, prior to N₂ adsorption, the deactivated samples expel liquid hydrocarbons during the pretreatment process in vacuum conditions. This is an indication that a portion of external coke (which can be desorbed at high temperature vacuum

conditions) is contained within the porous structure partially blocking the pores, fact that might be masking the results of this analysis.

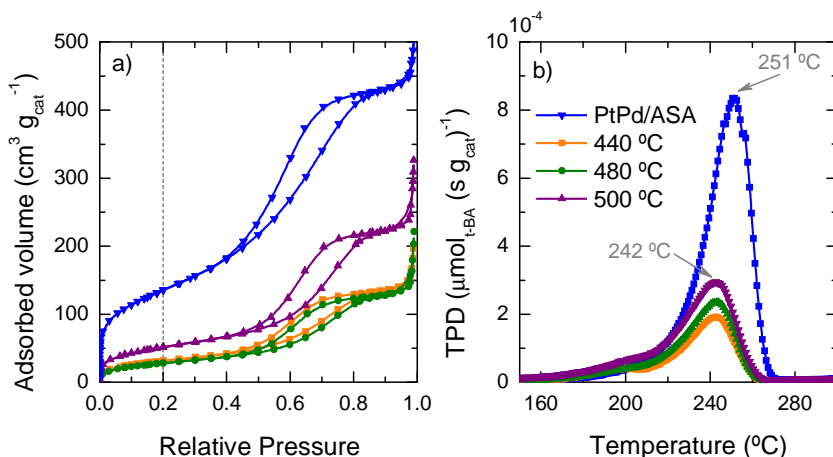


Figure 5.10. a) N₂ adsorption-desorption isotherms and b) t-BA TPD curves for the fresh and spent catalysts at different HC temperatures.

Table 5.2 lists the physical and acidic properties of the spent catalysts together with their corresponding coke contents. In all cases the catalysts have shown an important decrease in both specific surface (S_{BET}) (62-79 %) and pore volume (V_p) (30-58 %). This fact evidences that the location of coke is mostly blocking meso- and macropores [128]. The loss of specific surface and pore volume has been the lowest for the catalyst used at 500 °C. This might be because, at higher temperatures, cracking reactions are enhanced and therefore part of the condensed aromatics forming coke are cracked, partially avoiding pore blockage due to highly condensed aromatics. From these results, the hypothesis of the existence of a coke content steady state in this type of HC processes is reinforced [265].

Figure 5.10a shows that all the isotherms are type IV and with H1-type hysteresis, maintaining the same shape than that observed for the fresh catalyst. However, at low relative pressures, coke is blocking the adsorption of N₂ causing a decrease in the hysteresis phenomena (difference between the adsorption and desorption branches). In any case, for higher relative pressure values an important decrease in the N₂ adsorbed volume has also been observed.

As for total acidity of the spent catalysts (Figure 5.10b), there is a tendency with reaction temperature in such a way that, at higher temperatures, more residual acidity remains, as also pointed in Table 5.2. At 440 °C, the drop of the acidity is 73.7 %, decreasing down to 64.7 wt% and

45.6 wt% at 480 and 500 °C, respectively. This trend of residual acidity correlates with the activities displayed in Figure 5.9 in terms of conversion for HDS, HC and HDA.

Table 5.2. Physical and acidic properties of the spent catalyst, coke content and coke composition parameters.

Temperature	440 °C	480 °C	500 °C
Spent catalyst properties			
S_{BET} (m ² g ⁻¹)	110.4	99.3	179.1
ΔS_{BET} (%)	76.4	78.8	61.7
V_p (cm ³ g ⁻¹)	0.288	0.328	0.476
ΔV_p (%)	57.8	52.0	30.3
D_p (Å)	81.9	105.3	82.3
Acidity (mmol _{t-BA} g ⁻¹)	0.076	0.102	0.157
Δ acidity (%)	73.7	64.7	45.6
Coke content and composition			
Coke (wt%)	19.49	19.56	19.72
<i>G</i> band fraction	0.34	0.36	0.37
<i>G</i> band position (cm ⁻¹)	1591	1594	1598
<i>G</i> band width (cm ⁻¹)	52	43	43
<i>D</i> band fraction	0.48	0.41	0.41
<i>D/G</i> ratio	1.43	1.15	1.10

Considering that t-BA desorbed from the strongest acidic sites cracks at lower temperatures [304], it is remarkable that the deactivated samples show stronger but less numerous in total acidic sites compared with the fresh catalyst (Figure 5.10b). On the other hand, deactivated samples show a desorption maximum at 242 °C, whereas for the fresh catalyst is 251 °C. These results of N₂ adsorption isotherms (Figure 5.10a) and t-BA TPD (Figure 5.10b) point that the deposition of coke is homogeneous and non-selective, particularly at 440 °C where the values of ΔS_{BET} and Δ acidity are practically the same. The acidic sites cracking t-BA at 251 °C deactivate faster due to the fact that there are more numerous. The remaining acidic sites are therefore responsible for the steady state activity [277].

5.5.3. Coke deposition

Table 5.2 also summarizes the coke content of the deactivated catalysts measured by TG-TPO, with a previous N₂ stripping. This stripping is necessary to remove all the compounds adsorbed in the samples that might interfere in the analysis, and also to eliminate compounds that are actually part of the coke but most probably do not contribute to catalyst deactivation, as they are not strongly adsorbed and condensed on the catalyst surface.

It should be noted that coke contents correspond to the area under the TPO curves (Figure 5.11). Furthermore, TPO curves generally give an idea of the heterogeneity and condensation level of the coke [130], in such a way that, the higher the combustion temperature, the higher the coke condensation level and the lower the H/C ratio. Also, the wider the TPO peak, the higher the heterogeneity of the coke composition [125]. From the different types of coke that have been identified in bifunctional hydroprocessing catalysts [316, 321, 322], our results point out the existence of a single type of heavily condensed aromatic coke that is mainly located on the catalytic support, and whose combustion is not catalyzed by metallic sites.

The amount of coke deposited on the catalyst is practically the same independently of the temperature used in the hydrocracking. Interestingly, the temperature of maximum combustion TPO peak shifts from 545 °C up to 550 °C when increasing the temperature of the reaction. These results indicate that, at higher HC temperatures, coke shows a more condensed and aromatic nature, which makes its structure more difficult to burn [125, 323].

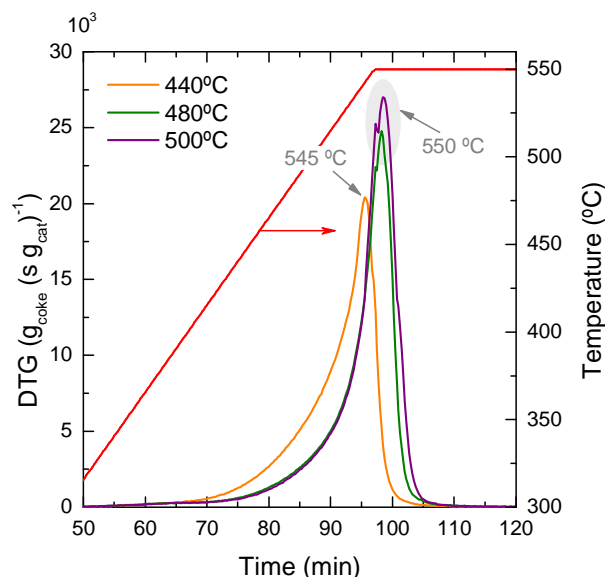


Figure 5.11. TPO curves of the spent catalyst at different temperatures.

5.5.4. Composition and nature of coke

5.5.4.1. Raman spectroscopy

The normalized Raman spectra of the deactivated catalysts at different HC temperatures within the 1000-2000 cm^{-1} region are shown in Figure 5.12. Analysis were carried out as detailed in Section 2.6.3, and the spectra have been deconvoluted in the following Lorentzian peaks [324]: 1250 cm^{-1} or $\nu_{\text{C-H}}$ band, corresponds to C-H vibrations; 1350 cm^{-1} or D band, attributed to disordered aromatic structures; 1508 cm^{-1} or D_3 band, a echo of the D band; and 1600 cm^{-1} or G band, assigned to ordered graphitic structures. These values are approximate due to the fact that position also is influenced by the intrinsic composition of the coke as explained later. Table 5.2 shows the intensities of the bands and the ratios of the D/G band intensities (characteristic of the development of carbonaceous solids). As observed, the proportion of the G band increases and the D band decreases with reaction temperature, which might indicate that the proportion of developed coke is related to the total amount of coke on the catalyst (Table 5.2). As a consequence, the D/G ratio becomes lower upon increasing temperature. These observations point to the higher aggregation of aromatic clusters in coke [325] deposited at 500 $^{\circ}\text{C}$, with particles bigger than 2 nm for this particular

case [326]. This higher level of coke condensation correlates with the increase in the combustion temperature observed in Figure 5.11.

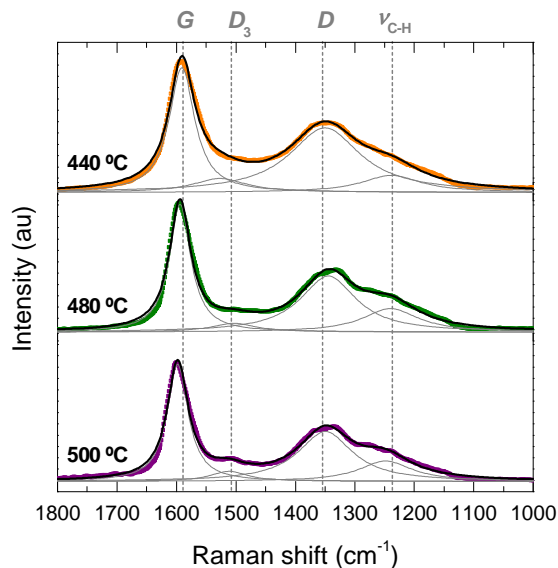


Figure 5.12. Raman spectra of the spent catalyst at different temperatures.

5.5.4.2. FTIR spectroscopy

Figure 5.13 shows the normalized intensities of the FTIR bands corresponding to the molecular bond vibrations of the coke deposited on the catalyst, identifying each band with a different bond of coke [327-329]: (i) 1580 cm^{-1} , polycondensed aromatic compounds (PAC) also referred to as “coke band”; (ii) 1610 cm^{-1} , double conjugated bonds (dienes) and olefinic coke; (iii) 2930 cm^{-1} , CH and CH_2 aliphatics; and (iv) 2960 cm^{-1} , terminal CH_3 aliphatics. The intensity of the coke band (1580 cm^{-1}) increases strongly upon increasing HC temperature, as a consequence of a higher coke aromatization and condensation, especially at 500 °C , confirming the Raman spectra results detailed above (Figure 5.12), and also correlating with the amount of coke deposited. According to this, as the level of aromatic condensation becomes higher, there is also a loss of aliphatic substituents in aromatics. Olefinic coke (1610 cm^{-1}) follows the same trend, as these two bands become more relevant at 500 °C , while at lower temperatures the FTIR bands corresponding to aliphatics are proportionally more intense.

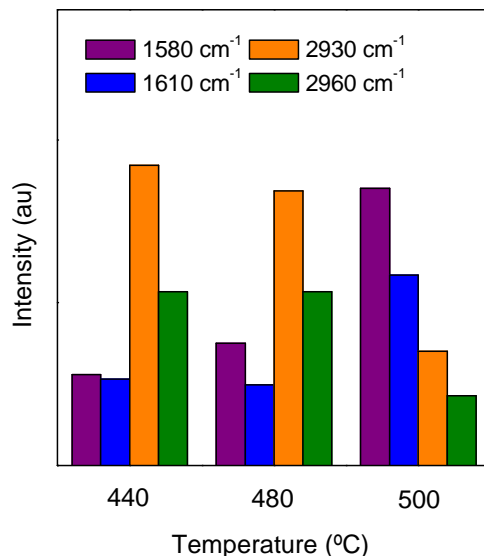


Figure 5.13. Intensities of the most characteristic FTIR bands for the spent catalyst at different temperatures.

5.5.4.3. FTIR-TPO

The FTIR and MS spectroscopy have been used during a TPO profile (Section 2.6.3), providing information of the processes involved during the combustion of coke. Figure 5.14a shows the CO₂ signals, and Figure 5.14b shows the evolution of the most representative FTIR bands of coke assigned in the previous Section 5.5.4.2.

It should be noted that, between the results of coke formed at 440 °C and 500 °C, important differences among the dA/dt signals are observed. At 440 °C, and correlating with the band intensities shown in Figure 5.13, compounds of aliphatic nature are predominant in coke. However, at higher temperatures (especially at 500 °C), coke shows a mainly aromatic nature due to further development and condensation degree, as a consequence of dehydrogenation, cyclization and hydrogen transfer reactions [130, 322]. These results are in agreement with the D/G ratios in Table 5.2 obtained from Raman spectroscopy.

There are two main transformation events in FTIR-TPO profiles that demonstrate the selective combustion of the coke compounds: transformation of aliphatics and combustion of aromatics. Decomposition of aliphatics occurs

at 300-350 °C and does not lead to a variation of the CO₂ or TG signal due to the fact that these bonds are not being burned off, as shown in Figure 5.14b. These aliphatics are dehydrogenated and cyclized to form dienes and aromatics, respectively. This hypothesis is supported by the positive formation of dienes and aromatics in this step (downward tendency of the dA/dt signal), and was also reported by Epelde et al. [330] and Ibáñez et al. [219]. The combustion maximum for aliphatics shifts in Figure 5.14b towards lower temperatures for the sample at 500 °C, which suggests that, at higher HC temperatures, the substituent number in coke molecules is not only lower (as deduced from Figure 5.13), but also consist of shorter aliphatic chains that burn more easily.

Coincident with the aliphatic combustion maximum, the second combustion event (that of aromatics) starts (opposite dA/dt tendency in Figure 5.14b), also observing a pronounced increase in the CO₂ signal in Figure 5.14a. Consistent with a higher aromatic condensation level, the combustion maximum for aromatics shifts towards higher temperatures upon increasing coke formation temperature (506 °C to 541 °C). On the other hand, CO₂ signals in Figure 5.14a show a low temperature shoulder (ca. 400 °C), whose intensity decreases for more developed cokes, and shows wider distributions.

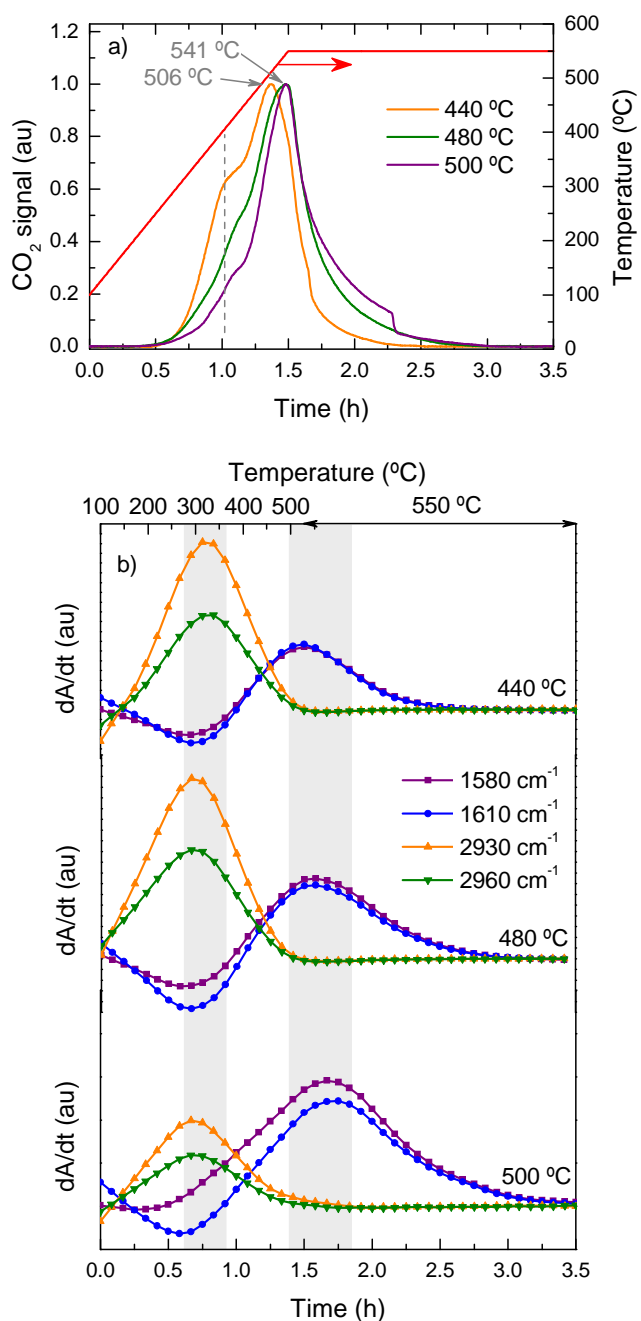


Figure 5.14. Evolution with time and temperature of a) the CO₂ signal in the combustion of coke and b) FTIR absorbances for the spent catalyst at different temperatures.

Section 6

KINETIC MODELING OF THE HYDROCRACKING OF HT-STPO ON A PtPd/SiO₂-Al₂O₃ CATALYST CONSIDERING DEACTIVATION

6. KINETIC MODELING OF THE HYDROCRACKING OF HT-STPO ON A PtPd/SiO₂-Al₂O₃ CATALYST CONSIDERING DEACTIVATION

In hydrocracking processes, heavy aromatic molecules are responsible for coke deposition during the first hours of reaction [331], while for higher time on stream values metal-bearing species are the main cause of permanent deactivation of the catalyst [332, 333]. Numerous kinetic studies have been conducted for hydrocracking reactions [197, 269, 331], but most of them in steady state conditions, with only a few considering catalyst deactivation during the first hours of reaction. To correctly estimate the performance of the catalyst under deactivation conditions (as a great conditioning for the economical viability of hydroprocessing), it is desirable to account for a model that simulates the evolution of the deactivation patterns accurately.

Coke deposition depends on the concentration of the coke precursors [125] and therefore, assuming that activity is only a function of time on stream is not a suitable approach for modeling the evolution of products with time on stream. Therefore, the dependence of deactivation on coke precursors should be considered in the kinetic model [268, 334].

The most common approach for modeling hydrocracking processes considering catalyst deactivation due to coke formation is through lumping, as reported by Martínez and Ancheyta [268] for predicting short-term catalyst deactivation. On the other hand, taking the evolution of deactivation into account, a 3-stage approach was proposed by Elizalde and Ancheyta [335] for modeling start-of-run, middle-of-run and end-of-run deactivation on the hydrotreating of a heavy oil.

A more detailed kinetic model was reported by Iranshihi et al. [336] for a naphtha reforming process in thermally coupled reactors considering deactivation on both the metallic and acidic phases of the catalyst and also as a function of the longitudinal and radial position on the reactor.

Based on previous works [275, 337], in this Section, and using the same kinetic equations applied in Section 4, hydroprocessing reactions have been modeled using the PtPd/SiO₂-Al₂O₃ catalyst, also studying the effect of space time for the three reaction pathways: (i) HDS, (ii) HC and (iii) HDA. The main difference between the models proposed in Section 4 and the ones used in this Section is the consideration of catalyst deactivation with time on stream, by including an activity parameter, a . Additionally, various models based on different dependences on coke precursors of the activity parameter have been proposed and compared by means of statistic analysis in order to determine the most suitable.

To collect the experimental kinetic data, the following operating conditions have been studied:

- Time on stream (TOS): 0-6h
- Space time (τ): 0-0.28 g_{cat} h g⁻¹_{feed}
- Temperature: 440-500 °C
- Pressure: 65 bar
- H₂/feed volumetric ratio: 1000 N m³/m³

6.1. METHODOLOGY FOR KINETIC MODELING

6.1.1. Deactivation models

The kinetic expressions when deactivation is not negligible consider the evolution of the concentrations of the components in the reaction media with space time and time on stream (TOS). In this sense, the kinetic equations describing the influence of space time in terms of HDS, HC and HDA of HT-STPO are similar to these used for the STPO (Sections 4.1.3, 4.2.3 and 4.3.3) with an additional term of deactivation, a :

$$\frac{dx_i}{dt} = \left(\sum k_i x_i \right) a \quad (6.1)$$

This activity parameter, a , has been defined as the ratio between the reaction rate at time t and the reaction rate a zero time on stream:

$$a = \frac{\left(\frac{dx_i}{dt} \right)_t}{\left(\frac{dx_i}{dt} \right)_0} \quad (6.2)$$

Activity is a parameter dependant on time on stream and other reaction variables (like temperature and/or the concentration of the different lumps in the reaction media), following the expression:

$$-\frac{da}{dt} = k_d \left(\sum x_i \right) a^d \quad (6.3)$$

6.1.2. Computation of the kinetic parameters

The calculations of the parameters for the different proposed kinetic models have been carried out by non-linear multiple regression methodology. Computing of the models has been achieved by minimizing an error objective function (f).

$$f = \sum_{i=1}^{n_c} \sum_{j=1}^p (x_{i,j}^* - x_{i,j})^2 \quad (6.4)$$

Where $x_{i,j}^*$ is the mass fraction of the component i at the experimental condition j , $x_{i,j}$ is the corresponding predicted value, n_c is the number of components in the kinetic scheme and p is the total amount of experimental conditions.

The parameters subjected to optimization in the kinetic models have been the kinetic constants (both those corresponding to the kinetic schemes and the deactivation constant), as defined by the reparametrized Arrhenius equation (Eq. 6.5) at the reference temperature (T_{ref}) of 390 °C, and the corresponding activation energies.

$$k_i = k_{i,T_{\text{ref}}} \exp \left[\frac{E}{R} \left(\frac{1}{T_{\text{ref}}} - \frac{1}{T} \right) \right] \quad (6.5)$$

In the case of the HDA model, the system of differential equations to be solved has included thermodynamic equilibrium constants of the different chemical groups. These constants have been expressed following the Van't Hoff equation (Eq. 6.6). In this case, equilibrium constants and specific heats are also to be optimized by the model.

$$K_i = K_{i,T_{\text{ref}}} \exp \left[\frac{\Delta H}{R} \left(\frac{1}{T_{\text{ref}}} - \frac{1}{T} \right) \right] \quad (6.6)$$

For the integration of the kinetic equations and non-linear multiple regression, a calculus program has been developed in Matlab, whose block diagram is similar to that shown in Figure 4.1 of Section 4. However, the computation is now rather complex, since now that calculus routine needs to be applied for every TOS value, with constant iterations for recalculating predicted values of x_i and activity parameter.

6.1.3. Significance and discrimination of kinetic models

The statistic significance [337, 338] of the kinetic parameters can be evaluated using the expression of the confidence intervals for the different calculated parameters. These confidence intervals are obtained from the following expression:

$$L_q = b_q \pm t_{\alpha/2} n \sqrt{\sigma^2 c_q} \quad (6.7)$$

Where q is the amount of kinetic parameters, c_q is the element of the variance-covariance matrix of those q parameters, b_q is the estimation of the q parameter, $t_{\alpha/2}$ is the critical value of the Student's t-test for a given α confidence level and σ^2 is the variance.

For evaluating the significance of a kinetic model, the ratio between the variances of the two properties s_i^2/s_j^2 has been used (s_i^2 is the variance of the lack of fitting and s_j^2 is the variance of the experimental error). This ratio

follows a Fischer's F type of distribution, with v_i and v_j degrees of freedom, which are calculated as:

$$v = pn_c - q \quad (6.8)$$

Where p is the number of experiments, n_c is the number of components in the kinetic scheme and q is the amount of kinetic parameters to be calculated in every model.

Model discrimination has been carried out by applying an F-test to the residual error of the models. This way, when two models (i and j) are compared with their residual variances being σ_{Ei}^2 and σ_{Ej}^2 and with $\sigma_{Ei}^2 > \sigma_{Ej}^2$, the improvement obtained with model j will be significative compared to model i if:

$$F_{i-j} = \frac{SSE_i / v_i}{SSE_j / v_j} = \frac{\sigma_{E,i}^2}{\sigma_{E,j}^2} > F_{1-\alpha}(v_i, v_j) \quad (6.9)$$

Where SSE is calculated as:

$$SSE = \sum_{i=1}^{n_c} \sum_{j=1}^p \left(\frac{X_{i,j}^* - X_{i,j}}{X_{i,j}} \right)^2 \quad (6.10)$$

6.2. HYDROCRACKING

6.2.1. Deactivation model discrimination

Due to the higher temperature and catalyst acidity used during the hydrocracking compared to those of hydrotreating, a significant amount of liquefied petroleum gas (LPG) has been produced. Therefore, the HC model includes an additional LPG lump and two additional kinetic constants compared to the HT model proposed in Section 4.2.3, as shown in Figure 6.1.

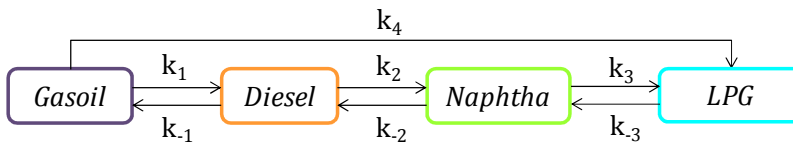


Figure 6.1. Proposed kinetic scheme for the HC of HT-STPO.

Considering the lumps in HC, deactivation models of different complexity have been proposed (Table 6.1). In the first place, models depending on only one of the main liquid lumps (one coke precursor) have been proposed: gasoil (Mod_G), diesel (Mod_D) and naphtha (Mod_N), depending on the mass fractions of each lump. Another model dependant on three coke precursors (gasoil, diesel and naphtha; Mod_GDN) has also been proposed, and two models depending on all the lump concentrations with either 1 (Mod_GDNL) or four different deactivation constants (Mod_kGDNL), so that the contribution of each lump to deactivation can be quantified. Deactivation kinetics has been assumed to be a first order reaction, since this assumption has proven to be valid for obtaining good initial estimations for the kinetic parameters [317]. Considering a higher kinetic order (exponential deactivation equation) would predict very rapid variations with time on stream, as observed by Calderón [339] in a previous work. The corresponding parameters for the discrimination of these models are listed in Table 6.2.

Table 6.1. Deactivation kinetic models proposed for the HC.

Model	Equation
Mod_G	$-\frac{da}{dt} = k_{d1}x_G a \quad (6.11)$
Mod_D	$-\frac{da}{dt} = k_{d1}x_D a \quad (6.12)$
Mod_N	$-\frac{da}{dt} = k_{d1}x_N a \quad (6.13)$
Mod_GDN	$-\frac{da}{dt} = k_{d1}(x_G + x_D + x_N) a \quad (6.14)$
Mod_GDNL	$-\frac{da}{dt} = k_{d1}(x_G + x_D + x_N + x_{LPG}) a \quad (6.15)$
Mod_kGDNL	$-\frac{da}{dt} = (k_{d1}x_G + k_{d2}x_D + k_{d3}x_N + k_{d4}x_{LPG}) a \quad (6.16)$

As deduced from the square sum error (SSE) values in Table 6.2, the single-precursor model that achieves the best fitting is the Mod_N, which considers naphtha as the coke precursor. However, as deduced from the fitting results, deactivation of the PtPd/SiO₂-Al₂O₃ catalyst is not selective, and occurs due to contribution of all the lump yields in products, and mainly due to heavier molecules, found in a greater extent in diesel and gasoil. Furthermore, when including all the lumps as coke precursors in the deactivation equation, better fitting is achieved, confirming that all the lumps have their role in coke formation, as considered by Mod_GDNL, depending on a single deactivation constant. However, according to the variance analysis in Table 6.3, the improvement is not significant. Based on this premise, a further consideration can be included, considering that not all the lumps contribute in the same extent to coke formation.

Including individual deactivation constants for each lump (considering the same activation energy for all of them) has allowed for obtaining the best fit with model Mod_kGDNL, significantly better than the model considering only gasoil as precursor (Mod_G), according to the statistics. The assumption of individual kinetic constants is also more accurate from a chemical point of view, considering that heavier molecules (those contained in the heaviest lumps) have proven to have greater tendency towards coke formation [125,

340], and therefore contribute in a more controlling way to deactivation than lighter molecules with a lower aromaticity and condensation level.

Table 6.2. Statistics and variance analysis for the proposed HC deactivation kinetic models.

Model	p	q	v_i	SSE	$\sigma_E^2, 10^3$	f
Mod_G	126	16	110	0.752	6.834	10.94
Mod_D	126	16	110	0.664	6.039	11.25
Mod_N	126	16	110	0.586	5.329	14.25
Mod_GDN	126	16	110	0.657	5.975	11.07
Mod_GDNL	126	16	110	0.576	5.238	12.06
Mod_kGDNL	126	19	107	0.528	4.937	10.78

Table 6.3. Significance analysis for the proposed HC deactivation models.

i	j	F_{i-j}	$F_{1-\alpha}(v_i, v_j)$
Mod_G	Mod_GDNL	1.304	1.370
Mod_D	Mod_GDNL	1.153	1.370
Mod_N	Mod_GDNL	1.017	1.370
Mod_G	Mod_kGDNL	1.384	1.374
Mod_D	Mod_kGDNL	1.223	1.374
Mod_N	Mod_kGDNL	1.079	1.374
Mod_GDNL	Mod_kGDNL	1.061	1.374

6.2.2. HC kinetic model fitting

The kinetic parameters obtained for the model considering the kinetic scheme of Figure 6.1 and the kinetic deactivation equation are listed in Table 6.4. As observed, hydrogenation of the 2-ring and 1-ring aromatics is favored at 390 °C compared to their reverse reactions ($k_1 \gg k_{-1}$ and $k_2 \gg k_{-2}$), which can be considered negligible. Additionally, according to the values of k_3 and k_{-3} , the transformation between naphtha and LPG is greatly favored towards naphtha yield (occurring even two orders of magnitude faster). These values, compared to those shown in Table 4.2 of Section 4.2.3, confirm the higher activity of PtPd/SiO₂-Al₂O₃ catalyst towards hydrogenation and cracking reactions compared to those of the NiMo/Al₂O₃ catalyst.

On the other hand, the deactivation constants for each lump confirm the greater contribution of heavier lumps as coke precursors, as their values

follow the same trend as the boiling point of the lumps they are associated to, as follows: $k_{d1} > k_{d2} > k_{d3} > k_{d4}$.

Table 6.4. Kinetic parameters for the kinetic model with the Mod_kGDNL deactivation equation.

Reaction	k_i	$k_{i,390\text{ °C}}$ (h^{-1})	E (kJ mol^{-1})
Gasoil→Diesel	k_1	43.41 ± 7.25	43.07 ± 11.2
Diesel→Gasoil	k_{-1}	1.88 ± 0.15	5.75 ± 2.30
Diesel→Naphtha	k_2	21.58 ± 1.31	44.14 ± 7.52
Naphtha→Diesel	k_{-2}	3.03 ± 0.54	39.94 ± 4.65
Naphtha→LPG	k_3	7.57 ± 1.85	30.61 ± 6.32
LPG→Naphtha	k_{-3}	$(3.25 \pm 0.66) \cdot 10^2$	2.80 ± 0.35
Gasoil→LPG	k_4	5.59 ± 0.89	65.94 ± 11.25
$k_{d1} = 1.01 \pm 0.08 \text{ g}_{\text{total}} \text{ g}_i^{-1} \text{ h}^{-1}$ $k_{d2} = (7.3 \pm 0.6) \cdot 10^{-2} \text{ g}_{\text{total}} \text{ g}_i^{-1} \text{ h}^{-1}$ $k_{d3} = (6.8 \pm 0.4) \cdot 10^{-2} \text{ g}_{\text{total}} \text{ g}_i^{-1} \text{ h}^{-1}$ $k_{d4} = (9 \pm 1.2) \cdot 10^{-3} \text{ g}_{\text{total}} \text{ g}_i^{-1} \text{ h}^{-1}$			$E_d = 1.35 \pm 0.35$

The good fitting of the model is proved by the parity diagram in Figure 6.2, as well as from the comparison between the experimental data (dots) and the model prediction (lines) in Figure 6.3 for the evolution of product lumps with TOS at 440 °C.

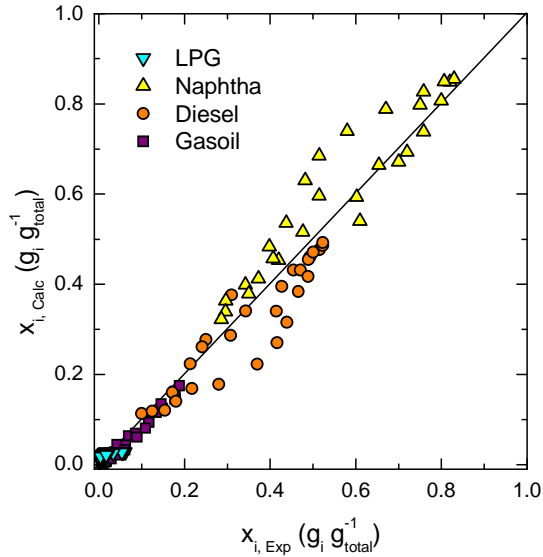


Figure 6.2. Parity diagram for the HC kinetic model with the Mod_kGDNL deactivation equation (65 bar; 440 °C).

Qualitatively, increasing TOS, and therefore the progression of deactivation, has the same effect at all space time values, with decreasing amounts of naphtha and LPGs (the lightest lumps) and increasing diesel and gasoil yields due to loss of cracking ability. As observed in Figure 6.3, and increase in space time implies obtaining higher naphtha yields and lower diesel yields in fresh catalyst conditions (TOS = 0 h), up to 83 wt% at $0.28 g_{cat} h g_{feed}^{-1}$, with naphtha being the main lump. As the reaction occurs and the cracking function of the catalyst deactivates, this trend inverts and diesel becomes the main product lump and significant amounts of gasoil are detected, except for $0.28 g_{cat} h g_{feed}^{-1}$ conditions at which naphtha prevails during the whole reaction time and gasoil yield does not surpass 6 wt%. Very similar effect of time on stream on deactivation was observed by Elizalde et al. [331] on the hydrocracking of atmospheric residue using the lumping approach.

As space time increases, the TOS at which diesel lump becomes the most abundant lump is also higher, as higher amounts of catalyst provide higher cracking activity for longer times, and require of larger TOS to reach the steady state, which is reached at TOS = 3 h and $0.05 g_{cat} h g_{feed}^{-1}$ conditions.

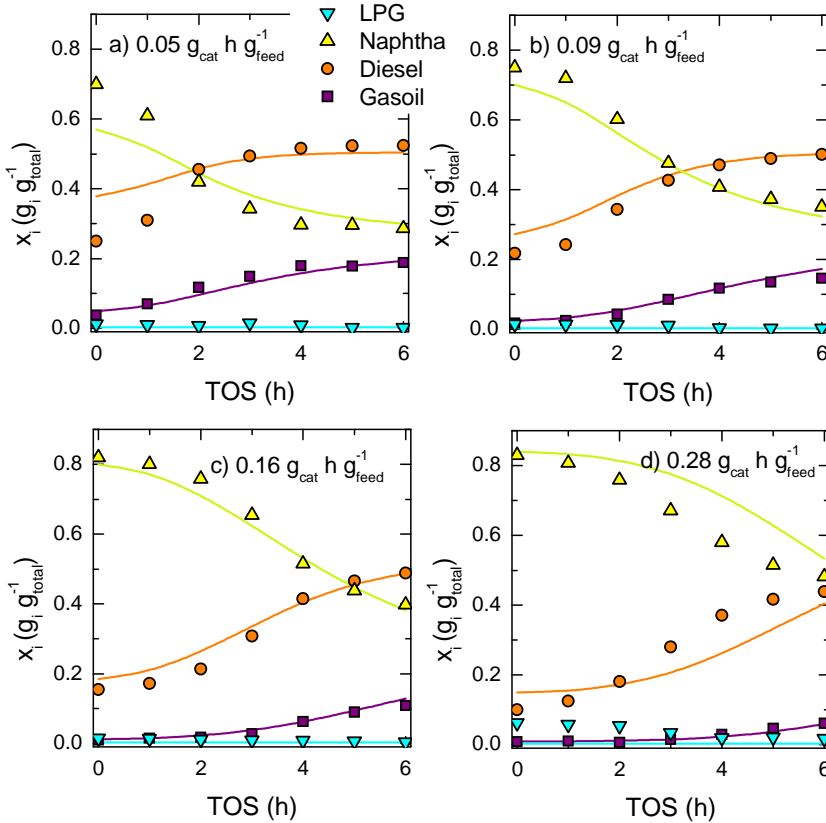


Figure 6.3. Evolution with TOS of the product lumps in HT-STPO hydrocracking at different space time conditions as obtained from experimental data (dots) and model prediction (lines) (65 bar; 440 °C).

As has been observed on the results corresponding to the evolution with time on stream of the different lump yields (Figure 6.3), the yield of naphtha rapidly decreases and diesel and gasoil yields increase until approximately a value of TOS = 6 h. Then, deactivation reaches an apparent equilibrium, and later on progresses very slowly. The obtained kinetic model quantifies deactivation during that initial 6 h period. As an example of the validity of the model for predicting lump yields at the beginning and the end of this period, Figure 6.4 compares the experimental (dots) and predicted (lines) results for TOS= 0 h (Figure 6.4a) and TOS = 6 h (Figure 6.4b)

In TOS = 0 h conditions, an increase in space time has strong effect, mainly within the 0-0.16 $\text{g}_{\text{cat}} \text{h g}_{\text{feed}}^{-1}$ range, with increasing yields of naphtha and decreasing yields of diesel and gasoil. For higher values, a steady state is reached and constant values of naphtha (ca. 82 wt%), diesel (ca. 12 wt%) and gasoil (ca. 9 wt%) are measured, with minor amounts of LPG. At TOS = 6 h, the trends maintain the same values, but variations in product yields occur in a much lesser extent (29-49 wt% naphtha, 45-50 wt% diesel, and 5-22 wt% gasoil, with negligible amounts of LPGs). In this case, no clear steady state is observed.

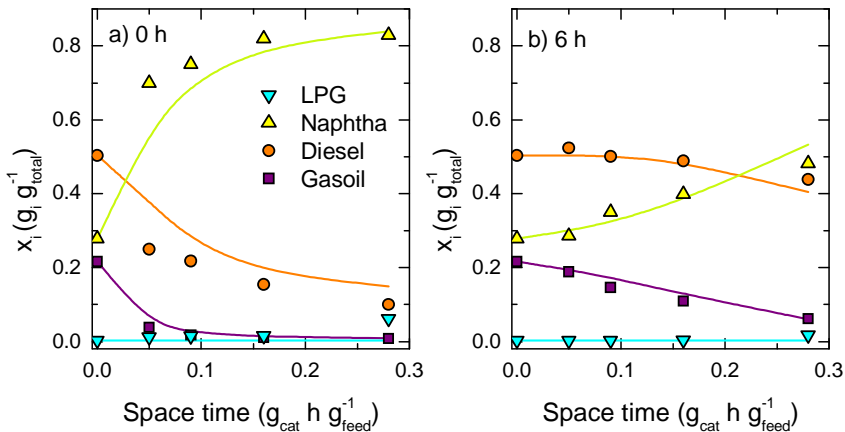


Figure 6.4. Evolution with space time of the product lumps in HT-STPO hydrocracking for TOS a) 0 h and b) 6 h (65 bar; 440 °C).

From an industrial perspective it is interesting to delve on the composition of the product stream once the steady state is reached (TOS = 6 h). The simulated distillations of the liquid HC products at steady state for different space time conditions are shown in Figure 6.5. Equally to what occurred for the effect of temperature, these results correlate to those of Figure 6.3, observing a significantly higher proportion of compounds in the liquid products within the naphtha and diesel boiling point range upon increasing space time.

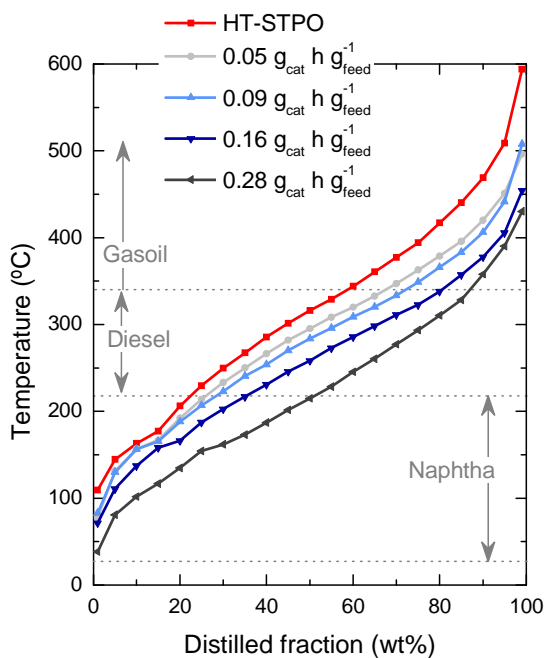


Figure 6.5. Simulated distillation of the liquid products in HT-STPO hydrocracking at different space time conditions (65 bar; 440 °C).

6.3. HYDRODEAROMATIZATION

6.3.1. Deactivation model discrimination

The HDA kinetic scheme applied in this Section has been equal to that used in Section 4.3.3. The proposed deactivation model equations for HDA are listed in Table 6.5. The models considering only one coke precursor have been Mod_A2, Mod_A1, Mod_N and Mod_P, including the concentrations of 2-ring aromatics, 1-ring aromatics, naphthenics and paraffins, respectively. One model with the total of the compositions (Mod_A2A1NP) has also been studied. Additionally, Mod_kA2A1NP has also been proposed including individual deactivation constants for each product fraction instead of only one. The kinetic constants have been expressed by the Arrhenius equation and deactivation order has been assumed to be 1.

The statistics and variance analysis parameters are summarized in Table 6.6, and the same variance analysis methodology as for the previous model has been applied.

Table 6.5. Deactivation kinetic models proposed for HDA.

Model	Equation
Mod_A2	$-\frac{da}{dt} = k_{d1}x_{A2}a$ (6.17)
Mod_A1	$-\frac{da}{dt} = k_{d1}x_{A1}a$ (6.18)
Mod_N	$-\frac{da}{dt} = k_{d1}x_Na$ (6.19)
Mod_P	$-\frac{da}{dt} = k_{d1}x_Pa$ (6.20)
Mod_A2A1NP	$-\frac{da}{dt} = k_{d1}(x_{A2} + x_{A1} + x_N + x_P)a$ (6.21)
Mod_kA2A1NP	$-\frac{da}{dt} = (k_{d1}x_{A2} + k_{d2}x_{A1} + k_{d3}x_N + k_{d4}x_P)a$ (6.22)

Table 6.6. Statistics and variance analysis for the proposed HDA deactivation kinetic models.

Model	p	q	v_i	SSE	$\sigma_E^2, 10^4$	f
Mod_A2	126	16	110	0.0874	7.945	4.040
Mod_A1	126	16	110	0.0921	8.373	4.221
Mod_N	126	16	110	0.0793	7.209	3.730
Mod_P	126	16	110	0.0790	7.182	3.189
Mod_A2A1NP	126	16	110	0.0738	6.709	3.489
Mod_kA2A1NP	126	22	104	0.0694	6.486	3.240

Mod_P fits better the experimental results among the deactivation models including one coke precursor, as deduced from the SSE values. However, the fitting is better when considering that all the lumps contribute to deactivation (Mod_A2A1NP), as seen on Table 6.6. Equally to what happened for the HC Mod_kGDNL model, including individual deactivation constants for each precursor assuming the same activation energy for all of them, provides even a better fitting. On the other hand, according to the variance analysis results in Table 6.7, none of the two models including the 4 coke precursors allow for obtaining a significant improvement over those considering a single precursor component. Due to the lowest SSE value, Mod_kA2A1NP has been selected as the best deactivation model.

Table 6.7. Significance analysis for the proposed HDA deactivation models.

Model i	Model j	F_{i-j}	$F_{1-\alpha}(v_i, v_j)$
Mod_A2	Mod_A2A1NP	1.184	1.370
Mod_A1	Mod_A2A1NP	1.247	1.370
Mod_N	Mod_A2A1NP	1.075	1.370
Mod_P	Mod_A2A1NP	1.070	1.370
Mod_A2	Mod_kA2A1NP	1.225	1.374
Mod_A1	Mod_kA2A1NP	1.291	1.374
Mod_N	Mod_kA2A1NP	1.111	1.374
Mod_P	Mod_kA2A1NP	1.107	1.374

6.3.2. HDA kinetic model fitting

The computed kinetic parameters for the HDA model and the Mod_kA2A1NP deactivation model, are summarized in Table 6.8. At 390 °C, the two aromatic hydrogenation stages are clearly favored over their reverses, and the last ones can be considered negligible due to their low kinetic constant values. The same thing occurs with ring opening and its reverse cyclization reactions, with the former taking place at a much fast rate than the latter. Furthermore, and as a consequence of the higher activity of the PtPd/SiO₂-Al₂O₃ catalyst (Table 6.4), the differences between the forward reactions (k_i , hydrogenation and cracking) and their reverses (k_{-i} , dehydrogenation and oligomerization) are more significant in this case than when using the NiMo/Al₂O₃ catalyst, based on the results shown in Table 4.3 of Section 4.3.3.

Table 6.8. Kinetic parameters for the Mod_kA2A1NP model.

Reaction	k_i	$k_{i,390\text{ °C}}$ (h ⁻¹)	E (kJ mol ⁻¹)
Hydrogenation	k_1	8.73±1.22	33.01±7.25
Dehydrogenation	k_{-1}	(8.49±2.16)·10 ⁻¹	
Hydrogenation	k_2	8.47±2.11	17.71±4.36
Dehydrogenation	k_{-2}	(3.18±0.37)·10 ⁻²	
Ring opening	k_3	19.40±4.10	31.76±9.50
Cyclization	k_{-3}	1.34±0.41	
Chain scission	k_4	1.40±0.36	33.78±4.52
		$k_{d1} = (5.94±2.60)·10^{-1} \text{ g}_{\text{total}} \text{ g}_i^{-1} \text{ h}^{-1}$	$E_d = 3.05±0.22$
		$k_{d2} = (6.12±1.22)·10^{-2} \text{ g}_{\text{total}} \text{ g}_i^{-1} \text{ h}^{-1}$	
		$k_{d3} = (1.57±0.77)·10^{-2} \text{ g}_{\text{total}} \text{ g}_i^{-1} \text{ h}^{-1}$	
		$k_{d4} = (1.39±0.49)·10^{-2} \text{ g}_{\text{total}} \text{ g}_i^{-1} \text{ h}^{-1}$	

Furthermore, the computed kinetic deactivation constants in Table 6.4 show that heavier compounds with a higher condensation level (particularly 2-ring aromatics) have a greater contribution to coke formation (k_{d1}).

The accuracy of the model is proved by the parity diagram of Figure 6.6 and the evolution with TOS of the model fitting (lines) and experimental data (dots) in Figure 6.7.

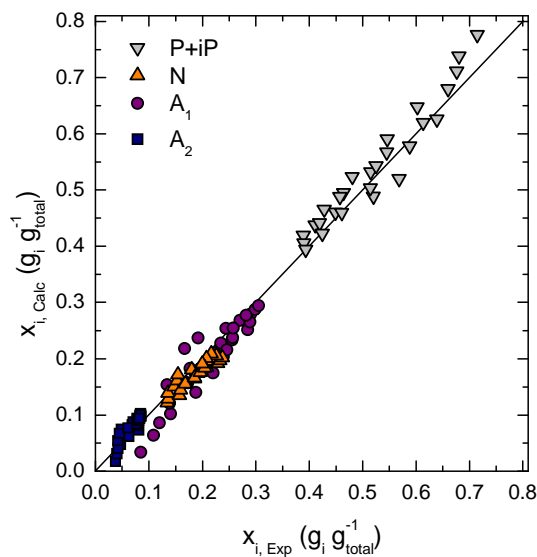


Figure 6.6. Parity diagram for the HDA kinetic model with the Mod_kA2A1NP kinetic equation.

The evolution of the different experimental (dots) and predicted (lines) composition fractions with time on stream and space time can be seen in Figure 6.7. The effect of TOS has already been analyzed in Section 5.5.1, observing a decrease in paraffins and isoparaffins and increasing amounts of naphthenics and aromatics. Upon increasing TOS, cyclic compounds appear in a greater extent, except for $0.28 g_{cat} h g_{feed}^{-1}$ conditions, when paraffins account for 52 wt% of the total. More saturated compounds, like paraffins and naphthenics, are obtained upon increasing space time, while unsaturated compounds (like aromatics) decrease.

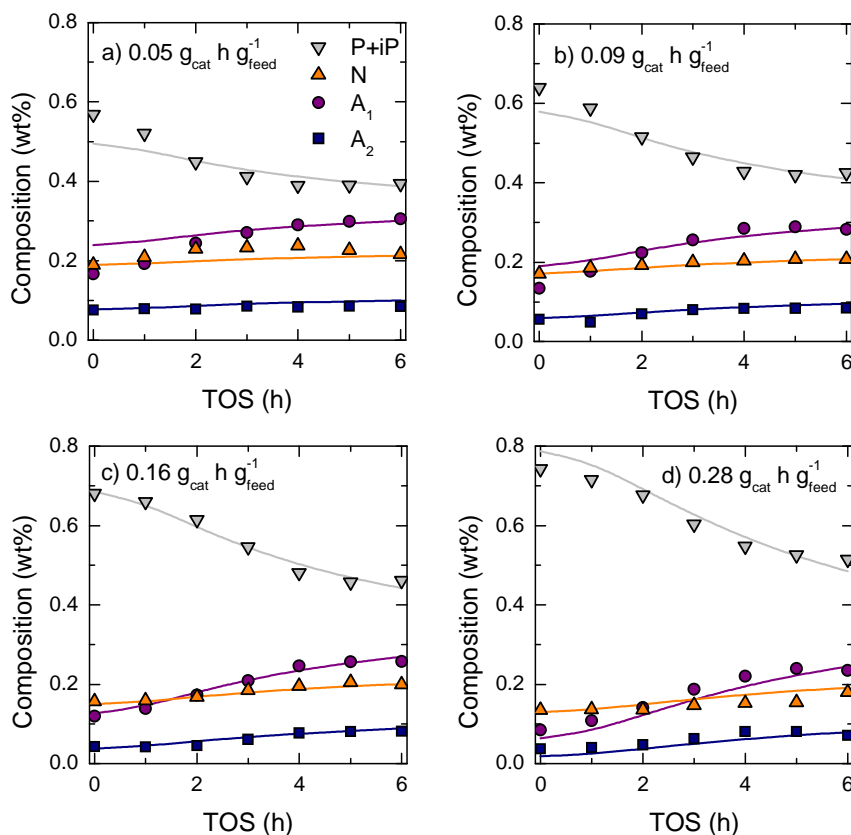


Figure 6.7. Evolution with TOS of the composition fraction in HT-STPO hydrocracking at different space time conditions as obtained from experimental data (dots) and model prediction (lines) (65 bar; 440 °C).

Equally to the HC model, the proposed kinetic model for HDA can be applied for predicting the evolution with time on stream of the composition fractions during the first reaction hours, as seen in Figure 6.8. For fresh catalyst conditions (TOS = 0 h), changes in composition occur mainly below $0.16 \text{ g}_{\text{cat}} \text{ h g}_{\text{feed}}^{-1}$, while for higher space time values a steady state is reached with 72 wt% paraffins and isoparaffins, 14 wt% naphthenics, 10 wt% 1-ring aromatics and 4 wt% 2-ring aromatics, approximately. At steady state (Figure 6.8b), the trends are maintained but no constant value is clearly reached for the space time conditions studied, with paraffins and 1-ring aromatics varying the most, with 15 wt% more and 8 wt% less, respectively.

While at TOS = 6 h, the model predicts practically an identical evolution to that of the experimental data, at TOS = 0 h lower accuracy is obtained.

The comparison of these results with those of Figure 4.18 in Section 4.3.3 shows the great reduction in aromatic compounds achieved with the 2-stage hydroprocessing strategy.

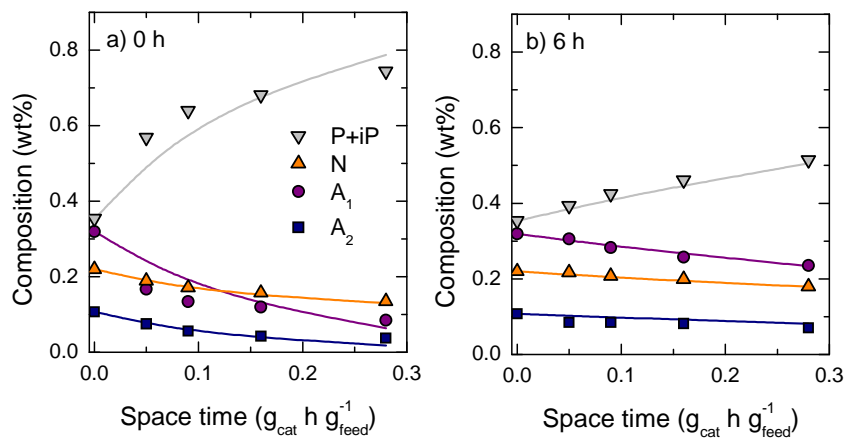


Figure 6.8. Evolution with space time of the composition fractions in HT-STPO hydrocracking for TOS a) 0 h and b) 6 h as obtained from experimental data (dots) and Mod_kA2A1NP prediction.

6.4. HYDRODESULFURIZATION

As pointed in Section 4.1.3, a LH kinetics is suitable for describing HDS reactions without considering deactivation (negligible for the NiMo catalyst). Taking the results of Sections 6.2 and 6.3 into account, and having proved that deactivation in HDS is a non-selective phenomena that occurs due to the contribution of all the lumps and composition fractions in the reaction media, for HDS it has been assumed that deactivation is not dependant on the concentration of the components in the reaction media, following the expression:

$$-\frac{da}{dt} = k_d a \quad (6.23)$$

The expression of the kinetic equation has been identical to that proposed in Section 4.1.3 for the HDS of STPO on NiMo catalysts, applying the equation to each sulfur species and incorporating the activity. The computed values for the kinetic constants and activation energies are listed in Table 6.9. As observed, the model predicts a more rapid HDS of the M₁DBT species, followed by M₄DBT, M₂DBT and M₃DBT, respectively ($k_1 > k_4 > k_2 > k_3$). Once again, as already discussed in the previous Sections and equally to what has been observed for the effect of temperature in Section 4.1.1, M₃DBT is the least reactive sulfur species.

Table 6.9. Kinetic parameters for the HDS model.

Kinetic constant	$k_{i,390\text{ °C}}$ (h ⁻¹)	E (kJ mol ⁻¹)
k ₁	(4.03±0.28)·10 ⁻⁴	11.78±1.32
k ₂	(2.31±0.07)·10 ⁻⁴	1.09±0.23
k ₃	(1.46±0.10)·10 ⁻⁴	7.33±1.25
k ₄	(2.81±0.09)·10 ⁻⁴	11.14±2.03
k _d	0.29±0.08	0.11±0.02

The quality and accuracy of the fitting can be evaluated from the parity diagram (Figure 6.9) representing experimental and calculated sulfur data.

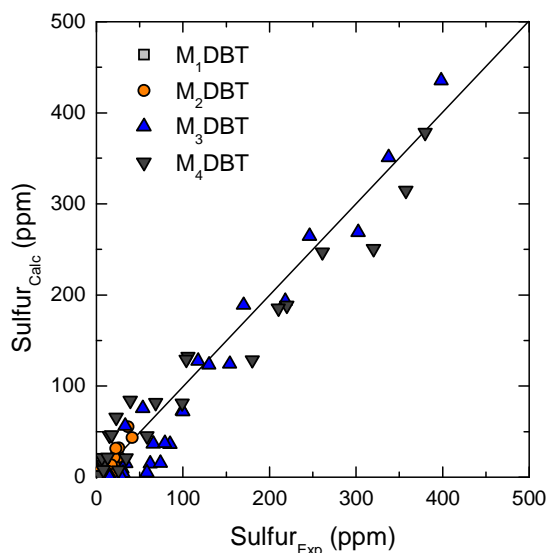


Figure 6.9. Parity diagram for the proposed HDS model (65 bar; 440°C).

The evolution of the four sulfur species with TOS for the different space time conditions is shown in Figure 6.10, in terms of both experimental data (dots) and kinetic model prediction (lines). Deactivation of the metallic phase takes place and increasing amounts of sulfur are detected in the products upon increasing TOS. However, space time has a more remarkable effect than temperature, as total sulfur increases up to ca. 800 ppm at the lowest space time of $0.05 \text{ g}_{\text{cat}} \text{ h g}^{-1}_{\text{feed}}$ and TOS = 6 h. On the other hand, when working at $0.28 \text{ g}_{\text{cat}} \text{ h g}^{-1}_{\text{feed}}$ conditions (and therefore with higher amounts of catalyst loaded in the reactor), less than 140 ppm total (mainly $M_3\text{DBT}$ compounds) were measured at all TOS values, with a much lower activity decay. This can be explained considering that, at lower space times, fewer amounts of metallic sites are available for HDS as less catalyst is loaded in the reactor. For all space times and due to their lower reactivity, the main remaining sulfur species were $M_3\text{DBT}$ and $M_4\text{DBT}$, as observed in Section 4.1.2.

As seen on Figure 6.10 for 440°C, accurate predictions can be obtained from the model, especially for lower space time values. However, for higher values of space time ($0.16\text{-}0.28 \text{ g}_{\text{cat}} \text{ h g}^{-1}_{\text{feed}}$), the model predicts higher removal rates than that obtained experimentally. Therefore, the lower the total amount of sulfur in the products, the higher error it is to assume in the model prediction. Equally to what happened using NiMo catalysts, no significant inhibition effect of H_2S has been detected, mainly due to the low sulfur amount in the HT-STPO feed. However, when working with Pt catalysts and mixtures

containing large amounts of H_2S , the formation of PtS, Pt and S chemisorbed on the support should be considered, as a potential source of catalytic activity loss [341].

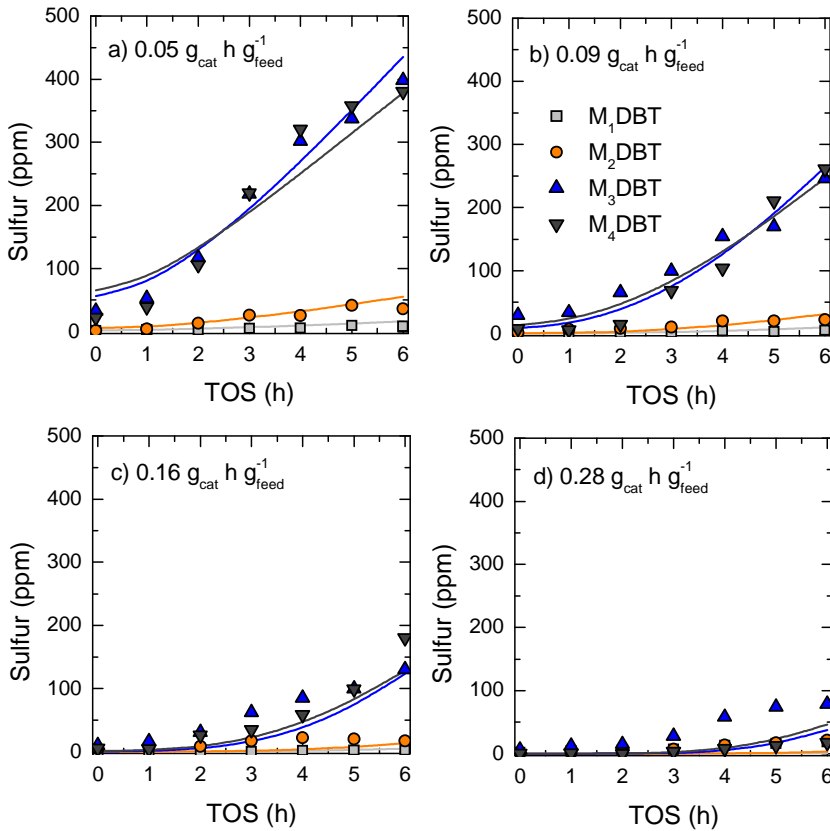


Figure 6.10. Evolution with TOS of the different sulfur species at different space time conditions as obtained from experimental data (dots) and model prediction (lines) (65 bar; 440 °C).

6.5. SIMULATION AND OPTIMAL OPERATION CONDITIONS

Applying the three kinetic models proposed in this Section for i) HC (Section 6.2), ii) HDA (Section 6.3) and iii) HDS (Section 6.4), and using the corresponding computed parameters, a simulation of the evolution with TOS (0-6 h) and space time (0-0.28 $\text{g}_{\text{cat}} \text{h g}^{-1}_{\text{feed}}$) of the three conversions at 440 °C has been carried out (Figure 6.11). The different conversion levels are explained as a color gradient, from the lowest value expected (blue) to the highest one (red).

A clear effect of space time and time on stream (with its consequent deactivation) has been observed. For HC (Figure 6.11a), conversions higher than 90 % can be achieved at space times higher than 0.20 $\text{g}_{\text{cat}} \text{h g}^{-1}_{\text{feed}}$. Within the 0.05-0.20 $\text{g}_{\text{cat}} \text{h g}^{-1}_{\text{feed}}$ range, also conversions between 85-100 % are reached. However, as TOS increases, deactivation becomes significative and conversion decreases below 40 %, with significant amounts of gasoil in the products due to the loss of cracking and hydrogenating ability of the catalyst (Figure 6.3). A more remarkable deactivation effect is observed with TOS for the case of HDA (Figure 6.11b), where conversions higher than 75 % can only be achieved working at space times above 0.2 $\text{g}_{\text{cat}} \text{h g}^{-1}_{\text{feed}}$, and during 1 h. After that period, rapid deactivation occurs and X_{HDA} drops down to ca. 50 %. Concerning HDS (Figure 6.11c), conversions higher than 80 % can be reached for almost the whole space time range studied. Below 0.05 $\text{g}_{\text{cat}} \text{h g}^{-1}_{\text{feed}}$, less than 50 % of the sulfur is removed, accounting for a total of ca. 1,000 ppm, as can be observed in the data shown in Figure 6.10a.

Considering these results, and in order to avoid deactivation and maintain acceptable HC, HDA and HDS performances once the catalyst has reached steady state (TOS > 6 h), there is a clear convenience in working at space time values above 0.15-0.20 $\text{g}_{\text{cat}} \text{h g}^{-1}_{\text{feed}}$, maintaining at least a 75 % HC conversion, 50 % of HDA conversion, and almost total sulfur removal.

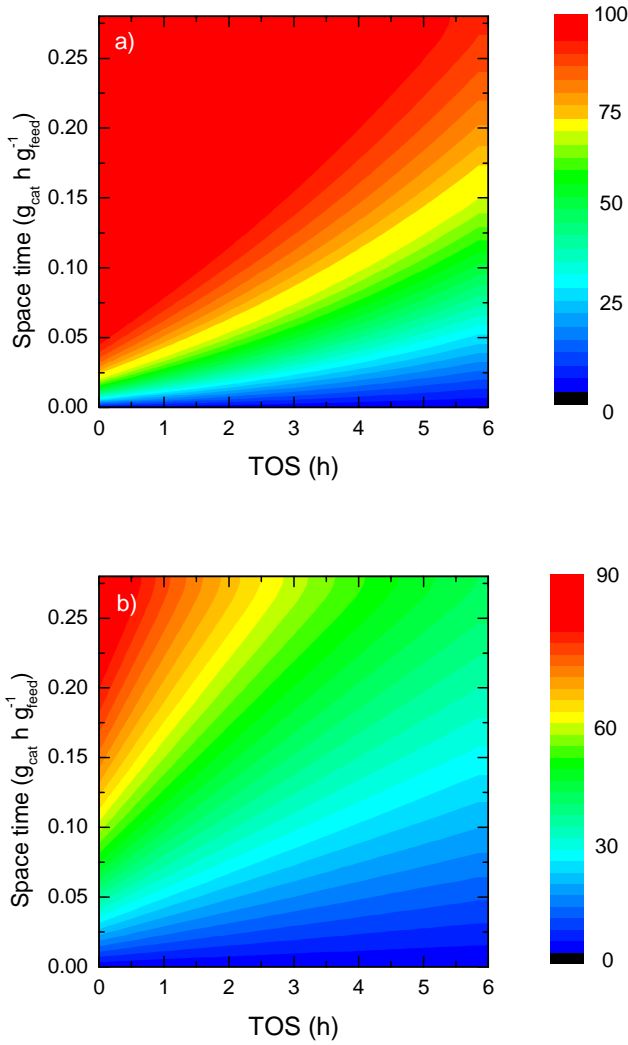


Figure 6.11. Simulation for a) HC, b) HDA and c) HDS conversion as a function of time on stream and space time.

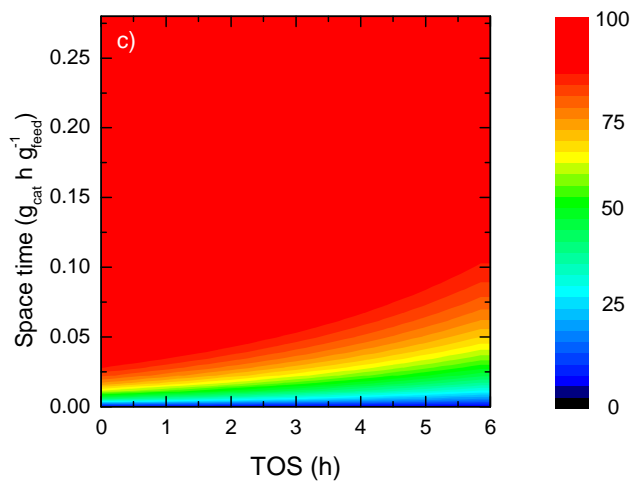


Figure 6.14. Continuation.

6.6. COMPARISON BETWEEN NiMo AND PtPd CATALYST PERFORMANCES

When comparing the results in Figure 6.11 with those of Figure 4.20 in Section 4.4, significant differences are observed among the two simulations for the different catalysts. Regarding HC (Figure 6.11a) the PtPd catalyst has allowed for obtaining almost total gasoil removal at high space time conditions, while the NiMo catalyst, with a less active metallic phase and a support with a milder acidity, only allowed for reaching conversions of 45 %, at high operation temperatures (400 °C) and greater amounts of catalyst were required. On the other hand, not only lower HDA conversions have also been observed using NiMo catalysts, but also a different behavior of the reaction, as using NiMo catalyst thermodynamics clearly governed HDA (lower temperatures favored the hydrogenation equilibriums), while for the PtPd kinetic control on HDA is observed (Figure 6.11b). Conversions up to 35 % could be obtained in hydrotreating, while hydrocracking conversions higher than 50 % can be achieved working above $0.12 \text{ g}_{\text{cat}} \text{ h g}^{-1}_{\text{feed}}$ space time conditions. For HDS, almost complete conversions can be achieved using both catalysts and working at relatively low space time values. However, PtPd catalyst would suffer very quick deactivation due to poisoning when processing feedstock with sulfur amounts as high as STPO, which justifies the necessity of a first hydrotreating stage before using PtPd catalysts.

6.6.1. Reaction rate

Considering the computed kinetic constant values listed in Tables 4.1, 4.2 and 4.3 of Section 4, and those of Tables 6.4, 6.8 and 6.9 of this Section 6, relative reaction rates can be calculated to compare the kinetic behavior of both catalysts (Table 6.10). For the comparison, removal of M₁DBT, the gasoil to diesel transformation and hydrogenation of the 2-ring aromatic fraction have been established as references (value 1) for the HDS, HC and HDA comparison, respectively.

Table 6.10. Comparison between the relative HDS, HC and HDA reaction rates for the NiMo/Al₂O₃ and PtPd/SiO₂-Al₂O₃ catalysts.

	NiMo/Al ₂ O ₃	PtPd/SiO ₂ -Al ₂ O ₃
HDS		
M ₁ DBT	1	1
M ₂ DBT	0.87	0.57
M ₃ DBT	0.66	0.36
M ₄ DBT	1.29	0.70
HC		
Gasoil→Diesel	1	1
Diesel→Gasoil	0.40	4.3·10 ⁻²
Diesel→Naphtha	0.49	0.50
Naphtha→Diesel	0.96	6.9·10 ⁻²
Gasoil→Naphtha/LPG	0.76	0.17
HDA		
Hydrogenation, k ₁	1	1
Dehydrogenation, k ₋₁	0.40	9.7·10 ⁻²
Hydrogenation, k ₂	0.42	0.97
Dehydrogenation, k ₋₂	0.45	3.6·10 ⁻³
Ring opening, k ₃	0.46	2.22
Cyclization, k ₋₃	4.4·10 ⁻²	0.15
Chain Scission, k ₄	4.6·10 ⁻³	0.16

For HDS, M₃DBT compounds have been the least reactive in both hydroprocessing stages, particularly using the PtPd catalyst, due to (i) the longer substituent chains and (ii) the position of the substituents with 4,6 positions being the least reactive. M₄DBT species have been more reactive than M₃DBT in both hydroprocessing stages, which might indicate that the substituents in M₃DBT are mainly located in positions 4 and 6, which has been previously commented in Section 4.1.2. Regarding HC results, clear differences are observed as, for the PtPd catalyst on hydrocracking, and due to the much higher cracking activity of the catalyst, the transformation of gasoil and diesel to lighter lumps is clearly favored over the reverse reactions, even by 2 orders of magnitude. This correlates with the results shown in Figure 6.3 and Figure 6.11a, where almost total gasoil conversion could be achieved. In the hydrotreating stage, however, gasoil transforms to diesel only twice as rapid as its reverse reaction, and further transformation of diesel into naphtha is hindered by reaction conditions. Very similar behavior of the PtPd catalyst has

been observed for HDA, with a much higher activity in hydrogenation reactions, with negligible dehydrogenations for both 1-ring aromatics and naphthenics. The significantly higher ring opening and chain scission rates of the PtPd catalyst compared to hydrogenation reactions should be highlighted, as they have greatly favored the removal of aromatics compared to the NiMo catalyst, as detailed in Sections 4.3 and 6.3 for HDA.

6.6.2. Overview

As explained in Section 4.6.1, it is a common industrial strategy to place different catalyst beds in series within a reactor in order to optimize catalyst and reactor performance according to the main hydroprocessing goal. The 2-stage hydroprocessing stage proposed in this Thesis has achieved great improvements regarding STPO composition in terms of HDS, HDA and HC, as observed in Figure 6.12, highlighting the main interest of each process.

The first hydrotreating stage, using NiMo catalyst, has allowed for reducing the total amount of sulfur from an initial content of 11,800 ppm in STPO to ca. 2,000 ppm in hydrotreated STPO (HT-STPO), thanks to the high activity towards hydrogenation reactions of this type of catalysts. Furthermore, 13.2 wt% less aromatics and 8 wt% less gasoil were obtained working in mild hydrocracking conditions. However, greater achievements in terms of HDA and HC have been obtained on the hydrocracking stage using the PtPd/SiO₂-Al₂O₃ catalyst, due to both the higher hydrogenating activity of the metallic phase and cracking ability of the acidic support, which have allowed for further reduction of 18.6 wt% and almost complete removal of the gasoil lump in upgraded STPO (Up-STPO). Additionally, sulfur has reached levels below 100 ppm.

On the whole, global conversions of 99.2 % in HDS, 99.7 % in HC and 57 % in HDA have been achieved. With very little amount of compounds within the gasoil lump, and an aromatic content even lower than that of some diesel-type feedstock [342, 343], Up-STPO comprises the required features for being co-fed with commercial diesel-type automotive fuels with promising performances in internal combustion engines. It is also to mention that the amount of remaining sulfur in Up-STPO can be the limiting factor when determining the proportions in the diesel-STPO blend to be used, in order to avoid excessive aromatic and particulate emissions and comply with the corresponding environmental policies.

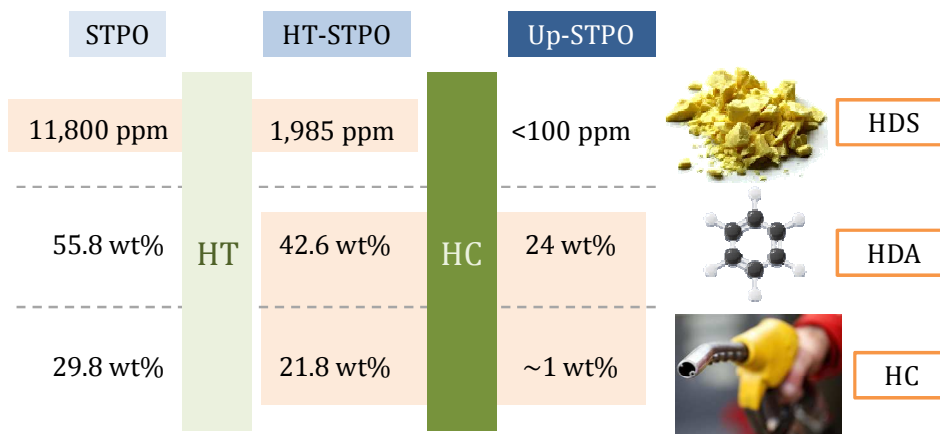


Figure 6.12. Sequential improvements in sulfur, aromatics and gasoil removal through the 2 hydroprocessing stages.

Section 7

SUMMARY

7. SUMMARY

In this Thesis, the upgrading of scrap tires pyrolysis oil (STPO) has been studied through a sequential 2-stage hydroprocessing strategy, consisting in (i) hydrotreating using NiMo catalysts supported on various micro- and mesoporous materials and (ii) hydrocracking using a bifunctional catalyst comprising PtPd metallic phase and amorphous silica-alumina acidic phase. The challenge has been to produce high quality fuels (naphtha and diesel) and, to this purpose, there are three barriers regarding STPO composition that have been solved simultaneously via hydroprocessing: sulfur, high-boiling point molecules and aromatics.

Hydroprocessing is a very versatile refinery operation that offers good perspectives for the valorization of waste hydrocarbon mixtures as STPO. Most of the literature on hydroprocessing delves with model compounds, and in a lesser extent with light cycle oil, vacuum gasoil, and diesel-type feedstock, among others, but is scarce for STPO. Besides, the research on STPO hydroprocessing, comprising catalyst activity and design, together with the kinetic modeling of the steps involved, is greatly innovative and represents for a challenge as it involves important inherent difficulty.

STPO has been obtained in a conical spouted bed reactor at 500 °C. Hydroprocessing runs were performed in a laboratory scale, high-pressure, trickle bed reactor, operating under hydrotreating conditions of: time on stream, 0-8 h; pressure, 25-65 bar; temperature, 300-375 °C; space time, 0-0.5 g_{cat} h g⁻¹_{feed}; H₂/oil ratio 1000:1 N m³/m³; and hydrocracking conditions of: time on stream, 0-6 h; pressure, 65 bar; temperature, 440-500 °C; space time, 0-0.28 g_{cat} h g⁻¹_{feed}; H₂/oil ratio 1000:1 N m³/m³. The analysis of the gaseous products has been carried out on-line by means of gas chromatography and liquids have been sampled every 1 h and analyzed by bi-dimensional gas chromatography using a flame ionization detector, coupled with mass spectrometry. The obtained data have been treated using a program developed in Matlab software. Sulfur measurements have been performed with another gas chromatography apparatus equipped with a pulsed flame photometric detector (PFPD).

Previous to its upgrading, STPO has been extensively characterized via elemental analysis, simulated distillation, and gas chromatography. Chromatographic data has allowed for determining its total sulfur amount as well as sulfur species distribution (benzothiazole, and dibenzothiophenes according to the number of C atoms in their substituents as M₁DBT, M₂DBT, M₃DBT and M₄DBT), its lump yields (LPG, C₃-C₄; naphtha, C₅-C₁₂, 36-215 °C; diesel, C₁₂-C₂₀, 215-350 °C; and gasoil, C₂₀₊, >350 °C) and compositional

fractions (paraffins and isoparaffins, P+iP; olefins, O; naphthenics, N; 1-ring aromatics, A₁; and 2-ring aromatics, A₂).

For the first hydrotreating stage of STPO, a set of five catalysts consisting in Ni and Mo supported on SiO₂-Al₂O₃, Al₂O₃, FCC, SBA-15 and MCM-41 have been prepared. The properties of these catalysts have been analyzed by elemental analysis, N₂ adsorption-desorption isotherms, H₂ chemisorption, *tert*-butylamine adsorption followed by a temperature programmed desorption, X-ray diffraction, X-ray photoelectron spectroscopy, and temperature programmed reduction. A preliminary catalyst screening has been performed using a synthetic STPO feed for selecting the most active ones on the basis of their hydrodesulfurization (HDS) activity. Those catalysts which showed the best performance have then been used on the hydrotreating of STPO studying their activity regarding the removal of: sulfur by hydrodesulfurization (HDS), gasoil by mild hydrocracking (MHC) and aromatics by hydrodearomatization (HDA), correlating these performances with the different physico-chemical properties of the catalysts.

Considering the improved performance of the NiMo/Al₂O₃ catalyst, it has been selected for carrying out a complete parametric study for determining the effect on catalyst activity of different operating variables as temperature, pressure and space time. From the results obtained, kinetic models for the HDS, MHC and HDA have been proposed. The values of the kinetic parameters have been computed using Matlab programming software. Finally, the models have been used for carrying out simulations with temperature and space time, from which the optimal operation conditions have been determined for optimizing compositional features of the hydrotreated STPO.

On the second hydrocracking stage, a hydrotreated scrap tires pyrolysis oil (HT-STPO) has been processed, collected from the mixture of the first stage products. In this stage, a unique bifunctional catalyst was studied based on a more active hydrogenating phase (Pt-Pd) and the best cracking support used earlier (SiO₂-Al₂O₃), since the stronger acidic sites of this catalyst enhance hydrocracking reactions. A parametric study has been carried out for determining the effect of time on stream (TOS), temperature and space time over catalytic activity. Characterization of the fresh and deactivated catalysts deserves special mention given that, through the utilization of a wide range of experimental techniques, it has been able to correlate the chemical and morphological properties of the catalysts with their performance. The physico-chemical properties of the deactivated catalysts have been correlated with the amount of coke formed as well as its nature, which has been analyzed by means of thermogravimetric analysis combined with temperature programmed combustion, Raman spectroscopy and Fourier transformed infrared spectroscopy.

Accounting these results and the kinetic models proposed for the hydrotreating of STPO, different kinetic models have been proposed on the hydrocracking of HT-STPO for each reaction pathway (HDS, HC, and HDA). Catalyst deactivation due to coke deposition plays a determining role in hydrocracking, and has been considered in the kinetic models. In order to obtain the best possible fitting, different non-selective deactivation kinetic equations have been proposed, based on the possible coke precursors, assuming (i) one coke precursor with one deactivation constant, (ii) various coke precursors with one deactivation constant and, (iii) various coke precursors with independent deactivation constants. The suitability and accuracy of each model has been evaluated by solving each model using Matlab software, and applying statistic significance and variance tests for further comparison among them. The best model for each reaction pathway (HDS, HC and HDA) has then been applied for a simulation, which has allowed not only for determining the best operational conditions, but also for comparing the noticeable performance differences between Ni-Mo and Pt-Pd based catalysts on hydroprocessing.

The results are encouraging for the implementation of the hydrotreating/hydrocracking strategy for the production of fuels from tire valorization that meet the environmental requirements. Furthermore, they can also contribute to the viability of co-feeding STPO to hydroprocessing refinery units.

Section 8

CONCLUSIONS

8. CONCLUSIONS

The following conclusions have been obtained as a result of this Thesis, for contributing to the understanding of the two stage hydrotreating-hydrocracking scrap tire pyrolysis oil (STPO) upgrading strategy, in terms of catalyst properties and performance, kinetic modeling and catalyst deactivation.

On the hydrotreating of STPO on NiMo catalyst using various supports

○ NiMo catalysts supported on different micro- and mesoporous materials offer good perspectives for the hydrotreating of STPO for decreasing the concentration of: sulfur through hydrodesulfurization (X_{HDS} 88-93 %), aromatics by means of hydrodearomatization (X_{HDA} 22-26 %) and gasoil removal through hydrocracking (X_{HC} 15-33 %), aiming for the production of potential quality fuels for internal combustion engines (ICE). The physico-chemical properties of the catalyst play a determining role on the conversion of each hydrotreating reaction pathway.

○ NiMo catalysts over $\text{SiO}_2\text{-Al}_2\text{O}_3$, Al_2O_3 and MCM-41 supports allow for reaching ultra low sulfur diesel (ULSD) levels (< 15 ppm) on the hydrotreating of a synthetic STPO feed (SSTPO) at temperatures above 325 °C, being 4,6-DMDBT the sulfur compound that presents the highest difficulty for HDS, mainly due to the shielded environment around the S atom in the molecule, and the presence of methyl groups near the S atom that hinder its hydrogenolysis reactivity compared to DBT compounds.

○ The catalytic acidic properties and pore topology govern HDS reactions, strongly conditioning reactant diffusion inside the porous structure and metallic dispersion. A combination between total mild acidity and a high amount of low-acidic sites, present in the NiMo/ Al_2O_3 catalyst, enhance HDS intrinsic activity.

○ Hydrodesulfurization (HDS) is favored by higher temperatures, achieving a conversion of ca. 90 % at 375 °C with the NiMo/ Al_2O_3 catalyst. This performance is relatively low compared to the one measured using SSTPO, result that can be explained by the inhibition effect caused by certain compounds on the STPO feed, like unsaturated compounds. The NiMo/ $\text{SiO}_2\text{-Al}_2\text{O}_3$ catalyst has stronger acidic sites compared to those of the NiMo/ Al_2O_3 catalyst and, as a result, mild hydrocracking (MHC) conversion is higher using this catalyst, as it eliminates the highest amount of gasoil, while NiMo/MCM-41, the catalyst with the highest total acidity, is the best for hydrodearomatization (HDA).

○ All studied NiMo catalysts hydrogenate olefins completely, and yield significant amounts of paraffins that end up in the naphtha and diesel lumps. On the other hand, aromatics are distributed mainly between diesel and gasoil lumps.

On the process variables and kinetic modeling of the hydrotreating of STPO on a NiMo/Al₂O₃ catalyst

On hydrodesulfurization:

○ Increasing pressure has the same qualitative effect as temperature, enhancing HDS reaction. Equal tendency is observed for space time, as higher space time values imply greater amount of catalyst loaded in the reactor and therefore higher contact time. M₃DBT is the slowest reacting sulfur species towards HDS, as an evidence of the lower reactivity of refractive S compounds (4- and/or 6- position substituted DBTs) compared to reactive S compounds (BTs and substituted DBTs).

○ Accurate predictions for the evolution of the different sulfur species with space time ($0-0.5 \text{ g}_{\text{cat}} \text{ h g}_{\text{feed}}^{-1}$) at different temperature conditions (300-375 °C) can be achieved by assuming a LH kinetic mechanism for HDS on the hydrotreating of STPO, including H₂ concentration in the media and the inhibition effect of H₂S in the kinetic equation. Computed kinetic constants predict the lowest reactivity of M₃DBT species.

On hydrocracking:

○ Higher diesel yields and lower gasoil yields are obtained upon increasing hydrotreating temperature, but with only marginal increase in the naphtha lump. This is a result of the low and mild catalyst acidity (with little/no Brönsted sites) which favors the production of middle distillates, while at the same time avoiding deactivation due to coke formation. Qualitatively, similar effect is observed upon increasing pressure, which allows for obtaining lighter products in MHC, especially at higher temperatures (375 °C), when hydrogenolysis and cracking are enhanced over hydrogenation reactions. Higher naphtha and diesel yields can also be obtained by increasing space time, being able to reduce gasoil yield down to ca. 20 wt% at 375 °C and $0.5 \text{ g}_{\text{cat}} \text{ h g}_{\text{feed}}^{-1}$.

○ A sequential gasoil↔diesel↔naphtha model considering an additional gasoil→naphtha transformation is a suitable model for predicting the evolution with space time of product lump yields at different temperatures (300-375 °C). At 390 °C, the model predicts that gasoil→diesel transformation is greatly favored over its reverse, contrary to what happens with the diesel→naphtha

transformation, which is twice as slower as its reverse. The formation of naphtha is mainly due to the cracking (mild hydrocracking) of gasoil.

- MHC conversions increase strongly with space time in the 0-0.28 $\text{g}_{\text{cat}} \text{h g}_{\text{feed}}^{-1}$ range, and then reach a steady state with constant conversion values. Steady state conversions are greatly dependant on temperature, being higher upon increasing hydrotreating temperature.

On hydrodearomatization:

- Pressure does not affect composition in the steady state in HDA. Paraffins are the main composition fraction at temperatures below 340 °C, while for higher temperatures naphthenics and 1-ring aromatics are controlling. A more remarkable effect is observed for space time, greatly increasing the amount of paraffinic compounds, with total removal of olefins and an important decrease of total aromatics and naphthenics, especially in the 0-0.28 $\text{g}_{\text{cat}} \text{h g}_{\text{feed}}^{-1}$ range. HDA conversion is controlled by thermodynamics at higher temperatures (375 °C) within the whole range of space time conditions studied. For lower temperatures, the space time span in which kinetics govern the reaction becomes wider upon decreasing temperature.

- A sequential $A_2 \leftrightarrow A_1 \leftrightarrow N \leftrightarrow P+iP$ model for HDA considering an additional $A_1 \rightarrow P+iP$ stage is suitable for predicting accurately the evolution of the composition fractions with space time (0-0.5 $\text{g}_{\text{cat}} \text{h g}_{\text{feed}}^{-1}$) for different temperature conditions (300-375 °C).

- The optimal hydrotreating operation conditions must satisfy a compromise between HDS, MHC and HDA reactions, since both HDS and MHC are controlled by kinetics in a wide range of space time conditions, while this occurs in a much reduced space time range for HDA transformations, due to the displacement of the hydrogenation equilibriums of aromatics towards higher hydrogenation rates at lower temperatures.

On the upgrading of HT-STPO through hydrocracking on a PtPd/SiO₂-Al₂O₃ catalyst

On hydrodesulfurization:

- A PtPd/SiO₂-Al₂O₃ (PtPd/ASA) catalyst allows for obtaining ULSD levels on HT-STPO hydrocracking products at time on stream (TOS) below 2 h, and temperatures higher than 480 °C. For higher TOS values, deactivation affects the metallic function of the catalyst (hydrogenation ability) and as a consequence, higher amounts of total sulfur are detected in products.

On hydrocracking:

○ Deactivation also affects the acidic function of the catalyst responsible for enhancing cracking reactions, reason why the yield of final products (LPGs and naphtha) decreases, with a parallel increase in reactants and intermediates (diesel and gasoil), reaching an steady state at TOS = 5 h. Deactivation occurs due to coke formation, given that sulfur (which could act as potential poison) has been reduced in the previous hydrotreating stage to low levels which do not represent for a serious poisoning issue, as observed in a previous work using PtPd catalysts.

○ Conversion of gasoil to lighter products is favored by temperature (X_{HC} 96 % at 480 °C and above), as HC is not limited by reversible exothermic reactions as hydrotreating. Temperature also greatly favors lighter products in both fresh catalyst conditions (92 wt% naphtha and 4 wt% diesel at 500 °C) and catalyst steady state (70 wt% naphtha and 28 wt% diesel at 500 °C), after deactivation has occurred. Preferential production of naphtha or gasoil can be tuned by increasing hydrocracking temperature.

On hydrodearomatization:

○ Lower amounts of paraffinic compounds and higher amount of saturated and unsaturated cyclic compounds (naphthenics and aromatics) are obtained upon increasing TOS, when steady state is reached. Paraffinic compounds represent for the most abundant chemical group in HC products (ca. > 45 wt%). The evolution of HDA products with TOS evidences deactivation affecting to both metallic and acidic phases of the catalyst.

○ Higher amounts of fractions like paraffins and isoparaffins (67-76 wt%) and naphthenics (9-13 wt%) are obtained in fresh catalyst conditions upon increasing temperature. However, at steady state conditions, paraffins decrease (39-52 wt%) and aromatics are obtained in a significant amount (31-38 wt%).

On PtPd/SiO₂-Al₂O₃ catalyst deactivation and coke content and nature

○ Deactivation of the PtPd/SiO₂-Al₂O₃ catalyst on the HC of HT-STPO is due to coke formation. Coke is deposited on the whole catalytic surface, affecting to both the metallic function and the acidic function.

○ Both superficial and acidic properties of the catalyst suffer deterioration after deactivation. At higher HC temperatures of 500 °C, part of the heavily condensed aromatics forming coked are cracked, partially avoiding the loss of specific surface due to pore blockage, indicating the existence of a coke content equilibrium. Coke also deposits on acidic sites, causing for total

acidity to decrease and maintaining higher residual acidities at higher HC temperatures.

- Only one type of aromatic coke is formed, as deduced from the TPO results on coke combustion, with a higher C/H ratio upon increasing HC temperature, due to its higher condensation degree. As a consequence of dehydrogenation, cyclization and hydrogen transfer reactions, coke formed at higher HC temperatures also shows a more homogeneous composition, with a higher proportion of aromatics with a lower amount of aliphatic substituents, as observed from the FTIR-TPO and Raman spectroscopy results.

On the kinetic modeling of the hydrocracking of HT-STPO on a PtPd/SiO₂-Al₂O₃ catalyst considering deactivation

- The same kinetic schemes for HC and HDA proposed for the hydrotreating of STPO are suitable for modeling the hydrocracking of HT-STPO. Including an activity parameter (a) in the kinetic equation is an accurate approach for modeling the evolution of the product lumps and composition fractions with time on stream.

- Coke precursors need to be included in the deactivation model for obtaining more accurate predictions, since coke depends on the concentration of reactants in the reaction media. Additionally, the most accurate assumption is to consider independent deactivation constants for each coke precursor.

- The contribution to deactivation of the different product lumps follows the same trend as their average boiling point, with gasoil lump being the main responsible for deactivation in HC (highest deactivation constant). On the other hand, 2-ring aromatics have the greatest contribution to deactivation in HDA transformations, followed by 1-ring aromatics, naphthenics and paraffins.

On the interest of the results for the viability of STPO upgrading

- The results obtained in this Thesis show good perspectives for the valorization of scrap tires in a large scale, upgrading an important liquid fraction obtained from pyrolysis, which can be complemented with the valorization of other materials present in tires, as carbon black, through other developing technologies.

- Both traditional commercial supports and recently developed mesoporous materials are promising for hydroprocessing heavy hydrocarbon feedstock like STPO, since the different physico-chemical characteristics of each support have proven to be able to enhance different hydroprocessing reaction pathways, which allows for directing the process towards the main hydroprocessing goal (either sulfur, aromatics or gasoil removal). This can be

intensified by choosing the adequate metallic phase: (i) NiMo when mainly sulfur removal is aimed and (ii) PtPd when higher hydrocracking activity is desired for aromatics and gasoil removal.

- Kinetic models, valid for a wide range of experimental conditions are a useful tool for exploring the possibilities for the large scale implementation of STPO hydroprocessing. This way, intervals of optimal operation conditions can be established through the simulation of the evolution of the hydroprocessing conversions with the different process variables.

Section 9

NOMENCLATURE

9. NOMENCLATURE

a	activity
Ca	Carberry number
C _C	Coke content, $\text{gr}_{\text{coke}} \text{g}_{\text{cat}}^{-1}$
d _p	Particle diameter, cm
d _r	Reactor diameter, cm
D _m	Diffusion coefficient, $\text{cm}^2 \text{s}^{-1}$
D _a	Damköhler number
D _{eff}	Efficient diffusion coefficient, $\text{cm}^2 \text{s}^{-1}$
E	Activation energy, KJ mol^{-1}
f	Objective function error
F _L	Liquid flowrate, $\text{cm}^3 \text{s}^{-1}$
k _d	Deactivation constant, $\text{g}_{\text{prod}} \text{g}_i^{-1} \text{h}^{-1}$
k _i	Kinetic constant, $\text{g}_i \text{g}_{\text{cat}}^{-1} \text{h}^{-1}$
K _i	Adsorption equilibrium constant of component i
L	Reactor length, cm
m ₀	Initial catalyst mass, μg
m _{cat}	Final catalyst mass, μg
n	Reaction order, Eq (2.8)
n _c	Number of components
p	Number of experiments
p _i	Partial pressure of component i, bar
P	Pressure, bar
Pe	Péclet number

Q	Number of kinetic parameters
Re	Reynolds number
R	Ideal gas constant, $\text{KJ mol}^{-1} \text{K}^{-1}$
R_i	Heating rate, $^{\circ}\text{C min}^{-1}$
S_{BET}	Specific surface (Brunauer-Emmett-Teller), $\text{m}^2 \text{g}_{\text{cat}}^{-1}$
S_{ppm}	Sulfur content, ppm
t_0	Initial time, h
t_c	Convection time, h
T_0	Initial temperature, $^{\circ}\text{C}$
T	Temperature, $^{\circ}\text{C}$
T_{ref}	Reference temperature, $^{\circ}\text{C}$
u_L	Superficial liquid velocity, cm s^{-1}
V	Reactor volume, cm^3
x_i	Mass fraction of component or lump i, $\text{g}_i \text{g}_{\text{total}}^{-1}$
x_i^*	Predicted mass fraction of component or lump i, $\text{g}_i \text{g}_{\text{total}}^{-1}$
X	Conversion, Eq. (2.8)
X_{HC}	Hydrocracking conversion, %
X_{HDA}	Hydrodearomatization conversion, %
X_{HDS}	Hydrodesulfurization conversion, %
X_{MHC}	Mild hydrocracking conversion, %
ΔH	Reaction heat, KJ mol^{-1}
α	Statistic significance
τ	Space time, $\text{g}_{\text{cat}} \text{h g}^{-1}_{\text{feed}}$
Θ	Particle size factor for hydrodynamic calculations
μ	Viscosity, $\text{kg s}^{-1} \text{m}^{-1}$

ρ_L Density, g cm⁻³

ACRONYMS FOR CHEMICALS, LUMPS AND FRACTIONS

A ₁	1-ring aromatics, wt%
A ₂	2-ring aromatics, wt%
BTX	Benzene-toluene-xylene
D	Diesel lump, wt%
LPG	Liquified petroleum gas, wt%
M _i DBT	Sulfur species with i number of C atoms in its substituents, ppm
N	Naphtha lump in HC, naphthenics fraction in HDA, wt%
NO _x	Nitrogen oxides
O	Olefins, wt%
P+iP	Paraffins and iso-paraffins, wt%
SO _x	Sulfur oxides

ACRONYMS

1DRT	1 st dimension retention time, min
2DRT	2 nd dimension retention time, min
ASA	SiO ₂ -Al ₂ O ₃ support
ALM	Al ₂ O ₃ support
ASTM	American society for testing and materials
BR	Butadiene rubber
BT	Bicycle tire
BTZ	Benzothiazole
CN	Cetane number
CSTR	Continuously stirred tank reactor
CSBR	Conical spouted bed reactor
CV	Calorific value, MJ kg ⁻¹
DBT	Dibenzothiophene

DDS	Direct desulfurization
DSC	Differential scanning calorimetry
EPA	Environmental protection agency
ETRMA	European tire & rubber manufacturers association
FBP	Final boiling point, °C
FCC	Fluid catalytic cracking
FID	Flame ionization detector
FTIR	Fourier transformed infrared spectroscopy
GC	Gas chromatography
HC	Hydrocracking
HCV	High calorific value, MJ kg ⁻¹
HDA	Hydrodearomatization
HDM	Hydrodemetallization
HDN	Hydrodenitrogenation
HDO	Hydrodeoxygenation
HDS	Hydrodesulfurization
HT	Hydrotreating
HT-STPO	Hydrotreated scrap tire pyrolysis oil
IBP	Initial boiling point, °C
ICP-AES	Inductive coupled plasma – atomic emission spectroscopy
LCO	Light cycle oil
LCV	Low calorific value, MJ kg ⁻¹
LH	Langmuir-Hinshelwood equation
LO	Light oil
MCM	MCM-41 support
MFC	Mass flow controller
MHC	Mild hydrocracking
MS	Mass spectrometry
NR	Natural rubber
PAH	Polyaromatic hydrocarbon

PC	Pressure controller
PCT	Passenger car tire
PFPD	Pulsed flame photometric detector
PID	Proportional integral derivative controller
PyGas	Pyrolysis gasoline
SBA	SBA-15 support
SBR	Styrene-butadiene rubber
SD	Simulated distillation
SEKM	Single-event kinetic modeling
SR	Synthetic rubber
SSE	Square sum error
ST	Scrap tire
SSTPO	Synthetic scrap tire pyrolysis oil
STPO	Scrap tire pyrolysis oil
TBP	True boiling point, °C
TC	Temperature controller
TCD	Thermal conductivity detector
TG	Thermogravimetric analysis
TOS	Time on stream, h
TPD	Temperature programmed desorption
TPO	Temperature programmed oxidation
TPR	Temperature programmed reduction
TT	Truck tire
Up-STPO	Upgraded scrap tires pyrolysis oil
ULSD	Ultra low sulfur diesel
VGO	Vacuum gas oil
VR	Vacuum residue
XPS	X-ray photoelectron spectroscopy
XRD	X-ray diffraction

Section 10

BIBLIOGRAPHY

10. BIBLIOGRAPHY

- [1] M.B. Larsen, L. Schultz, P. Glarborg, L. Skaarup-Jensen, K. Dam-Johansen, F. Frandsen, U. Henriksen, *Fuel* 85 (2006) 1335-1345.
- [2] S. Portofino, A. Donatelli, P. Iovane, C. Innella, R. Civita, M. Martino, D.A. Matera, A. Russo, G. Cornacchia, S. Galvagno, *Waste Manage.* 33 (2013) 672-678.
- [3] A. Zabaniotou, N. Antoniou, G. Bruton, *Waste Manage.* 34 (2014) 2335-2346.
- [4] N. Sunthonpagasit, M.R. Duffey, *Resour. Conserv. Recy.* 40 (2004) 281-299.
- [5] N. Antoniou, G. Stavropoulos, A. Zabaniotou, *Renew. Sust. Energ. Rev.* 39 (2014) 1053-1073.
- [6] M. Sienkiewicz, J. Kucinska-Lipka, H. Janik, A. Balas, *Waste Manage.* 32 (2012) 1742-1751.
- [7] N. Antoniou, A. Zabaniotou, *Renew. Sust. Energ. Rev.* 20 (2013) 539-558.
- [8] B. Lebreton, A. Tuma, *Int. J. Prod. Econ.* 104 (2006) 639-652.
- [9] J. Zebala, P. Ciepka, A. Reza, R. Janczur, *Forensic Sci. Int.* 167 (2007) 173-180.
- [10] S. Murugan, M.C. Ramaswamy, G. Nagarajan, *Waste Manage.* 28 (2008) 2743-2749.
- [11] H.J. Lee, H.S. Roh, *Constr. Build. Mater.* 21 (2007) 1016-1026.
- [12] S. Amirkhanian, in *Proceedings of the International Symposium, 2003*, pp. 543-552.
- [13] M. Wilczek, J. Bertling, D. Hintemann, *Int. J. Min. Proc.* 74 (2004) S425-S434.
- [14] R. Gieré, K. Smith, M. Blackford, *Fuel* 85 (2006) 2278-2285.
- [15] L. Lombardi, E. Carnevale, A. Corti, *Waste Manage.* 37 (2015) 26-44.
- [16] J. Caponero, J.A.S. Tenorio, Y.A. Levendis, J.B. Carlson, *Energy Fuels* 17 (2003) 225-239.
- [17] J. Caponero, J.A.S. Tenorio, Y.A. Levendis, J.B. Carlson, *Energy Fuels* 18 (2004) 102-115.
- [18] A. Donatelli, P. Iovane, A. Molino, *Fuel* 89 (2010) 2721-2728.
- [19] J.D. Martínez, N. Puy, R. Murillo, T. García, M.V. Navarro, A.M. Mastral, *Renew. Sust. Energ. Rev.* 23 (2013) 179-213.
- [20] J.D. Murphy, E. McKeogh, *Renew. Energ.* 29 (2004) 1043-1057.

-
- [21] G. Xiao, M.-J. Ni, Y. Chi, K.-F. Cen, *Energ. Conv. Manage.* 49 (2008) 2078-2082.
- [22] H. Karatas, H. Olgun, B. Engin, F. Akgun, *Fuel* 105 (2013) 566-571.
- [23] H. Karatas, H. Olgun, F. Akgun, *Fuel. Process. Technol.* 102 (2012) 166-174.
- [24] V.K. Sharma, F. Fortuna, M. Mincarini, M. Berillo, G. Cornacchia, *Appl. Energ.* 65 (2000) 381-394.
- [25] A.M. Fernández, C. Barriocanal, R. Alvarez, J. Hazard. Mat. 203-204 (2012) 236-243.
- [26] P.T. Williams, *Waste Manage.* 33 (2013) 1714-1728.
- [27] R. Murillo, E. Aylón, M.V. Navarro, M.S. Callén, A. Aranda, A.M. Mastral, *Fuel. Process. Technol.* 87 (2006) 143-147.
- [28] E. Aylón, A. Fernández-Colino, R. Murillo, M.V. Navarro, T. García, A.M. Mastral, *Waste Manage.* 30 (2010) 1220-1224.
- [29] C. Roy, A. Chaala, *Resour. Conserv. Recy.* 32 (2001) 1-27.
- [30] C. Roy, A. Chaala, H. Darmstadt, *J. Anal. Appl. Pyrol.* 51 (1999) 201-221.
- [31] I. de Marco Rodriguez, M.F. Laresgoiti, M.A. Cabrero, A. Torres, M.J. Chomón, B. Caballero, *Fuel. Process. Technol.* 72 (2001) 9-22.
- [32] M. Bianchi, G. Bortolani, M. Cavazzoni, A. De Pascale, I. Montanari, M. Nobili, A. Peretto, C. Tosi, R. Vecchi, *Energy Procedia* 45 (2014) 111-120.
- [33] H. Aydın, C. İlkılıç, *Fuel* 102 (2012) 605-612.
- [34] A.M. Cunliffe, P.T. Williams, *J. Anal. Appl. Pyrol.* 44 (1998) 131-152.
- [35] Y. Kar, *Waste Manage.* 31 (2011) 1772-1782.
- [36] P.T. Williams, S. Besler, D.T. Taylor, *Fuel* 69 (1990) 1474-1482.
- [37] M. Banar, V. Akyıldız, A. Özkan, Z. Çokaygil, Ö. Onay, *Energ. Conv. Manage.* 62 (2012) 22-30.
- [38] P.T. Williams, R.P. Bottrill, A.M. Cunliffe, *Process Saf. Environ.* 76 (1998) 291-301.
- [39] M.F. Laresgoiti, B.M. Caballero, I. de Marco, A. Torres, M.A. Cabrero, M.J. Chomón, *J. Anal. Appl. Pyrol.* 71 (2004) 917-934.
- [40] W. Kaminsky, C. Mennerich, *J. Anal. Appl. Pyrol.* 58-59 (2001) 803-811.
- [41] W. Kaminsky, M. Predel, A. Sadiki, *Polym. Degrad. Stab.* 85 (2004) 1045-1050.
- [42] W. Kaminsky, C. Mennerich, Z. Zhang, *J. Anal. Appl. Pyrol.* 85 (2009) 334-337.
- [43] W. Kaminsky, *J. Anal. Appl. Pyrol.* 8 (1985) 439-448.
- [44] P.T. Williams, A.J. Brindle, *J. Anal. Appl. Pyrol.* 67 (2003) 143-164.
- [45] X. Dai, X. Yin, C. Wu, W. Zhang, Y. Chen, *Energy* 26 (2001) 385-399.

- [46] A. Chaala, C. Roy, *Fuel. Process. Technol.* 46 (1996) 227-239.
- [47] A. Chaala, O.G. Ciochina, C. Roy, *Resour. Conserv. Recy.* 26 (1999) 155-172.
- [48] X. Zhang, T. Wang, L. Ma, J. Chang, *Waste Manage.* 28 (2008) 2301-2310.
- [49] B. Acevedo, C. Barriocanal, *Fuel. Process. Technol.* 131 (2015) 109-116.
- [50] W. Klose, W. Wiest, *Fuel* 78 (1999) 65-72.
- [51] S. Galvagno, S. Casu, T. Casabianca, A. Calabrese, G. Cornacchia, *Waste Manage.* 22 (2002) 917-923.
- [52] D. Vélez, Aspectos básicos de la tecnología de pirólisis de neumáticos en un reactor de spouted bed cónico, Universidad del País Vasco, Bilbao, 2004.
- [53] R. Aguado, M. Olazar, B. Gaisán, R. Prieto, J. Bilbao, *Chem. Eng. J.* 92 (2003) 91-99.
- [54] R. Aguado, M. Olazar, M.J. San José, G. Aguirre, J. Bilbao, *Ind. Eng. Chem. Res.* 39 (2000) 1925-1933.
- [55] M. Arabiourrutia, Productos y cinética de la pirólisis térmica y catalítica de neumáticos en un reactor de spouted bed cónico, Universidad del País Vasco, Bilbao, 2007.
- [56] G. López, M. Olazar, R. Aguado, J. Bilbao, *Fuel* 89 (2010) 1946-1952.
- [57] M. Olazar, M.J. San José, A.T. Aguayo, J.M. Arandes, J. Bilbao, *Ind. Eng. Chem. Res.* 31 (1992) 1784-1792.
- [58] M. Olazar, M.J. San José, A.T. Aguayo, J.M. Arandes, J. Bilbao, *Chem. Eng. J.* 51 (1993) 53-60.
- [59] M. Olazar, M.J. San Jose, F.J. Penas, A.T. Aguayo, J.M. Arandes, J. Bilbao, *Can. J. Chem. Eng.* 71 (1993) 189-194.
- [60] W. Kaminsky, H. Sinn, *Kunstst-Plast* 68 (1978) 14-17.
- [61] M. Kyari, A. Cunliffe, P.T. Williams, *Energy Fuels* 19 (2005) 1165-1173.
- [62] D.Y.C. Leung, X.L. Yin, Z.L. Zhao, B.Y. Xu, Y. Chen, *Fuel. Process. Technol.* 79 (2002) 141-155.
- [63] G.S. Miguel, G.D. Fowler, C.J. Sollars, *Ind. Eng. Chem. Res.* 37 (1998) 2430-2435.
- [64] A. Chaala, H. Darmstadt, C. Roy, *Fuel. Process. Technol.* 46 (1996) 1-15.
- [65] A.M. Cunliffe, P.T. Williams, *Environ. Technol.* 19 (1998) 1177-1190.
- [66] S.Q. Li, Q. Yao, Y. Chi, J.H. Yan, K.F. Cen, *Ind. Eng. Chem. Res.* 43 (2004) 5133-5145.
- [67] J.A. Conesa, I. Martín-Gullón, R. Font, J. Jauhiainen, *Environ. Sci. Technol.* 38 (2004) 3189-3194.

- [68] Z. Mikulova, I. Sedenkova, L. Matejova, M. Večeř, V. Dombek, J. Therm. Anal. Calorim. 111 (2013) 1475-1481.
- [69] J.F. González, J.M. Encinar, J.L. Canito, J.J. Rodríguez, J. Anal. Appl. Pyrol. 58-59 (2001) 667-683.
- [70] H. Teng, M.A. Serio, M.A. Wójtowicz, R. Bassilakis, P.R. Solomon, Ind. Eng. Chem. Res. 34 (1995) 3102-3111.
- [71] G. San Miguel, G.D. Fowler, C.J. Sollars, Carbon 41 (2003) 1009-1016.
- [72] R. Murillo, M.V. Navarro, T. García, J.M. López, M.S. Callén, E. Aylón, A.M. Mastral, Ind. Eng. Chem. Res. 44 (2005) 7228-7233.
- [73] E.L.K. Mui, D.C.K. Ko, G. McKay, Carbon 42 (2004) 2789-2805.
- [74] A.A. Zabaniotou, G. Stavropoulos, J. Anal. Appl. Pyrol. 70 (2003) 711-722.
- [75] M. Olazar, M.J. San José, S. Alvarez, A. Morales, J. Bilbao, Ind. Eng. Chem. Res. 43 (2004) 655-661.
- [76] S. Mirmiran, H. Pakdel, C. Roy, J. Anal. Appl. Pyrol. 22 (1992) 205-215.
- [77] H. Pakdel, D.M. Pantea, C. Roy, J. Anal. Appl. Pyrol. 57 (2001) 91-107.
- [78] A. Quek, R. Balasubramanian, J. Anal. Appl. Pyrol. 101 (2013) 1-16.
- [79] K. Unapumnuk, T.C. Keener, M. Lu, F. Liang, Fuel 87 (2008) 951-956.
- [80] E. Aylón, A. Fernández-Colino, M.V. Navarro, R. Murillo, T. García, A.M. Mastral, Ind. Eng. Chem. Res. 47 (2008) 4029-4033.
- [81] J.D. Martínez, M. Lapuerta, R. García-Contreras, R. Murillo, T. García, Energy Fuels 27 (2013) 3296-3305.
- [82] F.A. López, T.A. Centeno, F.J. Alguacil, B. Lobato, J. Hazard. Mat. 190 (2011) 285-292.
- [83] S. Uçar, S. Karagöz, J. Yanik, M. Saglam, M. Yuksel, Fuel. Process. Technol. 87 (2005) 53-58.
- [84] N.A. Dũng, S. Wongkasemjit, S. Jitkarnka, Appl. Cat. B. Environ. 91 (2009) 300-307.
- [85] P.T. Williams, D.T. Taylor, Fuel 72 (1993) 1469-1474.
- [86] P.T. Williams, R.P. Bottrill, Fuel 74 (1995) 736-742.
- [87] H. Pakdel, C. Roy, H. Aubln, G. Jean, S. Coulombe, Environ. Sci. Technol. 25 (1991) 1646-1649.
- [88] M. Arabiourrutia, G. Lopez, G. Elordi, M. Olazar, R. Aguado, J. Bilbao, Chem. Eng. Sci. 62 (2007) 5271-5275.
- [89] B. Benallal, C. Roy, H. Pakdel, S. Chabot, M.A. Poirier, Fuel 74 (1995) 1589-1594.
- [90] C. Roy, H. Darmstadt, B. Benallal, C. Amen-Chen, Fuel. Process. Technol. 50 (1997) 87-103.

- [91] G. Lopez, R. Aguado, M. Olazar, M. Arabiourrutia, J. Bilbao, *Waste Manage.* 29 (2009) 2649-2655.
- [92] M. Olazar, M. Arabiourrutia, G. López, R. Aguado, J. Bilbao, *J. Anal. Appl. Pyrol.* 82 (2008) 199-204.
- [93] E. Kwon, M.J. Castaldi, *Environ. Sci. Technol.* 43 (2009) 5996-6002.
- [94] M. Stanciulescu, M. Ikura, *J. Anal. Appl. Pyrol.* 75 (2006) 217-225.
- [95] M. Stanciulescu, M. Ikura, *J. Anal. Appl. Pyrol.* 78 (2007) 76-84.
- [96] M. Arabiourrutia, G. López, G. Elordi, M. Olazar, R. Aguado, J. Bilbao, *Int. J. Chem. React. Eng.* 5 (2007) A96.
- [97] M.Y. Wey, B.H. Liou, S.Y. Wu, C.H. Zhang, *J. Air Waste Manage.* 45 (1995) 855-863.
- [98] J. Weitkamp, A. Raichle, Y. Traa, *Appl. Cat. A. Gen.* 222 (2001) 277-297.
- [99] P.T. Williams, A.J. Brindle, *Fuel* 82 (2003) 1023-1031.
- [100] S. Boxiong, W. Chunfei, G. Binbin, W. Rui, Liangcai, *Appl. Cat. B. Environ.* 73 (2007) 150-157.
- [101] P.T. Williams, A.J. Brindle, *Fuel* 81 (2002) 2425-2434.
- [102] C. İlkılıç, H. Aydın, *Fuel. Process. Technol.* 92 (2011) 1129-1135.
- [103] S. Murugan, M.C. Ramaswamy, G. Nagarajan, *Fuel. Process. Technol.* 89 (2008) 152-159.
- [104] S. Hariharan, S. Murugan, G. Nagarajan, *Fuel* 104 (2013) 109-115.
- [105] A. Hooshmand Ahoor, N. Zandi-Atashbar, *Energ. Conv. Manage.* 87 (2014) 653-669.
- [106] E. Furimsky, *Appl. Cat. A. Gen.* 171 (1998) 177-206.
- [107] J. Uchytíl, E. Jakubíčková, M. Kraus, *J. Catal.* 64 (1980) 143-149.
- [108] A.V. Sapre, B.C. Gates, *Ind. Eng. Chem. Process Des. Dev.* 20 (1981) 68-73.
- [109] T.E. Klimova, D. Valencia, J.A. Mendoza-Nieto, P. Hernández-Hipólito, *J. Catal.* 304 (2013) 29-46.
- [110] D. Solís, A.L. Agudo, J. Ramírez, T. Klimova, *Catal. Today* 116 (2006) 469-477.
- [111] D. Valencia, T. Klimova, *Catal. Commun.* 21 (2012) 77-81.
- [112] L. Peña, D. Valencia, T. Klimova, *Appl. Cat. B. Environ.* 147 (2014) 879-887.
- [113] C. Song, X. Ma, *Appl. Cat. B. Environ.* 41 (2003) 207-238.
- [114] C. Song, *Catal. Today* 86 (2003) 211-263.
- [115] B.C. Gates, H. Topsøe, *Polyhedron* 16 (1997) 3213-3217.

-
- [116] P.R. Robinson, G.E. Dolbear, *Hydrotreating and Hydrocracking. Fundamentals.*, Springer Science and Business Media Inc., United States of America, 2006.
- [117] H. Topsoe, B.S. Clausen, F.E. Massoth, *Hydrotreating Catalysis*, Springer-Verlag New York, Berlin, 1996.
- [118] M. Göhlich, S. Böttcher, K. Räuchle, W. Reschetilowski, *Catal. Commun.* 12 (2011) 757-760.
- [119] L. Vradman, M.V. Landau, M. Herskowitz, *Fuel* 82 (2003) 633-639.
- [120] J.H. Gary, G.E. Handwerk, M.J. Kaiser, *Petroleum Refining. Technology and Economics*, CRC Press. Taylor & Francis Group, Florida, US, 2007.
- [121] J.G. Speight, *The Refinery of the Future*, William Andrew Publishing, 2011.
- [122] F. Regali, M. Boutonnet, S. Järås, *Catal. Today* 214 (2013) 12-18.
- [123] F. Regali, L.F. Liotta, A.M. Venezia, M. Boutonnet, S. Järås, *Appl. Cat. A. Gen.* 469 (2014) 328-339.
- [124] S.J. Ardakani, K.J. Smith, *Appl. Cat. A. Gen.* 403 (2011) 36-47.
- [125] P. Castaño, A. Gutiérrez, I. Hita, J.M. Arandes, A.T. Aguayo, J. Bilbao, *Energy Fuels* 26 (2012) 1509-1519.
- [126] M. Ibáñez, B. Valle, J. Bilbao, A.G. Gayubo, P. Castaño, *Catal. Today* 195 (2012) 106-113.
- [127] J.R. González-Velasco, J.A. González Marcos, M.P. González Marcos, J.I. Gutiérrez Ortiz, M.A. Gutiérrez Ortiz, *Cinética Química Aplicada*, Editorial Síntesis, Madrid, 1999.
- [128] H.S. Cerqueira, G. Caeiro, L. Costa, F. Ramôa Ribeiro, J. *Molec. Catal. A. Chem.* 292 (2008) 1-13.
- [129] A. Gruia, *Handbook of Petroleum Processing*, Springer Netherlands, The Netherlands, 2006.
- [130] M. Guisnet, P. Magnoux, *Appl. Cat. A. Gen.* 212 (2001) 83-96.
- [131] J.A. Moulijn, M. Makkee, A. Van Diepen, *Chemical Process Technology*, Wiley, England, 2001.
- [132] I.V. Babich, J.A. Moulijn, *Fuel* 82 (2003) 607-631.
- [133] E. Furimsky, *Catalyst for Upgrading Heavy Petroleum Feeds*, Elsevier, Amsterdam, 2007.
- [134] J. Ancheyta, M.S. Rana, E. Furimsky, *Catal. Today* 109 (2005) 3-15.
- [135] S.K. Maity, J. Ancheyta, L. Soberanis, F. Alonso, M.E. Llanos, *Appl. Cat. A. Gen.* 244 (2003) 141-153.
- [136] S.K. Maity, J. Ancheyta, F. Alonso, M.S. Rana, *Catal. Today* 98 (2004) 193-199.

- [137] P. Rayo, J. Ancheyta, J. Ramírez, A. Gutiérrez-Alejandre, *Catal. Today* 98 (2004) 171-179.
- [138] J. Ramírez, P. Rayo, A. Gutiérrez-Alejandre, J. Ancheyta, M.S. Rana, *Catal. Today* 109 (2005) 54-60.
- [139] M.S. Rana, M.L. Huidobro, J. Ancheyta, M.T. Gómez, *Catal. Today* 107-108 (2005) 346-354.
- [140] B. Caloch, M.S. Rana, J. Ancheyta, *Catal. Today* 98 (2004) 91-98.
- [141] P. Castaño, A.G. Gayubo, B. Pawelec, J.L.G. Fierro, J.M. Arandes, *Chem. Eng. J.* 140 (2008) 287-295.
- [142] P. Castaño, A. Gutiérrez, I. Villanueva, B. Pawelec, J. Bilbao, J.M. Arandes, *Catal. Today* 143 (2009) 115-119.
- [143] P. Castaño, J.M. Arandes, B. Pawelec, M. Olazar, J. Bilbao, *Ind. Eng. Chem. Res.* 47 (2008) 1043-1050.
- [144] P. Castaño, B. Pawelec, A.T. Aguayo, A.G. Gayubo, J.M. Arandes, *Ind. Eng. Chem. Res.* 47 (2008) 665-671.
- [145] P. Castaño, B. Pawelec, J.L.G. Fierro, J.M. Arandes, J. Bilbao, *Appl. Cat. A. Gen.* 315 (2006) 101-113.
- [146] A. Gutiérrez, J.M. Arandes, P. Castaño, M. Olazar, J. Bilbao, *Fuel. Process. Technol.* 101 (2012) 64-72.
- [147] R. Henry, M. Tayakout-Fayolle, P. Afanasiev, C. Lorentz, G. Lapisardi, G. Pirngruber, *Catal. Today* 220-222 (2014) 159-167.
- [148] F.A. Khowatimy, Y. Priastomo, E. Febriyanti, H. Riyantoko, W. Trisunaryanti, *Procedia Environ. Sci.* 20 (2014) 225-234.
- [149] J.L. Agudelo, B. Mezari, E.J.M. Hensen, S.A. Giraldo, L.J. Hoyos, *Appl. Cat. A. Gen.* 488 (2014) 219-230.
- [150] K. Inamura, A. Iino, *Catal. Today* 164 (2011) 204-208.
- [151] S. Chen, Y. Yang, K. Zhang, J. Wang, *Catal. Today* 116 (2006) 2-5.
- [152] J.F.M. Denayer, B. De Jonckheere, M. Hloch, G.B. Marin, G. Vanbutsele, J.A. Martens, G.V. Baron, *J. Catal.* 210 (2002) 445-452.
- [153] A. Corma, *J. Catal.* 216 (2003) 298-312.
- [154] H. Tüysüz, F. Schüth, *Adv. Catal.* 55 (2012) 127-239.
- [155] A. Taguchi, F. Schüth, *Micropor. Mesopor. Mater.* 77 (2005) 1-45.
- [156] W.J.J. Stevens, K. Lebeau, M. Mertens, G. Van Tendeloo, P. Cool, E.F. Vansant, *J. Phys. Chem. B* 110 (2006) 9183-9187.
- [157] F. Zhang, Y. Yan, H. Yang, Y. Meng, C. Yu, B. Tu, D. Zhao, *J. Phys. Chem. B* 109 (2005) 8723-8732.
- [158] R. Silva-Rodrigo, F. Hernández-López, K. Martínez-Juarez, A. Castillo-Mares, J.A. Melo Banda, A. Olivás-Sarabia, J. Ancheyta, M.S. Rana, *Catal. Today* 130 (2008) 309-319.

-
- [159] R. Silva-Rodrigo, H. Castillo Jimenez, A. Guevara-Lara, J.A. Melo-Banda, A. Olivas Sarabia, A.I. Reyes de la Torre, F. Morteo Flores, A. Castillo Mares, *Catal. Today*. doi: 10.1016/j.cattod.2014.09.007.
- [160] M. Hussain, S.-K. Song, S.-K. Ihm, *Fuel* 106 (2013) 787-792.
- [161] G.M. Esquivel, J. Ramírez, A. Gutiérrez-Alejandre, *Catal. Today* 148 (2009) 36-41.
- [162] A. Soriano, P. Roquero, T. Klimova, *Stud. Surf. Sci. Catal.* 175 (2010) 525-528.
- [163] O.Y. Gutiérrez, G.A. Fuentes, C. Salcedo, T. Klimova, *Catal. Today* 116 (2006) 485-497.
- [164] R. Huirache-Acuña, B. Pawelec, E. Rivera-Muñoz, R. Nava, J. Espino, J.L.G. Fierro, *Appl. Cat. B. Environ.* 92 (2009) 168-184.
- [165] K.K. Soni, P.E. Boahene, N. Rambabu, A.K. Dalai, J. Adjaye, *Catal. Today* 207 (2013) 119-126.
- [166] V. Sundaramurthy, I. Eswaramoorthi, A.K. Dalai, J. Adjaye, *Micropor. Mesopor. Mater.* 111 (2008) 560-568.
- [167] P.E. Boahene, K.K. Soni, A.K. Dalai, J. Adjaye, *Appl. Cat. A. Gen.* 402 (2011) 31-40.
- [168] P.E. Boahene, K.K. Soni, A.K. Dalai, J. Adjaye, *Catal. Today* 207 (2013) 101-111.
- [169] U.T. Turaga, C. Song, *Catal. Today* 86 (2003) 129-140.
- [170] H. Fukuyama, S. Terai, M. Uchida, J.L. Cano, J. Ancheyta, *Catal. Today* 98 (2004) 207-215.
- [171] E. Gonzalez-Serrano, T. Cordero, J. Rodriguez-Mirasol, L. Cotoruelo, J.J. Rodriguez, *Water Res.* 38 (2004) 3043-3050.
- [172] J.M. Rosas, R. Ruiz-Rosas, J. Rodríguez-Mirasol, T. Cordero, *Carbon* 50 (2012) 1523-1537.
- [173] J. Jaramillo, P.M. Álvarez, V. Gómez-Serrano, *Fuel. Process. Technol.* 91 (2010) 1768-1775.
- [174] Y. Gokce, Z. Aktas, *Appl. Surf. Sci.* 313 (2014) 352-359.
- [175] H. Shamsijazeyi, T. Kaghazchi, *J. Ind. Eng. Chem.* 16 (2010) 852-858.
- [176] J.-X. Guo, J. Liang, Y.-H. Chu, M.-C. Sun, H.-Q. Yin, J.-J. Li, *Appl. Cat. A. Gen.* 421-422 (2012) 142-147.
- [177] E. Auer, A. Freund, J. Pietsch, T. Tacke, *Appl. Cat. A. Gen.* 173 (1998) 259-271.
- [178] W.M.A.W. Daud, A.H. Houshamnd, *J. Nat. Gas Chem.* 19 (2010) 267-279.
- [179] R. Zarchin, M. Rabaev, R. Vidruk-Nehemya, M.V. Landau, M. Herskowitz, *Fuel* 139 (2015) 684-691.

- [180] T.T. Viet, J.H. Lee, F. Ma, G.R. Kim, I.S. Ahn, C.H. Lee, *Fuel* 103 (2013) 553-561.
- [181] N. Prabhu, A.K. Dalai, J. Adjaye, *Appl. Cat. A. Gen.* 401 (2011) 1-11.
- [182] H. Purón, J.L. Pinilla, I. Suelves, M. Millan, *Catal. Today*. doi:10.1016/j.cattod.2014.09.021 .
- [183] J.L. Pinilla, H. Purón, D. Torres, S. de Llobet, R. Moliner, I. Suelves, M. Millan, *Appl. Cat. B. Environ.* 148-149 (2014) 357-365.
- [184] S.K. Maity, J. Ancheyta, *Catal. Today* 150 (2010) 231-236.
- [185] G.C. Laredo, C.M. Córtes, *Appl. Cat. A. Gen.* 252 (2003) 295-304.
- [186] Z. Contreras-Valdez, J.C. Mogica-Betancourt, A. Alvarez-Hernández, A. Guevara-Lara, *Fuel* 106 (2013) 519-527.
- [187] B. Liu, Y. Chai, Y. Li, A. Wang, Y. Liu, C. Liu, *Fuel* 123 (2014) 43-51.
- [188] M.A. Rodríguez, I. Elizalde, J. Ancheyta, *Fuel* 100 (2012) 91-99.
- [189] J. Ancheyta, *Modeling and Simulation of Catalytic Reactors for Petroleum Refining*, Hoboken, New Jersey, 2011.
- [190] M.A. Callejas, M.T. Martínez, *Energy Fuels* 13 (1999) 629-636.
- [191] D.I. Orochko, I.Y. Perezhigina, S.P. Rogov, M.V. Rysakov, G.N. Chernakova, *Chem. Technol. Fuel. Oil.* 6 (1971) 561-565.
- [192] C. Botchwey, A.K. Dalai, J. Adjaye, *Can. J. Chem. Eng.* 82 (2004) 478-487.
- [193] S. Sánchez, M.A. Rodríguez, J. Ancheyta, *Ind. Eng. Chem. Res.* 44 (2005) 9409-9413.
- [194] R. Krishna, A.K. Saxena, *Chem. Eng. Sci.* 44 (1989) 703-712.
- [195] C.S. Laxminarasimhan, R.P. Verma, P.A. Ramachandran, *AIChE J.* 42 (1996) 2645-2653.
- [196] K. Basak, M. Sau, U. Manna, R.P. Verma, *Catal. Today* 98 (2004) 253-264.
- [197] I. Elizalde, M.A. Rodríguez, J. Ancheyta, *Appl. Cat. A. Gen.* 382 (2010) 205-212.
- [198] G.F. Froment, *Catal. Today* 98 (2004) 43-54.
- [199] G.F. Froment, *Curr. Opin. Chem. Eng.* 5 (2014) 1-6.
- [200] G.F. Froment, in *AIChE Annual Meeting, Conference Proceedings, 2005*, p. 9576.
- [201] V.V. Ranade, R.V. Chaudhari, P.R. Gunjal, in: V.V. Ranade, R.V. Chaudhari, R. Gunjal (Eds.), *Trickle Bed Reactors*, Elsevier, Amsterdam, 2011, pp. 77-116.
- [202] J.A.D. Muñoz, A. Alvarez, J. Ancheyta, M.A. Rodríguez, G. Marroquín, *Catal. Today* 109 (2005) 214-218.
- [203] A. Alvarez, J. Ancheyta, J.A.D. Muñoz, *Energ. Fuel.* 21 (2007) 1133-1144.

-
- [204] A. Alvarez, S. Ramírez, J. Ancheyta, L.M. Rodríguez, *Energy Fuels* 21 (2007) 1731-1740.
- [205] G. Elordi, M. Olazar, G. Lopez, M. Amutio, M. Artetxe, R. Aguado, J. Bilbao, *J. Anal. Appl. Pyrol.* 85 (2009) 345-351.
- [206] H. Yang, Z. Ring, Y. Briker, N. McLean, W. Friesen, C. Fairbridge, *Fuel* 81 (2002) 65-74.
- [207] D. Del Río, M. Rey, U. Sedran, G. de la Puente, *Fuel. Process. Technol.* 92 (2011) 2278-2284.
- [208] F.C.Y. Wang, W.K. Robbins, F.P. Di Sanzo, F.C. McElroy, *J. Chromatogr. Sci.* 41 (2003) 519-523.
- [209] M.R. Riazi, Y.A. Roomi, *Chem. Eng. Sci.* 62 (2007) 6649-6658.
- [210] P.T. Tanev, T.J. Pinnavaia, *Chem. Mater.* 8 (1996) 2068-2079.
- [211] D. Zhao, Q. Huo, J. Feng, B.F. Chmelka, G.D. Stucky, *J. Am. Chem. Soc.* 120 (1998) 6024-6036.
- [212] A.C.M. Van Den Broek, J. Van Grondelle, R.A. Van Santen, *J. Catal.* 167 (1997) 417-424.
- [213] P. Castaño, *Hidrocrackeo de aromáticos ligeros a n-alcanos C2+. Variables de proceso y modelado cinético.*, Universidad del País Vasco, Bilbao, 2006.
- [214] S. Narayanan, A. Sultana, Q.T. Le, A. Auroux, *Appl. Cat. A. Gen.* 168 (1998) 373-384.
- [215] A.G. Gayubo, A.T. Aguayo, M. Olazar, R. Vivanco, J. Bilbao, *Chem. Eng. Sci.* 58 (2003) 5239-5249.
- [216] A.T. Aguayo, J.M. Arandes, M. Olazar, J. Bilbao, *Ind. Eng. Chem. Res.* 29 (1990) 1621-1626.
- [217] A.G. Gayubo, P.L. Benito, A.T. Aguayo, M. Olazar, J. Bilbao, *J. Chem. Technol. Biotech.* 65 (1996) 186-192.
- [218] N. Márquez, M.T. Kreutzer, M. Makkee, J.A. Moulijn, *J. Chem. Eng. Data* 53 (2008) 439-443.
- [219] M. Ibáñez, M. Artetxe, G. Lopez, G. Elordi, J. Bilbao, M. Olazar, P. Castaño, *Appl. Cat. B. Environ.* 148-149 (2014) 436-445.
- [220] D. Li, Z. Li, W. Li, Q. Liu, Z. Feng, Z. Fan, *J. Anal. Appl. Pyrol.* 100 (2013) 245-252.
- [221] Z. Lei, L. Gao, H. Shui, W. Chen, Z. Wang, S. Ren, *Fuel. Process. Technol.* 92 (2011) 2055-2060.
- [222] W. Chaiwat, R. Gunawan, M. Gholizadeh, X. Li, C. Lievens, X. Hu, Y. Wang, D. Mourant, A. Rossiter, J. Bromly, C.-Z. Li, *Fuel* 112 (2013) 302-310.
- [223] M. Egorova, R. Prins, *J. Catal.* 225 (2004) 417-427.
- [224] F. Richard, T. Boita, G. Pérot, *Appl. Cat. A. Gen.* 320 (2007) 69-79.

- [225] J.V. Lauritsen, J. Kibsgaard, G.H. Olesen, P.G. Moses, B. Hinnemann, S. Helveg, J.K. Nørskov, B.S. Clausen, H. Topsøe, E. Lægsgaard, F. Besenbacher, *J. Catal.* 249 (2007) 220-233.
- [226] R. Nava, A. Infantes-Molina, P. Castaño, R. Guil-López, B. Pawelec, *Fuel* 90 (2011) 2726-2737.
- [227] J.M. Herrera, J. Reyes, P. Roquero, T. Klimova, *Micropor. Mesopor. Mater.* 83 (2005) 283-291.
- [228] F. Subhan, B.S. Liu, Y. Zhang, X.G. Li, *Fuel. Process. Technol.* 97 (2012) 71-78.
- [229] L. Vradman, M.V. Landau, M. Herskowitz, V. Ezersky, M. Talianker, S. Nikitenko, Y. Kolytyn, A. Gedanken, *J. Catal.* 213 (2003) 163-175.
- [230] S. Inagaki, M. Ogura, T. Inami, Y. Sasaki, E. Kikuchi, M. Matsuka, *Micropor. Mesopor. Mater.* 74 (2004) 163-170.
- [231] A. Tuel, L.G. Hubert-Pfalzgraf, *J. Catal.* 217 (2003) 343-353.
- [232] E. Epelde, A.G. Gayubo, M. Olazar, J. Bilbao, A.T. Aguayo, *Chem. Eng. J.* 251 (2014) 80-91.
- [233] D. Valencia, T. Klimova, *Catal. Today* 166 (2011) 91-101.
- [234] P. Topka, J. Karban, K. Soukup, K. Jirátová, O. Šolcová, *Chem. Eng. J.* 168 (2011) 433-440.
- [235] O.Y. Gutiérrez, G.A. Fuentes, C. Salcedo, T. Klimova, *Catal. Today* 116 (2006) 485-497.
- [236] J. Ren, A. Wang, X. Li, Y. Chen, H. Liu, Y. Hu, *Appl. Cat. A. Gen.* 344 (2008) 175-182.
- [237] C. De la Paz-Zavala, E. Burgos-Vázquez, J.E. Rodríguez-Rodríguez, L.F. Ramírez-Verduzco, *Fuel* 110 (2013) 227-234.
- [238] D.D. Link, P. Zandhuis, *Fuel* 85 (2006) 451-455.
- [239] T.E. Klimova, D. Valencia, J.A. Mendoza-Nieto, P. Hernández-Hipólito, *J. Catal.* 304 (2013) 29-46.
- [240] G. Castorena, C. Suárez, I. Valdez, G. Amador, L. Fernández, S. Le Borgne, *FEMS Microbiol. Lett.* 215 (2002) 157-161.
- [241] B. Pawelec, R.M. Navarro, J.M. Campos-Martin, A. López Agudo, P.T. Vasudevan, J.L.G. Fierro, *Catal. Today* 86 (2003) 73-85.
- [242] H.R. Reinhoudt, R. Troost, S. van Schalkwijk, A.D. van Langeveld, S.T. Sie, H. Schulz, D. CHDAwick, J. Cambra, V.H.J. de Beer, J.A.R. van Veen, J.L.G. Fierro, J.A. Moulijn, *Stud. Surf. Sci. Catal.* 106 (1997) 237-244.
- [243] C.N. Satterfield, S.H. Yang, *J. Catal.* 81 (1983) 335-346.
- [244] P. Castaño, A. Gutierrez, I. Hita, J.M. Arandes, A.T. Aguayo, J. Bilbao, *Energy Fuels* 26 (2012) 1509-1519.

- [245] P. Castaño, D. van Herk, M.T. Kreutzer, J.A. Moulijn, M. Makkee, *Appl. Catal. B: Environ.* 88 (2009) 213-223.
- [246] M. Nagai, T. Kabe, *J. Catal.* 81 (1983) 440-449.
- [247] H. Topsøe, B.S. Clausen, F.E. Massoth, *Hydrotreating Catalysis*, Springer-Verlag, Berlin, 1996.
- [248] M.A. Cambor, A. Corma, A. Martínez, V. Martínez Soria, S. Valencia, *J. Catal.* 179 (1998) 537-547.
- [249] A. Ishihara, T. Itoh, H. Nasu, T. Hashimoto, T. Doi, *Fuel. Process. Technol.* 116 (2013) 222-227.
- [250] M.J. Girgis, B.C. Gates, *Ind. Eng. Chem. Res.* 30 (1991) 2021-2058.
- [251] T. Kan, H. Wang, H. He, C. Li, S. Zhang, *Fuel* 90 (2011) 3404-3409.
- [252] K. Nakano, W. Pang, J.K. Lee, J.I. Park, Y. Seong-Ho, I. Mochida, *Fuel. Process. Technol.* 92 (2011) 1012-1018.
- [253] V. Rabarihoela-Rakotovao, S. Brunet, G. Perot, F. Diehl, *Appl. Cat. A. Gen.* 306 (2006) 34-44.
- [254] L.E. Kallinikos, G.D. Bellos, N.G. Papayannakos, *Fuel* 87 (2008) 2444-2449.
- [255] R. Shafi, G.J. Hutchings, *Catal. Today* 59 (2000) 423-442.
- [256] T. Kim, S.A. Ali, K. Alhooshani, J.-I. Park, M. Al-Yami, S.-H. Yoon, I. Mochida, *J. Ind. Eng. Chem.* 19 (2013) 1577-1582.
- [257] B. Celse, V. Costa, F. Wahl, J.J. Verstraete, *Chem. Eng. J.* doi: 10.1016/j.cej.2014.11.098
- [258] M. Lewandowski, *Appl. Cat. B. Environ.* 160-161 (2014) 10-21.
- [259] C.O. Castillo-Araiza, G. Chávez, A. Dutta, J.A. de los Reyes, S. Nuñez, J.C. García-Martínez, *Fuel. Process. Technol.* 132 (2015) 164-172.
- [260] J.C. García-Martínez, C.O. Castillo-Araiza, J.A. De los Reyes Heredia, E. Trejo, A. Montesinos, *Chem. Eng. J.* 210 (2012) 53-62.
- [261] X. Li, A. Wang, M. Egorova, R. Prins, *J. Catal.* 250 (2007) 283-293.
- [262] C. Ferreira, M. Tayakout-Fayolle, I. Guibard, F. Lemos, *Fuel* 129 (2014) 267-277.
- [263] A.T. Jarullah, I.M. Mujtaba, A.S. Wood, *Chem. Eng. Sci.* 66 (2011) 859-871.
- [264] G.F. Froment, L.C. Castaneda-Lopez, C. Marin-Rosas, *Catal. Today* 130 (2008) 446-454.
- [265] A. Gutierrez, *Valorización por hidrocrqueo de corrientes aromáticas en la refinería sostenible*, Universidad del País Vasco, Bilbao, 2010.
- [266] P. Rayo, J. Ramírez, P. Torres-Mancera, G. Marroquín, S.K. Maity, J. Ancheyta, *Fuel* 100 (2012) 34-42.

- [267] S. Ramírez, J. Martínez, J. Ancheyta, *Fuel* 110 (2013) 83-88.
- [268] J. Martínez, J. Ancheyta, *Fuel* 100 (2012) 193-199.
- [269] H. Puron, P. Arcelus-Arrillaga, K.K. Chin, J.L. Pinilla, B. Fidalgo, M. Millan, *Fuel* 117 (2014) 408-414.
- [270] C. Leyva, J. Ancheyta, A. Travert, F. Maugé, L. Mariey, J. Ramírez, M.S. Rana, *Appl. Catal. A. Gen.* 425-426 (2012) 1-12.
- [271] P. Rayo, J. Ramírez, P. Torres-Mancera, G. Marroquín, S.K. Maity, J. Ancheyta, *Fuel* 100 (2012) 34-42.
- [272] C. Leyva, J. Ancheyta, A. Travert, F. Maugé, L. Mariey, J. Ramírez, M.S. Rana, *Appl. Catal. A: Gen.* 425-426 (2012) 1-12.
- [273] J.H. Gary, G.E. Handwerk, M.J. Kaiser, *Petroleum Refining. Technology and Economics*, CRC Press, Boca Raton, 2007.
- [274] P. Castaño, J.M. Arandes, B. Pawelec, J.L.G. Fierro, A. Gutiérrez, J. Bilbao, *Ind. Eng. Chem. Res.* 46 (2007) 7417-7425.
- [275] A. Gutiérrez, P. Castaño, M.J. Azkoiti, J. Bilbao, J.M. Arandes, *Chem. Eng. J.* 176-177 (2011) 302-311.
- [276] W. Tang, M. Fang, H. Wang, P. Yu, Q. Wang, Z. Luo, *Chem. Eng. J.* 236 (2014) 529-537.
- [277] A. Gutiérrez, J.M. Arandes, P. Castaño, M. Olazar, A. Barona, J. Bilbao, *Fuel. Process. Technol.* 95 (2012) 8-15.
- [278] S. Melis, L. Erby, L. Sassu, R. Baratti, *Chem. Eng. Sci.* 59 (2004) 5671-5677.
- [279] S.A. Kishore Kumar, M. John, S.M. Pai, Y. Niwate, B.L. Newalkar, *Fuel. Process. Technol.* 128 (2014) 303-309.
- [280] M.S. Rana, J. Ancheyta, S.K. Sahoo, P. Rayo, *Catal. Today* 220-222 (2014) 97-105.
- [281] Y. Yoshimura, M. Toba, T. Matsui, M. Harada, Y. Ichihashi, K.K. Bando, H. Yasuda, H. Ishihara, Y. Morita, T. Kameoka, *Appl. Catal. A. Gen.* 322 (2007) 152-171.
- [282] A. Gutiérrez, J.M. Arandes, P. Castaño, A.T. Aguayo, J. Bilbao, *Energy Fuels* 25 (2011) 3389-3399.
- [283] A. Gutiérrez, J.M. Arandes, P. Castaño, M. Olazar, J. Bilbao, *Fuel* 94 (2012) 504-515.
- [284] A. Corma, A. Martínez, V. Martínez-Soria, *J. Catal.* 169 (1997) 480-489.
- [285] W.-H. Chen, Q. Zhao, H.-P. Lin, Y.-S. Yang, C.-Y. Mou, S.-B. Liu, *Micropor. Mesopor. Mater.* 66 (2003) 209-218.
- [286] A.M. Alsobaai, R. Zakaria, B.H. Hameed, *Chem. Eng. J.* 132 (2007) 173-181.

- [287] A.E. Barrón C, J.A. Melo-Banda, J.M. Dominguez E, E. Hernández M, R. Silva R, A.I. Reyes T, M.A. Meraz M, *Catal. Today* 166 (2011) 102-110.
- [288] M.-G. Seo, D.-W. Lee, K.-Y. Lee, D.J. Moon, *Fuel* 143 (2015) 63-71.
- [289] P.Y. Looi, A.R. Mohamed, C.T. Tye, *Chem. Eng. J.* 181-182 (2012) 717-724.
- [290] H. Jin, X. Yi, S. Sun, J. Liu, G. Yang, H. Zhu, W. Fang, *Fuel. Process. Technol.* 97 (2012) 52-59.
- [291] R. Tiwari, B.S. Rana, R. Kumar, D. Verma, R. Kumar, R.K. Joshi, M.O. Garg, A.K. Sinha, *Catal. Commun.* 12 (2011) 559-562.
- [292] A. Ishihara, N. Fukui, H. Nasu, T. Hashimoto, *Fuel* 134 (2014) 611-617.
- [293] G. Magendie, B. Guichard, D. Espinat, *Catal. Today*.
doi:10.1016/j.cattod.2014.10.023 .
- [294] B. Sun, L. Li, Z. Fei, S. Gu, P. Lu, W. Ji, *Micropor. Mesopor. Mater.* 186 (2014) 14-20.
- [295] D. Nedumaran, A. Pandurangan, *Micropor. Mesopor. Mater.* 169 (2013) 25-34.
- [296] A.K. Hossain, P.A. Davies, *Renew. Sust. Energ. Rev.* 21 (2013) 165-189.
- [297] M. Marafi, A. Stanislaus, E. Furimsky, in: M.M.S. Furimsky (Ed.), *Handbook of Spent Hydroprocessing Catalysts*, Elsevier, Amsterdam, 2010, pp. 231-257.
- [298] M. Marafi, A. Stanislaus, E. Furimsky, in: M.M.S. Furimsky (Ed.), *Handbook of Spent Hydroprocessing Catalysts*, Elsevier, Amsterdam, 2010, pp. 17-49.
- [299] H.R. Reinhoudt, R. Troost, A.D. van Langeveld, J.A.R. van Veen, S.T. Sie, J.A. Moulijn, *Stud. Surf. Sci. Catal.* 127 (1999). 251-258.
- [300] C.O. Castillo-Araiza, G. Chávez, A. Dutta, J.A. de los Reyes, S. Nuñez, J.C. García-Martínez, *Fuel. Process. Technol.* 132 (2015) 164-172.
- [301] Z. Vít, D. Gulková, L. Kaluža, M. Boaro, *Appl. Cat. B. Environ.* 146 (2014) 213-220.
- [302] A. Infantes-Molina, A. Romero-Pérez, E. Finocchio, G. Busca, A. Jiménez-López, E. Rodríguez-Castellón, *J. Catal.* 305 (2013) 101-117.
- [303] Y. Kanda, C. Temma, K. Nakata, T. Kobayashi, M. Sugioka, Y. Uemichi, *Appl. Cat. A. Gen.* 386 (2010) 171-178.
- [304] E. Epelde, A.G. Gayubo, M. Olazar, J. Bilbao, A.T. Aguayo, *Chem. Eng. J.* 251 (2014) 80-91.
- [305] G. Nagy, G. Pölczmán, D. Kalló, J. Hancsók, *Chem. Eng. J.* 154 (2009) 307-314.
- [306] J.L. Agudelo, E.J.M. Hensen, S.A. Giraldo, L.J. Hoyos, *Fuel. Process. Technol.* 133 (2015) 89-96.

- [307] S. Magyar, J. Hancsók, D. Kalló, *Fuel. Process. Technol.* 86 (2005) 1151-1164.
- [308] M.M. Hossain, *Chem. Eng. J.* 123 (2006) 15-23.
- [309] S.-W. Lee, S.-K. Ihm, *Fuel* 134 (2014) 237-243.
- [310] C. Botchwey, A.K. Dalai, J. Adjaye, *Energy Fuels* 17 (2003) 1372-1381.
- [311] D.S.J. Jones, P.R. Pujadó, *Handbook of Petroleum Processing*, Springer, Dordrecht, The Netherlands, 2006.
- [312] H. Martinez-Grimaldo, H. Ortiz-Moreno, F. Sanchez-Minero, J. Ramírez, R. Cuevas-Garcia, J. Ancheyta-Juarez, *Catal. Today* 220-222 (2014) 295-300.
- [313] M.F. Menoufy, H.S. Ahmed, M.A. Betiha, M.A. Sayed, *Fuel* 119 (2014) 106-110.
- [314] M.-G. Seo, D.-W. Lee, K.-Y. Lee, D.J. Moon, *Fuel* 143 (2015) 63-71.
- [315] V. Calemma, C. Gambaro, W.O. Parker Jr, R. Carbone, R. Giardino, P. Scorletti, *Catal. Today* 149 (2010) 40-46.
- [316] C.H. Bartholomew, *Appl. Cat. A. Gen.* 212 (2001) 17-60.
- [317] P. Castaño, D. van Herk, M.T. Kreutzer, J.A. Moulijn, M. Makkee, *Appl. Cat. B. Environ.* 88 (2009) 213-223.
- [318] H.S. Ahmed, S.A. Shaban, M.F. Menoufy, F.Y. El Kady, *Egypt. J. Pet.* 22 (2013) 367-372.
- [319] J. Aguado, D.P. Serrano, J.M. Escola, L. Briones, *Fuel* 109 (2013) 679-686.
- [320] E. Guillon, J. Lynch, D. Uzio, B. Didillon, *Catal. Today* 65 (2001) 201-208.
- [321] C.L. Pieck, C.R. Vera, C.A. Querini, J.M. Parera, *Appl. Cat. A. Gen.* 278 (2005) 173-180.
- [322] M. Guisnet, L. Costa, F.R. Ribeiro, *J. Molec. Catal. A. Chem.* 305 (2009) 69-83.
- [323] I. Sierra, J. Ereña, A.T. Aguayo, J.M. Arandes, J. Bilbao, *Appl. Cat. B. Environ.* 94 (2010) 108-116.
- [324] B. Guichard, M. Roy-Auberger, E. Devers, B. Rebours, A.A. Quoineaud, M. Digne, *Appl. Cat. A. Gen.* 367 (2009) 1-8.
- [325] F. Tuinstra, J.L. Koenig, *J. Chem. Phys.* 53 (1970) 1126-1130.
- [326] A.C. Ferrari, J. Robertson, *Phys. Rev. B.* 61 (2000) 14095-14107.
- [327] N. Arsenova, H. Bludau, W.O. Haag, H.G. Karge, *Micropor. Mesopor. Mater.* 23 (1998) 1-10.
- [328] P. Castaño, G. Elordi, M. Olazar, A.T. Aguayo, B. Pawelec, J. Bilbao, *Appl. Cat. B. Environ.* 104 (2011) 91-100.
- [329] J. Ibarra, E. Muñoz, R. Moliner, *Org. Geochem.* 24 (1996) 725-735.

-
- [330] E. Epelde, M. Ibañez, A.T. Aguayo, A.G. Gayubo, J. Bilbao, P. Castaño, *Micropor. Mesopor. Mater.* 195 (2014) 284-293.
- [331] I. Elizalde, J. Ancheyta, *Fuel. Process. Technol.* 123 (2014) 114-121.
- [332] A. Hauser, A. Stanislaus, A. Marafi, A. Al-Adwani, *Fuel* 84 (2005) 259-269.
- [333] K. Idei, T. Takahashi, T. Kai, Sekiyu Gakkaishi, *J. Jpn. Pet. Inst.* 46 (2003) 45-52.
- [334] P. Forzatti, L. Lietti, *Catal. Today* 52 (1999) 165-181.
- [335] I. Elizalde, J. Ancheyta, *Fuel* 138 (2014) 45-51.
- [336] D. Iranshahi, R. Rafiei, M. Jafari, S. Amiri, M. Karimi, M.R. Rahimpour, *Chem. Eng. J.* 229 (2013) 153-176.
- [337] M. Artetxe, G. Lopez, M. Amutio, J. Bilbao, M. Olazar, *Chem. Eng. Sci.* 116 (2014) 635-644.
- [338] A.G. Gayubo, A. Alonso, B. Valle, A.T. Aguayo, M. Olazar, J. Bilbao, *Chem. Eng. J.* 167 (2011) 262-277.
- [339] C. Calderón, *Condiciones de proceso y modelado cinético del reformado con vapor de etanol sobre catalizador Ni/La₂O₃-Al₂O₃*, Universidad del País Vasco, Bilbao, 2015.
- [340] S. Kim, E. Sasmaz, J. Lauterbach, *Appl. Cat. B. Environ.* 168-169 (2015) 212-219.
- [341] V.G. Baldovino-Medrano, S.A. Giraldo, A. Centeno, *Fuel* 87 (2008) 1917-1926.
- [342] J.D. Martínez, T. Ramos, O. Armas, R. Murillo, T. García, *Appl. Energ.* 130 (2014) 437-446.
- [343] R. Vihar, T. Seljak, S. Rodman Oprešnik, T. Katrašnik, *Fuel.* 150 (2015) 226-235.